University of Cyprus

DEPARTMENT OF CIVIL AND ENVIRONMENTAL ENGINEERING

MODELING THE BEHAVIOR OF SHEAR-CRITICAL REINFORCED CONCRETE COLUMNS UNDER LATERAL LOADS

DOCTOR OF PHILOSOPHY DISSERTATION

KONSTANTINOS G. MEGALOOIKONOMOU

2019

DEPARTMENT OF CIVIL AND ENVIRONMENTAL ENGINEERING

MODELING THE BEHAVIOR OF SHEAR-CRITICAL REINFORCED CONCRETE COLUMNS UNDER LATERAL LOADS

KONSTANTINOS G. MEGALOOIKONOMOU

A Dissertation Submitted in Partial Fulfillment of the Requirements for the Degree of Doctor of Philosophy at the University of Cyprus

December 2019

VALIDATION PAGE

Doctoral Candidate: Konstantinos G. Megalooikonomou

Dissertation Title: Modeling the Behavior of Shear-Critical Reinforced Concrete Columns Under Lateral Loads

The present Doctorate Dissertation was submitted in partial fulfillment of the requirements for the Degree of Doctor of Philosophy in the Department of Civil and Environmental Engineering, and was approved on 19th December 2019 by the members of the Examination Committee:

Research Supervisor: Stavroula J. Pantazopoulou, Adjunct Professor at the University of Cyprus, and Professor at York University, Canada,

_____

(Signature)

Other Members

Research Co-Supervisor: Petros Komodromos, Associate Professor at the University of Cyprus

_____

Committee Chair: Dimos C. Charmpis, Associate Professor at the University of Cyprus

_____

Committee Member: Michael F. Petrou, Professor at the University of Cyprus

_____

Committee Member: Christis Z. Chrysostomou, Professor at Cyprus University of Technology

_____

Committee Member: Marios C. Phocas, Associate Professor at University of Cyprus

_____

DECLARATION OF DOCTORAL CANDIDATE

The present doctoral dissertation was submitted in partial fulfillment of the requirements for the degree of Doctor of Philosophy of the University of Cyprus. It is a product of original work of my own, unless otherwise mentioned through references, notes, or any other statements.

Konstantinos G. Megalooikonomou

_____

(Signature)

ΠΕΡΙΛΗΨΗ

Το σύγχρονο δομημένο περιβάλλον στα αστικά κέντρα της Μεσογείου κυριαρχείται από κτίρια οπλισμένου σκυροδέματος (Ο.Σ.) είτε αποτελούμενα από μικτό σύστημα φερόντων στοιχείων, είτε αμιγώς πλαισιακού τύπου. Περίπου το 70% έχει κτισθεί με τους προ του 1985 Κανονισμούς, και σήμερα θεωρούνται περιορισμένης σεισμικής ικανότητας επειδή δεν ικανοποιούν τις σύγχρονες αντιλήψεις αντισεισμικού σχεδιασμού. Εικάζεται ότι σε ενδεχόμενο ισχυρό σεισμό πολλά από αυτά τα κτίρια είτε θα αναπτύξουν σημαντική βλάβη είτε και κατάρρευση, σε επανάληψη των τραγικών συμβάντων που έχουν παρατηρηθεί στο παρελθόν σε πολλά αστικά κέντρα της περιοχής με πολλά θύματα (π.χ. Πάρνηθα Αθήνα και Ιζμίτ της Τουρκίας το 1999, L'Aquila Ιταλίας το 2009, Αίγιο 1995). Ήδη από το 1985 μετά την εισαγωγή των ικανοτικών ελέγχων στον αντισεισμικό σχεδιασμό το ποιοτικό χάσμα σχεδιασμού νέων κτιρίων από τα παλαιότερα συνεχώς διευρύνεται ανησυχητικά. Η αναγκαιότητα για σεισμική αποτίμηση και αποκατάσταση των υφιστάμενων κτιρίων που δεν πληρούν τις σύγχρονες προδιαγραφές υπογραμμίζεται με κάθε ευκαιρία στο δημόσιο διάλογο, αν και ακόμα αναζητούνται τα σχήματα που θα επιτρέψουν την διεκπεραίωση των ελέγχων για το σύνολο των παλαιών κτιρίων.

Κομβικής σημασίας για την στατικότητα και την σεισμική επάρκεια του δομήματος έχουν τα υποστυλώματα του φέροντος οργανισμού σε κτίρια Ο.Σ. Αυτό επιβεβαιώνεται συχνά από την μορφολογία των καταρρεύσεων: όταν αστοχούν τα κατακόρυφα στοιχεία ή οι συνδέσεις τους, οι βαριές πλάκες των οικοδομών συσσωρεύονται η μία πάνω στην άλλη (pancake collapse) παγιδεύοντας ενοίκους και αντικείμενα. Αναφερόμενοι στο στάδιο της επικείμενης κατάρρευσης πολλοί ερευνητές σήμερα επικεντρώνονται στην εκτίμηση της ικανότητας παραμόρφωσης των στοιχείων στο στάδιο απώλειας στήριξης των υπερκείμενων φορτίων.

Προηγούμενες αναλυτικές διερευνήσεις καταρρεύσεων δείχνουν ότι συχνά, υποστυλώματα με ανεπάρκειες οπλισμών αστοχούν ψαθυρά είτε πριν διαρρεύσουν είτε αμέσως μετά την διαρροή και σε μικρά μεγέθη σχετικής στροφής χορδής. Τα μηχανικά φαινόμενα και η έκβασή τους εξαρτώνται από μεγάλο αριθμό παραμέτρων σχεδιασμού και από το ιστορικό φόρτισης. Στην προκείμενη διατριβή μελετάται η συμπεριφορά πλαισιακών στοιχείων Ο.Σ. υπό οριζόντια σεισμικά φορτία λαμβάνοντας υπόψη την ιεράρχηση των ενδεχόμενων μηχανισμών αστοχίας που μπορούν να ελέγξουν την φέρουσα ικανότητα. Η μεθοδολογία που αναπτύχθηκε έχει διατυπωθεί ως πεπερασμένο στοιχείο ραβδωτού πλαισιακού τύπου και χρησιμοποιήθηκε για την βελτιωμένη συσχέτιση πλήθους

πειραματικών δεδομένων από την βιβλιογραφία. Μέρος της μελέτης εφαρμογής του προσομοιώματος επικεντρώθηκε σε στοιχεία με παλαιού τύπου δομικά χαρακτηριστικά.

Για την εκτίμηση των δεικτών παραμορφωσιμότητας και ικανότητας στροφής αναθεωρήθηκε ο ορισμός του μήκους πλαστικής άρθρωσης δομικών στοιχείων, λαμβάνοντας υπόψη την υπέρβαση σε όρους παραμορφώσεων του ορίου διαρροής στους κύριους οπλισμούς του στοιχείου. Διατυπώθηκε η διαφορική εξίσωση του μηχανισμού συνάφειας ράβδου – σκυροδέματος και επιλύθηκε μέσω επιβολής κατάλληλων συνοριακών συνθηκών, συνυπολογίζοντας την διείσδυση παραμορφώσεων στον οπλισμό πριν και μετά την σταθεροποίηση της καμπτικής ρηγμάτωσης. Επιπρόσθετα αναπτύχθηκαν αλγόριθμοι για την ανάλυση κρίσιμων διατμητικά υποστυλωμάτων οπλισμένου σκυροδέματος και στην συνέχεια ενσωματώθηκαν στο λογισμικό Φαέθων© (για λειτουργικό σύστημα Windows©) σε κώδικα προγραμματισμού C++.

Για την μελέτη στοιχείων με ενισχύσεις, διατυπώθηκαν βελτιωμένοι καταστατικοί νόμοι για το σκυρόδεμα σε θλίψη με ιδιαίτερη έμφαση στην συμβολή της περίσφιγξης μέσω μανδυών ινοπλισμένων πολυμερών (ΙΟΠ). Τα εξαγόμενα προσομοιώματα ενσωματώθηκαν στο λογισμικό OpenSees και συσχετίσθηκαν επιτυχώς με πειραματικά δεδομένα από την βιβλιογραφία. Η συμβολή της έρευνας επικεντρώνεται στην αναλυτική ερμηνεία της συμπεριφοράς στοιχείων Ο.Σ. υπό συνθήκες οριζόντιας φόρτισης, και στην διατύπωση αναλυτικών εργαλείων για την περαιτέρω διερεύνηση και κατανόηση των επιδράσεων των παραμέτρων σχεδιασμού και των χαρακτηριστικών της φόρτισης στην σεισμική συμπεριφορά τους. Επίσης εξήχθησαν σημαντικά πρακτικά συμπεράσματα για το μέγεθος της πλαστικής άρθρωσης που αποτελεί βασική παράμετρο πρόβλεψης της ικανότητας παραμόρφωσης στοιχείων, και η οποία μέχρι σήμερα αντιμετωπίζεται με βάση εμπειρικές εκτιμήσεις και ορισμούς.

ABSTRACT

Existing reinforced concrete buildings constructed before the development of modern seismic design provisions represent one of the largest seismic safety concerns worldwide. Such buildings are vulnerable to significant damage and even collapse when subjected to strong ground shaking. Collapse of reinforced concrete buildings has resulted in many of the fatalities in past earthquakes. Since 1980 after the capacity design concept was introduced in the seismic design code provisions, the seismic safety gap between the newly designed seismic resistant buildings and those constructed before 1980 is widened causing worldwide concern. The crucial issue that was evident after the earthquakes in 1999 in Athens (Parnitha) and in Turkey (Kocaeli) and was underlined by the destructive earthquake of L'Aquila (2009) in Italy is the need to improve assessment and retrofit procedures for existing reinforced concrete buildings.

Columns play a very important role in the structural performance. Therefore, it was essential to apply a suitable analytical tool to estimate their structural behavior considering all failure mechanisms such as axial, shear, and flexural failures. In the present thesis a fiber beam-column element accounting for shear effects and the effect of tension stiffening through reinforcement-to-concrete bond was developed, in order to provide an analytical test-bed for simulation and improved understanding of experimental cases where testing of reinforced concrete columns actually led to collapse. Emphasis was particularly on lightly reinforced columns.

For the definition of deformability of such columns, the definition of plastic hinge length was reassessed through consideration of yield penetration effects. The required confined zone in critical regions of columns and piers undergoing lateral sway during earthquakes is related to the plastic hinge length where inelastic deformation and damage develops. The exact definition of the plastic hinge length stumbles upon several uncertainties, the most critical being that the extent of the inelastic region evolves and spreads with the intensity of lateral displacements. Design codes quantify a reference value for the plastic hinge length, through calibrated empirical relationships that account primarily for the length of the shear span and the diameter of primary reinforcing bars. The latter term reflects the effects of bar yielding penetration in the support of columns. Here a consistent definition of plastic hinge length was pursued analytically with reference to the actual strain state of the reinforcement. Finally, the column's structural behavior was assessed by considering all mechanisms of behavior involved, namely flexure with or without the

presence of axial load, shear and anchorage. The peculiar characteristics of lightly reinforced concrete columns are the outcome of the shear – flexure interaction mechanism which was studied based on the Modified Compression Field Theory and the significant contribution of the tensile reinforcement pullout from its anchorage to the total column's lateral drift. These features are embedded in the stand-alone Windows program named "Phaethon" -with user's interface written in C++ programming language code- aiming to facilitate engineers in executing such analyses both for rectangular and circular substandard reinforced concrete columns.

Confining wraps or jackets to rehabilitate and strengthen existing substandard RC columns such as those described in the present thesis has proven to be an efficient technique for seismic retrofit of structures. A new constitutive material law was developed and was added to the source code of OpenSees as a uniaxial material, i.e. the '*FRPConfinedConcrete*' material. In order to evaluate the relevance and accuracy of the proposed material model, its performance was corroborated through simulation of a series of cyclic loading tests performed on jacketed columns with a rectangular cross section.

ACKNOWLEDGMENTS

First of all, I would like to acknowledge my supervisor Professor S.J. Pantazopoulou. I always left my meetings with her, feeling both astounded at her high expectations and motivated to exceed them. I am grateful that she provided the opportunity to begin my academic career with this project, and I am inspired by her boundless optimism coupled with her steadfast refusal to accept the status quo.

I would like also to thank all the Professors and the Secretariat of the University of Cyprus whom I met during my studies. I thank in particular the members of my dissertation committee, for their valuable time and attention. I am also grateful to Assistant Professor Dr. P. Roussis for having served in my comprehensive exam committee, and to Assistant Professor Dr. S. Tastani for her valuable contribution in the research presented in Chapter 5 of this thesis.

Above all, I am grateful to the Alexander S. Onassis Public Benefit Foundation for providing me a triennial scholarship (Scholarship Code: F ZI 086-1 2012-2013/ 01/09/2012 – 29/02/2016) to pursue a Ph.D. degree in Civil Engineering at the University of Cyprus. Without this financial support during this worldwide economic crisis, this Ph.D. thesis would not have been realized.

To My Dedicated Parents and Brother

TABLE OF CONTENTS

LIST OF GRAPHS / ILLUSTRATIONS

LIST OF TABLES

1 Introduction

1.1 Background and Scope

Existing reinforced concrete buildings constructed before the development of modern seismic design provisions represent one of the largest seismic safety concerns worldwide. Such buildings are vulnerable to significant damage and even collapse when subjected to strong ground shaking. The collapse of reinforced concrete buildings has been the cause of many of the fatalities in past earthquakes. Since the 1980's, after the capacity design concept was introduced into the seismic design code provisions, the seismic safety gap between the newly designed seismic resistant buildings and those constructed before 1980 has widened, causing worldwide concern. The crucial issue that was evident after the earthquakes in 1999 in Athens (Partnitha) and in Turkey (Kocaeli) and was underlined by the destructive earthquake of L'Aquila (2009) in Italy (an event which the author experienced as a resident of L'Aquila at the time) is the need to improve assessment and retrofit procedures for existing reinforced concrete buildings. Note that intensive research and code development that has been going on the last twenty years focuses on this class of buildings, as their detailing is often found substandard with regards to what is considered today the accepted approach to earthquake resistant construction.

Reinforced concrete (RC) columns play a very important role in structural performance as their collapse brings about non-proportional consequences for the structure as a whole. Behavior of RC columns in combined axial load, shear and flexure has been studied for decades. In the case of flexural behavior, sectional analysis, or a fiber model in one-dimensional stress field may give acceptable estimations in terms of ultimate strength and yielding deformation. Performance of reinforced concrete columns dominated by shear or shear-flexure cannot be estimated from sectional analysis only, because the transfer of shear forces engages stress fields that run through the member to its supports. An example to a member-approach for modelling the effects of shear is the so-called strut and tie mechanism of behavior in D-regions of beams and columns, where shear engages a 45^o diagonal strut in the concrete member, extending diagonally over a distance at least equal to the member depth. Nevertheless, many code approaches attempt to treat the shear strength as a cross-sectional property (e.g. see ACI 318-14, 2014); strut and tie models and alternative shear design theories do exist (Model Code 2010, AASHTO Code 2013, Mörsh 1902, Ritter

1899) however their use is regulated and not transparent for many practitioners. More developed approaches that rely on strut and tie models are the so-called variable angle strut and tie models. One example is the case where the angle of inclination of the strut is not fixed at 45^o but depends on the amount of transverse reinforcement. This is reflected in the design method adopted by Eurocode 2 (2004), where the assumed strut angle measured with respect to the longitudinal axis of the member may range from 22.5^o to 45^o, leading to the minimum and maximum amounts of transverse reinforcement respectively. The detailed method of AASHTO 2013 and Model Code 2010 is based on the Modified Compression Field Theory (MCFT) (Vecchio & Collins 1986), which, today, is considered the most developed complete theory for shear of reinforced concrete members. With regards to its application in seismic assessment, there is a need to adapt the MCFT to the special characteristics of cyclic response; a limitation to this end is that most of the experimental work supporting its development has been conducted with monotonic loads (so there is little evidence as to the calibration of the model in the presence of the degrading mechanisms that develop due to cyclic displacement reversals); another limitation is the assumption of uniformly smearing the reinforcement, which is not appropriate in the case of older, sparsely reinforced construction. A third limitation is that the development of the method does not acknowledge explicitly the contribution of a degraded bond-slip to the behavior of R.C. in shear.

Despite its conceptual simplicity and computational versatility, the strut-and-tie approach prompted the effort for establishing a theoretical basis – resorting to first principles in order to illustrate the creation of a stress-field that resembles a compression strut with a parametric definition of the angle of inclination rather than postulating its value. This has been the objective of much research already from the 1970's. The difficulty arose from the brittleness of concrete in tension which disrupts direct application of the basic continuum mechanics framework even in the context of a hyper-elastic formulation. A first milestone formulation for studying complex stress states in a reinforced concrete elementary panel was proposed by Darwin and Pecknold (1974); the approach was formulated in plane stress on an elementary panel (i.e., neglecting the out-of-plane action in the panel) using an orthotropic model for concrete after cracking. Concrete and steel were superimposed in the plane of the panel, considering compatibility of strains between the two materials whereas stress equilibrium at any cross section of the panel was obtained from the sum of the concrete and steel contributions. Each such contribution was obtained from material constitutive

properties given the state of strain (state determination). Steel elements were modelled using uniaxial stress-strain laws, whereas concrete was modelled as an orthotropic material after cracking represented by uniaxial material laws in the directions of principal stress and strain. (Therefore, stress and strain transformations were required to convert from global to local coordinates and vice-versa.) A shear modulus was established from the requirements of symmetry of the material constitutive matrix in the principal directions (relating ν_{12} with ν_{21}), whereas the approach taken for solution of the problem relied on a hypo-elastic formulation (Chen, 1982)

The work of Darwin and Pecknold (1974) triggered many of the shear models that followed, and that were based on continuum mechanics principles. An essential assumption was smearing of reinforcement amount, and the use of average strains away from the crack (see Collins (1978)). Collins claimed that the approach taken was motivated by the already prominent theory of Diagonal Tension that had been developed in order to enable calculation of shear in thin plates such as occurring in steel beam webs. In the theory of diagonal tension, a square steel panel subjected to in-plane shear distortion would develop strength in the direction of principal tension (i.e. along the stretched diagonal) whereas the principal compressive stress along the compressed diagonal was neglected (set to zero) on account for the tendency for out-of-plane buckling. In this context the stress tensor for plane stress conditions was presented in terms of the Mohr circle; to account for the fact that compressive strength of thin plates was negligible due to buckling, the Mohr circle was drawn to go through zero (i.e., the least principal stress was set equal to zero), and extending in the direction of positive (tensile) stresses. This enabled calculation of shear strength of the panel as a function of the material yielding strength in tension. Collins adopted this idea by reversing the problem for concrete: here the stretched diagonal (direction of principal tension) develops no strength (on account of cracking, so the maximum principal stress is set equal to zero) whereas the compressed diagonal would attain the uniaxial strength of concrete in compression. Following this approach shear strength participation of concrete was related to the material's crushing strength in compression. This established the link of basic continuum mechanics to the concept of strut formation in the strut-and-tie approach. The Modified Compression Field Theory (MCFT) (Vecchio & Collins 1986) was developed as an amendment to the Compression Field Theory derived in 1978: first it was recognized that concrete that had already been cracked would crush at a lower stress than its uniaxial compressive strength, f_c'. This was introduced through an empirical coefficient that accounts

for the width of cracks referred to as a softening parameter. The MCFT was calibrated using a large number of membrane element tests; equilibrium and compatibility were both expressed in terms of average stresses and strains across the element, and it was supplemented by local crack checks to ensure bar stresses do not exceed the yielding capacity. Therefore, the MCFT recognizes that average reinforcement stresses vary from the crack location to the point away from cracks were strain compatibility between concrete and steel holds. The difference is attributed to a notional post-cracking strength of concrete referred to as "tension softening" which a surrogate device to bond stress. The MCFT was later implemented in the finite element context as was originally established by Darwin and Pecknold (1974) and developed by Barzegar and Schnobrich (1986), but adopting a hyper-elastic formulation for improved convergence [Vecchio 1988]. To address the need of prismatic members where, through the depth of a member cross section normal stresses and strains vary according with the requirements of flexural moment (e.g. plain sections remain plane), Vecchio and Collins (1988) introduced the MCFT in a layered model of analysis, known already in the literature as a fiber model (Zeris 1986). The kinematic assumption of flexure and shear (expressed by sectional curvature and shear strain) was used to drive the algorithm whereas principal stress/strain orientations were calculated through the member depth at the various layers. Nonlinear material constitutive laws (uniaxial stress and strain in the principal directions) were used for state determination and establishment of equilibrium of stress resultants. In this approach, concrete fibers are treated as biaxially stressed elements in the cross section and analyzed for in-plane stresses based on MCFT. Later, this approach was improved for determination of shear stress distribution on the cross section and advanced formulations were implemented into Response 2000 (Bentz 2000), which is a nonlinear member analysis computer program.

Recently, another aspect of column lateral load behavior that has raised the interest of researchers is consideration of the axial failure of columns that can lead to collapse of a building (Elwood and Moehle 2005). Before the introduction of special requirements in the 1970s, reinforced concrete building frames constructed in zones of high seismicity had details and proportions similar to frames designed primarily for gravity loads. Columns generally were not designed to have strengths exceeding beam strengths, so column failure mechanisms may often prevail in buildings dating from that era, particularly in regions without infills (Asteris et al, 2011) (e.g. soft storeys, e.g. Imperial County Hospital, or in the case of columns framing windows – see Van Nuys Holiday Inn hotel, Fig. 1.1 (Gicev V.,

Trifunac M.D., 2006)). Relatively wide spacing of transverse reinforcement was common, such that column failures may involve some form of shear or combined flexure – shear failure. As shear failure proceeds, degradation of the concrete core may lead to loss of axial load carrying capacity of the column. As the axial capacity diminishes, the gravity loads carried by the column must be transferred into neighboring elements. A rapid loss of axial capacity will result in the dynamic redistribution of internal actions within the building frame and may progressively lead to collapse.

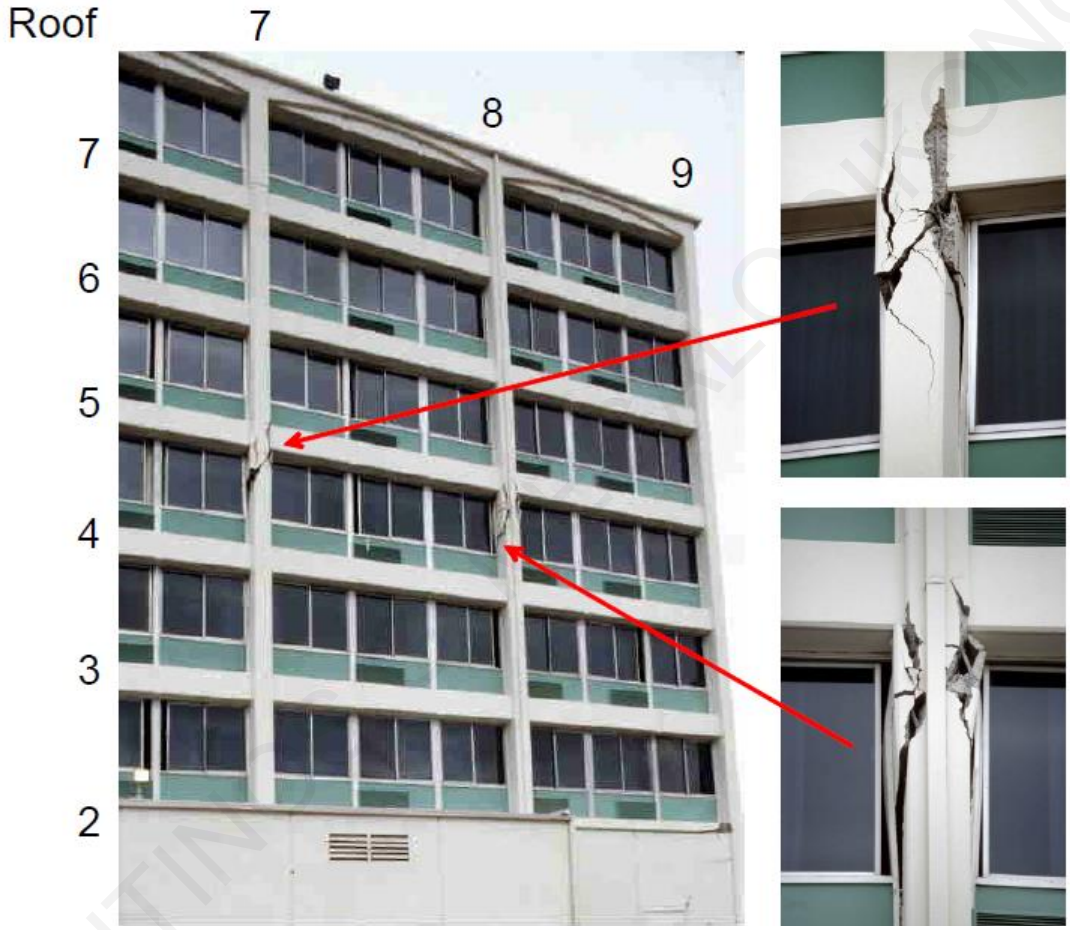

Figure 1.1: Post-earthquake view of damaged columns in Van Nuys Holiday Inn 7-storey Hotel in California (Gicev V., Trifunac M.D., 2006).

This kind of response has been witnessed repeatedly during past strong motion events throughout the world (Perachora Earthquake in Greece 1982, L'Aquila Earthquake in Italy 2009). In order to evaluate and assess the response of shear-dominated structural elements under lateral load action, a "member" model is needed, but geared towards the seismic response estimation, under combined flexure and fluctuating axial load effects. In this direction, despite the many analytical models and theories advanced to interpret shear

response, the problem of shear in reinforced concrete under lateral sway such as would occur during earthquakes is still understood imperfectly and a good deal of empiricism is vested in the design expressions for this problem.

During earthquake excitation columns can experience a wide variety of loading histories, which may consist of a single large pulse or several smaller-amplitude cycles, occasionally leading to either shear failure or even collapse – i.e. a loss of gravity-load bearing capacity of the column. Previous research has demonstrated that the onset of this type of collapse cannot be quantified unilaterally by a single combination of shear force and axial load values, but rather, it is characterized by an interaction envelope that depends on the history of loading and the peak magnitude of deformation exertion attained by the column (max. drift demand). In order to understand the effect of the loading history on the response of a column it is noted here that a particular characteristic of structural members undergoing lateral displacement reversals is the growth of their length due to the accumulation of permanent tensile strains in the longitudinal reinforcement crossing the diagonal shear cracks. As the displacement reversals increase in amplitude, so do the crack widths: this phenomenon is illustrated in the axial stress – strain diagram of reinforcement to the same level of stress after yielding. (Permanent strains are biased in tension due to the shift of the neutral axis towards the compression side of the member cross section after cracking). In this context axial load plays a significant role as it keeps cracks partly closed and therefore delays the process of ratcheting and elongation. Figure 1.2 depicts an example of a column under cyclic displacement reversals elongating due to strain accumulation: note that collapse is marked by the point where this elongation is reversed. This point may be linked to a number of local material failures – such as crushing of the compression zone, buckling of the compression reinforcement, exceedance of the strain capacity of longitudinal reinforcement (Syntzirma et al. 2010). Attainment of any of these conditions is entirely controlled by the amplitude of the imposed displacement cycles and the low cycle degradation and strain accumulation that occurs in the reinforcement and concrete under cycling (Syntzirma et al. 2010).

Recent studies (Chapter 2) attribute particular influence to the final mode and characteristics of failure by the occurrence of fluctuating axial load about a mean value, in some occasions the load becoming actually tensile due to the overturning effects imparted by the earthquake. Furthermore, it has been demonstrated that an increase in the number of cycles past the yield displacement can result in a decrease in the drift capacity at shear failure.

Understanding these effects and developing mechanistic tools by which to identify the characteristics of failure at the loss of axial load bearing capacity and the implications of drift demand intensity on the mechanics of deformation capacity of columns is one of the objectives of this research.

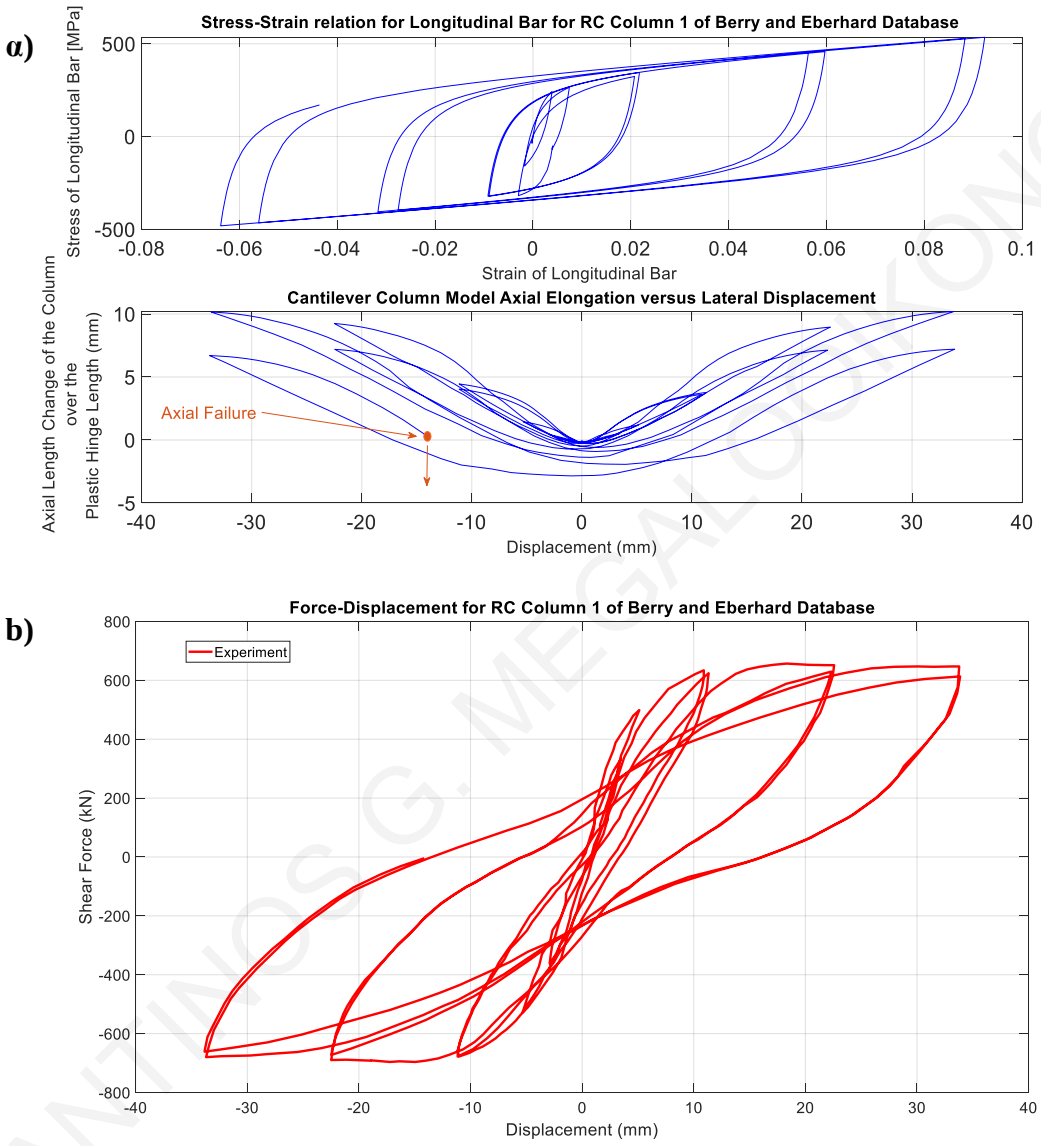

Figure 1.2: a) Axial stress vs. axial strain of tensile longitudinal reinforcement and axial length change of the first column in Table A.2. of Appendix over the plastic hinge length b) Experimental lateral response of the cantilever column under study.

In the present thesis a fiber beam-column element accounting for shear effects and the effect of tension stiffening through reinforcement-to-concrete bond was developed, in order to provide an analytical test-bed for simulation and improved understanding of experimental cases where the testing of RC columns actually led to collapse. Emphasis is

particularly laid on lightly reinforced columns. The combined experimental/numerical results provided useful information for the definition of plastic hinge length in columns through consideration of yield penetration effects. The required confined zone in critical regions of columns and piers undergoing lateral sway during earthquakes is related to the plastic hinge length where inelastic deformation and damage develops. The exact definition of the plastic hinge length stumbles upon several uncertainties, the most critical being that the extent of the inelastic region evolves and spreads with the intensity of lateral displacements. Design codes quantify a reference value for the plastic hinge length, through calibrated empirical relationships that account primarily for the length of the shear span and the diameter of primary reinforcing bars. The latter term reflects the effects of bar yielding penetration in the support of columns. Here a consistent definition of plastic hinge length is pursued analytically with reference to the actual strain state of the reinforcement.

In this direction, the definition of the deformability of RC columns was reassessed in the present thesis by proposing a new methodology for the determination of plastic hinge length through a consideration of yield penetration effects. Yield penetration occurs from the critical section towards both the shear span and the support of columns; physically it refers to the extent of the nonlinear region and determines the pull-out slip measured at the critical section. Contrary to the fixed design values adopted by codes of assessment, the yield penetration length is actually the only consistent definition of the notion of the plastic hinge length, whereas the latter determines the contribution of pullout rotation to column drift and column stiffness. In order to establish the plastic hinge length in a manner consistent to the above definition, this research pursued the explicit solution of the field equations of bond over the shear span of a column. Through this approach, the bar strain distributions and the extent of yield penetration from the yielding cross section towards the shear span were resolved and calculated analytically. By obtaining this solution, a consistent definition of plastic hinge length was established, by reference to the state of reinforcement strain (replacing the stress-based definition that was used previously in the literature). The true parametric sensitivities of this design variable for practical use in the seismic assessment of existing structures are illustrated. The numerical results show good agreement with the experimental evidence and are consistent with the experimental trends supported by test databases, confirming that the plastic hinge length is controlled by the residual bond that may be mobilized along the yielded reinforcement.

In addition, the developed fiber-element is incorporated in the stand-alone Windows program Phaethon with the user's interface written in C++ programming language code. The latter offers the possibility to obtain the capacity curve for shear-critical reinforced concrete cantilever columns while taking into account the shear–flexure interaction mechanism, as well as an important contribution to the final column's lateral displacement capacity owing to pull-out of the tensile longitudinal reinforcing bars of the column. This is available for both rectangular and circular reinforced concrete columns. Furthermore, the software resolves strain, slip and bond distributions along the anchorage length. Comparison with experimental results from the literature verifies the capability of this Windows software tool to assess the strength and deformation indices of shear-critical reinforced concrete columns. Moreover, the moment curvature as well as the shear force – shear strain analysis of the sections of these columns is also possible, all based on the Modified Compression Field Theory. The development of a new class fiber model that accounts for localized phenomena such as shear and reinforcement pull-out in a consistent iterative element formulation will help minimize the uncertainties that arise with the large collection of zero length nonlinear spring and fixed-length plastic hinge elements currently used in nonlinear bridge and building response simulations.

Over the past three decades, fibre-reinforced polymer (FRP) composites have emerged as an attractive construction material for civil infrastructure, rehabilitation, and renewal. These advanced materials have been successfully used for the strengthening/rehabilitation of piers and columns in existing bridges and buildings. The use of FRP composites, analysis and design, and techniques for installation are continually being researched and it is anticipated that the use of these advanced materials will continue to grow to meet the demands of the structural retrofitting needs in the construction industry. Recent seismic events around the world continue to underline the importance of seismic retrofit and strengthening of existing concrete structures leading to the need for new, practical, occupant-friendly and cost-effective remedial solutions.

In this context, one of the major applications of Fiber Reinforced Polymers (FRPs) in construction is in the confinement of RC columns. The performance of FRP-confined concrete in circular columns has been extensively investigated in literature and the efficiency of the available models is nowadays considered to be satisfactory. However, the case of confinement of rectangular RC sections with FRPs is a more complex problem, the mechanism of which has not yet been adequately described. Therefore, an iterative analytical

model was derived to simulate the axial and lateral stress-strain response of axially loaded FRP-confined rectangular and square reinforced concrete columns. In FRP-confined square or rectangular sections, no unconfined concrete regions are observed, as assumed in many models. Areas where arching effect is assumed in the section are described as partially confined, so their contribution to the column's total strength is limited by the limited kinematic restraint provided by the jacket against outwards expansion resulting from the longitudinal compressive forces supported. Thus, two different regions with different confining stress-states are identified. The two regions are uniaxially and biaxially confined (biaxial and triaxial stress-state, respectively). The contribution of each region to the total section strength is modelled as a system of parallel springs, whose axial stresses are added based on the corresponding constitutive law under biaxial or triaxial stress state. The lateral behavior develops along the diagonals of the section and can be represented by a system of springs in series. It was shown that both sides' lateral strains in the rectangular sections are equal, regardless of their aspect ratio. The reacting force of the confining device applied at the corners is shared among the two regions of different degree of confinement, based on the defined path of the confining forces and the geometry of the regions. The resulting lateral uniform pressures lead to the corresponding axial strength of the regions. The algorithm takes into account all parameters available to designers, such as corner rounding radius, stiffness of the FRP and concrete strength, while it can be easily understood and implemented. Results of the proposed modeling approach are found to correlate adequately to recent experimental data obtained from large-scale tests on FRP-confined rectangular RC columns. In addition, the performance of this material model was further investigated by its implementation in the simulation of a series of experimental tests of FRP-retrofitted square RC columns under cyclic lateral loading simulating earthquake loads and simultaneous constant axial compression. In particular, all specimens were modelled using nonlinear fiber elements, whereas the FRP-confined concrete was modelled using the developed material model. Comparison between the numerical and experimental hysteresis of the column is indicative of the effectiveness of the implemented modelling. Finally, this recently developed material model for FRP–confined concrete was implemented in OpenSees (2006) under the name *'FRPConfinedConcrete'* with no tensile strength and degraded linear unloading/reloading stiffness in the case of cyclic loadings.

1.2 Organization of the thesis

The thesis spans eight chapters organized as follows: Following the introduction of the thesis scope and objectives in Chapter 1, Chapter 2 presents a detailed literature review regarding the state of the art in the field of seismic assessment of RC columns. Chapter 3 presents the development of a fiber model for analysis of flexure-dominant members under cyclic load reversals: the performance of the model is correlated with the experimental results of a well-known experimental database. Chapter 4 reviews the mechanical behavior of lightly reinforced concrete columns and identifies the types of experiments where the fiber-model analysis would fail to reproduce the observed behavior. One source of the error in estimating the deformational response of columns under lateral sway is the empirical, insensitive nature of the plastic hinge length used in calculations. To address this limitation, Chapter 5 develops a new fundamentally consistent definition of the plastic hinge length in columns though consideration of yield penetration effects. Chapter 6 presents the development of a force-based fiber beam-column element that accounts for shear and tension stiffening effects that was incorporated in the stand-alone program for Windows called Phaethon. Chapter 7 presents new developments on FRP seismic retrofit of RC columns with confining wraps or jackets that has proven to be an effective technique for the seismic retrofit of structures. A new constitutive model for FRP – confined concrete is included in this Chapter. Important findings of the work are summarized along with the conclusions in the 8-th chapter of the present volume.

2 Literature Review

2.1 Introduction

The procedure of estimating the strength, the deformation capacity and the expected mode of failure in primary members of a RC frame structure, that is, the complete process of seismic assessment, has been recently supported by background documents in both Europe and the U.S. (KAN.EPE. 2014, EN 1998-3 2005, ASCE/SEI-41 2007, and 2017), and most recently by the Revised Draft (for 2020) of the Model Code by the fib). Currently, a new revised version of EN 1998-3 is also being drafted, to be released in the near future (2020), condensing the advancements that have occurred in the field over the last 20 years. In all cases, the core of the assessment process comprises a complex system of evaluation of demands and capacities; demands are associated with the performance point determined for the design earthquake. Capacities are linked to different levels of performance. They are often expressed in terms of deformation capacity at specific conditions of damage of the constituent materials (e.g. cracking, repairable damage, or near collapse) and are commonly referred to as "acceptance criteria". However, the various steps of this process are not vested with a uniform level of confidence as compared with the experimental results. Strength values can be estimated with sufficient accuracy only if the modes of failure involved are ductile. The level of accuracy is reduced when considering brittle mechanisms of resistance, and the associated deformation capacities, which are used as a basis for comparison with deformation demands to assess the level of performance (i.e. the damage), generally do not correlate well with proposed Code estimations, even after the many years of development that have gone into this topic of research.

From evidence collected in past building and bridge collapses it was observed that in many cases columns failed in a brittle manner prior to flexural yielding due to insufficient transverse reinforcement over lap-splices or as would be needed to resist shear (for example see 1999 Parnitha Earthquake in Athens and the Izmit-Kocaeli Earthquake in Turkey in the same year, the 2010 earthquake in L'Aquila, among other notable events) (Pardalopoulos et al. 2011). Due to the implications on public safety, this is considered a critical matter in the process of assessment: ductility in the member behavior may only be secured if the response is dominated by flexural yielding, (thus, it ought to precede shear failure). Even when flexural yielding may be supported it is also important to dependably estimate the ductility

level beyond which shear strength may be assumed to have degraded below the flexural strength, leading to a secondary post-yielding failure that limits the available deformation capacity (Fig. 2.1).

Stiffness properties and inelastic earthquake response of frame members are usually studied based on a statically-determinate structure comprising a cantilever reinforced concrete column under combined axial and lateral loading. Given the material properties (be they nominal, assumed or experimentally measured), geometry, the loading conditions and loading history, it is theoretically possible to analyze the cantilever so as to study the interactions between various aspects of its response such as flexure, shear and reinforcement development capacity (Syntzirma and Pantazopoulou 2007). In recent years lab experiments are conducted on full-height, fixed-ended column specimens. Lateral sway in this case causes double curvature with an inflection point at mid-height. This setup is preferred over the cantilever arrangement, since it is possible to achieve the interaction of the two end moments and to obtain realistic curvature distributions, reinforcement detailing at midspan may be representative of actual conditions (as compared to its being attached to loading fixtures), whereas they are more versatile in dynamic tests (as it is possible to mount masses on top of the restraining beam at the upper end of the column, thus simulating more realistically the actual circumstances in the field).

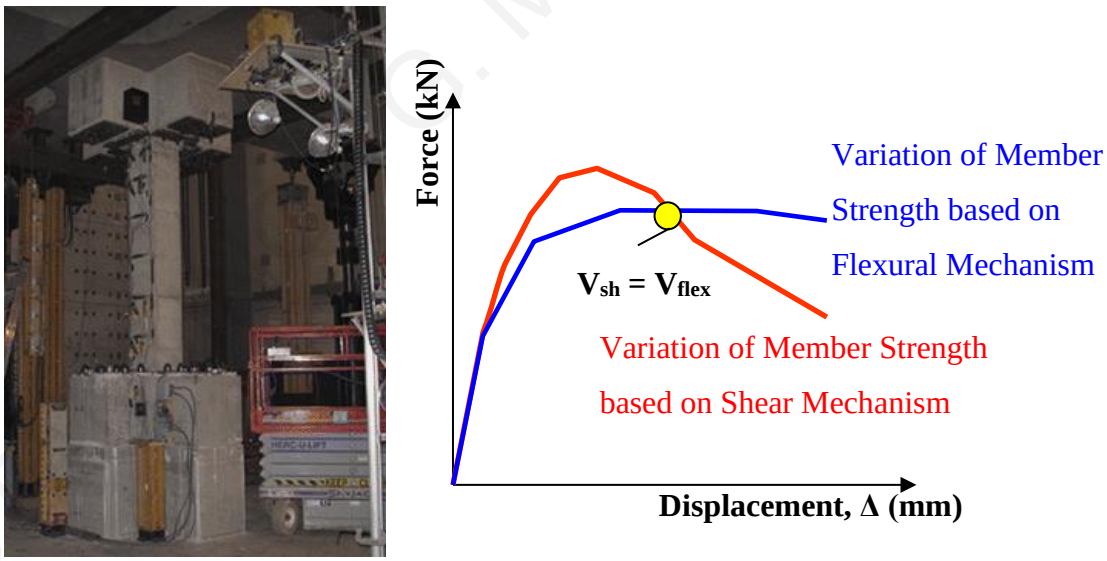

Figure 2.1: (a) Typical test setup of double curvature column (from Henkaus et al. 2013). (b) Capacity curve due to flexural or shear mechanism. Onset of shear failure is denoted with the yellow point.

Moreover, in the case of lightly reinforced concrete columns which are representative of older construction, major inclined shear cracks have been seen to occur in the column region at mid-height (near the point of column inflection), a crack pattern that cannot be

reproduced with the cantilever specimen since its tip is free to rotate (as it is only restrained in translation) and sustains no damage in that region. In addition, the elongation due to damage of the double curvature member is more representative of a typical building column under lateral sway simulating earthquake action. The assessment performance objectives in such experiments can be categorized and documented by obtaining the full inelastic response until the collapse of the RC column.

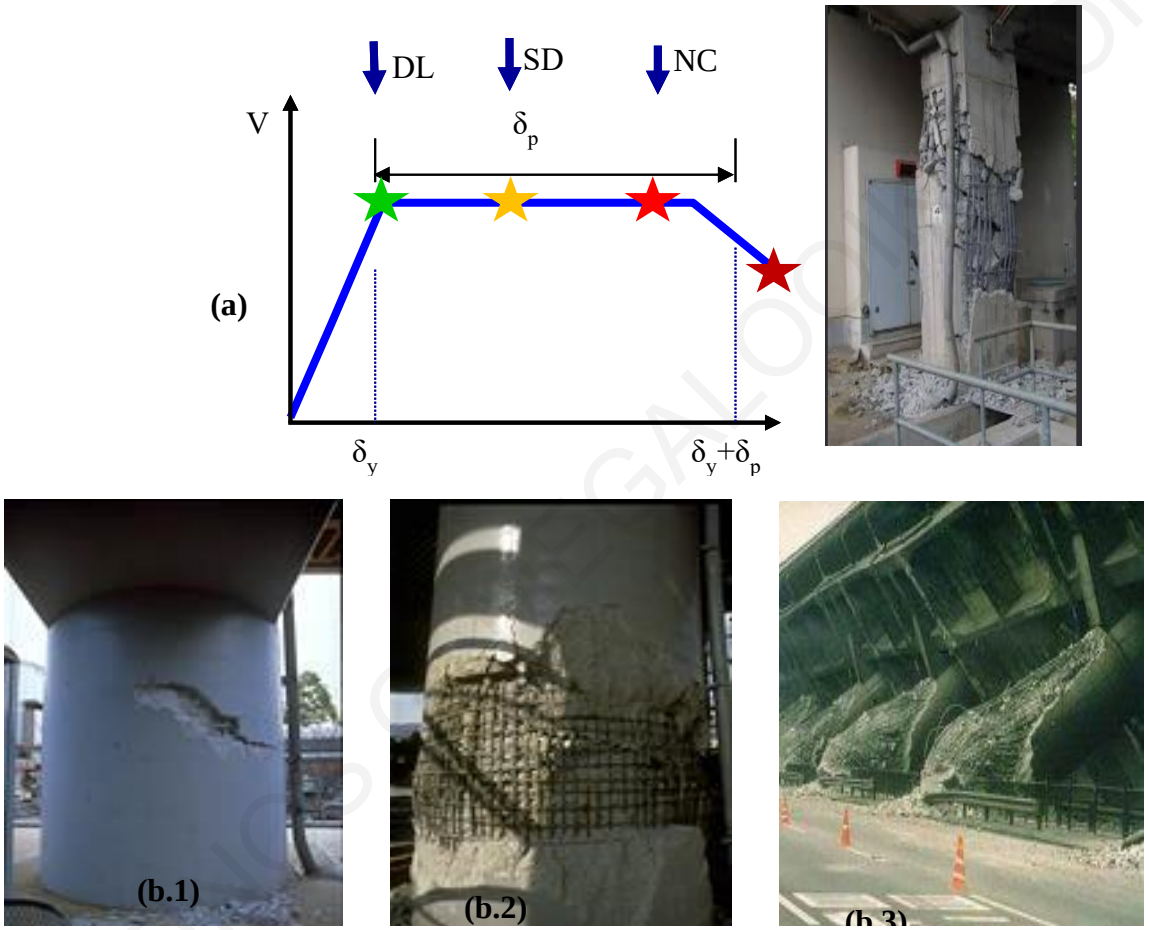

Figure 2.2: Evidence of the intensity of damage of bridge columns: (a.1) Member resistance curve and definition of limit states according with EN 1998-3 (2005). (a.2) Shear cracking at mid-height of column restrained at both ends. (b.1) Damage Limitation Limit State (b.2) Significant Damage Limit State (b.3) Near Collapse Limit State.

According to Eurocode 8, Part 3 (EN 1998-3, 2005), the fundamental performance criteria related to the state of the structural damage are defined through three Limit states that span the range of the member resistance curve (Fig. 2.2.a), and are defined according to the severity of damage that they represent as follows: “Damage Limitation (DL)”, “Significant Damage (SD)”, and “Near Collapse (NC)”. The target displacement of the

column based on the earthquake load defines which of these Limit States are reached. In the following figure (Fig 2.2.b) the performance objectives for these Limit States are documented in practical terms.

The objective of this chapter is to critically review and identify, through a thorough evaluation of the published experimental evidence, the critical issues affecting the resistance curve of columns during earthquake action (strength and deformation capacity) and the limiting brittle modes of failure. This is important since the column resistance curve eventually controls the overall resistance of the structure in a relatively straightforward manner (Fotopoulou et al., 2011) whereas a sudden loss of column strength to overbearing loads may lead to collapse and human loss. In the context of a displacement-based evaluation framework, not only the relevant shear strength is important, but also the corresponding column displacement capacity. In this regard, recent experimental evidence will be reviewed along with recently developed analytical models and the relevant state of the art of code assessment procedures.

2.2 Past Experimental Studies on Shear Dominated RC Columns

The behaviour of shear-critical reinforced concrete columns has been the subject of extensive study and research in recent years as this seems to remain a challenging concrete mechanics problem (Chapters 1 and 2). Shear dominant behaviour is reported in columns with a low aspect ratio (Arakawa et al. 1982, 1989, Calderone et al. 2000), but also in lightly reinforced columns containing low ratios of transverse reinforcement (Ngoc Tran and Li, 2013, Syntzirma and Pantazopoulou 2007). Section geometry (e.g. rectangular or circular sections) is one of the parameters that differentiates the available test results (Berry and Eberhard, 2004); cyclic pseudo-static, hybrid pseudo-dynamic and dynamic tests have all been used as alternatives to understand column behavior. Some experimental studies are dedicated to the influence of axial load fluctuation on the response of the column (Benzoni et al. 1996, Kim et al. 2011). Fluctuation occurs about the static axial load value of the overbearing loads, and in the experimental context it is intended to model the effect on its magnitude impacted by the overturning action of lateral loads during the seismic event. In actual field conditions the amplitude of the fluctuation is most significant in columns located at a distance from the center of mass of the building, i.e., on the perimeter of the structure.

The same effect is seen in bridge piers belonging to multiple-column bents where it may be easily demonstrated that the axial load fluctuation is proportional to the horizontal

(seismic) forces. Columns are also subjected to the vertical components of ground motion, which is not correlated concurrently with the horizontal loading. Past earthquake records have shown that in some cases, vertical ground motions cannot be ignored, particularly for near-fault situations (Kim et al. 2011). For example, the lateral displacement ductility of a column, designed based on constant axial load with a relatively low axial load ratio, can become unsatisfactory when the actual axial load due to the overturning effects (or where the vertical ground motion has a significant contribution) exceeds the "balanced" axial load limit (i.e., about 40% of the column crushing load, Park and Paulay 1975). The problem becomes even more significant when shear design is considered. The increase of axial load from the design level (which typically is in the order of 5% to 10% of the crushing load) to the level of the balanced value generally increases the column flexural capacity causing a commensurate increase in the design shear demand (based on capacity design principles). On the other hand, a change in the axial load value from compression to tension may compromise significantly the column shear strength (Kim et al. 2011).

2.2.1 A review of some influential Cyclic Tests on Columns

From among the multitude of published tests on cyclically loaded columns under lateral displacement reversals (see also Chapter 3), a number of tests have received greater attention as the specimen responses recorded were used as points of reference in calibrating the design expressions for shear published in the literature. On account of the weighty contribution of these experimental studies to the formation of the current assessment framework, these studies are reviewed separately in the present section.

Ang, Priestley and Paulay (1989) performed experimental tests to study the seismic shear strength of circular columns. A series of twenty-five 400 mm-diameter columns, considered to be approximately one-third scale models of typical bridge columns, were constructed and tested under cyclic lateral displacement reversals, as part of a major investigation into the strength and ductility of bridge pier columns. Variables in the test program included axial load level, longitudinal reinforcement ratio, transverse reinforcement ratio and aspect ratio. The column units were tested as simple vertical cantilevers. Results indicated that the shear strength was dependent on the axial load level, the column aspect ratio, the amount of transverse spiral reinforcement and the flexural ductility displacement factor. At low flexural ductilities, the additive principle for shear strength (i.e. $V_n=V_C+V_W$), based on a concrete contribution plus a 45-deg truss mechanism involving the spiral

reinforcement and diagonal concrete compression struts associated with the axial load action, described the behavior quite well. But at flexural displacement ductilities greater than two ($\mu_{\Delta} \geq 2$), the tests demonstrated a gradual reduction of lateral load strength with increasing ductility demand, whereas the inclination of the diagonal compression struts of the truss mechanism relative to the longitudinal axis decreased. Here it is worth noting that significant rotations occurred at the base of these specimens artificially distorting the data in the direction of more excessive strength loss due to P-Δ effects (Ioannou and Pantazopoulou, 2016).

Wong, Paulay and Priestley (1993) conducted a series of biaxial tests that included 16 circular (400 mm-diameter) reinforced concrete cantilever columns with an aspect ratio of two and different spiral reinforcement contents in order to investigate the sensitivity of the strength and stiffness of shear-resisting mechanisms to various displacement pattern and axial compression load intensities. Elastic shear deformations in squat circular columns with small or no axial compression load were found to be significant. It was concluded that shear deformation ought to be included explicitly in the estimation of initial stiffness of a column, so that a reliable relation between the ductility demand and the corresponding drift could be established. A general observation was that in comparison with uniaxial displacement paths, biaxial displacements led to more severe degradation of stiffness and strength, and thereby, increased energy dissipation. However, the reduction of initial shear strength and ductility capacity of squat columns (recall that the aspect ratio of the tested columns was equal to 2), subjected to biaxial displacement history was not very significant. The value of the dependable displacement ductility level attained during biaxial displacements was, on average, less (i.e. a value difference of 1) than that obtained in identical units subjected to uniaxial loading history. Initial shear strength of units with brittle shear failure was reduced by about 5 to 10 percent, depending on the axial load level when biaxial rather than uniaxial loading was considered. Finally, one more important finding was that the shear carried by spirals was underestimated when using a 45-deg potential failure plane; the observed major diagonal cracks developed in squat columns at much lower angles with respect to the longitudinal axis of the member.

Lynn et al. (1996) constructed and tested 8 full-scale square section (457 mm) columns that had widely-spaced perimeter hoops with 90-degree bends with or without intermediate S-hooks and with longitudinal reinforcement with or without short lap-splices. The columns had an aspect ratio of 3 and were loaded with constant axial load at low and

intermediate levels, and were subjected to lateral deformation cycles until the column was incapable of supporting a lateral or vertical load. Failure modes included localized crushing of concrete, reinforcement buckling, lap-splice and flexural bond splitting, shear and axial load collapse (Dhakal and Maekawa, 2002). Loss of gravity load capacity occurred at, or after significant loss of lateral force resistance. Where response was governed by shear, gravity load failure occurred soon after loss of lateral force resistance. Where response was initially governed by lap-splice deterioration and gravity loads were relatively low, gravity load resistance was maintained until eventual shear failure occurred. Where response was predominantly flexural, gravity load capacity was maintained to relatively large displacements.

As earthquakes and laboratory experience show that columns with inadequate transverse reinforcement are vulnerable to damage including shear and axial load failure, another study in this direction was conducted by Sezen and Moehle (2006). The latter included four full-scale square section (457 mm) columns with an aspect ratio equal to 3 and light transverse reinforcement that were tested quasi statically under unidirectional lateral loads with either constant or varying axial loads. Test results showed that responses of columns with nominally identical properties varied considerably depending on the magnitude and history of axial and lateral loads applied. For the column with a light axial load and reversed cyclic lateral loads (applied through a displacement history), apparent strength degradation triggered shear failure after the flexural strength was reached. Axial load failure did not occur until displacements had increased substantially beyond this point. The column with high axial load sustained brittle shear compression failure and lost axial load capacity immediately after shear failure, pointing out the necessity of seismic evaluations to distinguish between columns on the basis of axial load level. The column tested under varying axial load showed different behavior in tension and compression, with failure occurring under compressive loading.

The experiments by Pantazopoulou and Syntzirma (2010) on columns having different details were designed to encourage a specific hierarchy of modes of failure by adjusting the spacing of stirrups and the length of lap splices of longitudinal reinforcement in the critical region. The most interesting finding from that experimental study was that the deformation capacity is controlled by the dominant mode (the weakest mechanism) and may be estimated mostly by the deformation capacity of the specific failure mechanism; this

became later the basis for the rapid assessment procedure for identifying column strength (Pardalopoulos et al. 2011, Ioannou et al. 2018).

2.2.2 A review of relevant Pseudodynamic Tests

It was stated earlier that when submitted to lateral sway due to earthquake ground shaking, columns in RC structures carry axial forces owing to dead and live loads and a combined variable axial force, flexural moment and shear. The variable axial loads lead to simultaneous changes in the balance between the column strain capacity and demand at critical areas to an extent that eludes adequate estimation as it depends on load history. Recently, code models use strain limits to identify critical performance states (e.g. AASHTO LRFD 2013; CHBDC 2015; see Qi and Alam, 2018).

To consider the time varying effects of the ground motion on the combined actions, simulated dynamic loads were applied using a hybrid simulation of the earthquake effects on structural subassemblies wherein the column specimen is assumed to belong. Kim et al. (2011) used hybrid simulation, where an experimental pier specimen was tested simultaneously and interactively with an analytical bridge model which was simulated computationally; at each step of the dynamic test the forces applied on the specimen were calculated by solving the dynamic equation of motion for the structure where the stiffness contribution of the modelled column in the global structural stiffness was estimated from the measured resistance in the previous step. Additionally, two cyclic static tests with constant axial tension and compression were performed to study the effect of the axial load level on the bridge piers. It was found that by including vertical ground motion the axial force fluctuation on the test specimen increased by 100%, resulting at times in a net axial tension that was not observed under horizontal motion alone. This high axial force variation led to a fluctuation of lateral stiffness and a more severe outcome of cracking and damage. The confining spiral strains were significantly affected: whereas the maximum spiral strain of the specimen subjected to horizontal ground motion occurred at 20% of the pier height, in the case of an identical specimen subjected to combined horizontal and vertical excitations it occurred at 55% of the pier height. Thus, it was estimated that the spiral strain increased by 200% when vertical ground motion was included. Therefore, in this example, the deterioration of shear capacity due to vertical ground motion was experimentally demonstrated. Also, whereas the test specimen that was subjected to constant axial compression experienced brittle shear failure including rupture of the spiral reinforcement, the companion specimen that was subjected to moderate tension showed ductile behavior.

Comparing the strength at the first peak of displacement, it was found that the lateral load strength of a specimen with constant axial tension increased marginally with increasing displacement (probably engaging the strain hardening response of the reinforcement); the response of the specimen with axial compression showed significant strength degradation. Hence, considering observations from the two tests described above, it was clearly shown that different axial load levels influence the pier behavior significantly and can ultimately dictate the failure mode.

2.2.3 Shake Table Tests conducted on Columns

Shake table tests were conducted (Elwood 2002) to study the process of dynamic shear and axial load failures in reinforced concrete columns when an alternative load path is provided for load redistribution. The test specimens were composed of three columns fixed at their bases and interconnected by a beam at the upper level. The central square section column had a wide spacing of transverse reinforcement rendering it vulnerable to shear failure and subsequent axial load failure during testing. As the central column failed, the shear and axial loads were redistributed to the adjacent ductile circular columns. Two test specimens were constructed and tested. The first specimen supported a mass that produced column axial load stresses roughly equivalent to those expected for a seven-story building. In the second specimen hydraulic jacks were added to increase the axial load carried by the central column, thereby amplifying the demands for redistribution of the axial load when the central column began to fail. Both specimens were subjected to one horizontal component of a scaled ground motion recorded during the 1985 earthquake in Chile. A comparison of the results from the two specimens indicates that the behavior of the frame is dependent on the initial axial stress on the center column. The specimen with a lower axial load failed in shear- but maintained most of its initial axial load. For the specimen with a higher axial load, shear failure of the center column occurred at lower drifts and at an earlier stage in the ground motion record, and this event was followed by axial failure of the central column. Displacement data from immediately after the onset of axial failure suggest that there are two mechanisms by which the center column shortens during axial failure: first, by large pulses that cause a sudden increase in vertical displacement after a critical drift is attained; and second, by smaller oscillations that appear to ‘grind down’ the shear-failure plane. Dynamic amplification of axial loads transferred from the center column to the outside columns was observed during axial failure of the center column.

An additional study by Ghannoum and Moehle (2012) includes earthquake simulation tests of a one-third-scale, three-storey, three-bay, planar reinforced concrete frame which was conducted to gain insight into the dynamic collapse of older-type construction. Collapse of the frame was the result of shear and axial failures of columns with widely spaced transverse reinforcement. The frame geometry enabled the observation of the complex interactions among the failing columns and the surrounding frame. The tests showed that the failure type and rate depended on the axial load level, stiffness of the surrounding framing, and intensity and duration of shaking. Column shear and axial behavior, including strength degradation, was affected by both large lateral deformation excursions and cycling at lower deformations. Low-cycle fatigue caused column collapse at significantly lower drifts than anticipated. It was concluded that current models and standards for estimating the shear and axial failure of columns do not account for low-cycle fatigue and can be unconservative, particularly for columns subjected to long-duration seismic motions. Moreover, models for shear strength degradation of reinforced concrete columns should account for both deformation and cyclically-driven damage (Syntzirma et al. 2010). Finally, it was seen that structural framing surrounding the failing columns enabled vertical and lateral force redistribution that delayed or slowed down progressive structural collapse.

2.3 Code Criteria for Shear Strength Assessment of RC Columns

Behavior of reinforced concrete columns under lateral sway has been studied extensively through experiments simulating earthquake action by applying relative lateral displacement at the ends of the member (see also Chapter 3). The relative magnitude of shear strength and flexural force demand determines the intensity and type of anticipated failure. This in turn controls the accuracy of the estimation of the mechanistic models used to assess the lateral load resistance and deformation capacity of the member. In the case of behavior dominated by flexure, sectional analysis, or a fiber model considering normal stresses provides acceptable estimations in terms of ultimate strength and yielding deformation. Performance of reinforced concrete columns dominated by shear or shear-flexure cannot be estimated by applying only sectional analysis because shear behavior concerns the overall member and not a single cross section. In these cases it is necessary to couple a shear strength model with the flexural model – and by considering independently the degradation of each with increasing deformation, to determine the prevailing mechanism that controls the mode of

failure of the member at the reference performance limit. Several code assessment procedures define the shear strength and its rate of degradation with increasing displacement ductility by evaluating the concrete contribution and the transverse steel reinforcement contribution to shear strength. Actually the existing code methodologies are differentiated regarding the concrete contribution term whereas the truss analogy for steel contribution is adopted almost universally in all proposals with a minor point of discussion being the angle of inclination of the primary shear crack of the column that activates the steel stirrups contribution (Fig. 2.3). The various aspects of the code assessment of shear strength will be covered in the following sections.

It is generally acknowledged that shear failure of RC structures signifies rapid strength degradation and significant loss of energy dissipation capacity. Reconnaissance reports from past strong earthquakes highlight the susceptibility of RC column webs to diagonal tension cracking that frequently leads to a brittle shear failure. Shear strength degradation ensues after the opening of the diagonal cracks which eliminate the mechanism of force transfer via aggregate interlock. To avoid shear failure, shear strength should exceed the demand corresponding to attainment of flexural strength by a safety margin.

Figure 2.3: (a) Angle of inclination of the primary sliding shear crack. (b) Field evidence of shear failure

For the mechanics of shear in reinforced concrete, most issues relating to physical interpretation are still fraught with considerable debate. For example, consensus is lacking as to the physical significance of the concrete contribution term and to mathematical description of tension-based sources of shear-strength and their relationship to strain intensity and cyclic displacement history. According to EN 1998-3 (2005), the part of the cyclic shear resistance that depends on concrete and transverse steel contribution (excluding the part owing to axial load contribution), V_R, decreases with the plastic part of ductility

demand, expressed in terms of ductility ratio of the transverse deflection of the shear span (Fig 2.4) or of the chord rotation (Fig. 2.4) at member end: $\mu_\Delta{}^{pl} = \mu_\Delta - 1$. For this purpose $\mu_\Delta{}^{pl}$ may be calculated as the ratio of the plastic part of the chord rotation, θ_p, normalized to the chord rotation at yielding, θ_y.

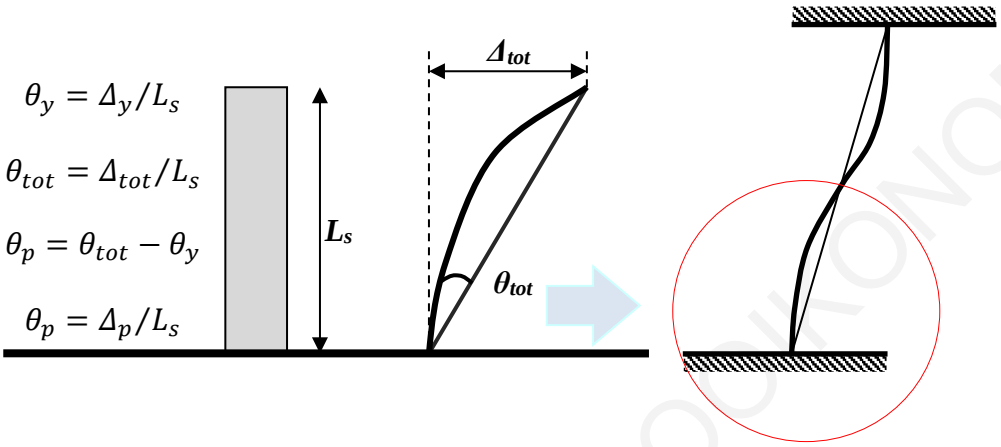

Figure 2.4: Definition of chord rotation of a cantilever reinforced concrete column (top) modeling the shear span of an actual column (bottom).

Thus, EN 1998-3 (2005) defines shear strength accounting for the above reduction as follows:

$$V_R = [(h-x)/2L_s] \cdot \min(N; 0.55A_c f_c) + [1 - 0.05min(5; \mu_\Delta{}^{pl})] \cdot \{0.16max(0.5; 100\rho_{tot})[1 - 0.16min(5; L_V/h)]\sqrt{f_c}A_c + V_w\} \quad (2.1)$$

where $\boldsymbol{h}$: is the depth of the cross-section (equal to the diameter D for circular sections); $\boldsymbol{x}$: is the compressive zone depth; $\boldsymbol{N}$: is the compressive axial force (positive, taken as being zero for tension); $\boldsymbol{L_s} = M/V$ is the shear span of the member; $\boldsymbol{A_c}$: is the cross-sectional area, taken as being equal to $\boldsymbol{b_w d}$ for a cross-section with a rectangular web of width (thickness) $\boldsymbol{b_w}$ and structural depth $\boldsymbol{d}$ or to $\boldsymbol{\pi D_c{}^2/4}$ (where $\boldsymbol{D_c}$ is the diameter of the concrete core to the inside of the hoops) for circular sections; $\boldsymbol{f_c}$: is the concrete compressive strength, and $\boldsymbol{\rho_{tot}}$: is the total longitudinal reinforcement ratio. Term $\boldsymbol{V_w}$ is the contribution of transverse reinforcement to shear resistance, taken as equal to

$$V_w = \frac{\pi}{2}\frac{A_{sw}}{S} f_{yw}(D - 2c) \quad (2.2a)$$

Where, $\boldsymbol{f_{yw}}$ is the yield stress of the transverse reinforcement, $\boldsymbol{A_{sw}}$ the area of the spiral wire, $\boldsymbol{c}$ the concrete cover, and $\boldsymbol{S}$ is the spiral step (spacing between successive turns of a spiral). Similarly, for rectangular cross-sections with a web having width b_w:

$$V_w = \rho_w b_w z f_{yw} \quad (2.2a)$$

where $\boldsymbol{\rho_w}$ is the transverse reinforcement ratio, $\boldsymbol{z}$ is height of the equivalent truss (internal lever arm between longitudinal tension and compression resultants, i.e., ***d-d'*** in beams and columns) (Fig 2.5).

Consider a typical column with a 350 mm circular section ($f_c' = 30\ MPa$) with $L_s = 1.5\ m$ (i.e., a clear height of 3.0m), clear concrete cover 20mm, reinforced with 14Φ12 longitudinal bars and Φ10/10 spiral reinforcement ($f_y = f_{yw} = 500MPa$) and axial load ratio of 0.2. The axial load, concrete, and transverse steel contribution to shear strength calculated from Eq. 2.1 are, 49 kN, 34 kN and 191 kN. The reduction factor for $\mu_\Delta = 3$ (i.e, $\mu_{\Delta P} = 2$), is 0.9. Therefore, the reduced contribution of concrete and transverse reinforcement is 203 KN. The variation of shear strength with spacing for the example under consideration leads to the following graph (Fig. 2.7a). Clearly, there is an inconsistency in the continuity of the above expression of V_w, in that even when the spiral step exceeds the diameter of the confined core a nonzero strength is dependent-upon to be contributed by the spiral. This shortcoming is even more transparent in the case of rectangular columns where the transverse steel contribution refers to the total stirrup forces that arise when a 45° diagonal sliding plane intersects stirrups along the members' critical region. To illustrate this point, consider a column with the same material properties as the one discussed in the preceding and same shear span length L_s. In the present example, the column has a 457 mm square cross section, reinforced with 8Φ20 longitudinal bars and a Φ10/20 transverse perimeter stirrup. For the same axial load ratio the axial load contribution to shear strength is 145 kN, whereas the concrete and transverse steel contribution are 104 and 147 kN respectively (253 kN). The latter will be reduced to the value of 227 kN for displacement ductility equal to 3. The variation of shear strength with spacing for this example under consideration leads to graph plotted in Fig. 2.7b.

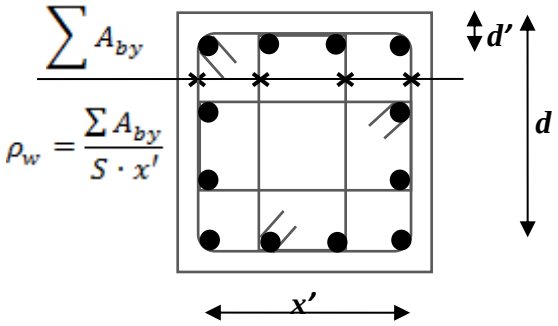

Figure 2.5: Definition of terms for calculating the transverse reinforcement ratio (*S*: stirrup spacing)

It is evident that for spacing greater than the effective depth of the section—which for the 45° degree truss analogy would mean that the shear crack doesn't intersect any stirrup—Eq. 2.2a simply leads to a lower value of steel contribution to shear strength. This is actually inconsistent – the value ought to be zero in this case; with reference to Fig. 2.7 Pantazopoulou and Syntzirma (2010) have suggested that the term be substituted by:

$$V_w = \sum_{n_i} A_{swi} \cdot f_{si}\,; \quad \text{where,} \quad n_i = <{}^{d}/_{S}> \ (greatest\ integer\ function) \qquad (2.2b)$$

Based on Fig. 2.7, the steel contribution component should be based on the requirement that at least one stirrup layer must be intersected by the diagonal cracking plane; otherwise the steel contribution term ought to be taken as equal to zero.

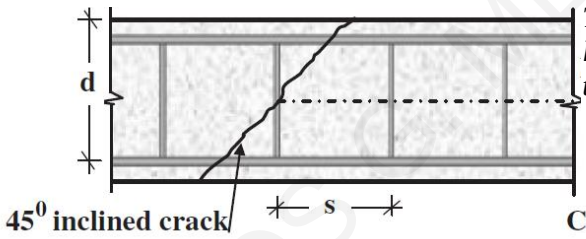

To find V_W, identify first the location where the least number of stirrup legs is intersected by the diagonal sliding plane.

Figure 2.6: The number of stirrups intersecting the sliding plane could be zero (Syntzirma and Pantazopoulou 2010))

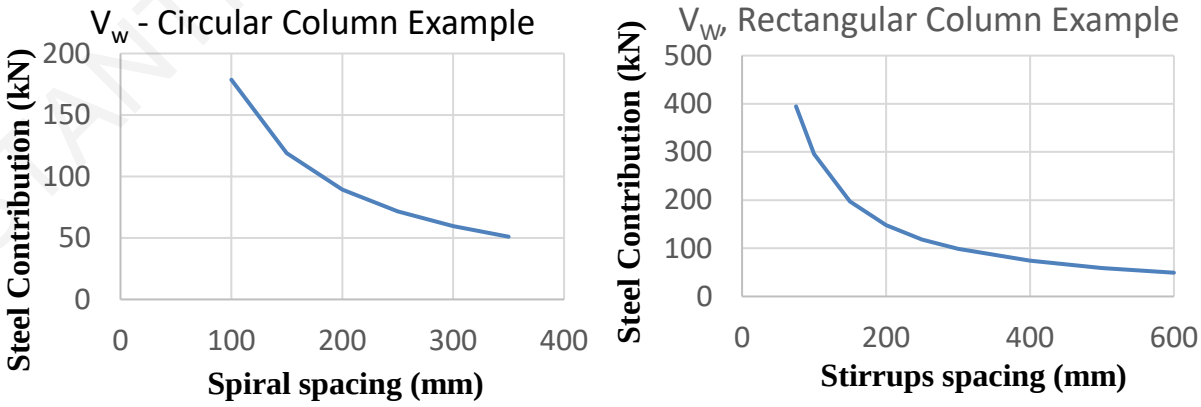

Figure 2.7: (a) Effect of spiral spacing on transverse steel contribution of a circular section in shear strength (b) Effect of stirrup spacing on transverse steel contribution of a square column section

In concrete columns with shear span ratio of L_s/h less or equal to 2, the shear strength, V_R cannot exceed the value corresponding to failure by web crushing along the diagonal of the column after flexural yielding, $V_{R,max}$, which under cyclic loading may be calculated from the expression:

$$V_{R,max} = (4/7)[1 - 0.02min(5; \mu_{\Delta}{}^{pl})][1 + 1.35(N/A_c f_c)][1 + 0.45(100\rho_{tot})] \cdot \sqrt{min(40; f_c)} b_w z \cdot sin2\delta \quad (2.4)$$

where $\boldsymbol{\delta}$ is the angle between the diagonal strut that is defined by the centroids of the compression zones at the column ends, and the axis of the column ($\tan\delta = h/2L_s$). By implementing this equation to the example of the cases described above but with a change on the shear span so that the column be compliant to the shear span ratio limit of Eq. 2.4, the following results are obtained (L_s=700mm). It can be seen that for the circular column case shear strength is close to web crushing along the diagonal.

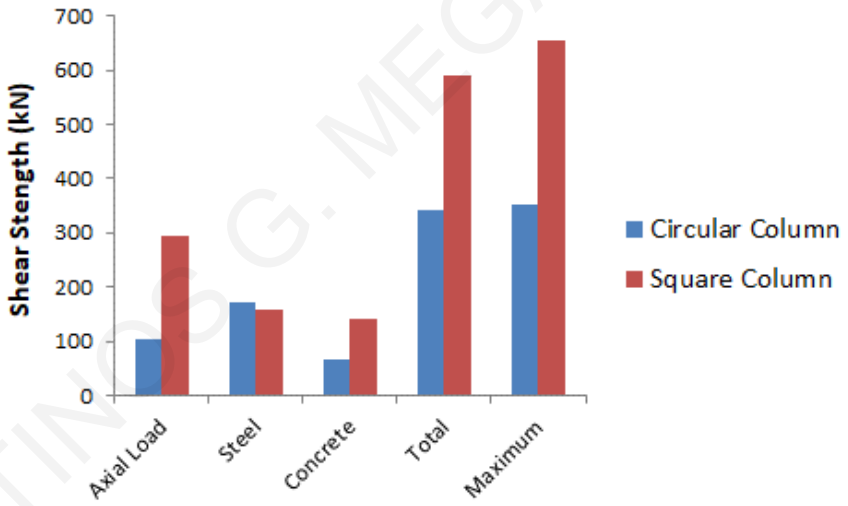

Figure 2.8: Shear Strength and its contributions for a typical reinforced concrete column.

ASCE/SEI 41 (2017) is the latest in a series of documents developed after the FEMA initiatives in the 1990s and 2000s towards the development of a consistent assessment framework for existing structures. The FEMA/ATC documents form the first integrated reference for performance-based engineering, whereby deformation and force demands for different seismic hazards are compared against the capacities at various performance limits (i.e. states of damage). At the outset of this momentous project by FEMA, available data on the performance of existing components were rather limited and therefore reliability

concepts were not applied evenly towards the establishment of performance criteria. The issue of dependably estimating the shear strength of a RC element appears to be rather complicated as it presumes the full understanding of the several interacting behavior mechanisms under reversed cyclic loading, whereas it is strongly affected by the imposed loading history, the dimensions of the element (e.g. the aspect ratio), the concrete strength, the longitudinal reinforcement ratio but mostly the ratio and the detailing of the transverse reinforcement. So far it has not been possible to theoretically describe the strength of the shear mechanism from first principles of mechanics without the use of calibrated empirical constants. Therefore, the shear strength estimates obtained from calibrated design expressions necessarily rely on the pool of experimental data used for correlation of the empirical expressions, as well as on the preconceived notions of the individual researchers as to the role each variable has in the mechanics of shear.

The following expression for estimation of the shear strength of tied rectangular-section reinforced concrete columns is proposed by the Code for seismic rehabilitation of existing buildings of the American Society of Civil Engineers ASCE/SEI 41 (2007):

$$V_R = V_c + V_w = k(\mu_\Delta)\left[\left(0.5\sqrt{f_c}/(L_s/d)\right)\sqrt{1 + N/\left(0.5A_g\sqrt{f_c}\right)}\right]0.8A_g + k(\mu_\Delta)\cdot \left[A_{sw}f_{yw}d/S\right] \quad (2.5)$$

where $\boldsymbol{V_c}$ is the concrete contribution in shear resistance; $\boldsymbol{V_w}$ is the contribution of transverse reinforcement; d is the effective depth; $\boldsymbol{L_s}$ is the shear span of the column; $\boldsymbol{N}$ is the axial force (compression positive, taken zero for tension); $\boldsymbol{A_g}$ is the gross cross-sectional area of the column; $\boldsymbol{A_{sw}}$ is the cross-sectional area of one layer of stirrup reinforcement parallel to the shear action; and $\boldsymbol{S}$ is the centerline spacing of stirrups along the length of the member. If S is equal to or greater than half of the effective depth of the column then the contribution of steel reinforcement V_w in shear strength is reduced to 50% of its estimated value from the above equation. If S is equal to or greater than the effective depth of the column then zero shear strength contribution from steel reinforcement V_w is considered; $\boldsymbol{f_c}$ is the concrete compressive strength; $\boldsymbol{k(\mu_\Delta)}$ is the shear strength reduction coefficient that depends on ductility demand. If ductility demand is less than or equal to 2 then the factor is set to equal to 1 (i.e. no strength reduction). If the ductility is greater than 6, then the reduction factor is

equal to 0.6. For ductility between 2 and 6 the reduction factor is linearly interpolated between the proposed values.

The V_c estimate given by Eq. 2.5 for the example of the rectangular column presented in this Section is: $V_{c,\text{ASCE}}$ = 233 kN, while EN 1998-3 (2005) resulted in $V_{c,\text{EC8-3}}$= 104 kN which, when combined with the axial load component (145.2 kN) leads to a total of 229.2 kN, which is comparable to the result of Eq.2.5. For the case of the circular column results to $V_{c,\text{ASCE}}$ = 81 kN whereas $V_{c,\text{EC8-3}}$=80 kN (49 kN from the axial load contribution and 31 kN concrete web contribution) – values calibrated well with each other. The effect of the stirrups' spacing to the steel contribution to shear strength is depicted in the following figures for ASCE/SEI-41 (2017) and it is compared with the results of EN 1998-3 (2005) (abbreviated as EC8-III).

Despite the convergence of the calibrated expressions of the two code approaches, the preceding comparisons highlight some of the uncertainties underlying the shear problem. For one, the concrete contribution term is taken—in both code documents—to be independent of the amount of transverse reinforcement, an omission that goes to the root of the truss-analogy model as originally introduced by Ritter and Moersch: there, the concrete contribution component was thought to be a minor correction to the main component that was owing to transverse reinforcement (the truss posts) so as to improve correlation with the tests – it was never meant to be a component of commensurate importance and magnitude to that of transverse reinforcement. Another source of uncertainty lies in the treatment of the axial load: in the EN 1998-3 (2005) approach, the axial load contribution is dealt with as a separate term, whereas in the ASCE/SEI 41 (2007) approach it is treated as an offset to the tensile strength of concrete in the member web. This difference causes a departure in the V_c values near the upper limit in the axial load ratio ($v=N/A_g f_c$) as depicted in Fig. 2.11.

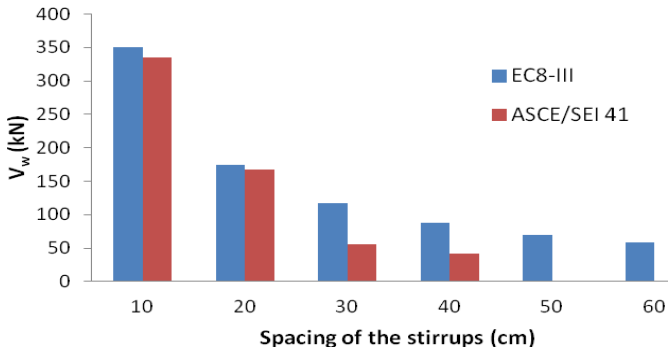

Figure 2.9: Effect of stirrup spacing on steel contribution of a rectangular section's shear strength.

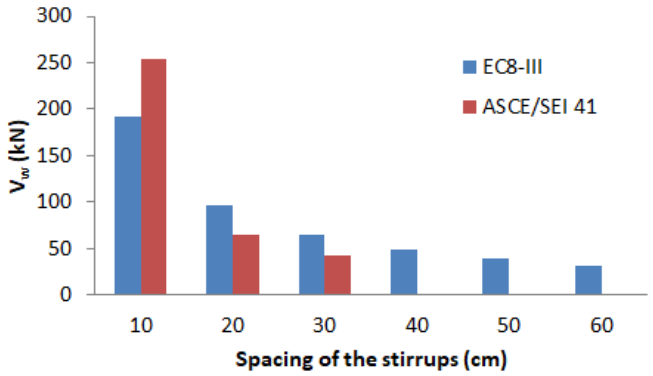

Figure 2.10: Effect of spiral step on steel contribution to shear strength of a circular section.

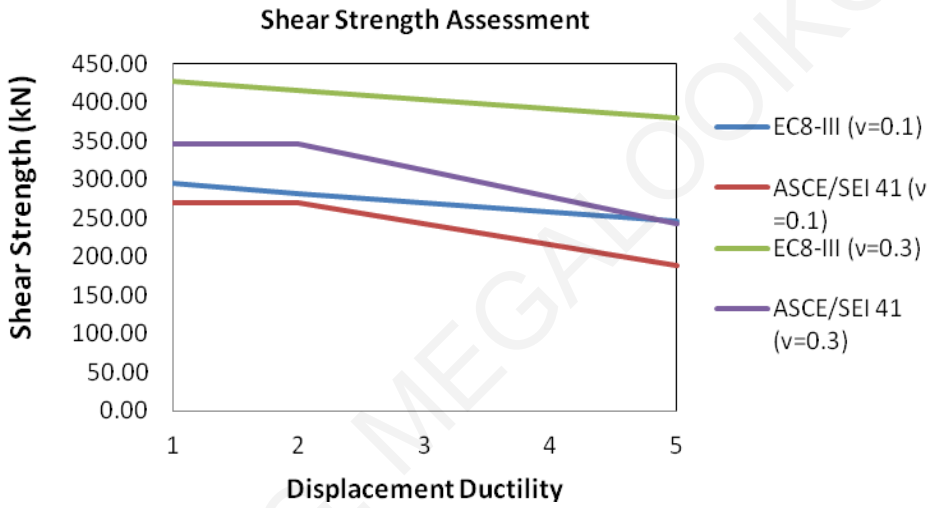

Figure 2.11: Shear strength vs. displacement ductility for the column with rectangular section.

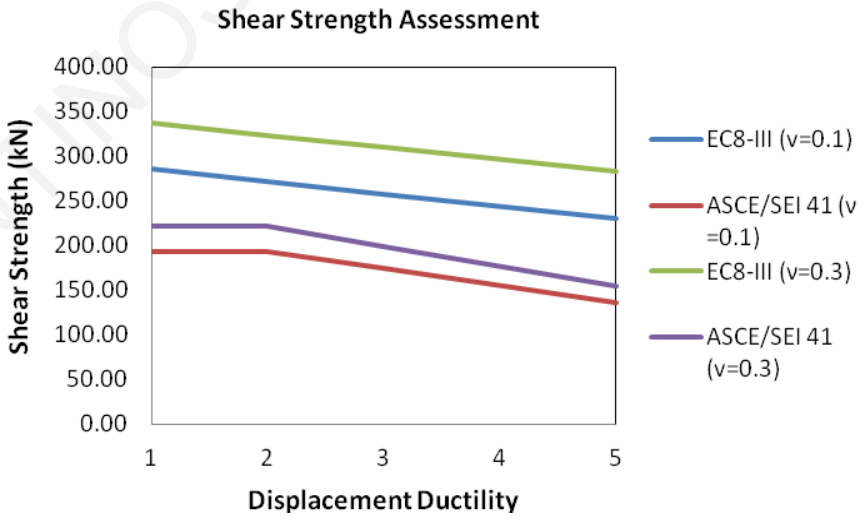

Figure 2.12: Shear strength vs. displacement ductility for the column with circular section.

Contrary to the shear strength assessment models of EN 1998-3 (2005) and ASCE/SEI 41 (2007), the shear model of fib Model Code (2010) is a design model which was not calibrated to specifically address members under seismic loads. The fib-MC2010 design section on shear provides the option of four different levels of model complexity depending on the level of detail needed at the time of calculation (intended to address the needs for preliminary design, for detailed design and for assessment). The four models are referred to here on as levels of approximation (LA) and are identified by Latin numbers. Thus, for members with shear reinforcement the LA-III model provides the point of reference since the higher the detail of the model, the greater the design effort required. This is also the case for shear strength assessment of members with low volume of shear reinforcement (Sigrist et al. 2013).

For members with shear reinforcement the fib Model Code 2010 shear provisions are based on a general stress field approach (Muttoni A. et al. 1997, Sigrist V. 2011), combined with Simplified Modified Compression Field Theory (SMCFT, Vecchio and Collins 1986, Bentz et al. 2006). As in all preceding code formulations the shear resistance V_R is determined by the sum of a concrete contribution and web steel contribution term:

$$V_R = V_c + V_w \tag{2.6}$$

For structural assessment, the strain dependence of the shear resistance may be taken into account by estimating the strain value ε_x at the mid-depth of the effective shear section as depicted in (Fig. 2.13(a), fib Model Code 2010; Fig. 2.13(b) illustrates the mechanics of formation of longitudinal tensile strains as a result of shear in cracked reinforced concrete). Other deformation parameters could be selected but this value has a clear physical meaning as it represents the average longitudinal strain in the web and can be found from the sectional forces. For a conventional reinforced concrete member, the effective shear depth z is assumed to be $0.9d$. The tension chord force can be found from moment equilibrium in the section (Fig. 2.13) and the tension chord strain is determined accordingly from the tension chord force:

$$T = 2 \cdot E_s \cdot \varepsilon_x \cdot A_s = \frac{M}{z} + \frac{V}{2}\cot a + N\left(\frac{1}{2} \pm \frac{\Delta e}{z}\right) \tag{2.7}$$

where $\boldsymbol{M}$ is the resisted moment, $\boldsymbol{V}$ is the applied shear force, $\boldsymbol{N}$ is the axial force, $\boldsymbol{\Delta e}$ is the eccentricity of the beam axis with respect to its mid-depth, $\boldsymbol{E_s}$ is the modulus of elasticity of longitudinal steel reinforcement and $\boldsymbol{A_s}$ is the area of tensile longitudinal reinforcement.

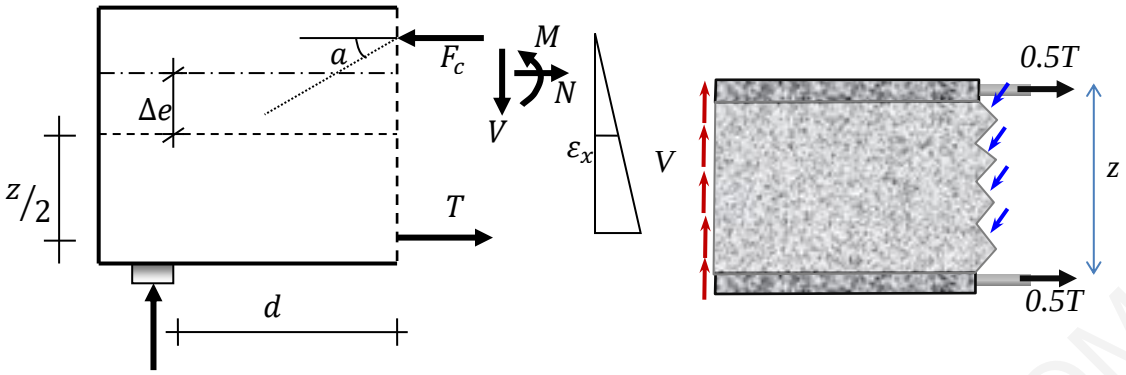

Figure 2.13: (a) Equilibrium at cross-section and corresponding approximation of strain profiles for end support region. (b) Cracked reinforced concrete: longitudinal tension is required to maintain equilibrium with the diagonal compressive struts (blue color)

For the sake of simplicity, and to avoid iteration (since the definition of the compressive stress field inclination angle a requires ε_x) for calculating the strain ε_x, the second item in Eq. 2.7 is approximated as $(V/2)\cot a \approx V$ (a compressive stress field inclination angle a close to 27^o is assumed) (Fig. 2.13). With the conservative assumption that the compression chord strain is zero, it may be shown that the mid-depth strain may be taken as half the tension chord strain (Fig.2.13). The resistance attributed to concrete is:

$$V_c = k_v \sqrt{f_c} b_w z \quad (f_c \; in \; MPa) \tag{2.8}$$

where $\boldsymbol{k_v}$ is a factor accounting for strain gradient effect and member size (Eq. 2.9), $\boldsymbol{f_c}$ is the concrete strength and $\boldsymbol{b_w}$ is the web-width. The k_v value, accounting for the demand in the concrete contribution term, is defined by:

$$k_v = \frac{0.4}{1+1500\varepsilon_x}\left(1 - \frac{V_{Ed}}{V_{Rd,max}(a_{min})}\right) \tag{2.9}$$

where $\boldsymbol{V_{Ed}}$ is the shear force demand at the control section.

The concrete contribution equation (Eq. 2.8) is limited to normal or moderately high concrete strengths up to f_c= 65MPa (the value $\sqrt{f_c}$ is limited to a maximum of 8 MPa); for higher strengths the equation may be deemed unconservative on account of the smoother crack faces where cracks pass through, rather than around, aggregate particles, resulting in larger variability in the shear resistance of members. For members with shear reinforcement, the shear resistance is the sum of the resistances provided by concrete (as per Eq. 2.8) and the contribution of stirrups:

$$V_w = \frac{A_{sw}}{S} z f_{yw} \cot a \tag{2.10}$$

where $\boldsymbol{A_{sw}}$ is the cross-sectional area of one layer of shear reinforcement, $\boldsymbol{f_{yw}}$ is the yield strength of shear reinforcement and $\boldsymbol{a}$ is the inclination of the compressive stress field relative to the longitudinal axis of the member (i.e., the angle of shear sliding cracks).

Shear strength is limited by the crushing of concrete along the inclined struts according with:

$$V_{R,max} = k_c f_c b_w z \sin \alpha \cos a \tag{2.11}$$

The strength reduction factor $k_c = k_\varepsilon \eta_{fc}$ accounts for the effect of compression softening due to transverse tensile strain through factor k_ε:

$$k_\varepsilon = \frac{1}{1.2+55\varepsilon_1} \leq 0.65 \tag{2.12}$$

and for the increasing brittleness of high strength concrete through factor η_{fc} which reduces the effective shear strength for $f_c > 30$ MPa:

$$\eta_{fc} = \left(\frac{30}{f_c}\right)^{1/3} \leq 1.0 \quad (f_c \; in \; MPa) \tag{2.13}$$

The principal tensile strain that causes the compression softening effect in k_ε above, $\varepsilon_1 = \varepsilon_x + (\varepsilon_x - \varepsilon_2)\cot^2 a$, is defined by a Mohr's circle of strain (Fig. 2.14); as an adequate approximation, the (negative) principal strain $-\varepsilon_2$ may be taken as the concrete peak strain $\varepsilon_{c0} = 0.002$ and ε_x from Eq. 2.7. Finally, the stress field or strut inclination (Fig. 2.14), relative to the longitudinal axis of the member, is limited to:

$$a_{min} \leq a \leq 45^o \tag{2.14}$$

$$a_{min} = 20^o + 10000\varepsilon_x \tag{2.15}$$

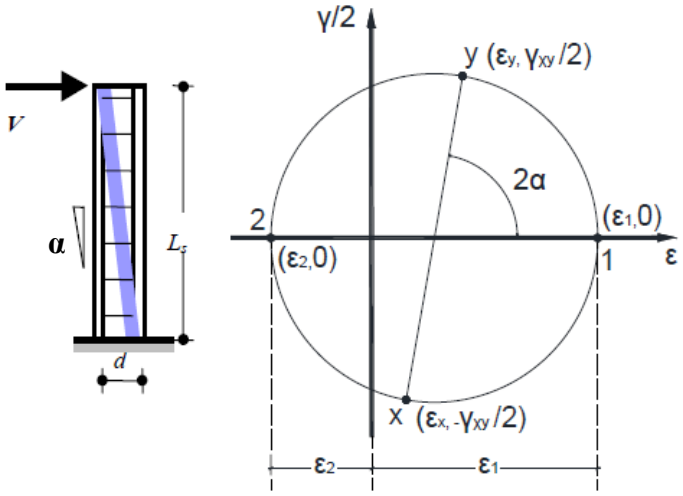

Figure 2.14: Strut inclination in a column and Mohr circle of strains.

A comparison of the assessment procedure described above based on the design model of *fib* Model Code 2010 with the assessment models of the previously presented Code requirements stated in this Section is illustrated in Figs. 2.16 and 2.17. The columns under study have similar properties with the already described example columns. It may be observed that the general method of the *fib* Model Code 2010 gives a more conservative estimation of the concrete contribution to shear strength.

Similar to the *fib* Model Code (2010), the design model of ACI-318-14 (2014) considers a concrete and a steel contribution to the shear strength of beam-columns:

$$V_R = V_c + V_w \tag{2.16}$$

The concrete term, V_c is taken as the shear force causing inclined cracking in the member, obtained by setting the maximum sectional shear stress equal to the principal tensile stress of concrete; after cracking, V_c is kept the same, but its presence is attributed to aggregate interlock, dowel action and the shear term transmitted across the concrete compression zone. As in all other codes, the shear strength is based on an average shear stress acting over the effective cross section $b_w d$ (b_w = web width or diameter of circular section, d = effective depth of cross section).

For non-prestressed members with axial compression, V_c is calculated from:

$$V_c = 0.17\left(1 + \frac{N_u}{14A_g}\right)\lambda\sqrt{f_c}\,b_w d \tag{2.17}$$

where $\boldsymbol{N_u}$ is the axial force normal to cross section- to be taken as positive for compression, (Newton), $\boldsymbol{A_g}$ is the gross area of concrete section, in mm^2, $\boldsymbol{f_c}$ is the specified compressive

strength of concrete (MPa), and $\boldsymbol{\lambda}$ is a modification factor to account for the reduced mechanical properties of lightweight concrete relative to normal weight concrete of the same compressive strength. For non-prestressed members with significant axial tension, V_c is calculated from:

$$V_c = 0.17\left(1 + \frac{0.29 \cdot N_u}{A_g}\right)\lambda\sqrt{f_c}\, b_w d \geq 0 \qquad (2.18)$$

Required shear reinforcement is obtained from a modified truss analogy, wherein the force in the truss posts (vertical ties, Fig. 2.15) is resisted by the shear reinforcement. However, considerable research on both non-prestressed and prestressed members has indicated that shear reinforcement needs to be designed to resist the shear demand exceeding the force that causes inclined cracking, assuming the diagonal struts in the truss panels to be inclined at 45 degrees (Fig. 2.15).

From equilibrium it may be easily shown that V_w supported by web reinforcement is:

$$V_w = \frac{A_v f_{yt} d}{S} \qquad (2.19)$$

where $\boldsymbol{S}$ is the longitudinal spacing of transverse reinforcement (or the spiral pitch of tied columns with spiral transverse steel), mm; $\boldsymbol{A_v}$ is the cross sectional area of shear reinforcement parallel to the shear force within a single stirrup pattern, mm^2, and $\boldsymbol{f_{yt}}$ is the specified yield strength of transverse reinforcement, MPa. Observe the similarity with the EN 1998-3 (2005) equation for the $\boldsymbol{V_w}$ term. In the ACI & ASCE approaches, for circular ties or spirals, $\boldsymbol{A_v}$ is two times the area of the spiral bar or wire. For calculation of $\boldsymbol{V_c}$ and $\boldsymbol{V_w}$ in solid circular sections, d is approximated by 0.8 times the diameter and $\boldsymbol{b_w}$ is taken as the diameter.

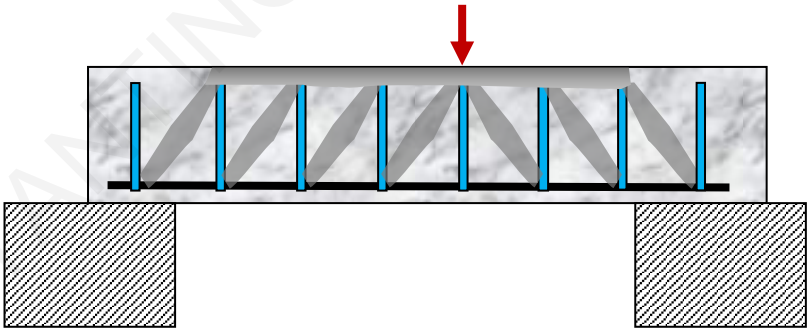

Figure 2.15: Original 45° Truss Model underlying the ACI (2014) requirements.

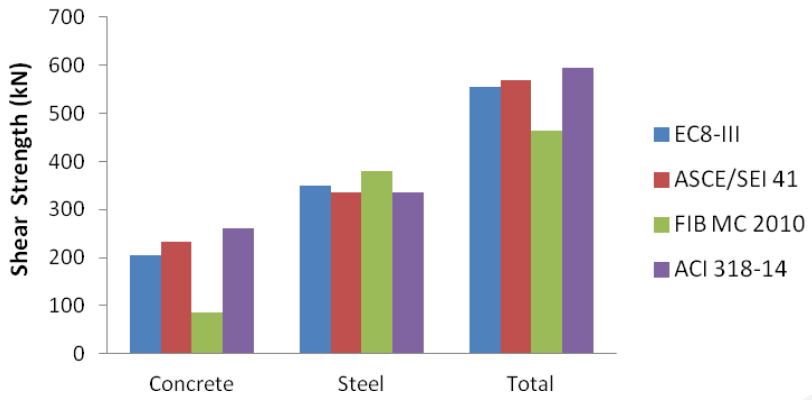

Figure 2.16: Comparison of shear strength assessment models for the square column example under study.

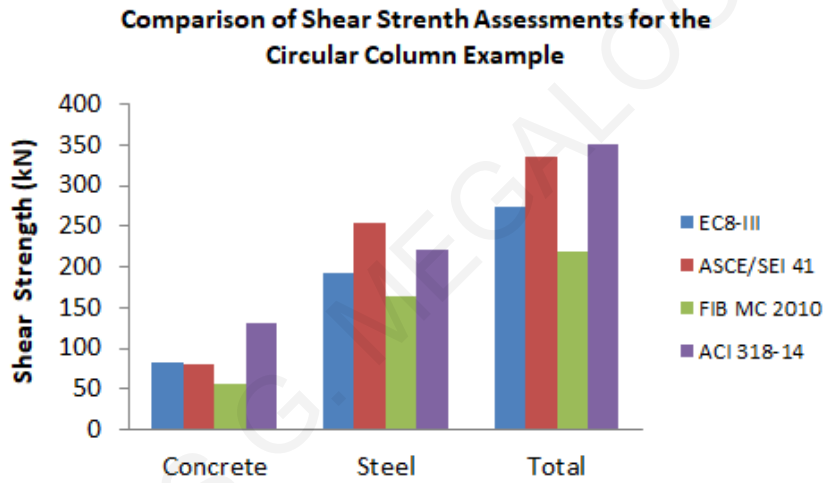

Figure 2.17: Comparison of shear strength assessment models for the circular column example under study.

Figures 2.16 and 2.17 compare the values obtained from the shear strength models of the various code provisions including ACI 318-14 (2014) for the example columns considered. Note that ACI 318-14 (2014) gives a higher shear strength estimation for concrete contribution with respect to the other code models but it is closely calibrated to both EN 1998-3 (2005) and ASCE/SEI-41 (2007).

Finally, it should be mentioned that the Hellenic Code for Seismic Assessment (KAN.EPE. 2014) containing the necessary provisions for structural assessment and interventions for reinforced concrete buildings adopts the EC8-III procedures (EN 1998-3, 2005), already introduced in the preceding.

2.4 Milestones in the Development of Models for Shear Strength Assessment of RC Columns

Reviewed Code provisions were developed and based on past research which was motivated by the extensive damages observed in modern engineered construction in the earthquakes that occurred worldwide after 1990. In particular, defining the degradation of shear strength due to increasing inelastic deformations has been the objective of several models (Aschheim and Moehle 1992, Priestley et al. 1994, Sezen and Moehle 2004) that were developed within the ATC/FEMA 273 (1997) and FEMA 356 (2000) initiatives in response to the catastrophic failures observed in California bridges and hospitals after the Loma Prieta (1989) and Northridge (1994) earthquake.

The study by Aschheim and Moehle (1992) was the first to propose a degrading pattern for the shear strength envelope of columns and beams on account of the accumulated effects of damage due to inelastic deformation. They proposed a degradation coefficient as a function of displacement ductility demand, μ_{Δ}, after calibrating an empirical relationship with a database of laboratory data from cantilever bridge column tests. The data indicated that the rate of degradation also depended on the amount of available transverse reinforcement and axial load. By adhering to the general practice of estimating shear strength as the summation of strength contributions from transverse reinforcement and concrete, (where V_W is obtained from Eq. 2.19) it was proposed that V_C be estimated from:

$$V_c = 0.3\left(k + \frac{N}{14A_g}\right)\sqrt{f_c}0.8A_g \tag{2.20}$$

$$\text{where } 0 \leq k = \frac{4-\mu_{\Delta}}{3} \leq 1 \tag{2.21}$$

Thus, this model associates the entire amount of strength degradation with deterioration of the concrete contribution term (through factor *k*). This model was intended to evaluate the shear strength in plastic hinge zones and was later adopted in FEMA 273 (1997). The approach by Priestley et al. (1994) further de-aggregates the shear strength of columns under cyclic lateral loads as comprising three distinct contributions – that of the concrete web, V_c, the truss mechanism (or transverse reinforcement), V_w, and an arch mechanism component, V_N, associated with the horizontal component of a diagonal strut (this develops through the member in order to transfer the axial load N to the base), as follows:

$$V_R = V_c + V_w + V_N \tag{2.22}$$

The concrete component V_c is given by:

$$V_c = k\sqrt{f_c'}A_e \tag{2.23}$$

where $A_e = 0.80A_g$ and the parameter k depends on the member displacement ductility level as defined in the following equations:

$$For\ \mu_\Delta \leq 2\ ,\ \ k = 0.29$$
$$For\ 2 < \mu_\Delta < 4\ ,\ \ k = -0.095\mu_\Delta + 0.48$$
$$For\ \mu_\Delta \geq 4\ ,\ k = 0.1 \tag{2.24}$$

The contribution of transverse reinforcement to shear strength is based on a truss mechanism using a 30-degree angle between the diagonal compression struts and the column longitudinal axis. For rectangular cross-section columns, the truss mechanism component, V_w, is estimated from:

$$V_w = \frac{A_{sw}f_{yw}(d-d')}{s}cot30^o \tag{2.25}$$

where $d - d'$ is the internal lever arm of the idealized truss. For circular cross-section columns, the truss mechanism component, V_w, is defined from:

$$V_w = \frac{\pi}{2}\frac{A_{sw}f_{yw}D'}{s}cot30^o \tag{2.26}$$

where D' is the distance measured parallel to the applied shear between centers of the perimeter hoop or spiral.

The arch component refers to the horizontal component of the inclined axial strut carrying the axial load to the support. In this model this term is given by

$$V_N = N\ tan\alpha = \frac{d-x}{2L_s}N \tag{2.27}$$

where α is the inclination of the diagonal compression strut with respect to the longitudinal axis of the column and x is the depth of the compression zone, whereas d is the effective depth of the section. It should be noted that the depth, x, depends on both the axial load and aspect ratio (i.e. the amount of curvature required to develop a certain displacement ductility). Thus, with an increasing aspect ratio the axial load contribution to shear strength decreases. Similarly, a higher depth of compression zone (for higher axial load) affects the value of V_N, showing a subtle increase for higher compressive N. The effect of the axial tensile load on the shear strength is not defined in the model.

Sezen and Moehle (2004) updated the earlier model of Aschheim and Moehle (1992) also relating column shear strength to the displacement ductility demand; the novelty here is that the strength degradation factor k was taken to operate on both concrete and steel contributions (Fig. 2-18):

$$V_n = k(V_c + V_s) = k\left(\frac{0.5\sqrt{f_c'}}{L_s/d}\sqrt{1+\frac{N}{0.5\sqrt{f_c'}A_g}}\right)0.8A_g + k\frac{A_{sw}f_{yw}d}{s} \quad (2.28)$$

This model was later adopted in the ASCE/SEI 41 (2017) assessment provisions. The reasoning in applying a reduction to both terms is that the concrete component is expected to diminish owing to increased cracking and degradation of the aggregate interlocking mechanism, whereas the steel component is assumed to degrade due to a reduction in the bond stress capacity required for an effective truss mechanism.

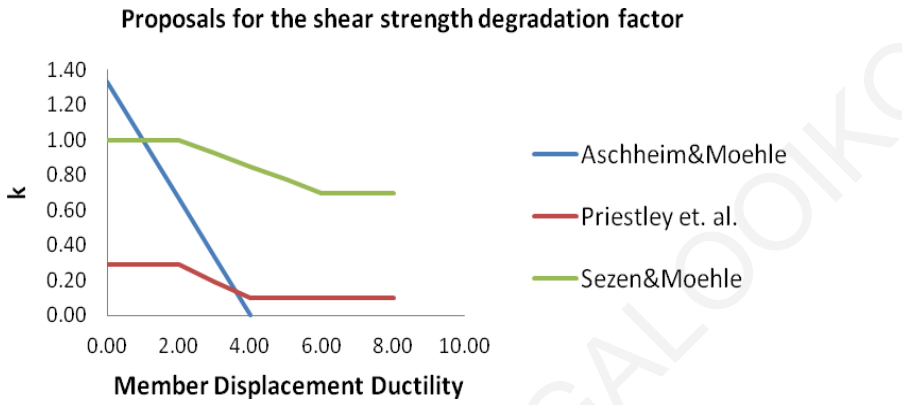

Figure 2.18: Variation of degradation coefficient k with displacement ductility. Note however that k does not operate on all terms in the same manner in the different models, so the relationship between alternative proposals is not transparent.

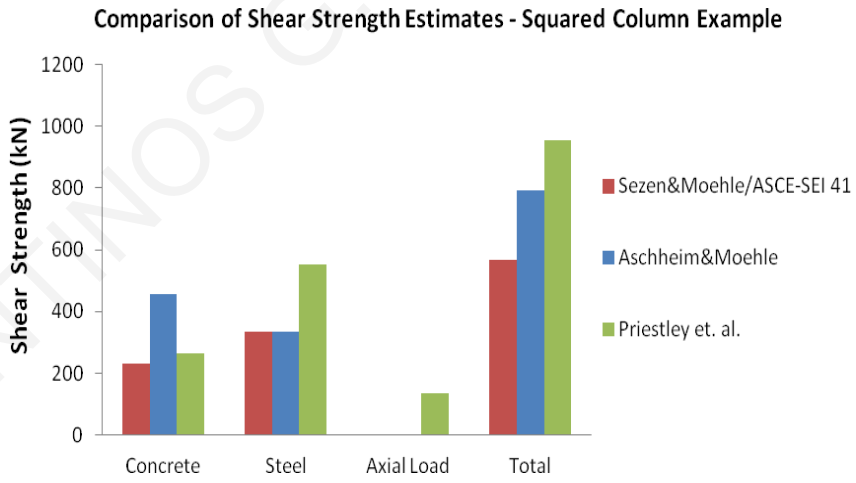

Figure 2.19: Comparison of shear strength assessment models for the square column example.

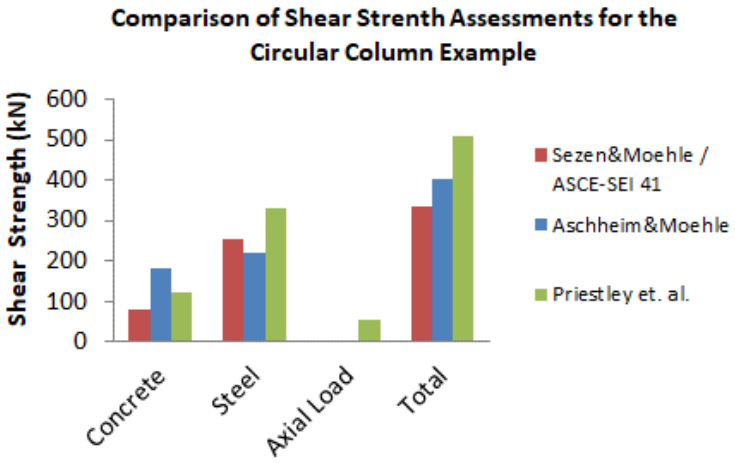

Figure 2.20: Comparison of shear strength assessment models for the circular column example. Mechanistic Definition of the V_C term

The comparison of the models included in this Section for the example columns under study of this Chapter is illustrated in Figs. 2.19 and 2.20. Differences in the estimation of the transverse reinforcement contribution to shear strength between the 30-degree truss model (Priestley et al 1994) and the 45-degree truss model adopted by Aschheim and Moehle (1992), Sezen and Moehle (2004) underscore the degree of approximation of the existing approaches. For the same stirrup arrangement, the 30-degree truss model gives a higher steel contribution to shear strength.

(a) The MCFT theory

An alternative framework suitable for interpretation of strength degradation with increasing deformation demand is that of the Modified Compression Field Theory (MCFT) (Vecchio and Collins, 1986). The model is derived from first principles (employs a smeared, continuum mechanics approach to establish equilibrium and compatibility) and uses experimentally verified stress-strain relationships for the behavior of cracked concrete. A fundamental relationship in the MCFT relates the shear stress on a cracked surface due to aggregate interlock to the crack's width, the maximum aggregate size and the concrete strength. The aggregate effect was first codified when a general method for shear design was derived based on the MCFT and implemented in the AASHTO-LRFD bridge design guidelines (2013). In 1994 the general method of shear design was implemented in the CSA concrete design code for buildings in Canada. An updated and simplified version of the general method has been developed (Bentz et al., 2006) and implemented in the 2004 CSA Design Code. The new general method, referred to as the Simplified Modified Compression

Field Theory (SMCFT) has been found by some to be simpler than the original general method with, in many cases, improved predictive capabilities (Sherwood et al., 2006).

According to SMCFT simple expressions have been developed for β (a parameter that models the ability of cracked concrete to transfer shear), the crack angle a, and the normal average strain in the web's longitudinal centroidal axis ε_x, thereby eliminating the need to iterate in order to solve for these values. The following general relationship is used to determine the shear resistance of a concrete section:

$$V_R = V_c + V_w = \beta\sqrt{f_c}b_w d_v + \frac{A_v f_y}{s} d_v \cot a \tag{2.29}$$

Term β in Eq. 2.29 is a function of 1) the longitudinal strain at the mid-depth of the web ε_x, 2) the crack spacing at the mid-depth of the web and 3) the maximum coarse aggregate size, a_g. It is calculated using an expression that consists of a strain effect term and a size effect term:

$$\beta = (\text{strain softening term}) \cdot (\text{size effect term}) = \frac{0.40}{(1+1500\varepsilon_x)} \cdot \frac{1300}{(1000+s_{ze})} \tag{2.30}$$

The longitudinal strain at the mid-depth of a beam web is conservatively assumed to be equal to one-half of the strain in the longitudinal tensile reinforcing steel as is adopted in the fib Model Code 2010 previously presented (see Fig. 2.13(b)). For sections that are not prestressed, ε_x is calculated according to Eq. 2.31 which is practically the same as Eq. 2.7 (here, M is the resisted moment, V is the applied shear force, N is the normal force [positive if it is tensile], E_s the modulus of steel, and A_s is the area of tension reinforcement):

$$\varepsilon_x = \frac{M/d_v + V + 0.5N}{2E_s A_s} \tag{2.31}$$

The effect of the crack spacing at the beam mid-depth is accounted for by the use of a crack spacing parameter s_z. This crack spacing parameter is equal to the smaller of either the flexural lever arm ($d_v = 0.9d$ or $0.72h$, whichever is smaller) or the maximum distance between layers of longitudinal crack control steel distributed along the height of the web.

The term s_{ze} is referred to as an "equivalent crack spacing factor" and has been developed to model the effects of different maximum aggregate sizes on the shear strength of concrete sections by modifying the crack spacing parameter. For concrete sections with less than the minimum quantity of transverse reinforcement and constructed with a maximum aggregate size of 20mm, s_{ze} is taken as equal to s_z. For concrete with a maximum aggregate size other than 20mm, s_{ze} is calculated as follows:

$$s_{ze} = \frac{35 s_z}{15 + a_g} \geq 0.85 s_z \tag{2.32}$$

To account for aggregate fracture at high concrete strengths, an effective maximum aggregate size is calculated by linearly reducing a_g to zero as the compressive concrete strength f_c increases from 60 to 70 MPa. Term $a_g$is taken equal to zero for higher concrete strengths on account of the observation that cracks go through the aggregates in higher strength concretes (i.e., for f_c>70 MPa). The square root of the concrete strength is limited to a maximum of 8 MPa as in the fib Model Code 2010 previously reviewed. The angle of inclination of the cracks at the beam mid-depth, α, is calculated by the following equation:

$$a = (29^o + 7000\varepsilon_x)(0.88 + s_{ze}/2500) \leq 75^o \quad (2.33)$$

For the example columns of this Chapter, Eq. 2.33 results in $a = 43^o$ for the square column and $a = 41^o$ for the circular column.

(b) *Compressive Zone Definition of V_C*

A campaign to re-evaluate the shear strength models for the V_C term was conducted by Tureyen and Frosch in 2003. As part of this effort, a new model was developed, taking the compressive zone part of the cross section (i.e. the part above the neutral axis) as the primary contributor to shear strength. As shown in Fig. 2.21, the model considers that whereas shear can be transferred over the entire effective depth d between cracks, at the location of a crack, shear stress can only be transferred through the uncracked concrete above the neutral axis. The shear stress distributions shown in Figure 2.21 (a) are theoretical; however, these can be simplified by considering average stress distributions as shown in Figure 2.21 (b).

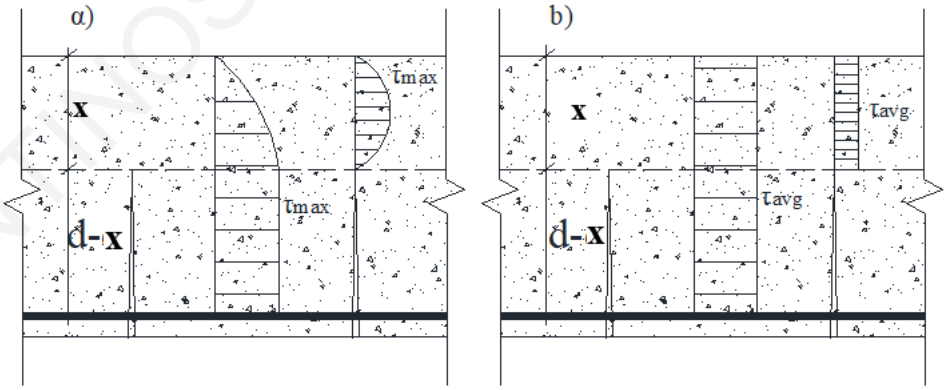

Figure 2.21: Theoretical (a) and Average (b) Shear Stress Distribution.

Using this model and considering the average shear stress distribution at a crack, a simplified expression for concrete contribution to shear strength was developed:

$$V_c = \frac{2}{5}\sqrt{f_c}b_w x \approx 0.4\sqrt{f_c}b_w x \quad (2.34)$$

where $\boldsymbol{x}$ is the depth of compression zone (mm) (or distance of the neutral axis from the compression face of the cracked, transformed cross section of the member). An advantage of this approach is that the effect of axial load is implicitly accounted for in the value of $\boldsymbol{x}$.

Mechanics-based definitions of shear-strength models such as those presented in the preceding are useful in estimating the available strength of members in conventional strength-based design and assessment. However, for seismic assessment, the strength-based approaches overlook a significant aspect that is essential in the performance context (i.e. when the focus is on the intensity of damage sustained in order for the strength to be developed) – namely, the deformation capacity of the member and the mode of failure associated with the exhaustion of the shear strength terms, and the margin of safety required between this, brittle occurrence and the more ductile mechanisms of behavior before safety may be compromised. The above-mentioned limitation motivated the effort for the development of displacement-based models in order to obtain a dependable estimation of the drift capacity of flexure-shear critical columns, i.e., columns that become critical in shear immediately after flexural yielding for a known axial load magnitude and member aspect ratio (L_s/h).

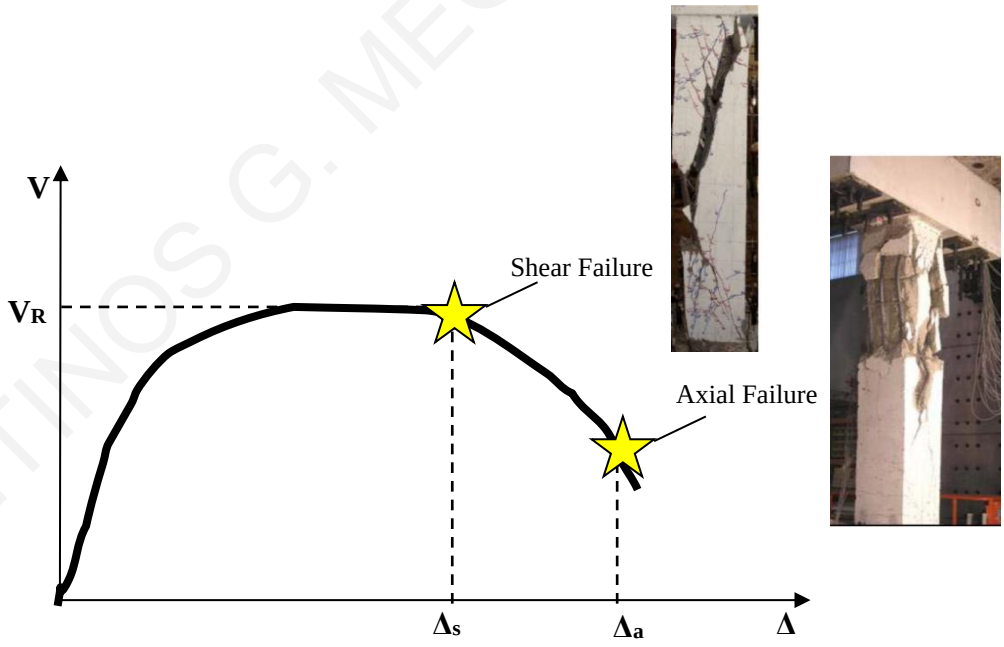

Figure 2.22: Definition of Deformation Limits at Shear and Axial Failure of a Reinforced Concrete Column.

The occurrence of a steep shear crack in a reinforced concrete column signifies the process of strength degradation that eventually leads to shear failure (see Fig. 2.3). If the reinforcement anchorages are sufficient, then, beyond this point the steep shear crack

developed on the column leads to progressive sliding between the crack surfaces, permanent distortion of the web with simultaneous buckling of longitudinal reinforcement and fracturing of transverse reinforcing bars crossing the sliding plane; this type of failure eliminates the ability of the column to carry the overbearing loads and is therefore considered an axial failure. These two stages are distinct and not interchangeable; for the sake of clarity the two points of failure are marked on the notional element backbone curve in Fig 2.22.

The model developed by Pujol et al. (1999) related the magnitude of drift at shear failure with the aspect ratio of the column (L_s/d, where L_s is the column shear-span and d is the section depth from the center of tension reinforcement to the extreme compression fiber of the column), the shear reinforcement ratio ρ_w (yield stress of f_{yw}), and with the column shear stress τ at shear failure (defined as the shear force at shear failure divided by the web area, $b_w d$). Based only on a statistical evaluation of the results of an experimental database that comprised 15 series of tests containing 94 specimens, and in an effort to establish a conservative estimate of the drift ratio at shear failure, Pujol et al. (1999) recommended the following relationship (L = clear height of column):

$$100\frac{\Delta_s}{L} = \frac{\rho_w f_{yw}}{\tau} \cdot \frac{L_s}{d} \leq \begin{cases} L_s/d \\ 4 \end{cases} \tag{2.35}$$

All the column specimens considered in the study were subjected to nominal shear stresses that may be assumed to be high enough so as to produce inclined shear cracking (shear stresses that exceed the tensile strength of the concrete). Failure was due to disintegration of the concrete core caused by sliding along inclined cracks and crushing of the concrete under compression. The ranges of the parameters for the employed experimental data leading to Eq. 2.35 were:

f_c: 21-86 MPa;

ρ_s (Longitudinal reinforcement ratio): 0.5-5.1%;

$\rho_w f_{yw}$: 0-8 Mpa ;

$\nu = N/(f_c A_g)$: 0-0.2 ;

L_s/d: 1.3-5;

$\tau/\sqrt{f_c}$: $>$ 0.17.

Figure 2.23 depicts the results from Pujol et al. (1999) model applied on an independent database of column tests assembled by Sezen and Moehle (2002); the database consists of 50 flexure-shear-critical columns representative of columns from older reinforced concrete buildings. The test columns were selected from the literature for specimens tested

under unidirectional cyclic lateral load with low transverse reinforcement ratios ($\rho_w \leq 0.007$), yielding of longitudinal reinforcement prior to loss of lateral load capacity, and shear distress observed at failure suggesting that loss in lateral load capacity was due to degradation of the shear-transfer mechanism. In testing Eqn. 2.35 against the database, Elwood (2003) observed that the proposed expression for drift at shear failure is not conservative for six of the columns in the employed database. Three of those columns were subjected to axial loads in excess of the axial loads considered when developing the model. Although conservative with respect to the other specimens, there is nevertheless still significant discrepancy between calculated and measured drift values.

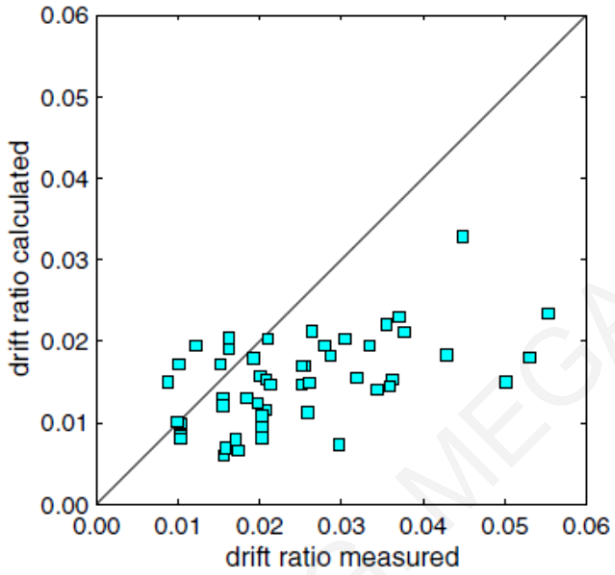

Figure 2.23: Comparison of calculated and measured drifts for Pujol et al. 1999 (Elwood 2003).

Elwood and Moehle (2005) proposed an empirical model that relates the shear demand to the drift at shear failure (Δ_s/L) based on the transverse reinforcement ratio ρ_w, shear stress ratio $\left(\tau/\sqrt{f_c}\right)$, and axial load ratio $\left(\nu = N/A_g f_c\right)$. The point of shear failure in the developed model was determined by the intersection of shear-drift curve for the column and the limit surface defined by a postulated drift capacity model (the limit surface is the outcome of Equation 2-36 for different pairs of shear force (and the corresponding shear stress) and the resulting displacement Δ_s plotted along with the element resistance curve-Figure 2.24). The proposed equation is:

$$\frac{\Delta_s}{L} = 3\% + 4\rho_w - 0.002 \cdot \frac{\tau}{\sqrt{f_c'}} - 0.025 \cdot \nu \geq 1\% \qquad (2.36)$$

For the example of the square column under study in this Chapter with S=200 mm Eqn. 2.35 results in a 1.7% relative drift ratio (RDR) at shear failure whereas Eqn. 2.36

estimates 2.4 % RDR for the same event (depicted in Fig. 2.25 by the red and the blue dots, respectively). Therefore, the drift model by Pujol et al. (1999) is more conservative.

To date, a limited number of models (Elwood and Moehle 2005, Ngoc-Tran and Li 2013) have been developed to estimate the axial-drift failure of non-ductile columns. The model by Elwood and Moehle (2005) was developed considering the free body diagram of a column failed in the shear (Fig. 2.3); here the only possible resistance is provided through shear friction along the sliding interface – collapse is imminent. Figure 2.26 depicts the free-body diagram of the upper portion of a column under shear and axial load at imminent axial load failure. The lower boundary of the free-body diagram delineates the inclined plane of sliding failure where shear friction demand exceeds the shear-friction resistance along the crack.

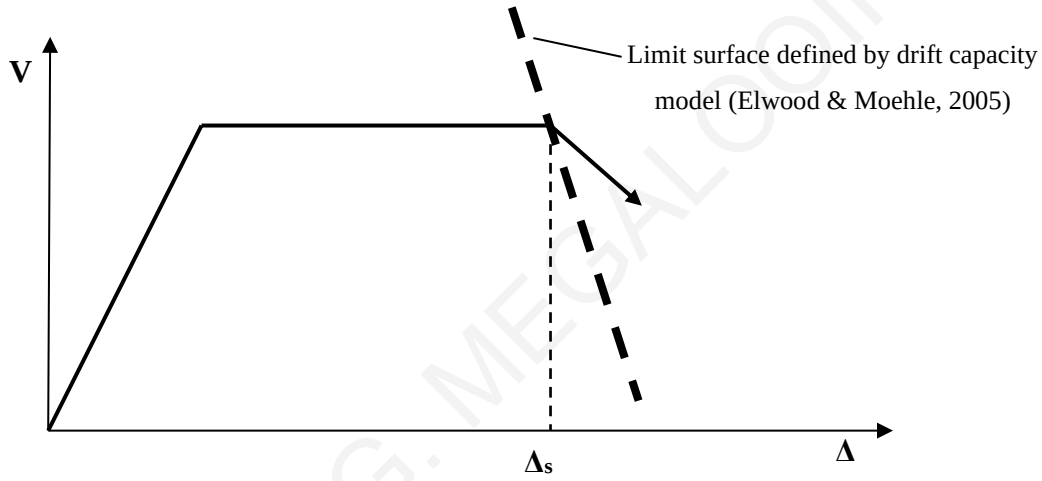

Figure 2.24: Shear failure by the drift capacity model of Elwood and Moehle (2005)

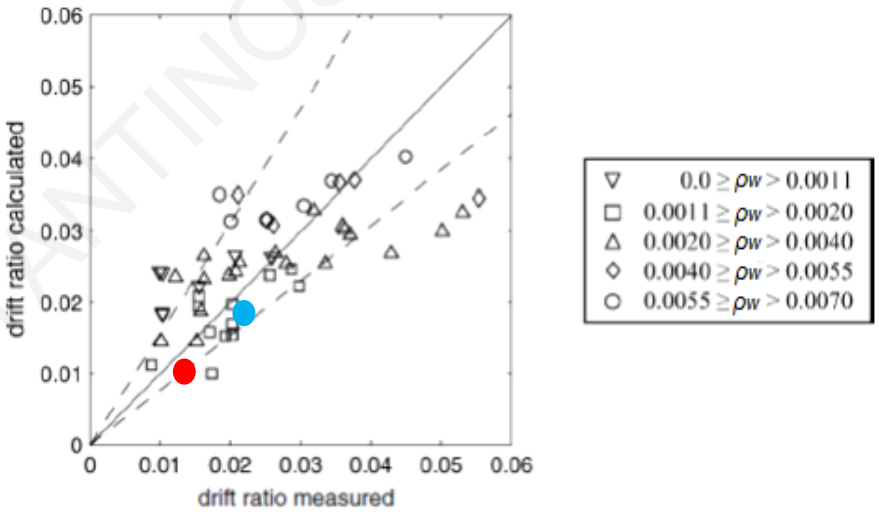

Figure 2.25: Comparison of calculated drift ratio at shear failure using Eq. 2.36 with database by Elwood. (Elwood 2003 – Dashed lines are +/- one standard deviation from the mean.)

Simplifications were made where terms were fraught with significant uncertainty (e.g. dowel forces from the transverse reinforcement crossing the inclined crack were neglected; their effect is considered to be part of the shear-friction force developing along the cracked plane. Similarly, the dowel action of longitudinal bars was neglected as in older structures spacing and diameter of transverse reinforcement are not sufficient to provide noticeable resistance to lateral dislocation of the longitudinal reinforcement (see Fig. 2.3)). Based on the observations of failed columns at that stage it is seen that upon axial crushing the longitudinal reinforcement has buckled, and therefore its axial force capacity was assumed equal to zero. Last, at incipient axial failure any source of shear resistance except the frictional action is assumed to have diminished to zero and may therefore be neglected. Equilibrium of forces for the free body diagram shown in Fig. 2.26 results in the following:

$$\sum F_x = 0 \rightarrow P \sin a' + V = V_{sf} \cos a' + \frac{A_{sw} f_{yw} d_c}{S} \tan a' + n_{bars} V_d \quad (2.37)$$

$$\sum F_y = 0 \rightarrow N = P \cos a' + V_{sf} \sin a' + n_{bars} P_s \quad (2.38)$$

Equation 2-37 after consideration of the simplifications made in the preceding is written:

$$P \sin a' = V_{sf} \cos a' + \frac{A_{sw} f_{yw} d_c}{S} \tan a' \quad (2.39)$$

From Eqns. 2-38 and 2-39 and assuming a frictional relationship between P and V_{sf}, an expression is obtained that relates axial load, N, transverse reinforcement, A_{sw}, stirrup spacing S, and drift ratio at axial load collapse:

$$\left(\frac{\Delta_a}{L}\right)_{axial} = 4\% \cdot \frac{1+(\tan 65^o)^2}{\left[\tan 65^o + N \cdot \left(\frac{s}{A_{sw} \cdot f_{yw} \cdot d_c \cdot \tan 65^o}\right)\right]} \quad (2.40)$$

where $d_c = d - d'$ is the depth of the column core between the centerlines of the ties. Based on experimental observation it was estimated that the angle of the sliding plane is about 25^o from vertical (65^o with respect to the transverse direction). Similar to the shear-failure model described in the previous section, the axial drift model defines a limit surface at which axial failure is expected to occur (Fig. 2.27). For the square column under study in this Chapter and for a 200 mm stirrup spacing, the drift ratio at axial load failure or collapse was estimated at 3.9%.

Ngoc-Tran and Li (2013) presented analytical and experimental investigations carried out on RC columns with light transverse reinforcement. A semi-empirical model was developed to estimate the ultimate displacement (displacement at axial failure) of RC columns with light transverse reinforcement subjected to simulated seismic loading. The following basic assumptions were employed in deriving the model:

- The applied axial load at the point of axial failure is transferred through the shear failure plane.
- The angle of the shear failure plane of 60^o as defined by Priestley et al. 1994 was adopted. (30^o angle between the diagonal compression struts and the column longitudinal axis as stated already in the description of Priestley et al. (1994) shear strength model).
- The shear demand on the columns was considered to be negligible and therefore ignored at the point of axial failure.
- Once the shear strength had initiated its degradation - corresponding to a displacement ductility of 2 for unidirectional lateral loading – then it was assumed that any additional deformation of the columns was owing to sliding between cracking surfaces as shown in Fig. 2.28.

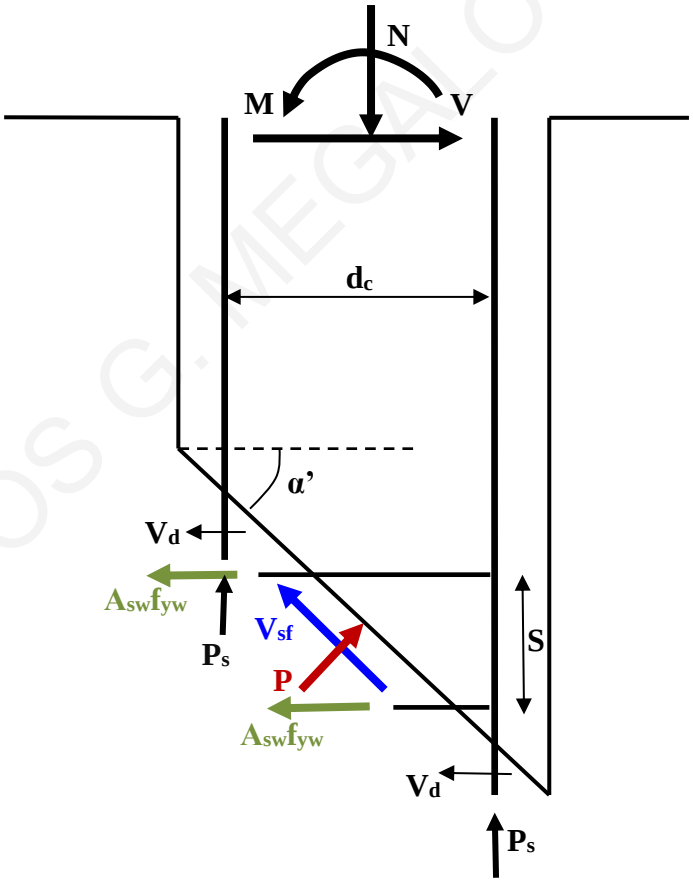

Figure 2.26: Free-body diagram of upper end of column (Elwood and Moehle 2005).

At the point of axial failure as shown in Fig. 2.28, the external and internal works W_{ext}, W_{int}, developed by the column were calculated according to the following:

$$W_{ext} = N \times \Delta_{av}^{*} \quad (2.41)$$

$$W_{int} = W_c + W_{sv} + W_{sl} \quad (2.42)$$

W_c, W_{sv}, and W_{sl} are the internal works done by deformation of concrete, transverse reinforcement and longitudinal reinforcement, respectively. As illustrated in Fig. 2.28, Δ^*_{av} is the vertical displacement due to sliding between cracking surfaces at the point of axial failure. Equating the external and the internal work leads to the following equation:

$$N = P_{sl} + P_{st} + P_c \quad (2.43)$$

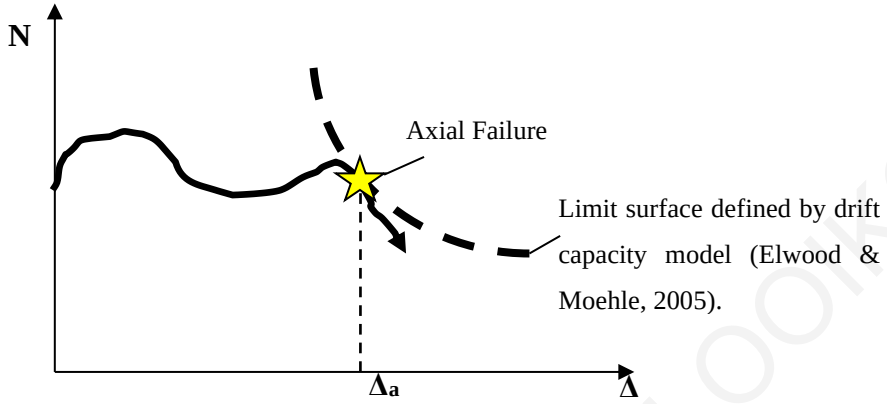

Figure 2.27: Axial Failure defined by the drift-capacity model of Elwood and Moehle 2005.

where P_{sl}, P_{st}, P_c are the axial forces resisted by longitudinal reinforcement, transverse reinforcement, and concrete at imminent axial failure, respectively. Axial strength of longitudinal reinforcing bars at axial failure normalized by their nominal yield strength defines the yield strength ratio, η_{sl}, as follows:

$$\eta_{sl} = (N - P_{st} - P_c)/(\rho_l b_w h f_{yl}) \quad (2.44)$$

$$P_{st} = (d_c f_{yw} A_{sw})/S \quad (2.45)$$

$$P_c = V_c \cot a' \quad (2.46)$$

where d_c is the depth of the core (centerline to centerline of ties) ρ_l is the total longitudinal reinforcement ratio; b_w and h are the width and the height of the column's cross section respectively; f_{yl} the yield strength of the longitudinal reinforcement. V_c is defined by Eq. 2.23. With reference to Fig. 2.28 the damaged length L_d is given by:

$$L_d = h \tan \alpha' \quad (2.47)$$

The ratio of horizontal displacement due to sliding between cracking surfaces at axial failure divided by the damaged length has the physical significance of a drift ratio, associated here with axial collapse. This term, δ^*_a , is given as:

$$\delta_a^* = \left[\underbrace{\left(\Delta_\alpha - 2\Delta_y\right)}_{\Delta_\alpha^*} / (h \tan \alpha') \right] \times 100\% \quad (2.48)$$

In the above, the yield displacement Δ_y is defined as the displacement associated with the secant to yield line in the force-displacement resistance curve of the member.

The equations derived above are calibrated using an assembled database comprising 47 RC columns tested to the point of axial failure. These columns encompass a wide range of cross-sectional sizes, material properties, and column axial loads. They were subjected to a combination of an axial load and unidirectional cyclic loadings to simulate earthquake actions. Based on the employed database, an empirical equation was developed so as to relate the ratio of- the axial strength of longitudinal reinforcing bars to the yield strength of the longitudinal reinforcing bars- to the ratio of - the horizontal displacement due to the sliding between cracking surfaces to the damaged length - as follows:

$$\eta_{sl} = 1/(0.2046 \times \delta_a^* + 1) \quad (2.49)$$

A series of experiments was conducted on five RC columns with light transverse reinforcement to validate the applicability and accuracy of the developed model [Ngoc-Tran and Li (2013)]. These tests were not included in the experimental database from which the developed semi-empirical model was derived. It is concluded from the study that the mean ratios of the experimental to estimated ultimate displacements and the corresponding coefficients of variation were 1.077 and 0.194, respectively. A comparison of the results obtained from the proposed equation by Ngoc Tran and Li (2013) with the model by Elwood and Moehle (2005) is depicted in Fig. 2.29. When applying Eqn. 2.48 to the example square column under study in this Chapter with 200 mm stirrup spacing, the estimated drift at axial failure is 2.8 %. This value is much more conservative as compared to the result by Elwood and Moehle (2005) (3.9%; note the red and blue dots in the Figure 2.29, respectively).

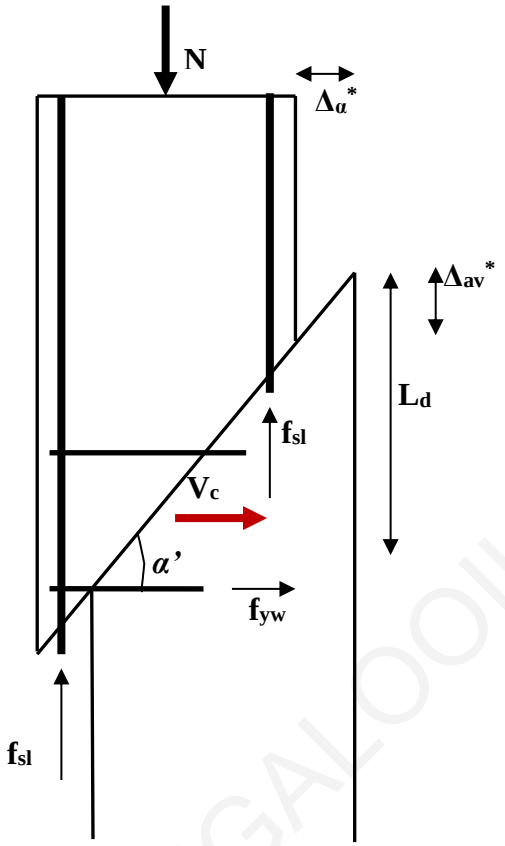

Figure 2.28: Assumed failure plane at the point of axial failure (Ngoc-Tran and Li, 2013).

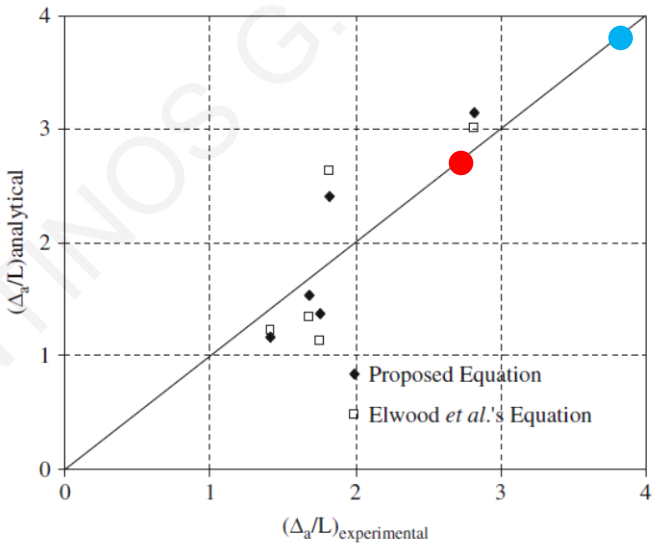

Figure 2.29: Comparisons between experimental and analytical ultimate displacements at axial failure of various equations.

3 Performance of the existing models applied to the RC columns of PEER Structural Performance database

3.1 Introduction

The mode of failure of structural members such as reinforced concrete columns depends on several factors, such as their geometric characteristics, the longitudinal reinforcement, the efficiency of confinement through the transverse reinforcement and the loading history. Their behavior throughout the loading range is controlled by competing mechanisms of resistance such as flexure, shear, buckling of longitudinal bars when they are subjected to compressive loads, and in the case of lap splices, the lap-splice mechanism of bar reinforcement development. Very often a combination of such mechanisms characterizes the macroscopic behavior of the column, especially in cases of cyclic load reversals. Various predictive models have been developed in the past to determine both the strength as well as the deformation capacity of the columns, the uncertainty being at least one order of magnitude greater in terms of deformation capacity rather than strength, as evidenced by comparisons with test results.

In this Chapter, some of the models described analytically in Chapter 2 are tested for their performance against a widely used experimental database (2003, https://nisee.berkeley.edu/spd/) originally assembled by Berry and Eberhard (2004). Known as the PEER Structural Performance Database, it assembles the results of over 400 cyclic, lateral-load tests of reinforced concrete columns. The database describes tests of spiral or circular hoop-confined columns, rectangular tied columns, and columns with or without lap splices of longitudinal reinforcement at the critical sections. For each test, where the information is available, the database provides the column geometry, column material properties, column reinforcing details, test configuration (including P-Delta configuration), axial load, digital lateral force displacement history at the top of the column, and top displacement that preceded various damage observations.

First, the parametric dimensions of the employed database are explored and a sensitivity analysis is conducted in order to highlight the statistical content and parameter trends with regards to basic indices that define the column behavior. Subsequently, flexure-dominant columns having either a circular or a rectangular cross section are studied so as to attempt to reproduce (and therefore fully comprehend) their hysteretic lateral experimental

response. Shear critical columns are studied as a separate group - in terms of strength and deformation capacity. Some of the models presented in Chapter 2 for shear strength are tested against this group of experimental data. Lastly an experimental database for cyclic tests of reinforced concrete columns under variable axial load is assembled for the needs of the present study, and are used to corroborate the models outlined in Chapter 2 with regards primarily to deformation capacity as the axial load varies from compressive to tensile (modeling the overturning effects of the earthquake on perimeter frame columns in structures).

3.2 Parametric Sensitivity of PEER Structural Performance Database

The statistical profile of the data available in the PEER structural performance database (https://nisee.berkeley.edu/spd/) is outlined here. Distributions of key column properties (depth, aspect ratio, axial load ratio, longitudinal reinforcement ratio and transverse reinforcement ratio) provide the overall scope and limitations of the experimental investigations, and the degree of overlap and knowledge gaps between the available studies. The value of such collected databases is in crossing the boundaries of the individual experimental studies that have been conducted before, which, owing to the difficulty due to the size and expense of specimens, never include more than a handful of tests, always much smaller in number than the number of independent parameters and rarely if ever presented in replicas of two or three. In the context of understanding the scope of the database, principal indices of deformability (i.e. displacement ductility) are presented in correlation with key design parameters (concrete strength, axial load ratio, aspect ratio, maximum shear force and transverse reinforcement ratio).

3.2.1 Characteristics of Available Data

Table 3.1 provides the mean values (Mean), Standard deviation (*std*) and Coefficient of variation (*CoV*) of key column properties for 306 rectangular-reinforced columns and 177 spiral-reinforced columns. Statistics are provided for the column depth, aspect ratio, axial-load ratio, longitudinal reinforcement ratio (ρ_l) and transverse reinforcement ratio (ρ_s).

Table 3.1: Column Property Statistics

	Rectangular-Reinforced (306 tests)			Spirally-Reinforced (177 tests)		
Column Property	**Mean**	**Std**	**CoV**	**Mean**	**Std**	**CoV**
Depth (mm)	323.43	116.5	0.36	420.97	202.11	0.48
Aspect Ratio	3.44	1.44	0.42	3.31	1.96	0.59
Axial-Load Ratio	0.27	0.19	0.73	0.14	0.14	1.04
$\rho_{l\,(\%)}$	2.45	1.00	0.41	2.62	1.02	0.39
$\rho_{s\,(\%)}$	1.34	1.07	0.80	0..93	0.74	0.80

The distributions of column depth used by researchers are illustrated in Figs. 3.1 and 3.2. Evidently, the rectangular-reinforced data is approximately normally distributed about a mean value of 300 mm. On the other hand, the spiral column reinforcement data does not follow a normal distribution. Figure 3.2 depicts a box plot (BP) for each of the two groups of specimens. (A box plot describes the five-number summary of a distribution that consists of the smallest (Minimum) observation, the first quartile (Q1), the median (Q2), the third quartile (Q3), and the largest (Maximum) observation written in the order of lowest to largest. The central box spans the quartiles. A line within the box marks the median. Lines extending above and below the box mark the smallest and the largest observations (i.e. the range). Outlying samples may be additionally plotted outside the range.

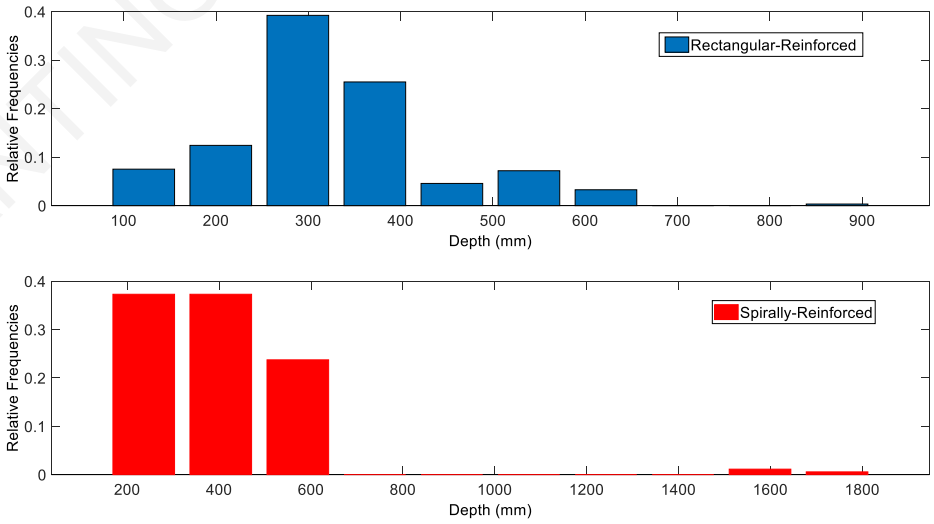

Figure 3.1: Distribution of column depth.

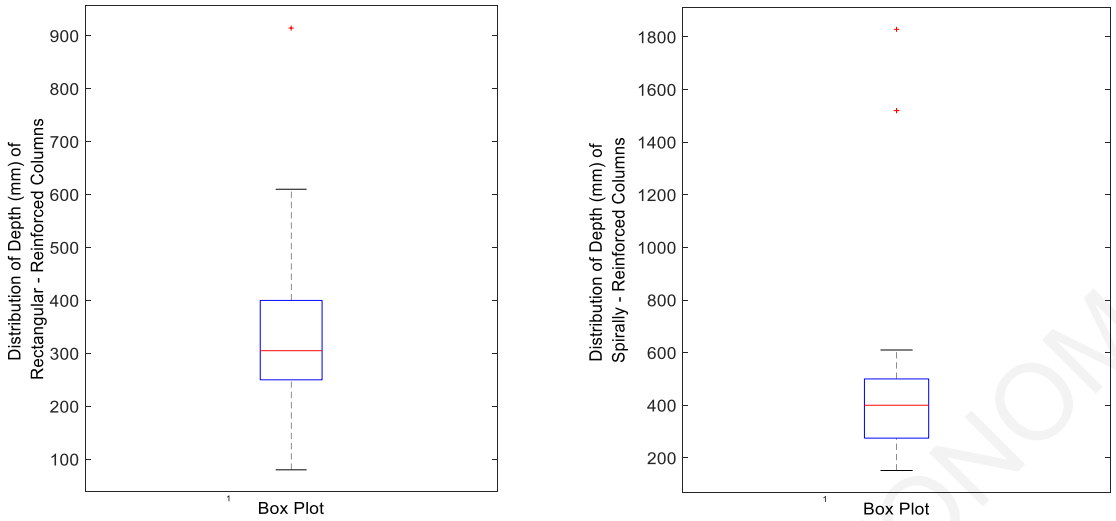

Figure 3.2: Box plot of column depth.

The database distributions regarding column specimen aspect ratio are illustrated in Fig. 3.3 & 3.4. The rectangular-reinforced data is approximately normally distributed about its mean value with a skew towards the lower aspect ratios. The spiral reinforced data is also weighted towards the lower aspect ratios. Figure 3.4 depicts the box plot for the two groups of specimens. It should be noted that the length for the determination of the aspect ratio of each column is the equivalent cantilever column length.

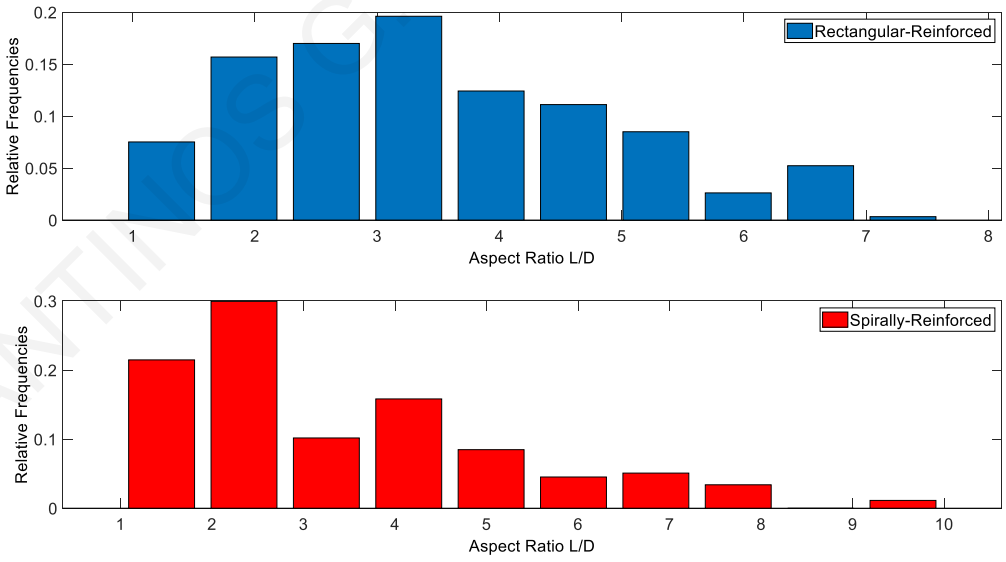

Figure 3.3: Distribution of column aspect ratio.

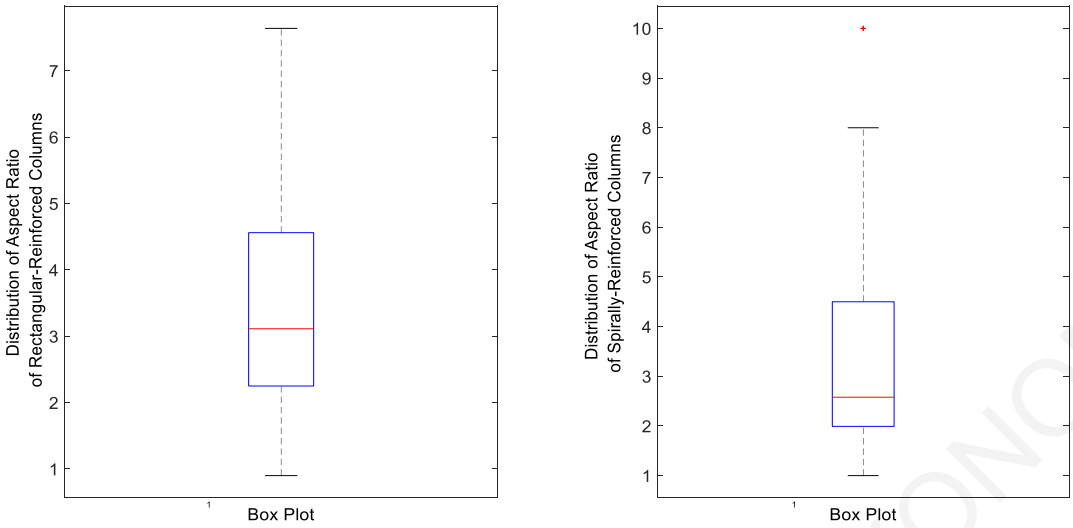

Figure 3.4: Box plot of column aspect ratio.

The distributions of the axial-load ratio values used in the tests are illustrated in Figs. 3.5 and 3.6. The spirally-reinforced column data is approximately normally distributed about the mean value with a skew towards the lower axial load ratios – thus, failure data in this group are most likely dominated by ductile flexural failures with little evidence of other limit states. The rectangular section reinforced column data is also a distribution weighted towards the lower axial-load ratios. Figure 3.6 depicts the box plot for the two groups of specimens.

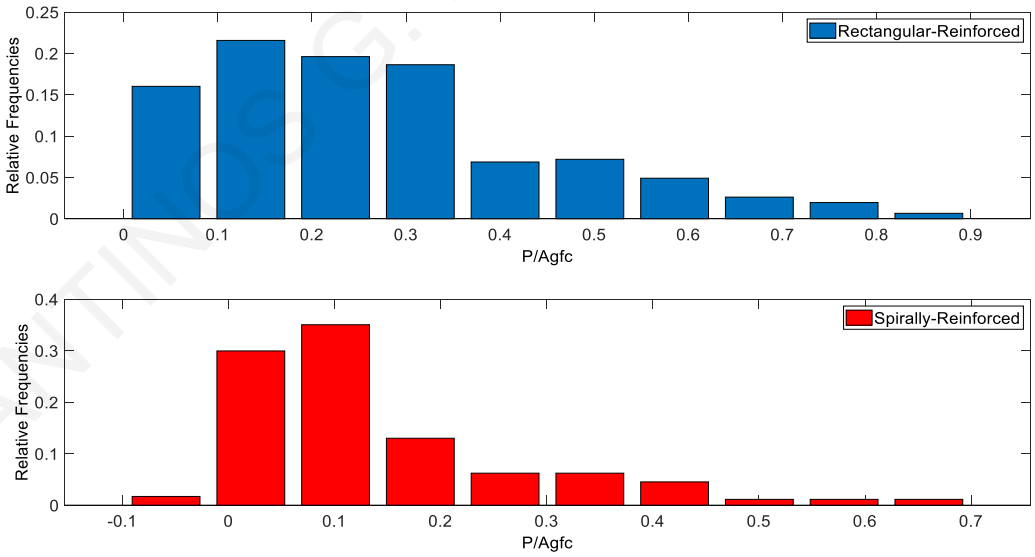

Figure 3.5: Distribution of axial-load ratio.

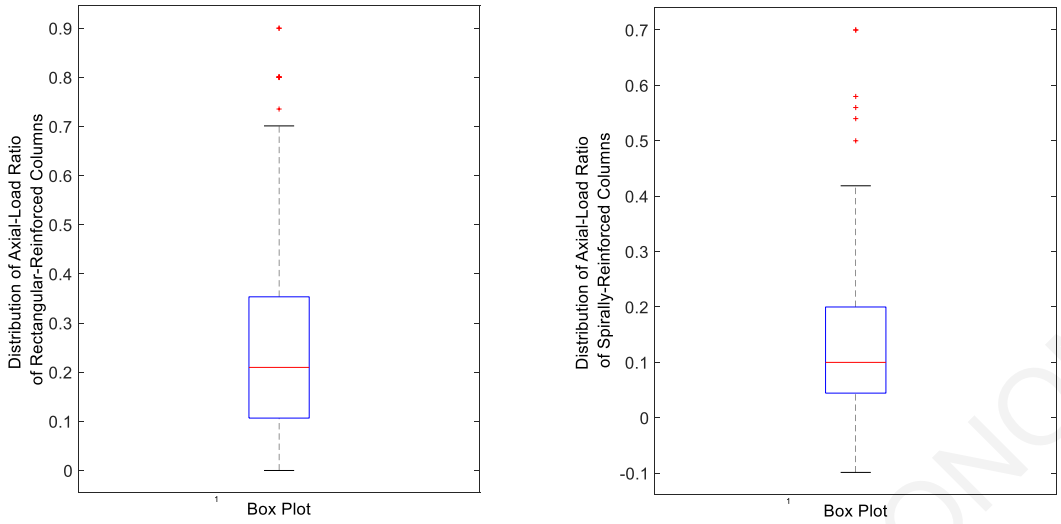

Figure 3.6: Box Plot of axial-load ratio.

Figures 3.7 and 3.8 plot the distributions of the total longitudinal-reinforcement ratio, ρ_l and the corresponding box plot. The group of rectangular section columns form an approximately normal distribution about the mean with a skew towards lower reinforcement ratios. Again, the spirally-reinforced column data is not distributed normally, underscoring the limitations of the database in the cases of brittle performance. Considering the low axial load ratio, it is concluded that the effective tension reinforcement ratio is less than ρ_l.

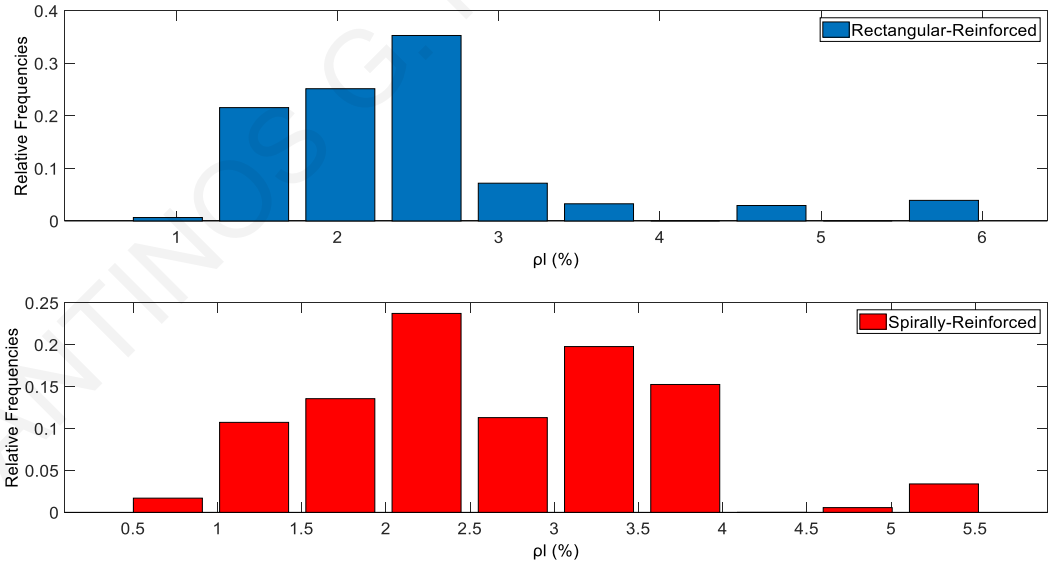

Figure 3.7: Distribution of longitudinal-reinforcement ratio.

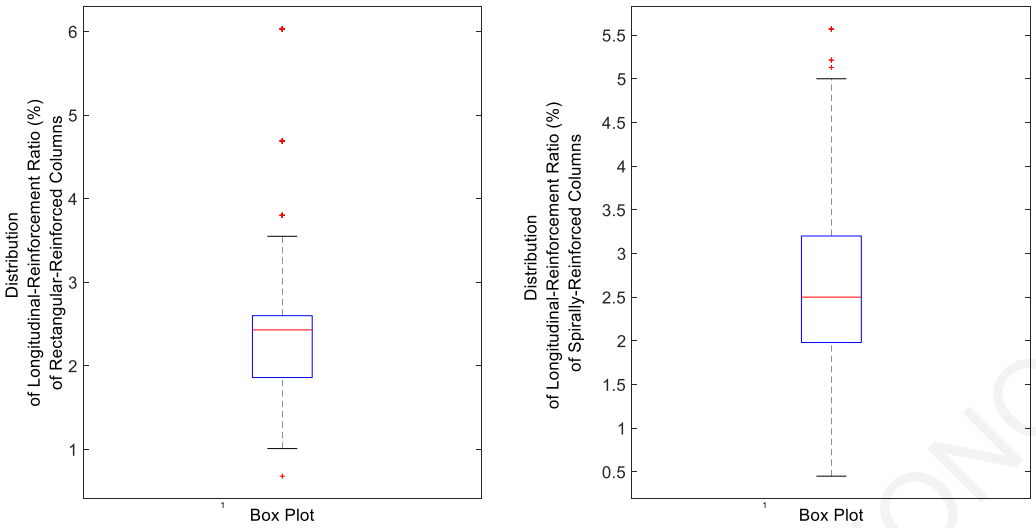

Figure 3.8: Box plot of longitudinal-reinforcement ratio.

Distributions of transverse reinforcement ratio are presented in Figs. 3.9 and 3.10. Both the rectangular-reinforced and spirally-reinforced columns have distributions weighted towards the lower transverse reinforcement ratios and cannot be assigned a specific distribution type. The sample is therefore populated primarily by lightly reinforced specimens.

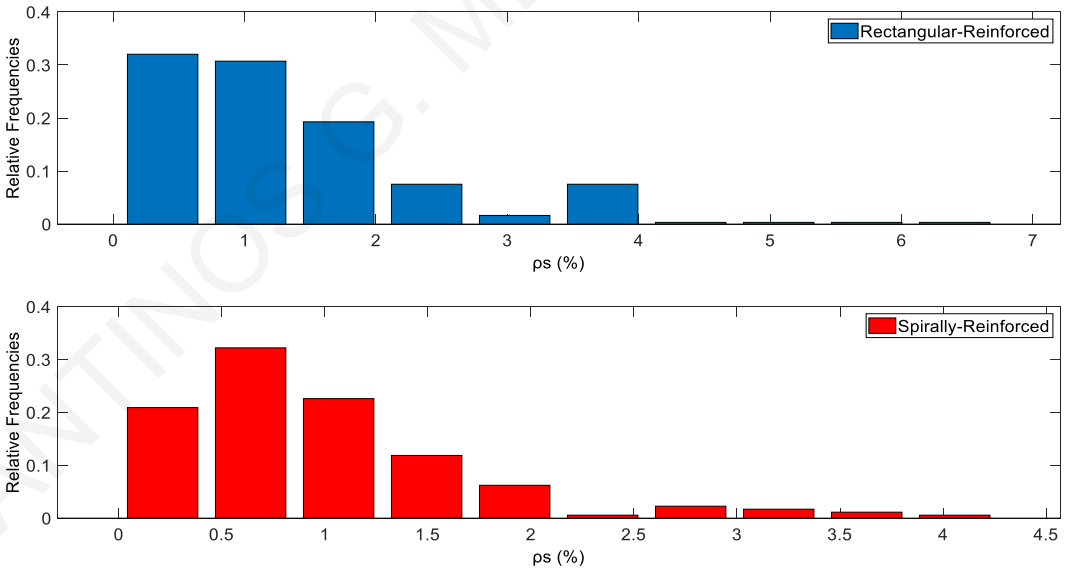

Figure 3.9: Distribution of transverse-reinforcement ratio.

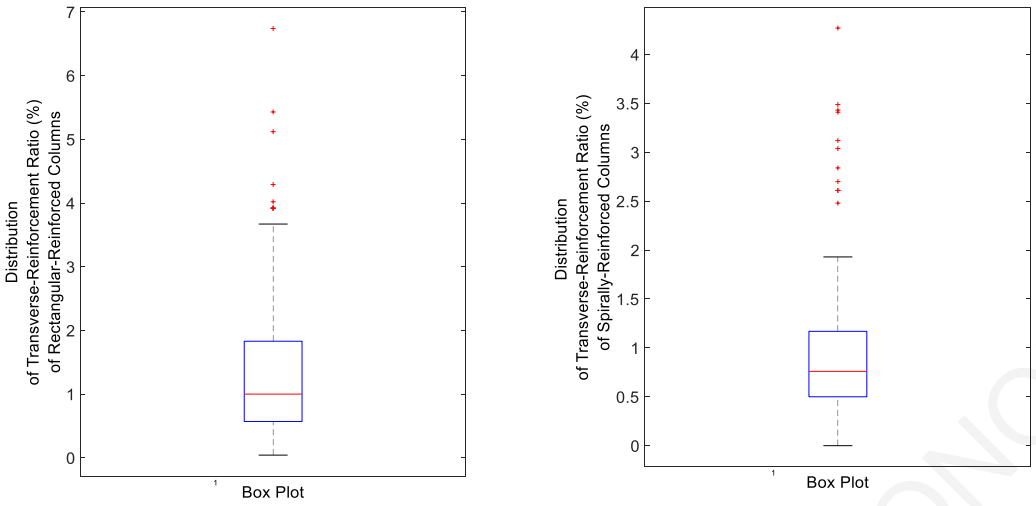

Figure 3.10: Box plot of transverse-reinforcement ratio.

3.2.2 Principal Indices of Deformability

One important goal in the seismic structural assessment procedures is the reliable estimation of the available capacity of structural members for inelastic deformation, as well as their available ductility. Ductility drives assessment since its magnitude underlies the general design philosophy (i.e., through the q-μ-T relationships it controls the magnitude of strength reduction from the elastic demands that may be tolerated before failure) and, in current code practice (EN 1998-1 2004 and AASHTO LRFD 2004, 2013, FEMA 440 2005), its magnitude is reflected on the specific reinforcing requirements of members and structures.

In this section the displacement ductility value clouds—as defined from the reported experimental responses—are correlated against important design parameters and plotted in graphs to illustrate the parametric dependencies of this variable.

For example, considering the concrete strength, the following points are made: (a) Higher strength materials are marked by lower ultimate strain, (b) strain can be enhanced through confinement, (c) a higher concrete strength results in a lower compression zone both at yielding and at failure. In general, it can be said that higher concrete strength causes a reduction in ductility. This finding is confirmed by both groups of rectangular-tied columns and by the spiral-reinforced columns as can be seen in Figs. 3.11, 3.12. For the spirally-reinforced columns it is more clearly evident that the ductility is increased for specimens with lower concrete strengths.

During the flexural analysis of a section both at yielding and at failure the presence of a compressive axial load increases the depth of the compressive zone as compared to an

identical section without axial force. Based on the above remark the presence of the compressive axial load reduces the curvature ductility of a section. The experimental data confirm this tendency with brittleness being more evident in the cases where the axial load ratios exceeded the point of balanced failure (see Figs. 3.13 and 3.14.)

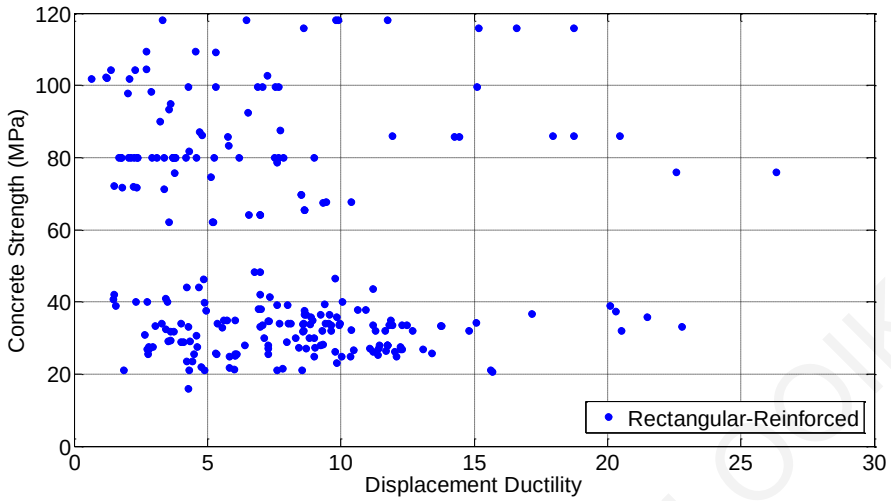

Figure 3.11: Effect of concrete strength on displacement ductility for the rectangular-reinforced columns of the database.

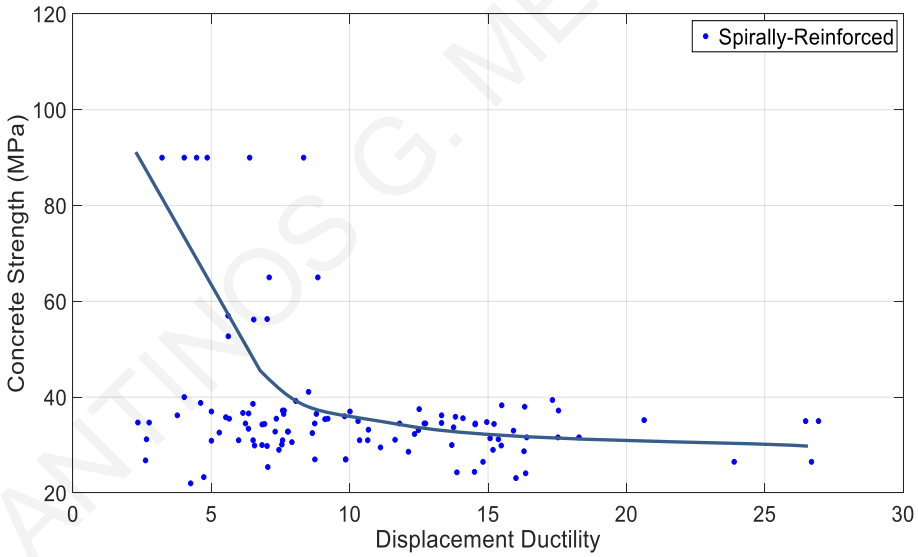

Figure 3.12: Effect of concrete strength on displacement ductility for the spirally - reinforced columns.

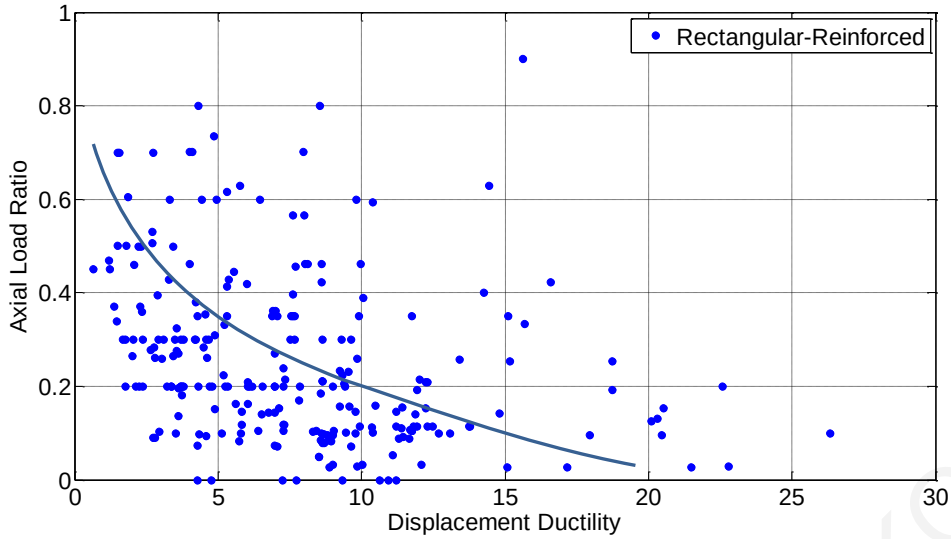

Figure 3.13: Effect of axial load ratio on displacement ductility for the rectangular section columns.

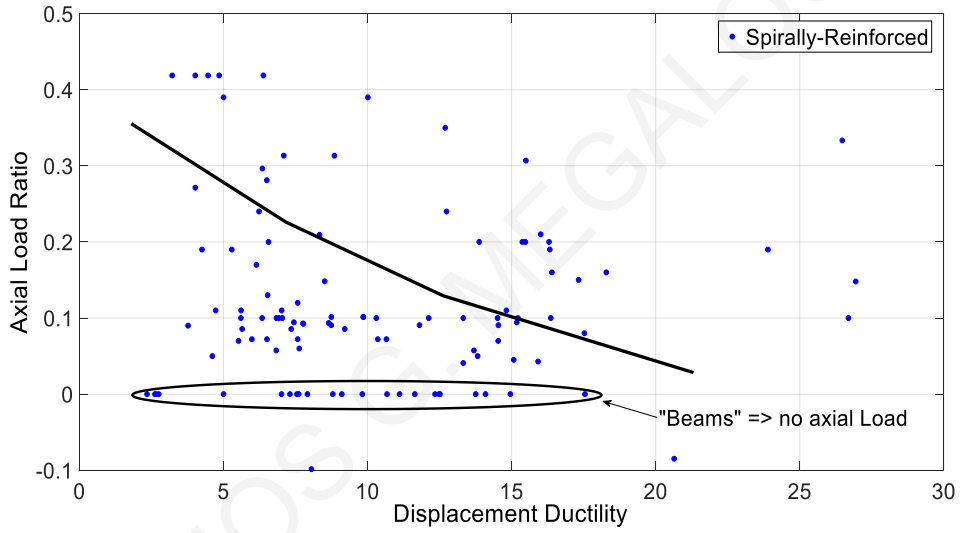

Figure 3.14: Effect of axial load ratio on displacement ductility for the spirally-reinforced columns.

Shear-span to depth ratio, known as aspect ratio, a=L_s/h, has a determining influence on the characteristics of shear behavior. In a column of small shear-span-to-depth ratio, shear deformation may become appreciable compared with the flexural deformation. A dominant shear response causes a more pronounced pinching in the force-deformation (hysteresis) curve, and a faster degradation of the hysteresis energy dissipation capacity. Interestingly, the experimental data show that the ductility ratio increases with a decreasing aspect ratio (Figs. 3.15, 3.16); this perplexing result is attributed to the fact that the yield displacement increases at a quadratic rate with shear span length L_s, whereas the ultimate displacement is linear with L_s – and thus the ductility estimate is inversely proportional to L_s/h or a. The

following expressions relate the flexural component of column response with aspect ratio, illustrating the source of the observations interpreting the experimental trend:

-Yield Curvature: $\varphi_y = 2.1 \cdot \frac{\varepsilon_{sy}}{h}$ (3.1)

-Yield Displacement: $\Delta_y = \frac{1}{3} \cdot \varphi_y \cdot L_s^2 \approx \frac{2}{3} \cdot \varepsilon_{sy} \cdot \frac{L_s}{h} \cdot L_s = \frac{2}{3} \cdot \varepsilon_{sy} \cdot a \cdot L_s$ (3.2)

-Ultimate Displacement: $\Delta_u \approx \Delta_y + \varphi_{pl} \cdot \ell_{pl} \cdot L_s = \Delta_y + \frac{\varepsilon_{pl}}{\frac{2h}{3}} \cdot \ell_{pl} \cdot L_s =$

$= \Delta_y + 1.5\varepsilon_{pl} \cdot \ell_{pl} \cdot \mathrm{a}$ (3.3)

-Displacement Ductility: $\mu_\Delta \approx 1 + 2.3(\mu_\varepsilon - 1) \cdot \frac{\ell_{pl}}{L_s}$ (3.4)

where ℓ_{pl} is the plastic hinge length (approximated as 0.5h in practical calculations), ε_{pl} the nonlinear (past yielding) part of the tension reinforcement total strain, and μ_ε the required bar strain ductility.

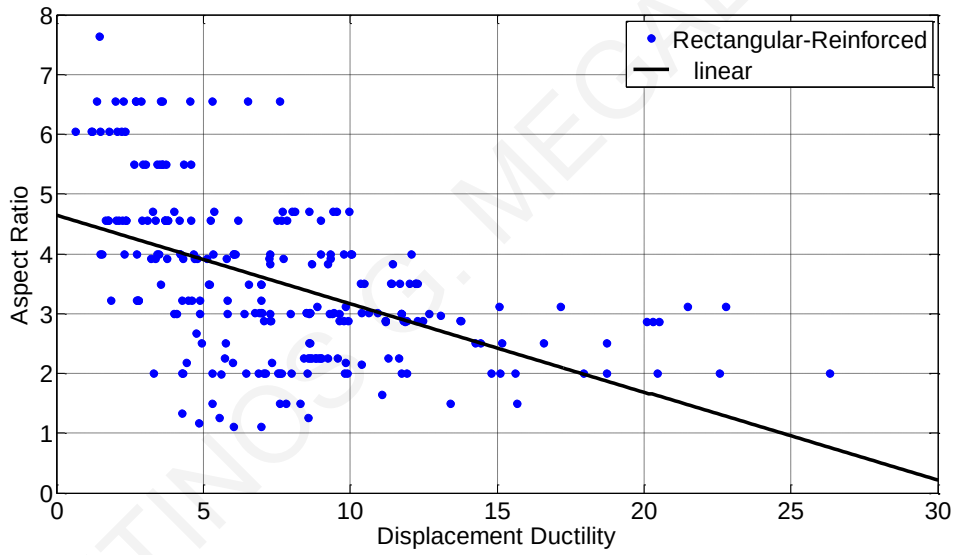

Figure 3.15: Effect of aspect ratio on displacement ductility for the rectangular - section columns.

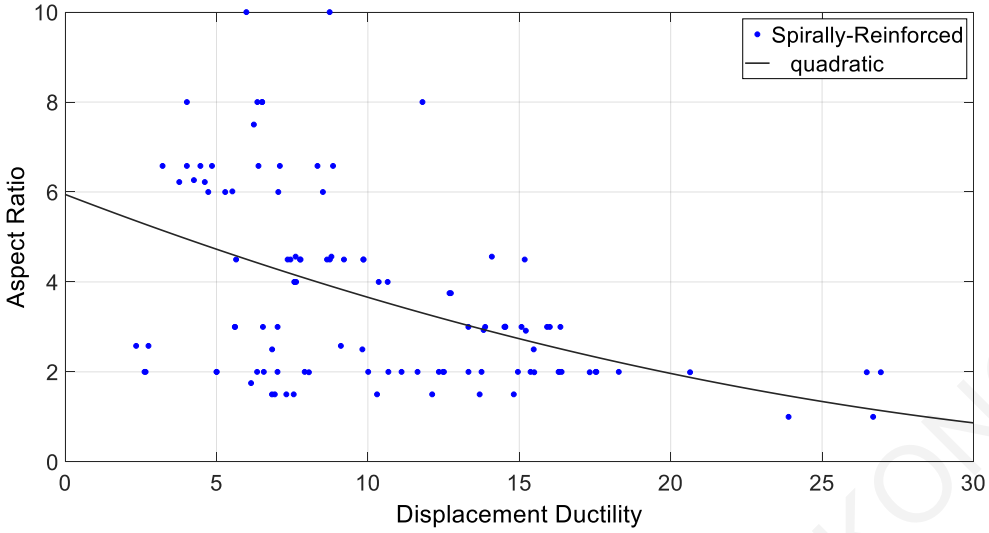

Figure 3.16: Effect of aspect ratio on displacement ductility for the spirally - reinforced columns.

Figures 3.17 and 3.18 depict the relationship between the maximum shear stress (maximum experimental shear force divided by the gross area of the column) normalized by the square root of concrete strength of each column and the associated displacement ductility. Columns with a higher ductility also supported a higher shear force, as both parameters are correlated to the same variable, i.e., the quality and quantity of detailing. The observation is also consistent with the trends of Figs. 3.15, 3.16, which illustrate that displacement ductility is inversely proportional to aspect ratio, which in turn, for a given member flexural resistance, is inversely proportional to shear demand (since $V_{Ed}=M_{Ed}/(h\cdot a)$).

The database trends are also examined with reference to lateral confinement – which is generally acknowledged to enhance the deformation capacity of the column. The arrangement of confining reinforcement is important in this regard; a column with closely spaced stirrups and well-distributed longitudinal reinforcement shows very little strength decay even when being subjected to very high axial forces with magnitudes exceeding the limit of balanced failure. The plotted trends confirm this general expectation: the displacement ductility increases with the transverse reinforcement ratio as shown in Figs. 3.19 and 3.20.

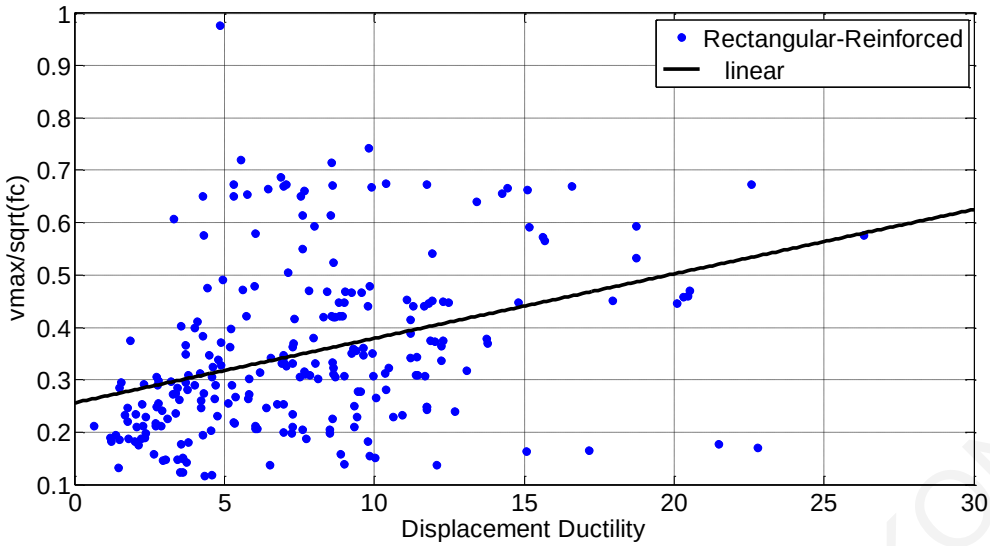

Figure 3.17: Maximum shear stress vs. displacement ductility for the rectangular - section columns.

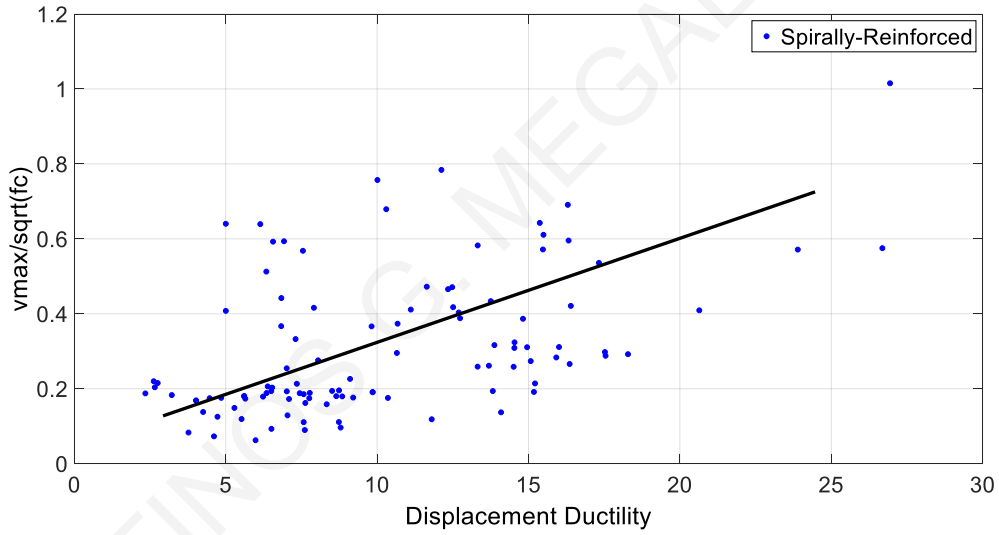

Figure 3.18: Maximum shear stress vs. displacement ductility for the spirally reinforced columns.

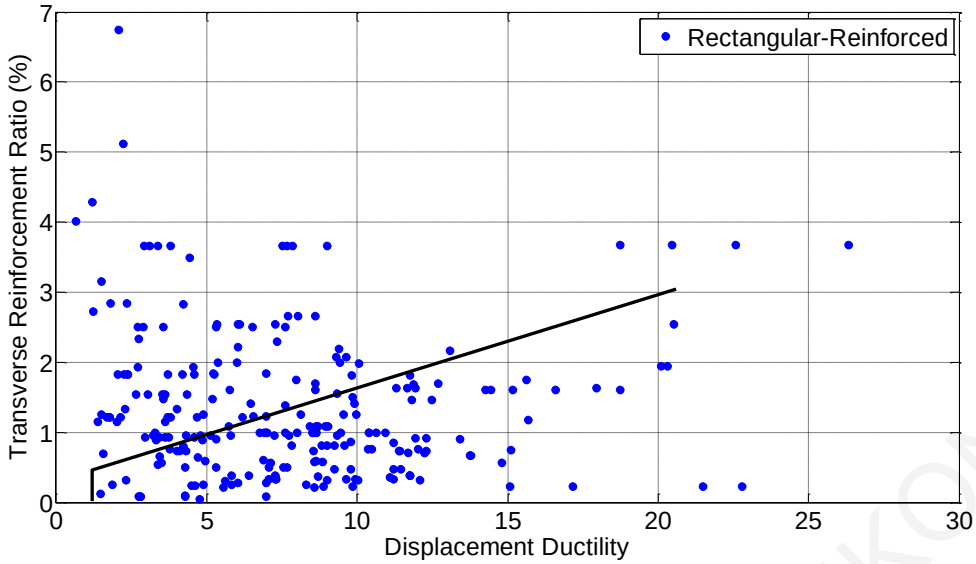

Figure 3.19: Effect of transverse reinforcement ratio on displacement ductility for the rectangular-section columns.

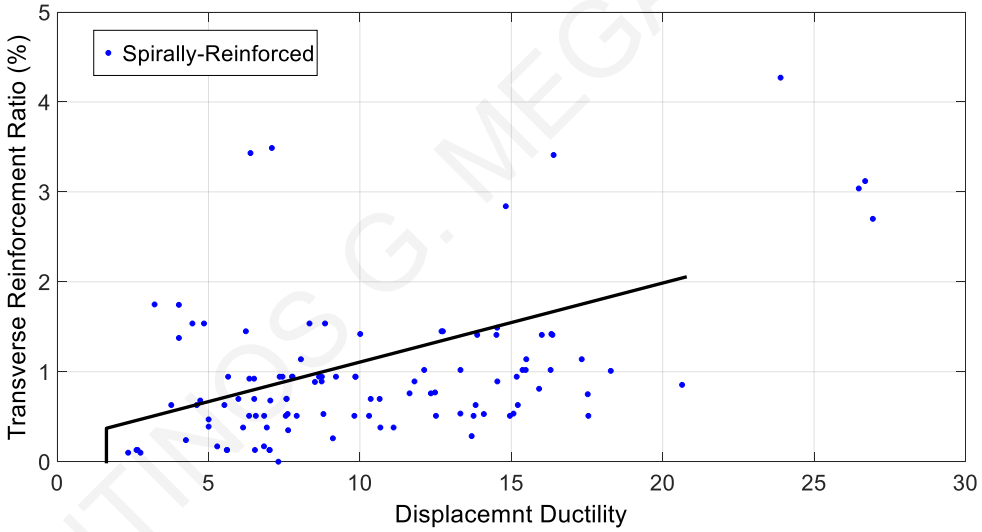

Figure 3.20: Effect of transverse reinforcement ratio on displacement ductility for the spirally - reinforced columns.

3.3 Analytical (F.E.) Simulation of RC Columns failed in Flexure

In the experimental database report of Berry and Eberhard (2004), the nominal column failure mode was classified as (a) flexure-critical, (b) flexure-shear-critical, or (c) shear-critical, according to the following criteria:

-If no shear damage was reported by the experimentalist the column was classified as flexure-critical.

-If shear damage (diagonal cracks) was reported, the absolute maximum effective force (F_{eff}: absolute maximum measured force in the experimental column response) was compared with the calculated "ideal" force corresponding to a maximum axial compressive strain in the concrete cover set equal to 0.004, which corresponds to spalling of unconfined concrete ($F_{0.004}$). The failure displacement ductility at an effective force equal to 80% of maximum, μ_{fail}, was determined from the experimental envelope. If the maximum effective force $F_{eff} < 0.95 \cdot F_{0.004}$ or if the failure displacement ductility was less than or equal to 2 ($\mu_{fail} \leq 2$), the column was classified as shear-critical. Otherwise, the column was classified as flexure-shear-critical. In the present section, only columns failed in flexure (i.e. classified as flexure-critical) will be examined through simulation. These are divided into two sub-groups according to cross-sectional shape (rectangular and circular section columns.)

3.3.1 A Force-Based Fiber Element incorporating Euler-Bernoulli Beam Theory

In order to conduct the analysis of those specimens in the experimental database that demonstrated a flexurally dominant response a computer code was developed and implemented in the MatLab toolbox FEDEAS lab 'Finite Elements for Design Evaluation and Analysis of Structures' (Filippou and Constantinides, 2004). The computational model uses the Euler-Bernoulli beam theory (Timoshenko,1953), which considers flexural deformations only. In Chapter 6 of this thesis the computational model is expanded further and implemented in a standalone Windows program written in C++ programming language, implementing the "Exact" beam theory that considers both flexural and shear deformations.

To account for material nonlinearity that occurs in the plastic hinge regions the formulation calculates the flexibility matrix of the member by using a fiber-type analysis and employing uniaxial hysteretic nonlinear material stress-strain relations for confined and unconfined concrete and reinforcement (Scott et al. 1982, Mander et al. 1988, Menegotto and Pinto, 1973). The stress-strain relations are endowed with mathematical expressions for the envelope, for the hysteresis loops and for the transition from the envelope to the unloading/reloading branches (Karsan and Jirsa (1969). Work-equivalent flexibility terms are obtained by conducting numerical integration at pertinent sampling points along the length (Gauss-Lobatto integration, Gil et al, 2007); the member deformational stiffness is

obtained by inversion of the flexibility matrix; the mathematical formulation is summarized in the following section.

3.3.2 Euler-Bernoulli Beam Theory

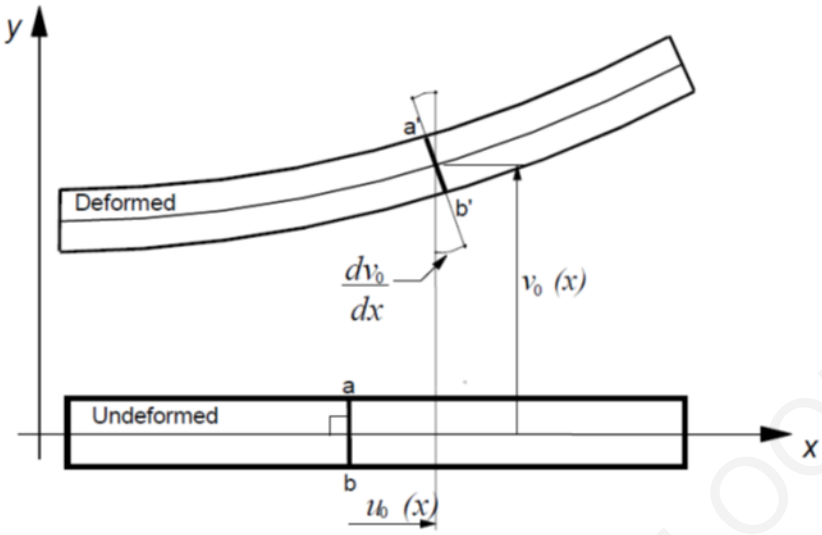

Figure 3.21: Deformation of Euler-Bernoulli beam.

The fundamental assumption of the Euler Bernoulli beam theory is that plane sections remain plane and normal to the longitudinal axis of the beam (Fig. 3.21). The cross section (*ab*) is normal to the longitudinal axis of the undeformed beam. In the deformed configuration the deformed cross section (*a'b'*) is plane and normal to the longitudinal axis of the deformed beam axis. This implies that the displacements at a point in a longitudinal fiber of the beam located a distance *y* from the longitudinal axis are:

$$u = u_0 - y \cdot \frac{dv_o}{dx} \tag{3.5}$$

$$v = v_o \tag{3.6}$$

The corresponding sectional deformations are (longitudinal and shear distortion):

$$\varepsilon = \frac{du}{dx} = \frac{du_o}{dx} - y\frac{d^2v_o}{dx^2} = \varepsilon_o - y \cdot \varphi \tag{3.7}$$

$$\gamma = \frac{du}{dy} + \frac{dv}{dx} = -\frac{dv_o}{dx} + \frac{dv_o}{dx} = 0 \tag{3.8}$$

Where, the reference axial strain (at *y=0*) and the corresponding sectional curvature are given by:

$$\varepsilon_o = \frac{du_o}{dx} \; and \; \varphi = \frac{d^2v_o}{dx^2} \tag{3.9}$$

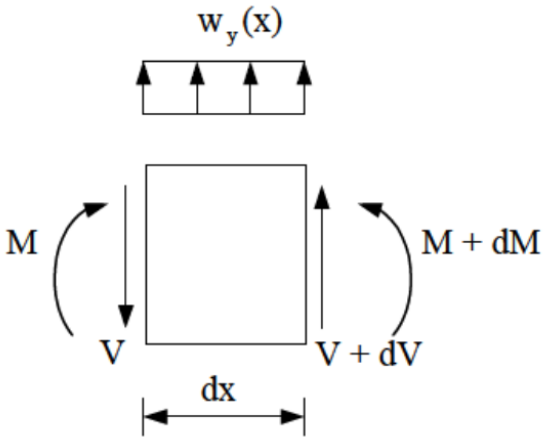

Figure 3.22: Beam segment of infinitesimal length, dx.

Based on Figure 3.22 the differential equation that governs the Euler- Bernoulli beam involves 4th order derivatives of the elastic vertical displacement of the deformed member:

Differential equation: $$\frac{d^2}{dx^2}\left(EI(x)\frac{d^2v_o}{dx^2}\right) = w_y(x) \quad (3.10)$$

Where, $w_y(x)$ is the load function acting on the beam in the y direction (normal to the longitudinal beam axis) and v_o the transverse deflection (see Fig. 3.23).

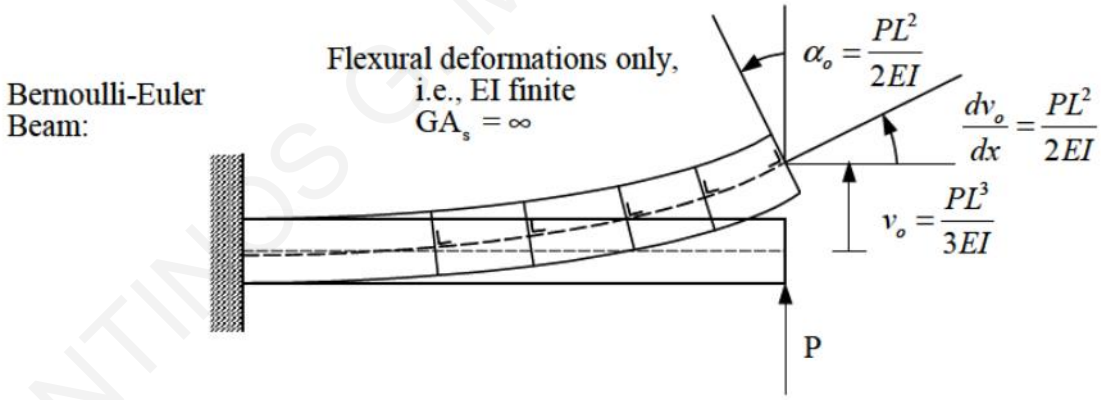

Figure 3.23: Bernoulli- Euler beam with flexural deformations only. Boundary conditions for a linear elastic cantilever with point load at the tip.

3.3.3 Fiber Sectional Model

The strains at a fiber/layer point of the beam cross section (*2-D* case) are related to the section deformations as follows (Spacone et al, 1996)):

$$\varepsilon_x(x) = \varepsilon_0 - y_\varepsilon \cdot \varphi(x) \quad (3.11)$$

where ε_0 is the axial deformation at the center of the coordinate system of the section (center of mass) and y_ε is also defined with respect to the same point of reference. Parameter $\varphi(x)$ is the curvature of the cross-section. Therefore, the strains at a material point *m* of the section can be expressed in matrix form as follows:

$$\varepsilon(x, y_\varepsilon) = \{\varepsilon_x\} = [1 \quad -y_\varepsilon] \cdot \begin{Bmatrix} \varepsilon_0 \\ \varphi \end{Bmatrix} = B_s(y_\varepsilon) \cdot e(x) \tag{3.12}$$

$$B_s(y_\varepsilon) = [1 \quad -y_\varepsilon] \tag{3.13}$$

The internal forces at a section level are given by:

$$N = \int \sigma_x dA = Axial\ force \tag{3.14}$$

$$M = -\int y_\varepsilon \sigma_x dA = Bending\ Moment \tag{3.15}$$

The section work-equivalent forces can be written in a matrix format as follows:

$$f_s(x) = \int {B_s}^T(y_\varepsilon) \cdot \sigma(x, y_\varepsilon) dA \tag{3.16}$$

where:

$$f_s(x) = \begin{Bmatrix} N \\ M \end{Bmatrix}, B_s(y_\varepsilon) = [1 \quad -y_\varepsilon], \quad \sigma(x, y_\varepsilon) = \{\sigma_x\} \tag{3.17}$$

Taking into account the section discretization into fibers/layers, the total forces on the beam section are obtained by summation of the contributions of each *i*-th fiber/layer:

$$N = \sum_{i=1}^{n.layer} \sigma_x^i A^i \ , \ M = -\sum_{i=1}^{n.layer} \sigma_x^i {y_\varepsilon}^i A^i \tag{3.18}$$

where A^i is the area of the *i*-th fiber/layer.

Therefore, section forces are determined from the known sectional deformations. If section forces are known, then the associated sectional deformations need be evaluated through iterative calculations till convergence (this means that iteration is done on the value of the deformation while the force is kept at the given value within a tolerance). The tangent section stiffness matrix k_s is defined as the derivative of the section force vector f_s with respect to the section deformation vector *e*, where the explicit reference to *x* is dropped for brevity of notation:

$$k_s = \begin{bmatrix} \frac{\partial f_{s_1}}{\partial e_1} & \frac{\partial f_{s_1}}{\partial e_2} \\ \frac{\partial f_{s_2}}{\partial e_1} & \frac{\partial f_{s_2}}{\partial e_2} \end{bmatrix} \tag{3.19}$$

$$k_s = \frac{\partial f_s}{\partial e} = \int {B_s}^T(y_\varepsilon) \cdot \frac{d\sigma(x,y)}{\partial \varepsilon(x,y)} \cdot \frac{\partial \varepsilon(x,y)}{\partial e} dA = \int {B_s}^T(y_\varepsilon) \cdot \frac{d\sigma(x,y)}{d\varepsilon(x,y)} B_s(y_\varepsilon) dA \tag{3.20}$$

$$\sigma(x, y_\varepsilon) = \{\sigma_x\} \qquad \varepsilon(x, y_\varepsilon) = \{\varepsilon_x\} \tag{3.21}$$

$$\frac{d\sigma(x,y)}{d\varepsilon(x,y)} = [E_m] \tag{3.22}$$

where E_m is the tangent modulus of the stress – strain relations at a point *m* of the section. By establishing (through equilibrium) interpolation functions for the member forces along the element and the fiber section scheme provided above, the element state determination, leading to calculation of element nodal forces and displacements along with its tangent stiffness at each analysis step, is defined. Since in structural engineering applications the maximum response values usually arise at the ends of the integration interval, for example bending moments and corresponding curvatures in a structural member, the Gauss-Lobatto quadrature integration scheme is usually applied for the element state determination (Fig. 3.24).

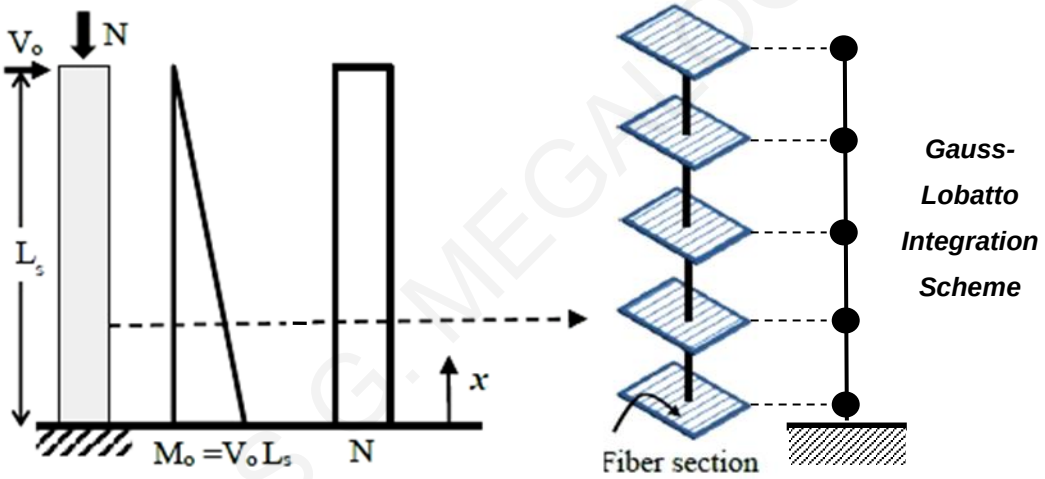

Figure 3.24: Force-based fiber element incorporating Euler-Bernoulli Beam theory.

3.3.4 Force-based vs. Displacement-based Fiber Beam Element

Figure 3.25a, b illustrates one of the main differences between the displacement-based and the force-based formulation by comparing schematically the response of cantilever models D_1 and F_1 (one displacement-based element vs. one force-based element). The bending moment and curvature profiles are shown for the cantilever after the plastic hinge has formed. The plastic curvature is labeled φ_p. Figure 3.25a shows the response of a single two-node displacement-based element. The formulation enforces linear curvature (Hermite shape functions). This linear curvature profile prevents the element from reproducing a nonlinear jump from elastic to plastic curvature. Because equilibrium is satisfied in a weak sense and not pointwise, the moment diagram, shown with a dashed line deviates from the expected

linear profile. On the other hand, Figure 3.25b shows the response of the force-based frame element. For concentrated load at the cantilever tip, the linear shape function for the bending moment distribution strictly satisfies equilibrium. Thus, the formulation enforces a linear bending moment diagram leaving the element free to deform without constraint. After the plastic moment capacity is reached, the base integration point experiences plastic curvature with the remaining integration points remaining elastic.

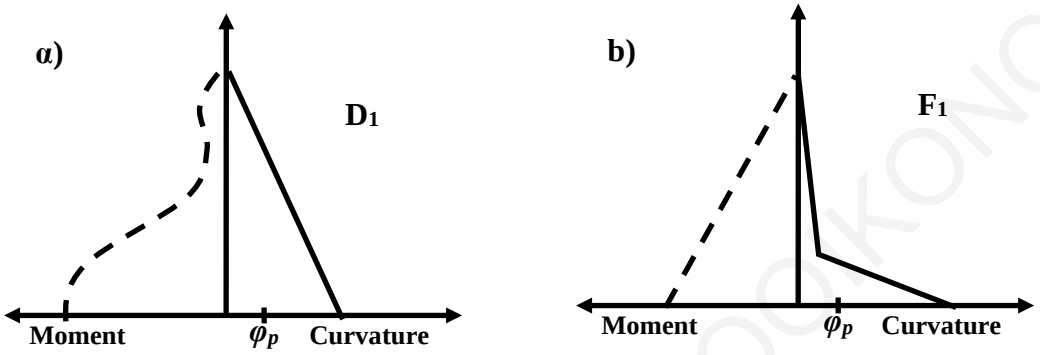

Figure 3.25: a) Single Displacement-Based Fiber Element b) Single Force-based Fiber Element incorporating Euler-Bernoulli Beam theory.

3.3.5 Circular-Reinforced Columns Failed in Flexure

Columns with a circular cross section that, upon lateral displacement reversals exhibited flexural failure are listed in Table A.1 in the Appendix of this Chapter. The hysteretic responses of several specimens from this group are analyzed in the present section using finite element cyclic static analysis.

The objective in conducting this analysis is to evaluate the available theories regarding their success and limitations in reproducing the experimental responses of those column specimens that did not experience failures beyond the scope of the models (as would be for example the case of shear failure). Numerical simulations were conducted using a nonlinear fiber beam-column element that considers the spread of plasticity. In this type of analysis the longitudinal beam element uses a force-type formulation with linear moment distribution to derive a flexibility matrix for the element with progressing nonlinearity (step by step); the strain-displacement relationships are therefore defined implicitly after inversion of the flexibility matrix to obtain the stiffness. Assuming strain compatibility between materials comprising the member, the formulation samples sectional response at selected integration points along the length. At the sectional level the Bernoulli hypothesis (plane

sections remaining plane and normal to the axis of the member) is used to relate strains in the different fibers to the sectional curvature and longitudinal axis normal strain. Nonlinear uniaxial material laws are used to relate normal stress with normal strain in the fibers, thereby neglecting the effect of shear in modifying the principal orientations through the height of the cross section. Typical discretization of a column section is shown in Fig. 3.21. Sectional stress resultants (Moment and Axial load) are obtained from the equilibrium of the contributions of fiber stress resultants [FEDEAS Lab (2004)].

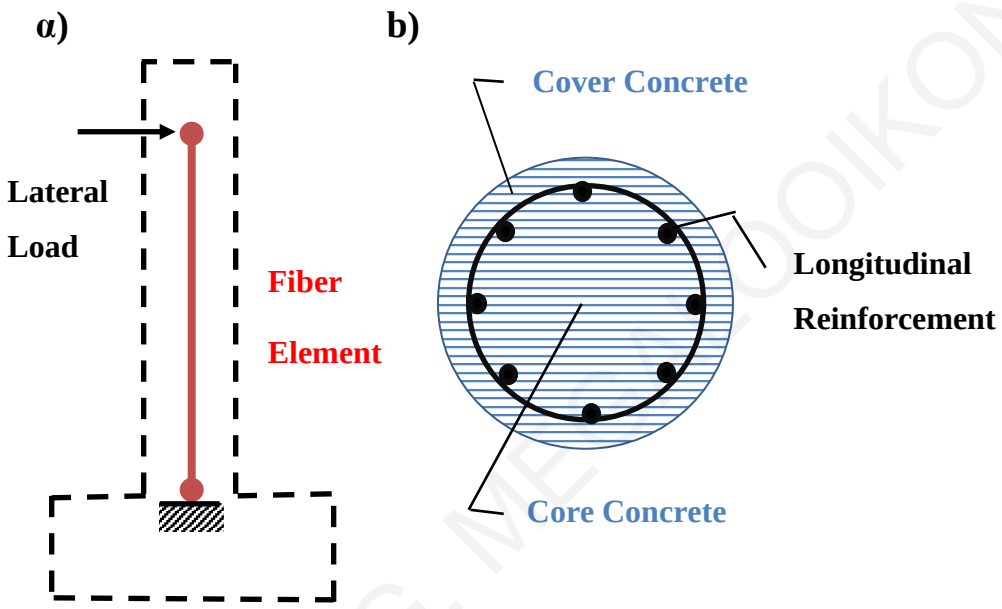

Figure 3.26: a) Numerical model for Spiral-Reinforced Columns failed in flexure b) Section discretization in fibers/layers.

For example, for the column with ID#43 in Table A.1 (axial load ratio ν=0.19), as it is depicted also in Fig. 3.26, a single beam-column element is assigned to the entire length of the cantilever column and five Gauss-Lobatto integration points [FEDEAS Lab (2004)] were defined along the element. Uniaxial material stress-strain laws for the concrete and steel fibers are depicted in Fig. 3.27(a) (Scott et al. 1982) for concrete and in Fig. 3.27(b) for steel (Menegotto and Pinto, 1973). The effect of confinement on the confined concrete core was modelled using pertinently modified properties for the uniaxial stress-strain law of concrete in compression (Scott et al.,1982, Mander et al., 1988). No P-Δ effect was considered in this simulation. The calculated lateral Force – lateral Displacement response of the numerical simulation of the column is plotted for comparison with the experimental results in Fig. 3.28. The good correlation up to a drift of 3.75% underscores the fact that

flexural behavior is controlled by steel inelasticity which is stable and may be reproduced without the consideration of other secondary effects or the interaction of flexural with shear response. However, correlation deteriorates significantly beyond that point, on account of the fact that second order effects have been neglected and there is no accounting for the ensuing degradation and progressive collapse.

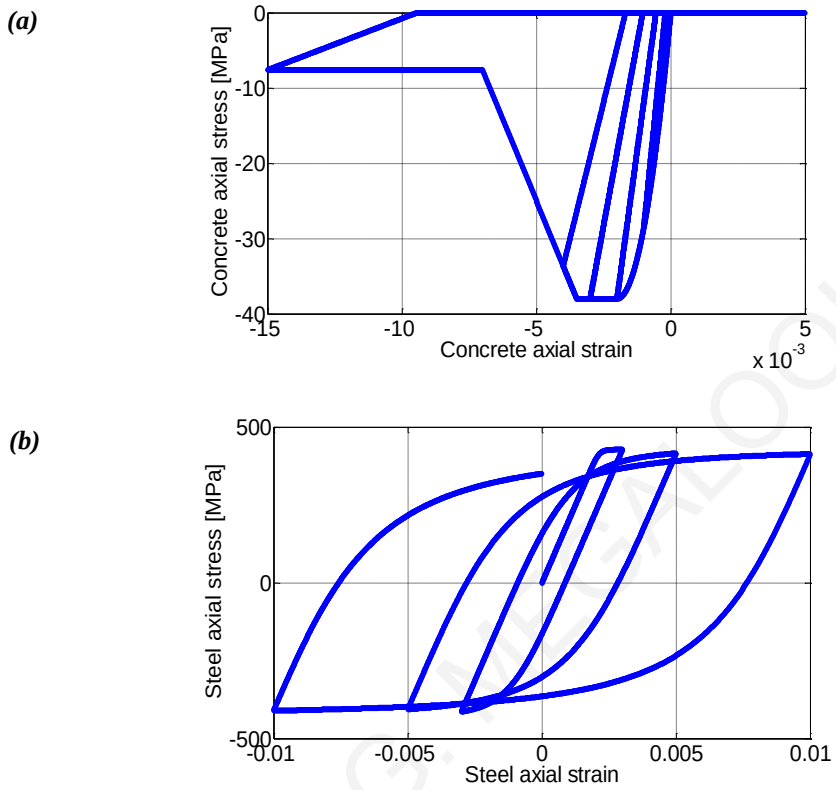

Figure 3.27: (a) Scott et al. (1982) constitutive law assigned to the concrete fibers. (b) Menegotto and Pinto constitutive law assigned to the longitudinal steel fibers.

Another example (column ID#45) from Table A.1 in the Appendix of this Chapter is shown here: the approach used for simulation is identical to that of the previous example, the only difference being in the use of a more complex stress-strain model for the confined core (Mander et al. 1988; here the strain capacity of the confined core is related to the strain energy that may be absorbed by the stirrups before fracture), as depicted in Fig. 3.29. Figure 3.30 compares the calculated and experimental lateral force vs. lateral displacement hysteresis – again the correlation is satisfactory up to a drift of 2.5%, however, the model cannot reproduce the loss of lateral load bearing capacity near the end of the test; note that this column was identical to the previous one but carried twice the amount of axial load. Therefore, second order effects would cause an apparent loss of 22.6 kN for an increment of lateral displacement from 20mm to 30mm (and 67.8 kN total reduction of the yield lateral

force due to P-Δ effect at the displacement level considered); the additional loss which occurs in repeated cycles at the same displacement excursion is owing to material degradation.

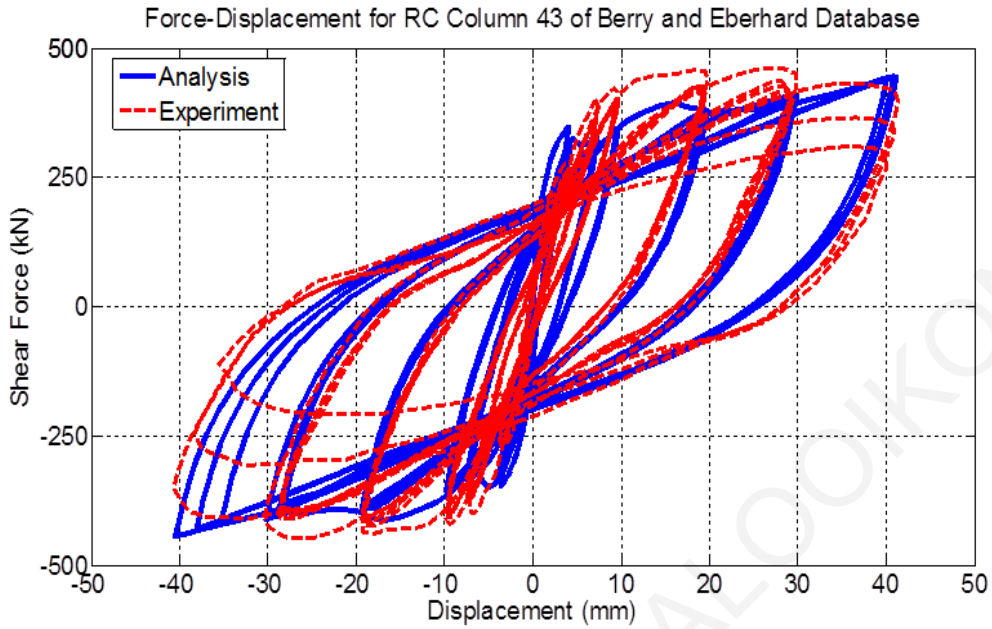

Figure 3.28: Comparison between numerical and experimental response of circular column (ID#43) (specimen case obtained from the Berry and Eberhard Database 2004 and was analyzed herein).

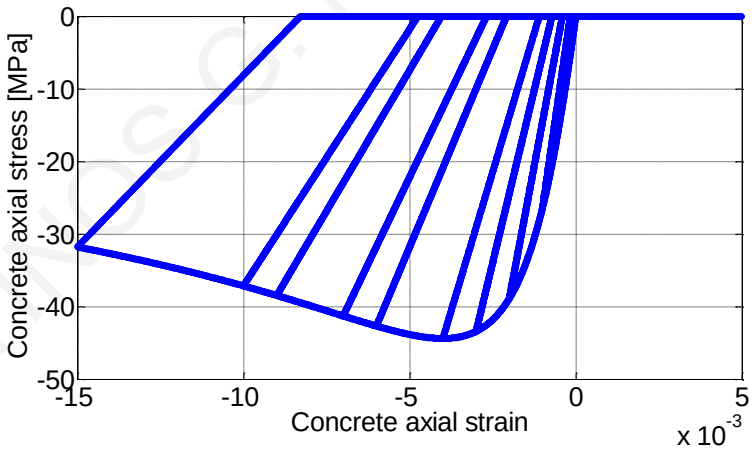

Figure 3.29: Mander et al. (1988) stress-strain model assigned to the confined concrete fibers.

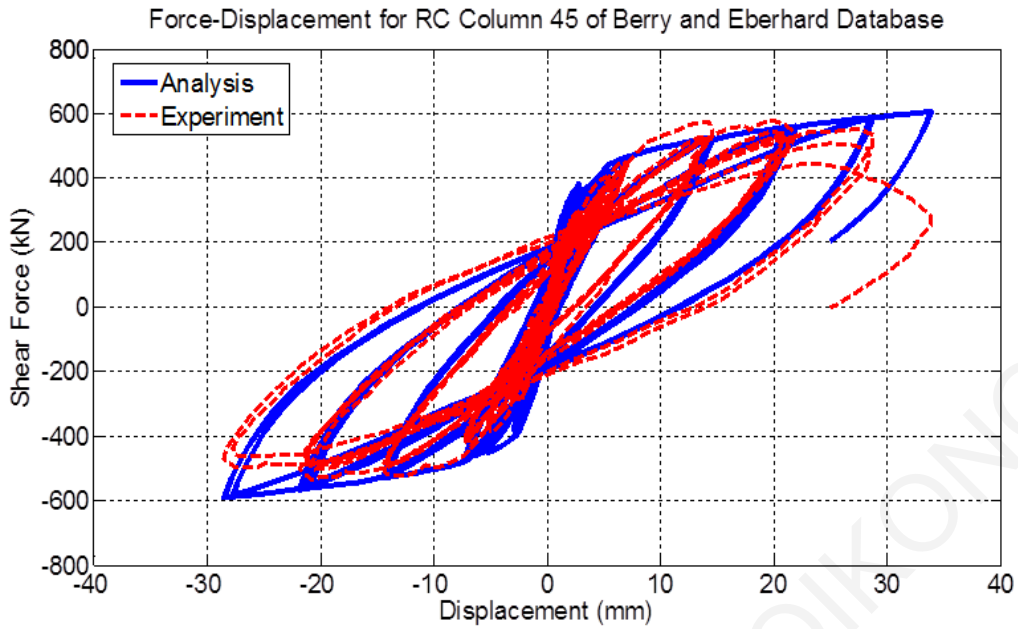

Figure 3.30: Comparison between numerical and experimental response of circular column (ID#45) obtained from the Berry and Eberhard Database (2004).

Several other examples are presented in Figures A.1 – A.26 in the Appendix to the present Chapter. Correlation in flexure dominant cases follows the general pattern discussed in the preceding case studies. It is noteworthy that some cases demonstrated significant pinching, which was not reproduced by the purely flexural nonlinear model; such examples are specimens with ID#47, ID#53, ID#55, ID#56, ID#57, ID#58, ID#59, ID#60, ID#116, ID#120, ID#141, ID#142 and ID#157. In the case of these specimens, which had a low volumetric ratio of transverse reinforcement (0.6%) and early yielding with strain penetration along the anchorage, the observed pinching was owing to reinforcement pull-out and shear deformation in the plastic hinge region, both phenomena neglected in the numerical model used here. The aspect of yield penetration and lumped rotation occurring at the support of the column is addressed in Chapter 5 of the thesis.

3.3.6 Rectangular-Reinforced Columns Failed in Flexure

The group of rectangular-reinforced specimens is summarized in Table A.2 in the Appendix of this Chapter; again, only specimens that reportedly failed in flexure are considered in this section, to test the performance of formulations that only consider normal stress response at the sectional level.

The force-based nonlinear fiber beam-column element which considers the spread of plasticity available in FEDEAS Lab (2004) was used in this Section's numerical simulations. As previously, a single frame element is considered using flexibility formulation with assumed linear variations of moments along the length; sampling of sectional response is done at five Gauss-Lobatto integration points along the member length. The typical discretization of rectangular column sections is shown in Fig. 3.31.

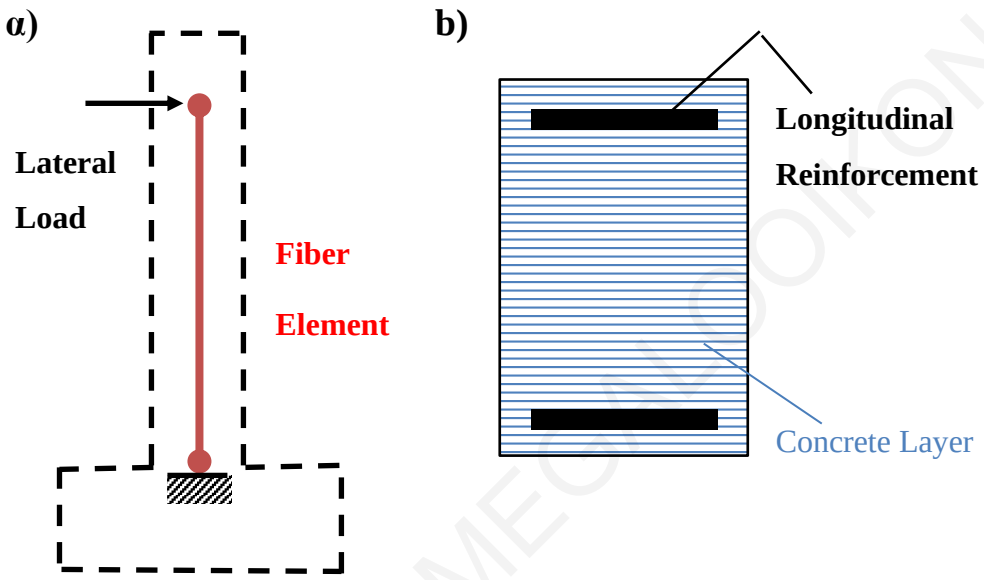

Figure 3.31: a) Numerical model for Rectangular RC Columns failed in flexure b) Section discretization in fibers/layers.

For the first column (No. 1 in the Database) of Table A.2 (with a square cross section and an axial load ratio of 0.26), as shown in Fig. 3.32, a unique fiber element is assigned to the entire height of the cantilever column and five Gauss-Lobatto integration points were defined along the element. Uniaxial concrete stress strain response was modeled using the relationship by Mander et al. (1988, Fig. 3.29). The different confinement effect of the unconfined concrete cover and the confined concrete core was not considered in the discretization of the section (Fig. 3.31). The stress-strain response of longitudinal reinforcement was modeled by the model of Menegotto and Pinto (1973, Fig. 3.22b). Again, the P-Delta effect was not accounted for in the simulation. The comparison of the lateral Force – lateral Displacement response of the numerical simulation of the column with the experimental results can be seen in Fig. 3.27. As was seen in the case of circular section columns, while the axial load ratio is kept low, a good agreement between numerical and

experimental results is found up to drift levels of 2.5% (where the strength loss owing to P-Δ is only 45kN i.e., about 7% of the column strength).

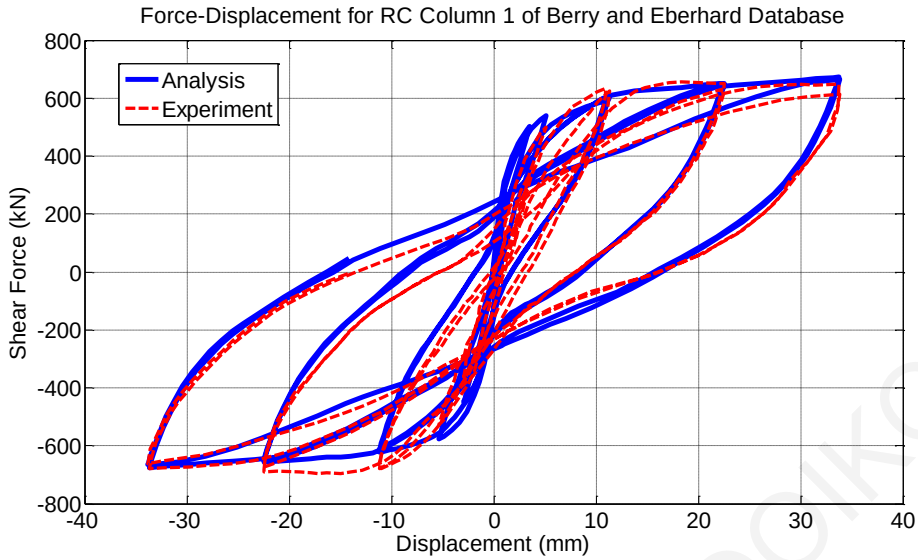

Figure 3.32: Comparison between numerical and experimental response of rectangular column (ID#1) of Berry and Eberhard Database (2004).

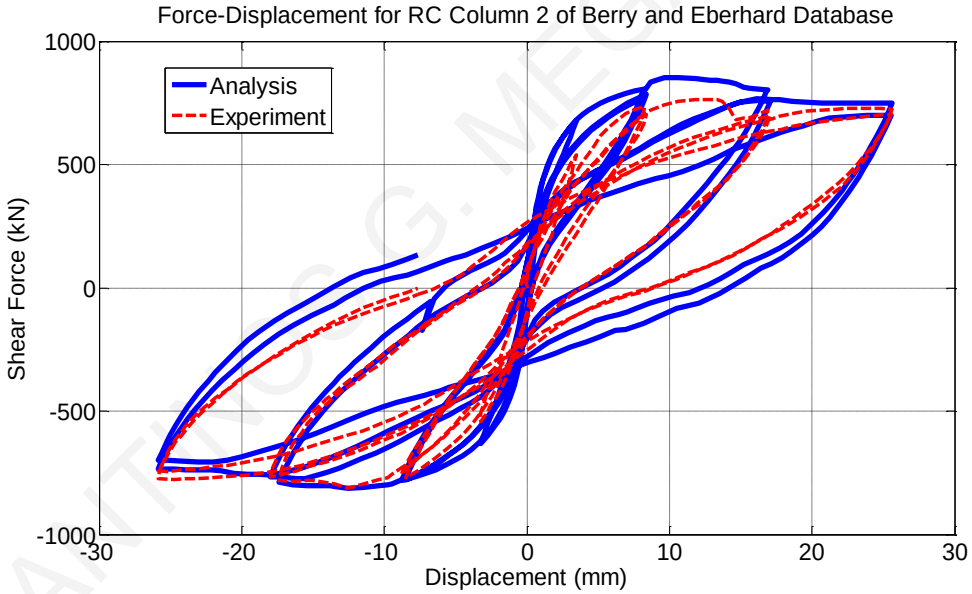

Figure 3.33: Comparison between numerical and experimental response of rectangular column (ID#2) of Berry and Eberhard Database (2004).

The performance of the same numerical model applied to the second column example listed in Table A.2 – (again having an axial load ratio of v=0.22) is compared to the experimental force - displacement response curve in Fig. 3.33. Response is adequately well modeled, reproducing faithfully the loss of cover (spalling) at a drift of 1.2%; therefore, it

may be concluded that the efficacy of distributed plasticity beam column models based on the force formulation successfully estimates the flexural behavior also in the case of reinforced concrete columns with rectangular sections.

Several other examples are presented in Figures A-27 – A.76 in the Appendix to the present Chapter. Correlation in flexure dominant cases follows the general pattern discussed in the previous two examples. Correlation deteriorates beyond drift levels in the range of 3% or more, when the column carries a significant axial load ratio. It is noteworthy that some cases demonstrated significant pinching, which was not reproduced by the purely flexural nonlinear model; such examples are specimens with ID#32, ID#105 and ID#106. Again, as was seen in some circular section columns of the preceding section, specimens with a low transverse reinforcement ratio and strain penetration along the anchorage developed pinching in the experimental response due to reinforcement pullout and shear deformation in the plastic hinge region. This aspect is addressed separately in Chapter 5. Finally, in one case (ID#91) the experimental response was not symmetrical in the two directions of loading due to buckling of compressive reinforcement.

3.4 Analytical (F.E.) Simulation of RC Columns Failed in Shear

Performance of the shear critical columns (flexure-shear or shear failure) of the experimental database in terms of strength and deformation capacity is also examined so as to test again the performance of the analytical procedure described in the preceding sections. Again, the columns are divided into two groups according to cross sectional shape.

3.4.1 RC Columns with Rectangular Cross-Section Failed in Shear

Columns with a rectangular cross section that developed shear failure are summarized in Table A.3 of the Appendix of this Chapter. Figure 3.34 plots the shear strength degradation models adopted by EN 1998-3 (2005) and ASCE-SEI 41 (2007) (also see Chapter 2) in order to describe the envelope of the resistance curves of reinforced concrete columns as a function of displacement ductility; this is used as the basic criterion in order to detect shear failure before or after flexural yielding (point of intersection with flexural capacity curve). Therefore, it is necessary to define the flexural capacity curve based on classic flexural analysis and to also combine it with the reduction of the shear strength curve postulated by the codes, in order for the strength and deformation of the reinforced concrete column at shear failure to be defined. This procedure is followed in the present Section in order to

analyze the shear critical columns of the experimental database under study and to examine how successful the code provisions are in predicting the strength and deformation of columns failing in shear before or after flexural yielding. In addition, the models by Elwood (2003) introduced also in Chapter 2 that define the drift capacity of shear-critical columns at shear failure and at loss of axial load carrying capacity are included in the calibration study. The force-based nonlinear fiber beam-column element which considers the spread of plasticity available in the FEDEAS Lab (2004), was used also in this section's numerical simulations for the definition of flexural capacity curve. The modelling procedure was the same as that used in earlier paragraphs for columns with rectangular cross sections.

Figure 3.35 compares the analytical and experimental response of the rectangular column –ID#28 (Table A.3). Clearly, correlation is poor even with regards to the initial stiffness defined by flexural analysis. This is owing to the fact that the contributions to deformation resulting from reinforcement pullout and shear deformation have been neglected. It can be observed that only the degrading shear strength model of ASCE-SEI 41 (2007) intersects the flexural capacity curve and therefore (correctly) identifies the triggering of shear strength failure after flexural yielding as a result of shear strength degradation. However, the displacement when this event takes place occurs earlier than the actual onset of strength degradation as observed in the experimental response. The proposal of Elwood (in parentheses next to the drift ratios the corresponding displacements are given for the column under study based on its shear span) overestimates the actual drifts associated with shear and axial failures as observed in the experimental results.

In the next column example (Fig. 3.36) the code provisions fail to detect shear failure despite the fact that, based on the experimental report, shear failure was observed. Again, the drift models by Elwood (2003) overestimate the displacements at which shear and axial failure occurred. The force-based fiber element used for the flexural analysis reproduces the peak strength well but it fails to converge after that point, and cannot detect the strength degradation owing to shear failure. As mentioned before, the initial stiffness of the numerical model is overestimated as compared with the experiment. Several other examples are presented in Figures A.77 – A.100 in the Appendix to the present Chapter. Correlation in shear dominant cases follows the general pattern discussed in the previous two examples.

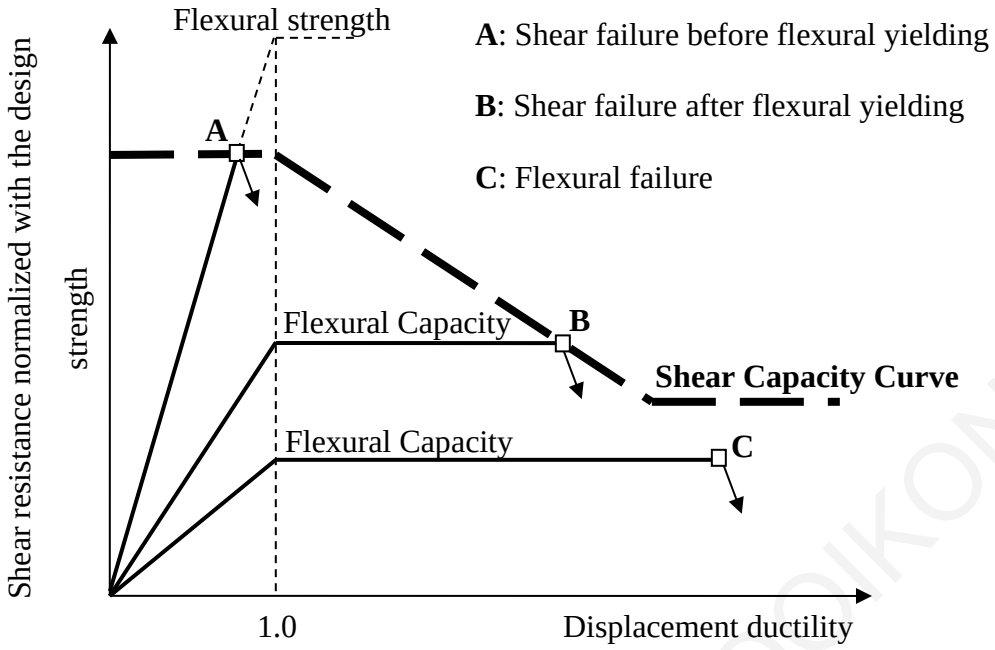

Figure 3.34: Shear strength degradation model adopted by current codes of assessment.

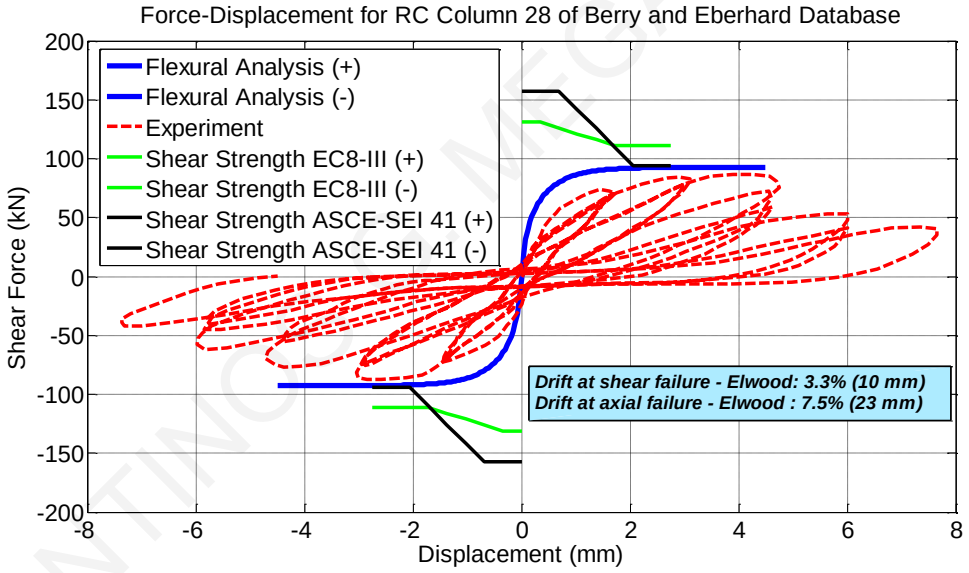

Figure 3.35: Comparison between numerical and experimental response of rectangular column (ID#28) of Berry and Eberhard Database (2004).

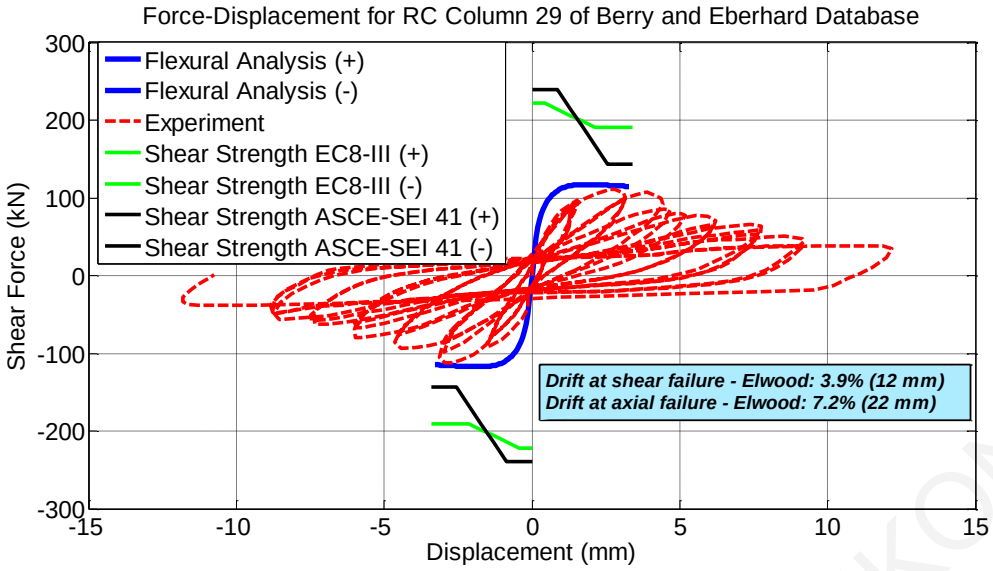

Figure 3.36: Comparison between numerical and experimental response of rectangular column (ID#29) of Berry and Eberhard Database (2004).

3.4.2 RC Columns with Circular Cross-Section Failed in Shear

Spiral-reinforced specimens with a circular cross section that failed in shear are presented in Table A.4 of the Appendix of this Chapter. Monotonic analysis is conducted following the same procedure as described in the circular section Column (second case) of the previous Section.

As previously stated (Fig. 3.34), the shear strength degradation models such as those adopted by EN 1998-3 (2005) and ASCE-SEI 41 (2007) (Chapter 2), are used to determine the deformation limit at shear failure from intersection with the flexural force – displacement envelope. The flexural capacity curve is based on classic flexural analysis. After the application of this procedure to specimen #14 in the experimental database, the following response envelope is determined (plotted in Fig. 3.37 against the experimental result).

Both the shear strength degradation models shown in Fig. 3.37 detected shear failure after yielding at a displacement much lower than the corresponding experimental one. The strength at shear failure was better assessed by the model of EN 1998-3 (2005) compared to the alternative of ASCE-SEI 41 (2007). The drift model at shear failure by Elwood (2003) performed very well as compared to the experimental shear failure limit; however, drift at axial failure was overestimated (83mm as compared to 30mm). The same comments are valid for the column in Fig. 3.38.

In the comparison showcased by Fig. 3.39, only the shear capacity curve by ASCE-SEI 41 intersects the flexural force-displacement envelope, thereby detecting shear failure after flexural yielding. The strength at shear failure was well predicted by the latter model but the corresponding displacement was much lower than in the experimental response. The drift model at shear failure by Elwood (2003) performed well compared to the experimental response but overestimated the drift at the loss of axial strength.

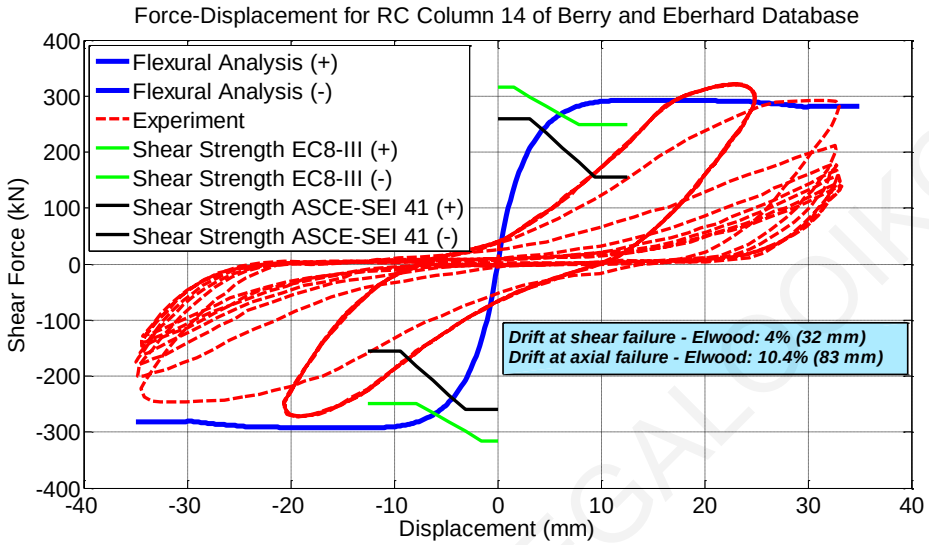

Figure 3.37: Comparison between numerical and experimental response of circular column (ID#14) of Berry and Eberhard Database (2004).

Several other examples are presented in Figures A.101 – A.118 in the Appendix to the present Chapter. Correlation in shear dominant cases follows the general pattern discussed in the previous three examples.

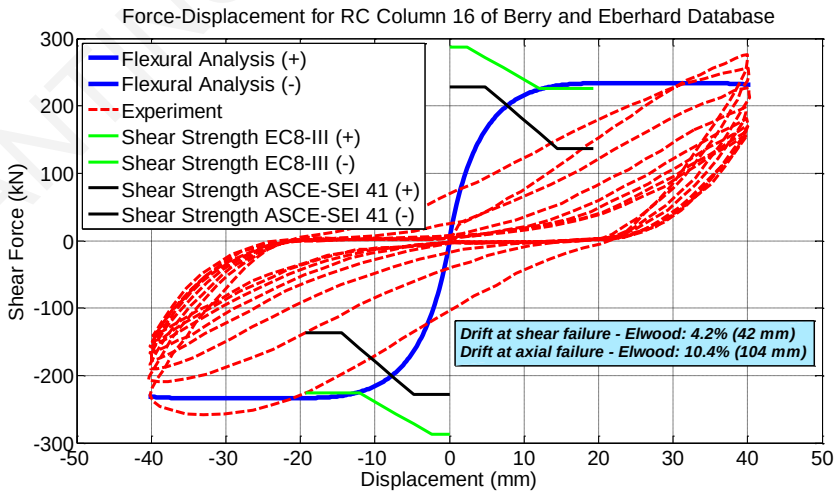

Figure 3.38: Comparison between numerical and experimental response of circular column (ID#16) of Berry and Eberhard Database (2004).

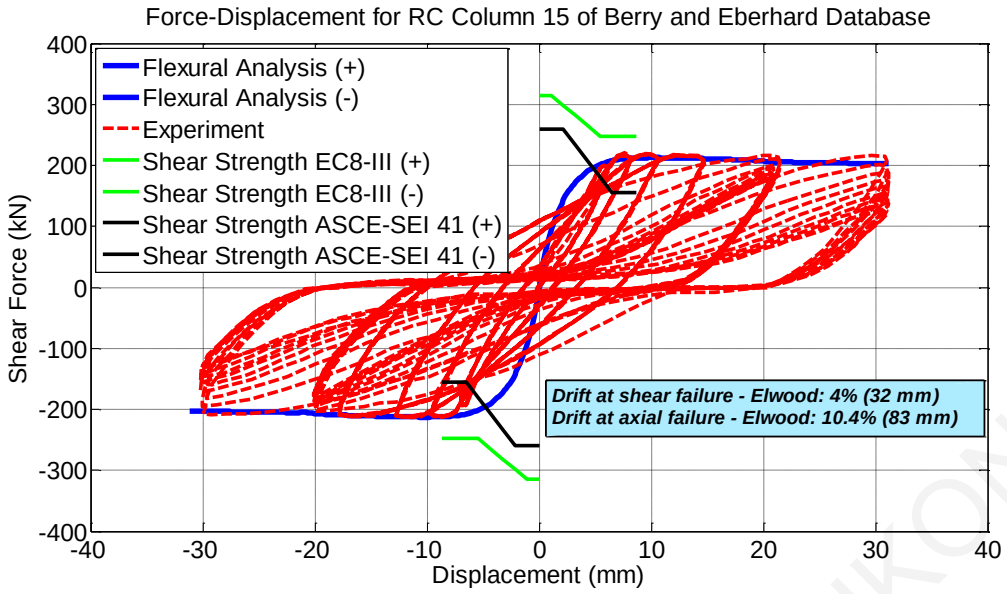

Figure 3.39: Comparison between numerical and experimental response of circular column (ID#15) of Berry and Eberhard Database (2004).

3.5 The Effect of Variable Axial Load on RC Column Behavior

Owing to the overturning moment, columns in multiple-column bents experience variable axial forces corresponding to the direction of, and typically being proportional to the horizontal forces. Columns are also subjected to the vertical components of ground motion, which is not correlated concurrently with the horizontal loading. Past earthquake records have shown that in some cases, vertical ground motions cannot be ignored, particularly for near-fault situations. For example, the lateral displacement ductility in a column, designed based on a constant axial load, with a relatively low axial load ratio, can become unsatisfactory when the actual axial load due to the overturning effects or the vertical ground motion exceeds the value that corresponds to balanced failure. The problem becomes even more significant when shear design is considered. The increase of axial load from the design level (typical values of axial load ratio can be as low as 0.1 particularly in bridge piers) to the level of the balanced axial load results in the increase of column flexural capacity, thus increasing shear demand. On the other hand, changes of axial load from compression to tension can result in a significant decrease in column shear strength.

In Table A.5 of the Appendix of this Chapter, an experimental database of reinforced concrete columns under cyclic lateral loading and variable axial load has been assembled for the needs of the investigation. For these cases, the experimental response envelope will be

assessed using monotonic static analysis. Analytical procedures are identical to those used in the previous section. For the sake of comparison with the numerical models and code specifications of the previous section, only pairs of specimens of the above experimental database tested under constant compressive or tensile axial load will be considered in the following correlation with the experimental results. In this way, the effect of the load on a column's shear strength will be demonstrated along with the effectiveness of code standards to assess this influence.

The first columns under study are the specimens ICC and ICT by Elnashai et al. (2011). Two columns with identical properties reported in Table A.5 are tested under cyclic lateral loading and constant compressive axial load (ICC) or constant tensile axial load (ICT). In the comparison of Fig. 3.40 with the experimental response it is observed that the shear strength degradation model of ASCE-SEI 41 (2007) detects shear failure after yielding of the studied column while in the EN 1998-3 (2005) shear capacity curve it does not. The estimated point of the detected shear failure corresponds well to the specimen strength, but in terms of displacement the shear failure is identified to occur much earlier as compared to the experimental response. The drift models by Elwood (2003) defined well the displacement at shear failure, but again, the axial failure drift was overestimated.

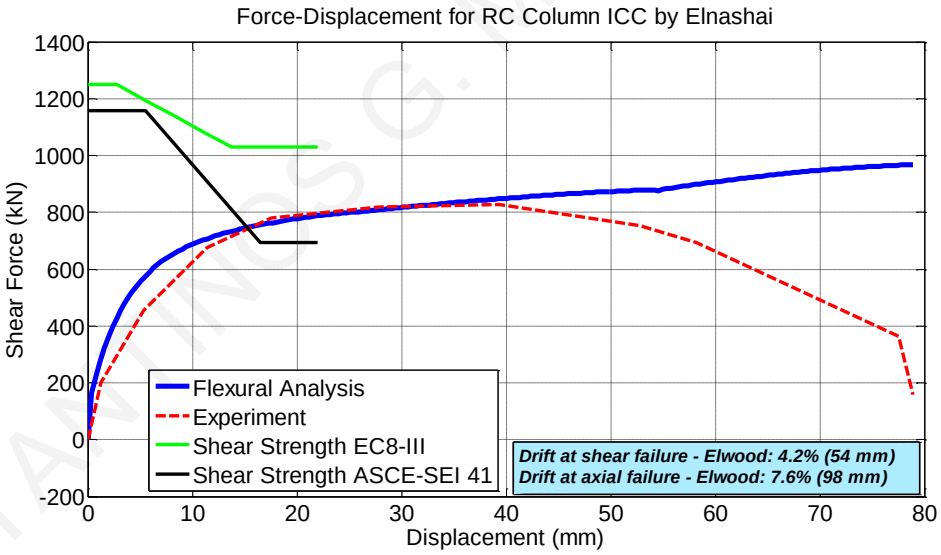

Figure 3.40: Comparison between numerical and experimental response of circular column (ICC) by Elnashai (2011).

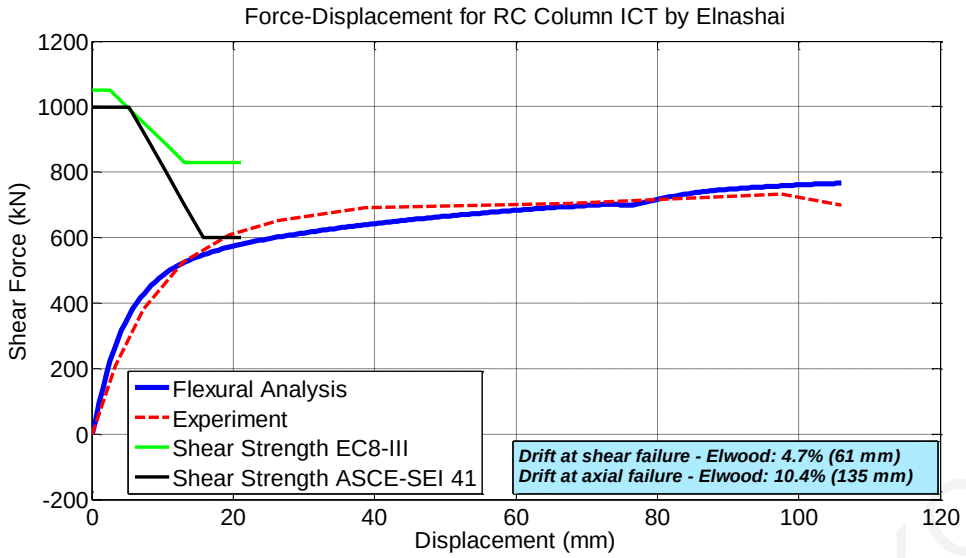

Figure 3.41: Comparison between numerical and experimental response of circular column (ICT) by Elnashai (2011).

For the case of the same specimen under constant tensile load (Fig. 3.41) it is noted that the degradation model of EN 1998-3 (2005) for shear strength reproduced the experimental response satisfactorily since it did not detect shear failure for the specimen which, during the tests reportedly failed in flexure. Finally, since no shear failure occurred, the drift models by Elwood (2003) were not relevant in the tensile-axial load case either.

The next column examples for investigation of the effect of variable axial load on shear strength are specimens CS1 and CS2 by Priestley et al. (1996) which were tested under cyclic lateral loading and constant compressive and tensile axial load respectively. From the comparison in Fig. 3.42 it can be observed that only the shear strength degradation model by ASCE-SEI 41 detects shear failure for the column under study, but at a somewhat lower strength and displacement capacity as compared to the experimental response. In addition, the drift model of Elwood at shear failure overestimates the corresponding displacement, while the drift model at axial failure underestimates the displacement where the loss of axial bearing capacity is observed.

Finally, the comparison of the same specimen by Priestley et al. (1996) under tensile axial load is depicted in Fig. 3.43. The degraded shear capacity models of the design codes (both) detect the shear failure of the column, but at lower strength and displacement compared to the experimental results. The drift model at shear failure by Elwood (2003) estimates the displacement at the onset of shear failure with good accuracy, however, the drift model at axial failure overestimates the experimental column response.

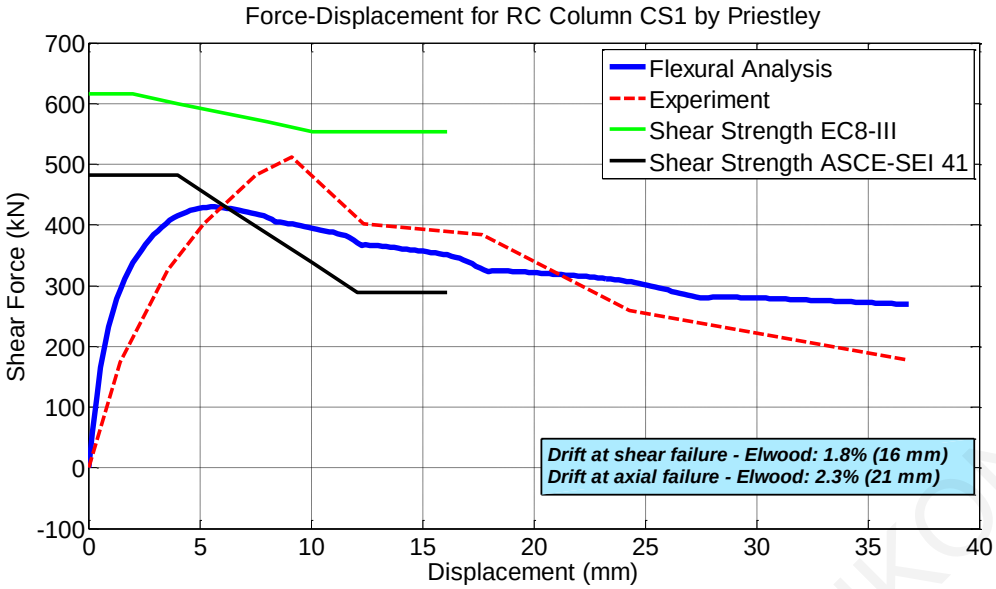

Figure 3.42: Comparison between numerical and experimental response of circular column (CS1) by Priestley (1996).

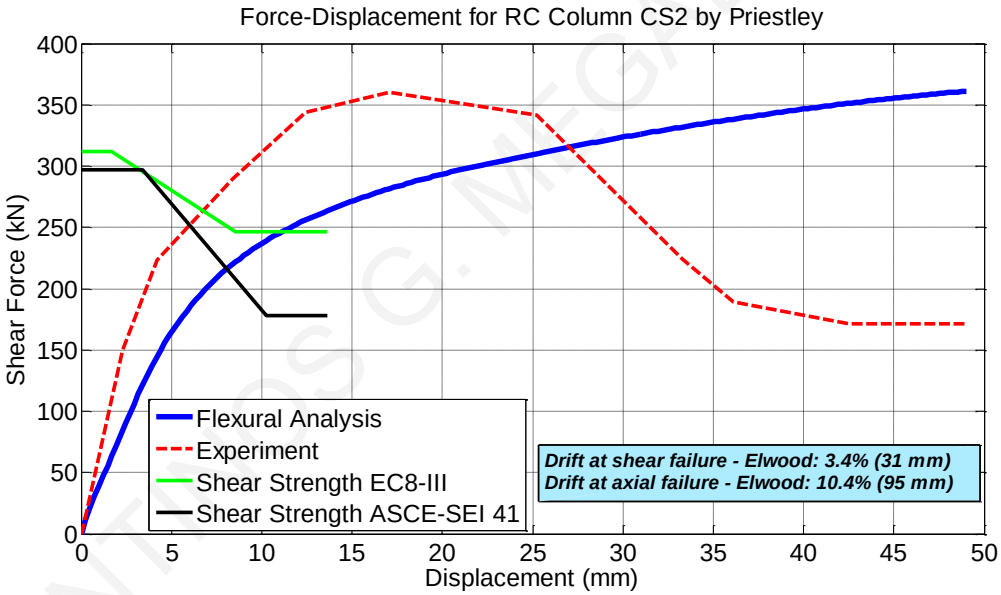

Figure 3.43: Comparison between numerical and experimental response of circular column (CS2) by Priestley (1996).

Clearly, based on the preceding analysis, the state of the art modeling of the lateral load response of columns leaves a lot to be desired: improved response estimation of the behavior of columns that are susceptible to shear failure after flexural yielding; better procedures to estimate shear strength and the pattern of degradation thereof, with increasing displacement ductility; the need to account for reinforcement pullout and its effects on

stiffness; the shape of the hysteresis loops; the detrimental effects of axial load at large displacement limits; and the magnitude of deformation (drift ratio) associated with milestone events in the response curve of the column member, are open issues that need to be settled before the performance-based assessment framework may be considered complete and dependable. Some of these issues (improved response estimation of the behavior of columns that are susceptible to shear failure after flexural yielding; better procedures to estimate shear strength and the pattern of degradation thereof, with increasing displacement ductility; the need to account for reinforcement pullout and its effects on stiffness; the detrimental effects of axial load at large displacement limits; and the magnitude of deformation (drift ratio) associated with milestone events in the response curve of the column member) are addressed in the following Chapters of the present thesis.

4 Mechanical Behavior of Lightly Reinforced Concrete Columns

4.1 Introduction

This chapter deals with reinforced concrete columns that do not conform to modern standards for earthquake resistant detailing. Existing concrete structures constructed before the development of modern seismic design provisions represent one of the largest seismic safety concerns worldwide. Such structures are vulnerable to significant damage and even collapse when subjected to strong ground shaking. Collapse of concrete structures has resulted in many of the fatalities in past earthquakes, leading to several efforts in recent years to improve assessment and retrofit procedures for existing structures. In these structures, columns are important structural elements that support the weight of a structure and resist earthquake story shear. Such columns often comprise materials of substandard quality. In the present thesis, columns that do not meet modern requirements for reinforcement detailing are referred to as "old-type" or non-conforming members (NC).

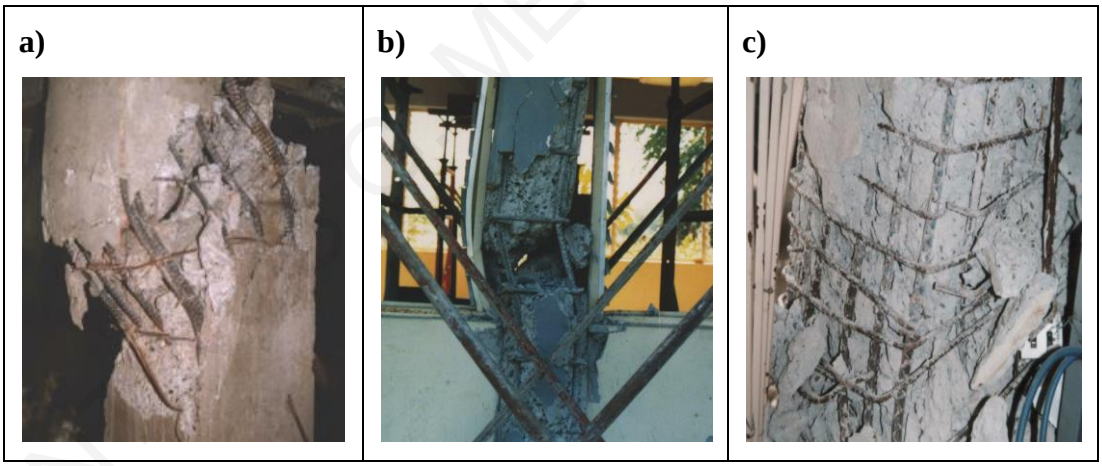

Figure 4.1: Brittle failure of old-type building columns. a) Thin and widely spaced plain bars as lateral reinforcement b) Spacing of the large diameter lateral reinforcement almost as wide as the width of the column c) Shear failure by opening of ties at a 90º bend.

Depending on the global characteristics of the structural system and the imposed local deformation demand, poorly detailed elements may become the critical components during seismic excitation, as they generally possess inadequate resistance to reversed cyclic loading (Fig. 4.2). Experience from past earthquakes has repeatedly shown that when subjected to cyclic inelastic deformation reversals, old-type columns undergo fast

deterioration and degradation of strength, failing in a brittle fashion with fatal consequences for the integrity of the structure as a whole (Fig. 4.2) (fib bulletin 24 2003).

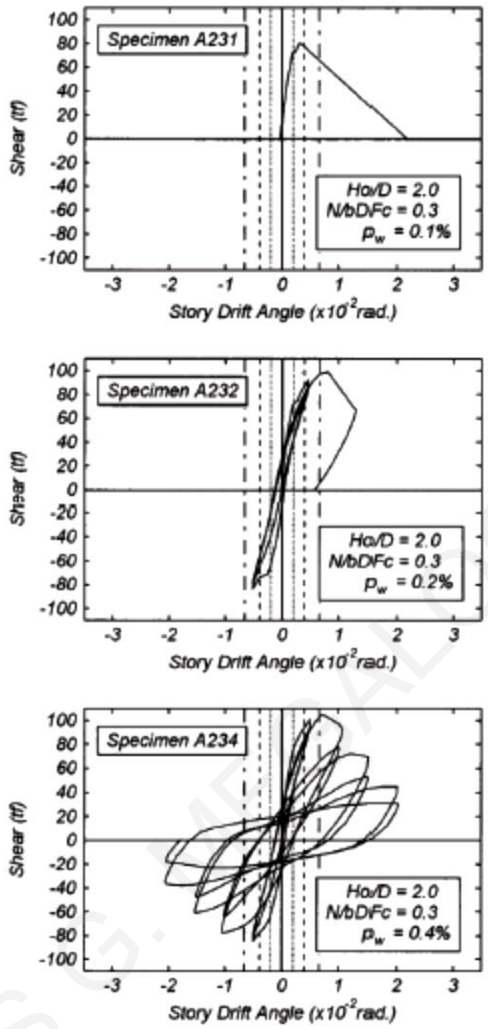

Figure 4.2: Effect of lateral reinforcement on shear strength (Tsukamoto, Kuramoto and Minami et al. 1989)

A special category of columns are those in bridge piers, whether these are arranged in single-column or multiple-column bents. Bridges differ in terms of dynamic response from buildings in that sectional sizes are much larger, normalized axial loads lower, and comprise various types of superstructures, substructures, and foundations with complex geometries and dynamic response characteristics; the modern concept is for strong-girder / weak-column capacity design which is the exact reverse from that prevailing in buildings. Furthermore, the degree of static indeterminacy is generally much lower in bridges than in buildings. Hence failure of a column can lead to collapse of the total bridge system.

The destructive damage in the 1995 Kobe Earthquake revealed the fact that there are a number of highway bridges that are vulnerable to strong ground motion. Major reasons of

the damage in that event were the tendency for shear failure of RC columns that were designed and constructed in accordance with the pre-1980 Design Specifications. The premature shear failure occurred near the end of lap-splices above the base. The practice of termination of longitudinal bars with insufficient development length resulted in the major damage at various sites. Apparently, the allowable shear stress design practice had overestimated the concrete capacity to shear, and the design development length of longitudinal bars at the cut-off point was insufficient in the pre-1980 Design Specifications (Fig 4.3). But the more critical occurrence, seen time and again in reconnaissance reports was the poor detailing of transverse reinforcement, marked by excessively small tie bar diameters, lack of tie support at the corners against dislocation and bending, and sparse arrangement without intermediate tie legs (i.e. use of conventional perimeter ties only) which could not provide any countable confinement of the encased concrete for the size of cross sections encountered in bridges, nor could they prevent lateral buckling of compression reinforcement.

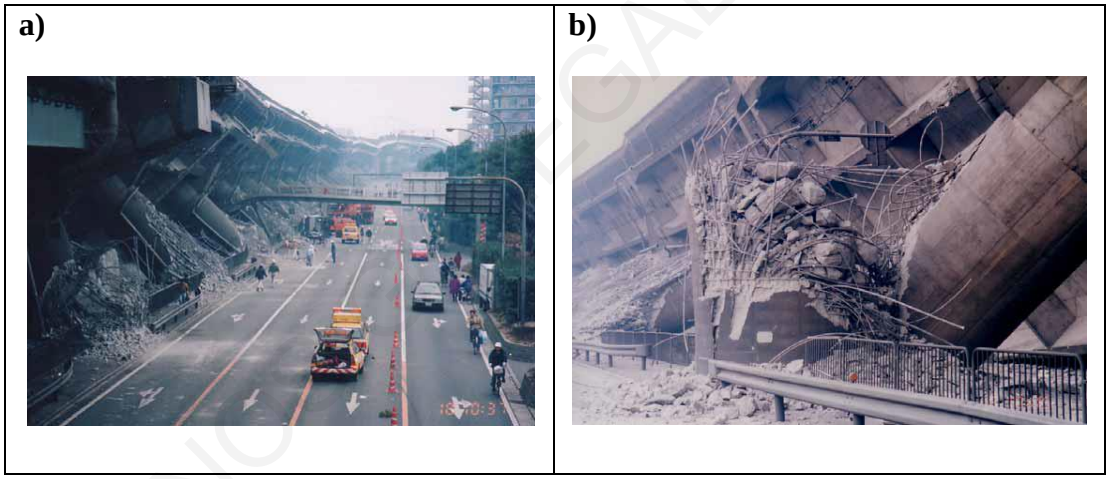

Figure 4.3: a) Collapse of Fukae Viaduct 1995 Kobe Earthquake b) Premature shear failure of reinforced Concrete bridge pier, Fukae Viaduct.

4.2 Typical characteristics of older type construction

Structural deficiencies encountered in older type reinforced concrete construction may be classified in three major groups owing to systematic oversights/flaws in design, detailing, structural system form, and construction. For example, design deficiencies include:

- Inadequate provisioning of lateral-load resisting members (e.g., lack of shear walls or special moment-resisting frames);

- Lack of redundancy (alternative load paths) in the structural system (i.e. system structural collapse is triggered in the event of damage occurring in few members);
- Irregularities in plan or elevation (e.g. L or T-shaped plan, or vertical setbacks);
- Presence of short columns, which usually fail in specific patterns that involve shear-type dislocation which is catastrophic;
- Strong- beam weak-column joints, that is, cases where the beams are stronger than the columns they connect to (in buildings).

Key detailing deficiencies include:

- Inadequate transverse reinforcing bars (Fig. 4.1).
- Short overlap lengths at spliced joints (Fig. 4.3).
- Large amounts of longitudinal reinforcement (over-reinforced sections)

Adverse conditions such as those listed above may be further aggravated by construction deficiencies, such as low-quality workmanship, use of inferior materials and deviations from structural drawings and specifications during the construction phase. Additional deterioration is owing also to ageing, the accumulated effects of corrosion or other damage caused by the long-term exposure of the structure to natural phenomena (e.g. scouring at bridge piers).

4.2.1 Material characteristics

The correspondence between older and newer codes regarding the concrete strength values is depicted in Table 4.1 where the characteristic compressive strengths f_{ck} are reported with their nowadays definition (cylindrical specimen, characteristic strength with a 95% probability of exceedance by a random sample) adjusted to correspond to other specimen shapes and practices such as those used in preceding codes (mean strength value obtained from 200mm cubic specimens was the standard practice until 1991 in Greece). It is shown in the table that the testing time of 28 days from casting has not changed ever since it was first introduced in the German codes in 1907; however the test was conducted on cubic specimens until 1991, when the American standard of the cylindrical specimen was adopted throughout Europe, according to the prevailing tendency for harmonization of international practices (particularly through the Eurocodes). Under the same objective falls also the change in nomenclature (Concrete in lieu of Beton) and in the measuring units (from kg/cm^2 to N/mm^2 (MPa)).

Steel reinforcement varies in terms of quality (strength and ductility) and surface characteristics (smooth bars or G class in DIN488, and ribbed bars or class R in DIN488). Under normal circumstances properties of steel reinforcement present much less variability than concrete. In very old construction even bars of non-rectangular cross sections may be found. According to the Greek code of 1954 (Table 4.2) the qualities of reinforcing steel (I, III, IV) had allowable stresses 1400 to 2400 kg/cm^2. These values resulted approximately from the yielding limit after division by a safety factor ranging between 1.5 and 1.75. The reduced values of the allowable stresses for reinforcing steel accounted for the expected construction uncertainties. The modulus of elasticity was taken constant and equal to 2.1x10^6 kg/cm^2 for all steel qualities. After 1991 the reinforcing steel is characterized by its yield strength value (MPa). The modulus of elasticity is taken constant, equal to E_s = 2.0x10^5 N/mm^2.

Table 4.1: Categories and Strengths of Concrete in 20th century (Karaveziroglou 2009)

1) Cubic specimen with the age of 28 days 2) Length of the edge of the cubic specimen (mm) 3) Mean value of 3 specimens [kg/cm^2] 4) Characteristic strength of cylinder f_{ck} [N/mm^2] 5) C30/37 after 2010 and increase of the qualities to C90/105

	Period	W_{28} 1)	Nominal value of compressive strength of concrete							
1	1907-16	300 2)	W_{28}	W_{28}	W_{28}	W_{28}				
		M 3)	100	150	180	230				
		f_{ck} 4)	5	6	7	8				
2	1916-25	200 2)	W_{28}	W_{28}	W_{28}					
		M 3)	150	180	245					
		f_{ck} 4)	7	8	9					
3	1925-32	200 2)	W_{b28}	W_{b28}	W_{b28}					
		M 3)	100	130	180					
		f_{ck} 4)	6	8	11					
4	1932-43	200 2)	W_{b28}	W_{b28}	W_{b28}					
		M 3)	120	160	210					
		f_{ck} 4)	8	10	12					
5		200 2)	B	B	B	B	B	B	B	

	1954-91	M [3]	80	120	160	225	300	450	600		
		f_{ck} [4]		8	10	16	20	28	35		
6	1991-present	150 [2]	C	C	C	C	C	C	C	C	C
		5% [3]	10	15	20	25	30	35 [5]	45	50	55
		f_{ck} [4]	8	12	16	20	25	30	35	40	45

Table 4.2: Steel qualities according to the Greek code 1954 (Karaveziroglou 2009)

Category	Yielding Limit Min f_y [MPa]	Tensile Strength f_t [MPa]	Allowable stress f_{al} [Kg/cm^2]
I	220	340-500	1200-1400
IIIa	420 (d≤18mm) 400 (d>18mm)	500 (min)	2000-2400
IIIb	420 (d≤18mm) 400 (d>18mm)	500 (min)	2000-2400
IV	500	-	2000-2400

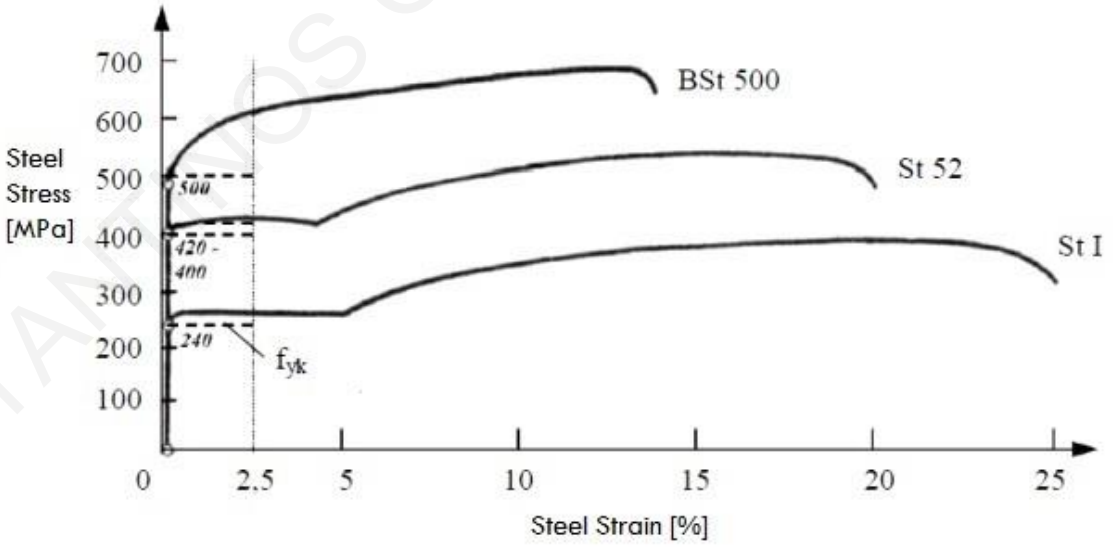

Figure 4.4: Stress – Strain diagrams of older reinforcing steel (Karaveziroglou 2009).

4.2.2 Older – type detailing

In the presence of confinement in an RC member, many of the imperfections of the materials described above can be overcome. The essential difference in design philosophy between nowadays and 40 years ago lies in the importance of transverse reinforcement as a means of confinement. In the older codes the use of stirrups was recommended for: a) the support of the longitudinal reinforcement against buckling, b) partial contribution to shear strength, c) torsion. The German DIN 1045/1972 reflects the point of view in Europe, for that period: The approach taken was to place reinforcement so that ties may intersect all possible cracks – so as to restrain the crack width. Based on this point of view the designer was expected to bend the primary reinforcing bars in strategic locations in the vicinity of minimum moment so as to enhance the shear strength of the prismatic elements.

This practice was widespread in Europe and North America. Note for example the emphasis on the most advantageous placement of primary reinforcement in the case of corner connections so as to improve the flexural mechanism and the anchorage of longitudinal reinforcement in the joints but without any reference to regulations regarding the use of stirrups.

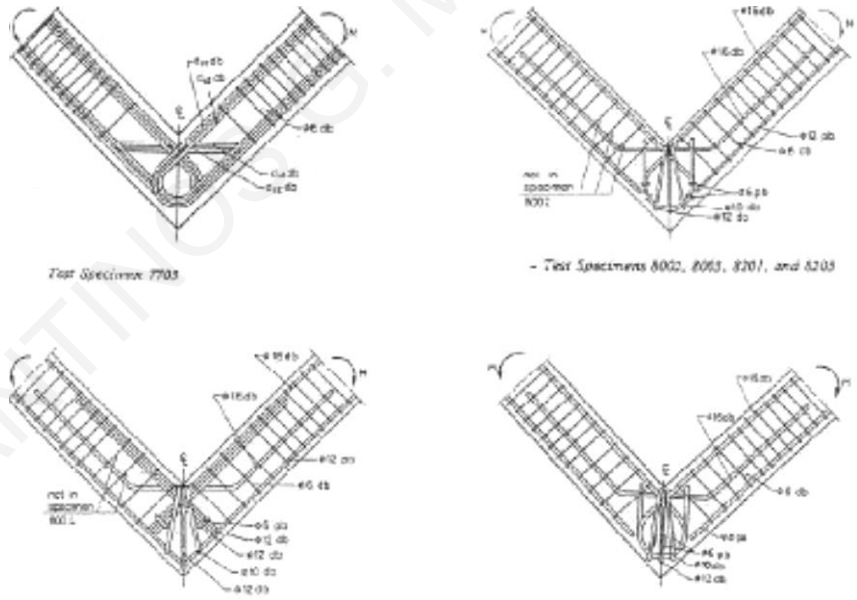

Figure 4.5: Characteristic example of reinforcement detailing in "old-type" elements. (fib Bulletin No. 24 2003)

4.3 Deformation Capacity of Lightly Reinforced Concrete (RC) Columns

Figure 4.6 depicts the typical brittle hysteretic response of a lightly reinforced concrete column. The hysteretic loops of the column show the degradation of stiffness and load carrying capacity during repeated cycles due to cracking of concrete and yielding of the reinforcing bars. Pinching is a dominant characteristic of the response. The occurrence of a wide and steep shear crack resulted in a reduction in the shear-resisting capacity of the column. Near axial failure, a steep shear crack developed in the column, which led to sliding between the crack surfaces followed by buckling of longitudinal bars and fracturing of transverse bars along the shear crack (Ngoc Tran & Li 2013).

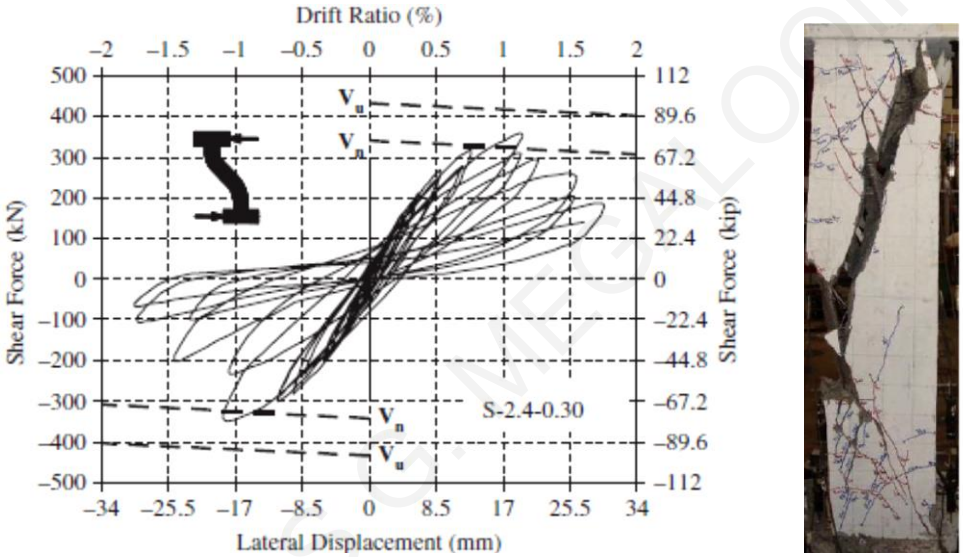

Figure 4.6: Hysteretic characteristics and failure mode of a lightly reinforced concrete column. (Ngoc Tran & Li 2013)

Results of previous studies (Fenwick and Davidson 1995, Lee and Watanabe 2003, Matthews et al. 2004, Peng et al. 2011) indicate that the concrete shear resistance of RC columns decreases with increasing longitudinal strains. This increase in longitudinal strains after the onset of flexural yielding widens the diagonal cracks, which leads to sliding of the crack surfaces; overall, an increase in the principal tensile strain occurs. As a result, the effective concrete compressive strength is reduced and the member possibly fails in shear. Longitudinal strains and axial elongations substantially increase during reversed cyclic loading (Fig. 4.7). The residual strains in the reinforcements accumulate in each cycle; hence, beam elongation increases during load reversals. Furthermore, dislocations in the local geometry occur preventing the cracks from closing completely. Elongation and

longitudinal strains in the plastic hinge region not only influence the concrete resistance in shear but also the inelastic deformation, respectively, and hence, the rotation capacity up to flexural failure. (Fig 4.7) (Syntzirma et al. 2010, Mehrabani and Sigrist 2015).

The total lateral response of a lightly reinforced concrete column is usually modeled by representing flexural action, reinforcement slip and shear deformation response as springs in series, where the force in each spring is the same and the total deformation is the sum of individual spring deformations. In the established modelling methods, flexural deformations are evaluated by the nonlinear beam-column element. Zero-length elements located at the top and bottom of the column are attached to the nonlinear beam-column element. The zero-length elements are defined by three uncoupled material models describing: (1) the moment-rotation relationship representing reinforcement slip response (rotational spring); (2) the shear-horizontal displacement relationship representing the shear force-displacement response (shear spring) and (3) the axial load-vertical displacement relationship (axial spring). (Shoraka and Elwood 2013).

A critical step in the direction of determining the deformation response is to identify the weak link of behavior, where localization is expected to occur (minimum lateral strength based on the various mechanisms of resistance). In this approach, it is postulated that deformation components are additive only if the hysteretic response is controlled by flexure, demonstrating stable loops. In all other cases, the deformation component associated with the controlling mode of failure dominates the overall deformability of the member (Syntzirma and Pantazopoulou 2007).

In order to demonstrate the above statement, the modelling technique of Fig. 4.8 was applied to an example reinforced concrete column fully fixed at both ends with properties similar to the rectangular column of the experimental campaign of Elwood and Moehle (2008) in the software OpenSees (OpenSees 2.5). The Base Shear vs. Lateral Drift response of the column along with the shear failure (initiation of degrading slope) and the axial failure (end of the response) is depicted in Fig. 4.9.

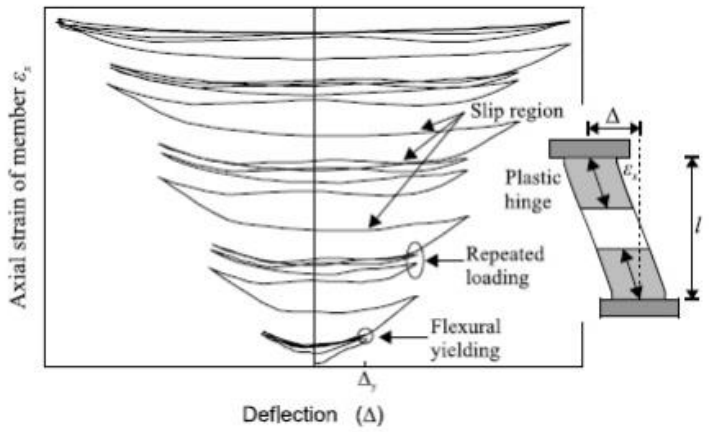

Figure 4.7: Average axial strains versus deflection of a RC column failing in shear after flexural yielding (Mehrabani and Sigrist 2015).

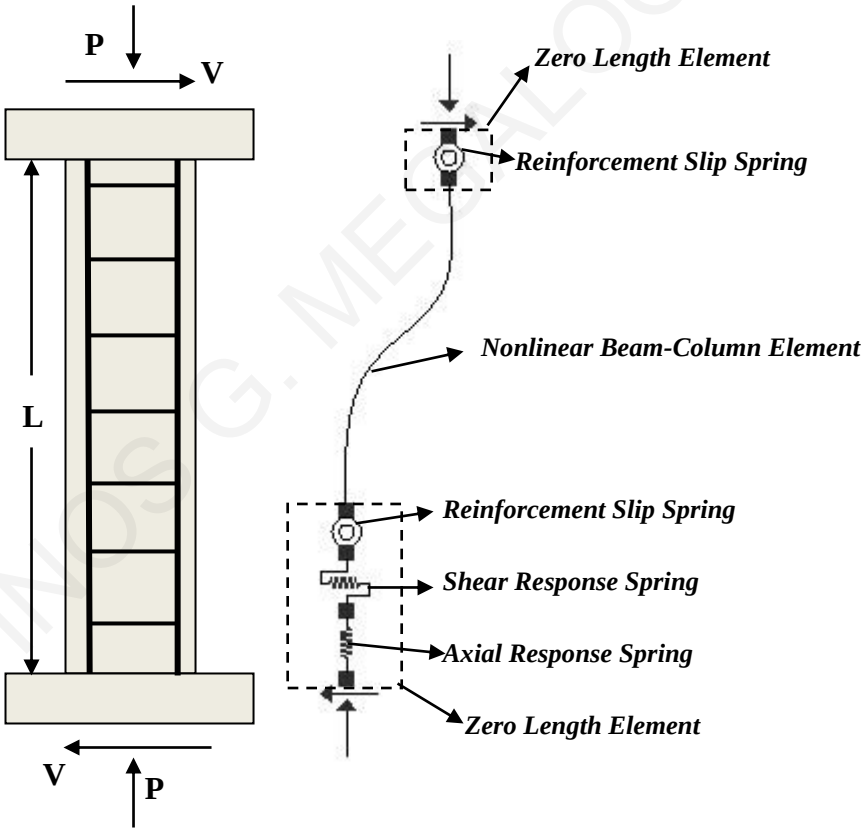

Figure 4.8: Shear, axial and rotational spring in series model with the nonlinear beam-column element (shear and axial springs are set where axial and shear failures are expected to occur).

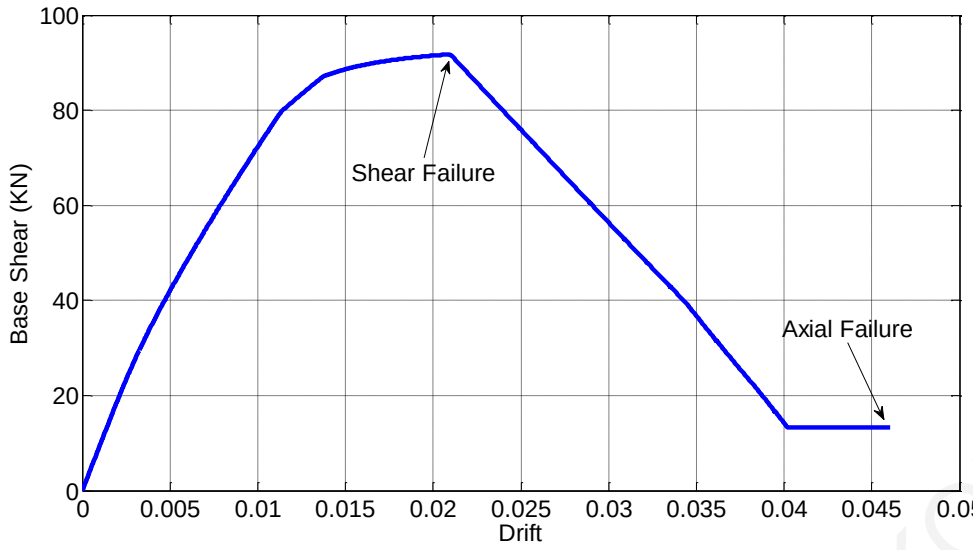

Figure 4.9: Base Shear vs. Lateral drift of a RC square column simulating shear and axial failures.

4.3.1 Local to Global Transformation of Stress and Deformation Resultants

Capacity prioritizing in order to identify the weakest link of member behavior is a prerequisite for determination of the tendency for localization of material deformation. Failure may occur as a consequence of exhaustion of some material strength or deformation capacity; each such event may have implications that could be catastrophic for the stability of the member, or alternatively, it could simply lead to redistribution of internal forces. For example, an event in member response curve could be exhaustion of the cracking strain on the tension face, and later-on the delamination strain on the compression face in the concrete cover, exhaustion of the compressive strain capacity of the encased core concrete, yielding or fracturing in transverse reinforcement, exceedance of the buckling limit in the longitudinal compression reinforcement, and tensile yielding or fracturing in the longitudinal tension reinforcement. These events occur in different locations of the cross-section or of the member (Fig. 4.10). A Reinforced Concrete (RC) section under combined flexure and axial load is usually analyzed using the following simplifying assumptions (Fig 4.10): 1) A plane section before bending remains plane and normal to the longitudinal member axis after bending, 2) The stress-strain relation (constitutive model) of materials is known, and the state of stress is simplified to only consider normal stresses and strains, 3) External forces are in equilibrium with the internal stress resultants. The first assumption, known as the Bernoulli hypothesis, simplifies the analysis and gives linear distribution of longitudinal strain across the section with null strain at the neutral axis. The location of the neutral axis

of the section is determined by the equilibrium of axial forces acting on the section.

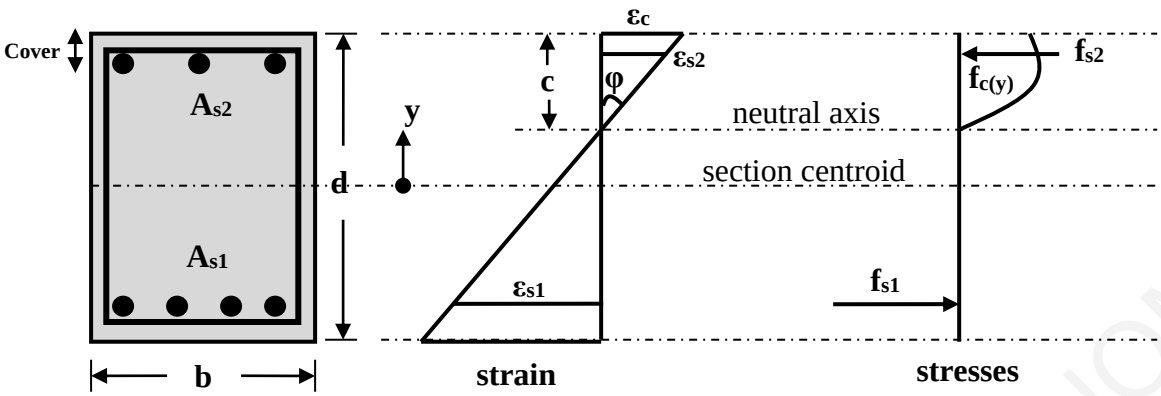

Figure 4.10: Reinforced concrete section under bending.

Prioritizing the sequence of occurrence of above described events is done on the basis of member shear forces, as this is a common attribute to all mechanisms of resistance: in this manner, a local event that occurs at the material level, is reflected in the global scale by the acting member shear force, *V*. Possible material failure problems that would limit the strength of a column are:

1) Cover delamination: It occurs at a compressive concrete strain equal to the ultimate compressive strain of unconfined concrete (0.004) (Fig. 4.10). Cover spalling appears at a displacement less than or near the yield displacement (Fig 4.11).

Figure 4.11: Concrete Cover Spalling of a Reinforced Concrete Column.

2) Attainment of the ultimate compressive strain of confined concrete core (Figs. 4.10, 4.12). In this case concrete crushes in compression and it is a flexural mode of failure. Flexural compression failure is followed potentially by the loss of gravity load carrying capacity.

3) Splitting of the cover concrete along the weak plane formed by the lapped bars resulting in a loss of bond. In case of cyclic loading conditions, the contribution of concrete confinement to lap splice strength is insignificant.
4) Bar strain exceeds the strain development capacity of the reinforcement which is the minimum of the tensile strain that can be sustained by the lap splice or anchorage at the critical section or the fracture strain of the bar.

Figure 4.12: Flexural Compression Failure of a Reinforced Concrete Column

5) The compressive longitudinal reinforcement enters the instability conditions which result to buckling of the longitudinal bars. The occurrence of buckling is affected by the presence (spacing) of transverse reinforcement and the diameter of the bars. In lightly reinforced concrete columns the unsupported length of longitudinal reinforcement is high and equal to the spacing of the stirrups. Buckling results to spalling of concrete cover (Fig 4.13).
6) Occurrence of web diagonal tension cracking: The tensile stresses carried by the concrete before onset of significant shear cracking should be resisted by shear reinforcement once shear cracks open. If this doesn't happen diagonal tension failure occurs (exhaustion of concrete contribution to shear V_c) (Fig. 4.1 a).
7) Onset of stirrup yielding: According to Mörsch truss analogy stirrup yielding refers to the steel contribution in shear strength of the column, estimated as the yielding forces of those stirrups which are crossing the diagonal shear crack.
8) Occurrence of large postyielding strains in the stirrups which signals high shear strain in the column and it can be tracked along the descending branch of the member response curve –associated with the degraded shear strength of the member.

Conversion from the material scale to the stress resultant of the column follows from equilibrium of forces and moments (Eq. 4.1). Normal strains over the cross section are

assumed to follow a plane sections profile, where, for states of stress past flexural yielding, the normalized neutral axis depth ξ, is assumed to remain approximately constant (alternatively its value may be obtained from interpolation depending on the value of the gravity axial load, N_g, acting on the cross section, which is taken here as a reference, average value). Thus, for criteria 1) – 5) above, which refer to the occurrence of a milestone event in some component of normal strain, the corresponding shear force of the cantilever (half the column's length is L_s) is obtained from (M = Moment at column end, d = the effective depth of the column, h = height of the section of the column, ; A_{s1}= area of tensile reinforcement):

Figure 4.13: Buckling of compressive longitudinal reinforcement.

$$V = {}^{M}/_{L_s} = \left[f_{s1}A_{s1}d(1-0.4\xi) + N_g(0.5h - 0.4\xi d)\right]/L_s \quad (4.1)$$

In the above, $f_{s,1}$ is the axial stress in the steel tension reinforcement, obtained from the stress-strain diagram of the reinforcement, given the corresponding axial strain. This is the tension bar strain associated with each of the milestone events listed in 1) to 5) above. For criteria 6)-8) the stress resultant is given by the shear strength of the column.

Values obtained for the milestone events listed above limit the strength of some of the mechanisms of resistance in series, namely *Flexural* ($V_{u,fl.}$), *Shear* ($V_{u,sh.}$), *Anchorage/Lap Splice* ($V_{u,sl.}$), or *Compression Bar Stability* ($V_{u,buckl.}$). Therefore, for any drift level, the above terms are organized in a hierarchy, with the term with the lower strength, V_{fail}, controlling the mode of damage and possibly, failure of the member:

$$V_{fail} = min\{V_{u,fl.}V_{u,sh.}, V_{u,sl.}, V_{u,buckl.}\} \quad (4.2)$$

4.3.2 Strain – Displacement Transformations

Geometric relations are required to identify the magnitude of column drift or tip displacement of the model cantilever (strain resultants), for each of the milestone events listed in the preceding section. The mechanisms of deformation participating to total drift are flexural drift due to curvature along the member, rigid body rotation owing to reinforcement pullout from the support anchorage or lap splice, and shear distortion which results in lateral offset of the member (Fig 4.14).

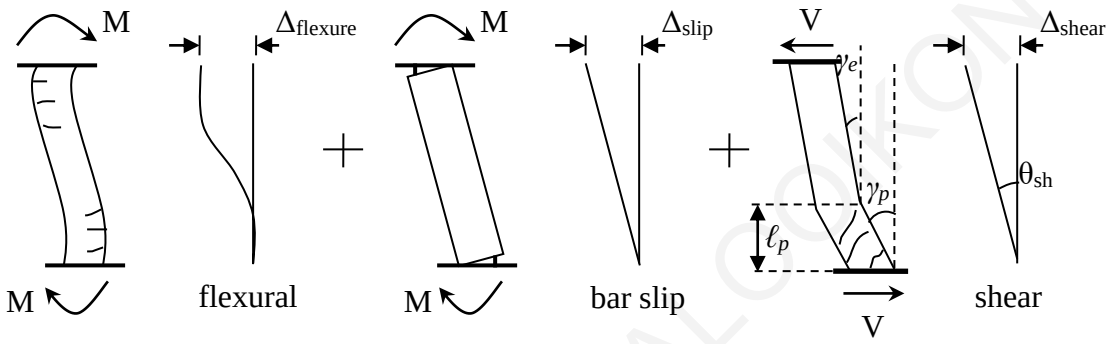

Figure 4.14: Lateral deformation components contributing to member drift.

Special considerations are as follows:

(a) Strain resultants due to flexural curvature:

The moment curvature relation of a cross section provides the basis of understanding the nonlinear behaviour of reinforced concrete columns such as cracking, crushing and spalling of concrete, and yielding and buckling of longitudinal reinforcement. The typical flexural deformation characteristics are shown in Fig. 4.15.

In the loading branch of the member while it is in pristine condition, flexural cracking near the critical section of maximum moment reduces the initial elastic stiffness. The specimen continues to soften with loading after cracking due to the spreading of cracking along the specimen length, crack opening associated with tension softening of concrete and bond-slip of the reinforcement between cracks. Yielding of tensile reinforcement causes an abrupt and sharp reduction in stiffness. Even after the flexural yielding, the resistance continues to increase due to the shift of neutral axis and later due to strain hardening of reinforcement. Spalling of the concrete in compression has a negative effect on the resistance. Upon unloading after post-yielding, the unloading stiffness is generally high, but gradually softens at lower loading level. A significant residual deformation exists even after

the removal of loads caused by permanent strain in longitudinal reinforcement and residual bar slip. Cracks remain open at the removal of loads due to the residual bar slip. The overall unloading stiffness degrades with increasing plastic deformation amplitudes. Reloading stiffness immediately after load reversal is generally low until opened cracks close; the compression by bending moment must be resisted by the compressive reinforcement. The reloading stiffness gradually recovers with the closing of cracks. Although the first post-elastic excursion may be considered as first loading in the reloading direction, the softening is more gradual than in the initial yielding direction partly attributable to the Bauschinger effect of the steel. The resistance at the previous maximum displacement reaches the level of the previous maximum resistance. When the reloading branch reaches the previous maximum response point, further loading proceeds along the continuation of the first loading branch. Flexural failure of columns due to cyclic loading is gradual, controlled by progressive deterioration in the compressive zone such as spalling of concrete followed by local buckling of the longitudinal reinforcement. The reinforcement sometimes fractures in tension in the subsequent half cycle after compression bucking. Clear definition of failure is difficult in flexure-dominated members unless tensile fracture of longitudinal reinforcement is observed. Therefore, failure is often defined in the experiment as a point where the resistance cannot be recovered to a level exceeding 80 percent of the maximum resistance. It should be noted that this definition of failure point is affected by the loading history.

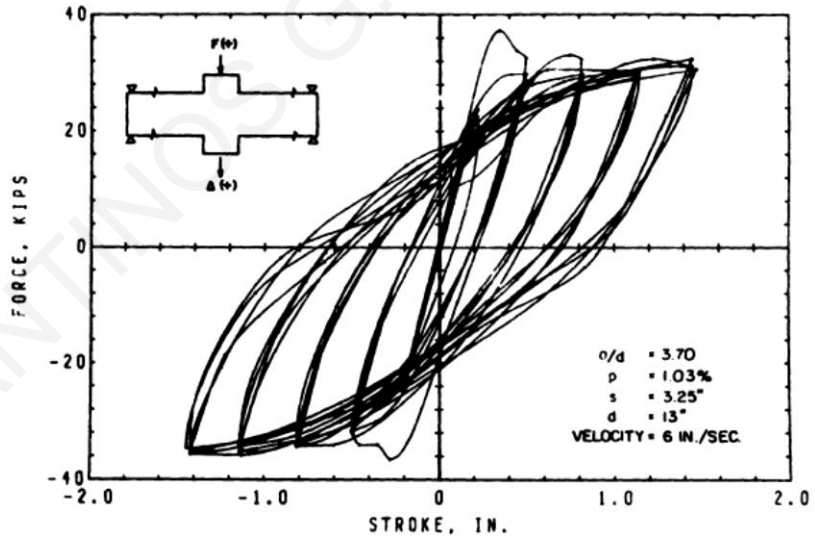

Figure 4.15: Flexural deformation characteristics (Celebi and Penzien 1973).

The flexural force-displacement response of a cantilever reinforced concrete column (statically equivalent to the half-length of a fixed ended column under horizontal force) can be derived analytically from the moment curvature response based on the "plastic hinge"

concept which is defined as the length over a seismically swaying column, where flexural moments exceed the yielding capacity. This length, measured from the critical section towards the shear span, signifies the region where intense inelasticity occurs during the earthquake. However, this transformation doesn't represent the flexural deformation in a strict sense because a plane section does not remain plane in a region where an extensive shear deformation occurs as it occurs for example, in lightly reinforced concrete columns.

Based on Fig. 4.16 the transformation of moment curvature diagram of the critical section of a bridge pier to a force displacement curve for a cantilever of identical cross section and half its free length can be applied. Part of the plastic hinge length is attributed to the yield penetration of the reinforcement into the anchorage (See also Chapter 5). The following equations are useful for the determination of yielding Δ_y and ultimate displacement Δ_u of the column (L_{yp} = length of yield penetration):

$$\Delta_y = \varphi_y \cdot \left(H + L_{yp}\right)^2/3,$$

$$\Delta_p = \varphi_p \cdot L_p \cdot \left(H - L_p/2\right)^2 \approx \varphi_p \cdot L_p \cdot H$$

$$\varphi_p = \varphi_u - \varphi_y\ ,\ \ \Delta_u = \Delta_y + \Delta_p \tag{4.3}$$

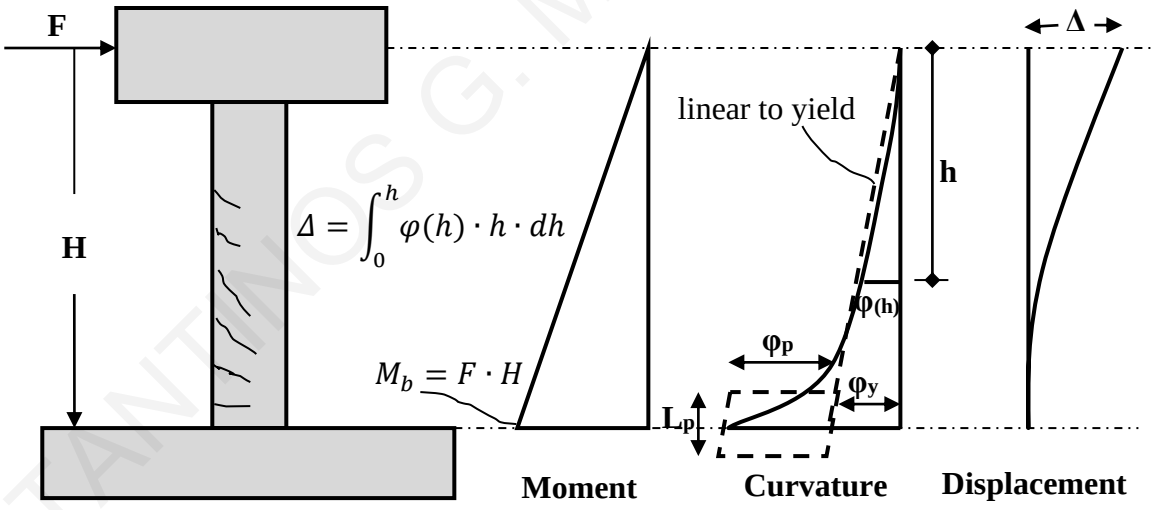

Figure 4.16: Moment, Curvature and Displacement Distribution of a cantilever bridge pier.

The most recent versions of the relevant assessment standards (e.g. Eurocode-8 Part III, draft of the 2020 edition) completely bypass the notion of a plastic hinge length by providing direct expressions for estimation of plastic rotation (tip displacement divided with the length of the column) without need for integration of inelastic curvatures.

(b) Strain resultants owing to bar pullout / slip

When a reinforced concrete column is subjected to bending moment, strain accumulates in the anchorage length of the tensile reinforcing bars: a phenomenon known as strain penetration. This causes the bars to extend or slip relative to the anchoring concrete at column fixed end(s) (see Chapter 5). The extension is commonly known as reinforcement slip and leads to rigid-body rotation of the column (Fig. 4.14). This results in an additional lateral displacement component. The general shape of the moment-bar slip rotation curve is demonstrating a pronounced pinching of a hysteresis loop (Fig 4.17). Flexural deformations determined from conventional fiber section analysis (Chapter 6) do not account for lateral deformations caused by reinforcement slip at column ends. Therefore, these deformations along with the displacement/rotation due to slippage of the reinforcing bar anchored in the shear span of a reinforced concrete column must be calculated separately and added to the other deformation components due to flexure and shear to calculate the total lateral displacement. This procedure is described extensively in Chapter 5.

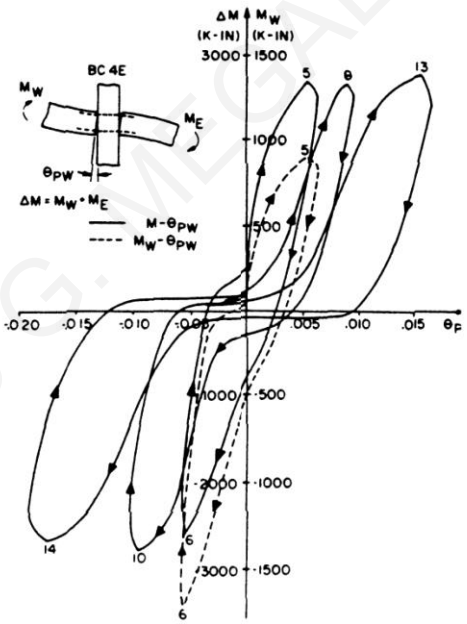

Figure 4.17: Rotation due to bar slip (Bertero and Popov 1977).

(c) Distortion resultants

Shear distortion is elastic prior to web cracking, obtained from the nominal code value for concrete contribution, divided by the member's shear stiffness (Eurocode 8, Paulay and Priestley 1992): (Basic mechanics – strength of materials: $\gamma=V/GA$; where $G=E/2/(1+v)$,

A_{sh} = 5/6A, v=0.2)

$$\gamma_e = V_c / \left[0.4 \cdot E_c \cdot 0.8 A_g\right] \tag{4.4}$$

After web cracking, shear distortion is set equal to stirrup strain, ε_{st}. From the Mörsch truss geometry it may be shown that the shear strain $\gamma = \varepsilon_{st} = (V - V_{c,cr}) / [E_s \Sigma A_{st,i}]$, where the numerator in this calculation represents the total force carried by the stirrups crossing a diagonal crack, and the denominator represents the extensional stiffness of the stirrups. Here, $V_{c,cr}$ is the total shear force carried by the cracked concrete web:

$$For\ \frac{N}{f_c A_g} \geq (\rho_{s1} - \rho_{s2}) \cdot \frac{f_y}{f_c} \Rightarrow V_{c,cr} = 0.5\sqrt{f_c}\left[\frac{d}{L_s} \cdot \sqrt{1 + \frac{N}{0.5\sqrt{f_c} A_g}}\right] \cdot A_g \tag{4.5}$$

$$otherwise\ V_{c,cr} = 0$$

Eq. (4.5) has been derived from equilibrium of forces on the cross section: a concrete contribution is assumed to exist if there is a nonzero compressive force in the concrete (i.e. once the cracks have been closed). With particular reference to columns with distributed reinforcement on all sides of the cross section, it is necessary to establish the neutral axis location prior to estimating the effective tension and compression reinforcement ratios, ρ_{s1}, ρ_{s2}, to be used with the inequality of Eq. (4.5).

The contribution of web reinforcement to shear strength should be calculated from the sum of forces developed in all stirrup legs crossing the critical shear crack, while also considering the limited development capacity of inadequately anchored stirrups: $V_w = A_{st} \cdot \sum_i f_{st,i} \neq A_{st} \cdot f_{y,st} \cdot (d - d_{s2}) / S$ (here an angle of inclination 45° of the critical shear crack is assumed).

Thus, for old-type construction it is necessary that stirrups be accounted for discretely and not smeared through the d/S term, as it is essential that the least number of stirrups crossing a crack plane need be determined, rather than an average value. If it is possible to determine a shear crack path along the member that does not interrupt any stirrup legs at all, then the V_w term is zero (Syntzirma 2010), whereas Eurocode 8 (2005) would yield a nonzero value even for excessively large stirrup spacing, S. This point was also illustrated through practical examples in Chapter 2.

Degradation of shear strength occurs after web cracking, as the value of the stirrup strain, ε_{st}, increases. The principal tensile concrete strain, $\varepsilon_{c1} \approx \sqrt{2}\varepsilon_{st}/2$ occurs in directions

orthogonal to the concrete struts of the Mörsch truss causing the "so-called" compression softening of the struts according with the Modified Compression Field Theory. The compression softening coefficient is, $\lambda=1/(0.8+0.27\varepsilon_{c1}/\varepsilon_{co})$ – this is responsible for the degradation of the nominal shear strength, expressed empirically through the degradation coefficient of shear strength that depends on ductility $k(\mu_{\Delta})$ (Martin-Perez and Pantazopoulou 2001).

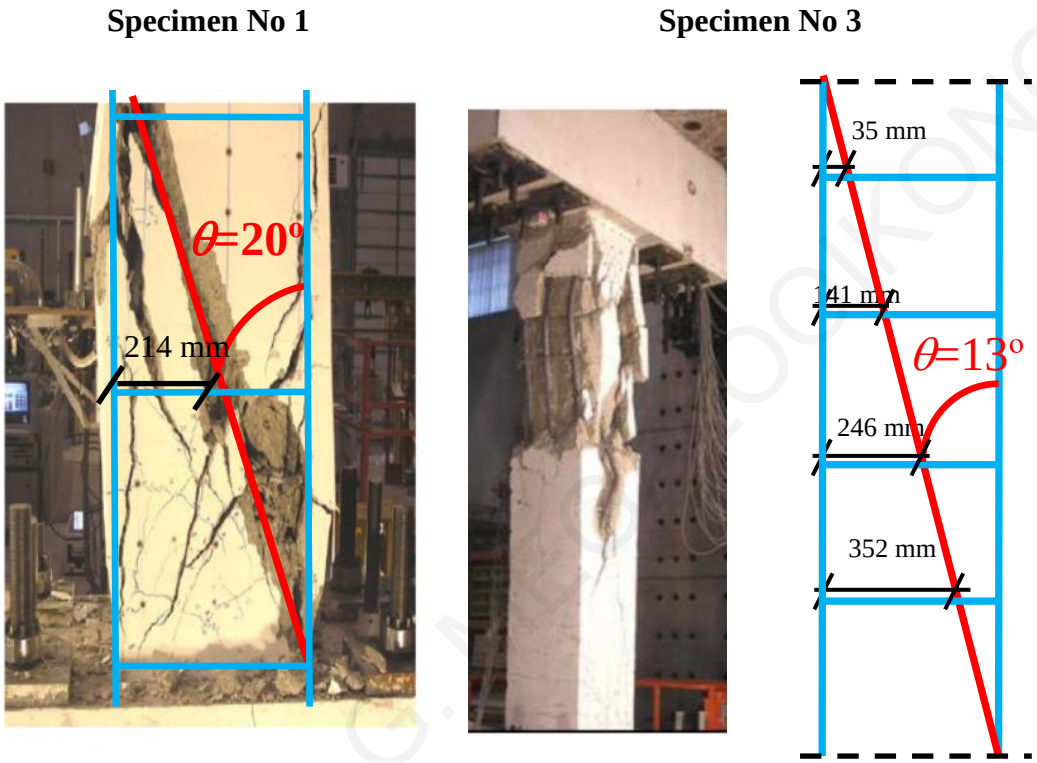

Figure 4.18: Truss geometry for typical lightly reinforced concrete columns (Experiments by Matamoros and Woods 2010).

An unresolved issue in calculations is the angle of inclination of the critical shear crack : a variety of tests (Fig. 4.18) demonstrate that the aspect ratio and the axial load ratio both affect the concrete and steel contributions in shear strength; whereas this effect is considered in all alternatives for the concrete contribution term, it is generally neglected both by the Code Models and by Mechanistic expressions for the steel contribution term, which is generally obtained from a 45° crack assumption. The value of the angle θ forming between the primary diagonal crack at tension failure with the longitudinal axis of the member, departs from the 45° postulate. Actually, this particular variable has a critical influence on the determined strength since the inclination of the major sliding plane (i.e. the angle θ) determines the number of stirrup layers mobilized in shear.

(d) Bar buckling considerations:

Bar buckling threatens members that do not fail prematurely, but experience extensive flexural yielding. The theoretical value of total column's rotation that is related to bar buckling can be expressed in terms of critical strain as follows:

$$\theta_{buck,u} = \theta_{sc,u}^{f} + \theta_{sc,u}^{s} = -\left[\varepsilon_{cc,u}/(c_u - d')\right] \cdot L_p + \frac{1}{3}\varphi_y \cdot \left(L_s - L_p\right) + \theta_{sc,u}^{s} \quad (4.6)$$

where $\varepsilon_{cc,u}$ is the concrete strain at the level of compressive reinforcement when it reaches the critical strain of buckling $\varepsilon_{sc,u}$ and $\theta_{sc,u}^{s}$ is the contribution to pull-out of the tensile reinforcement when the bar enters the critical instability conditions (Figs. 4.10, 4.14, 4.16). Here, for the definition of curvature the compressive strain of concrete and corresponding depth of the compression zone are used, instead of the tensile bar strain and the depth of the tension zone, since the bar strains are affected by slippage and the assumption of plane sections is not valid anymore.

The loading history is a crucial factor for the definition of ductility of rotation or displacement which is related to bar buckling initiation. Due to load reversal the bar reaches instability conditions under a compression stress but with significant residual tensile strain. The critical total strain ductility at buckling, is defined from the longitudinal reinforcing bar's critical buckling load (solution of the steel bar's stability differential equation) and can be obtained from pertinent interaction diagrams that depend on the bar's unsupported length to bar diameter ratio and the peak inelastic tension strain (envelope), attained by the reinforcement during previous displacement reversals. Therefore, under cyclic excitation, bar buckling will take place with the bar under compressive stress but with a high amount of residual tensile axial strain. This residual strain of the buckled bar is increasing (i.e. more tensile) as is increasing the value of maximum tensile strain that has been reached in the previous cycles.

4.4 Demonstration of Failure Prioritizing through an Example

A reinforced concrete column with rectangular cross section is under consideration in this example as depicted in Fig. 4.19. The column's axial load ratio is 0.2 and the material properties is C20 for concrete and S500 for steel longitudinal and transverse reinforcement. The concrete cover is 20 mm and the clear height of the column is 2.7m. The prioritizing of failures and the different deformation mechanisms that contribute to the final response are going to be demonstrated for two steps of relative lateral displacement. One is equal to 0.6%

and the other to 1.5% of the clear height accordingly. The goal is to determine the curvature in the critical section of the column along with the axial deformation of the longitudinal reinforcement.

For the first step of targeted displacement, the contribution deformation mechanisms are those of flexure, shear and that of the lap-splice:

$$\Delta_u = \Delta_u^{fl} + \Delta_u^{sh} + \Delta_u^{lap} = 0.006 \cdot 2700 = 16.2\ mm$$

Now the yielding displacement of the column is defined taking into account that is fully fixed at both ends:

$$\Delta_y = 2 \cdot \Delta_y^{fl} + 2 \cdot \Delta_y^{sh} + 2 \cdot \Delta_y^{lap}$$

The yielding displacement due to flexure is:

$$\Delta_y^{fl} = \frac{1}{3} \cdot \varphi_y \cdot L_s^2 = \frac{1}{3} \cdot \frac{\varepsilon_{sy}}{d - \xi d} L_s^2 = \frac{1}{3} \cdot \frac{500/200000}{(450 - 20) - 0.25 \cdot (450 - 20)} \cdot \left(\frac{2700}{2}\right)^2$$

$$\Delta_y^{fl} = \frac{1}{3} \cdot \frac{0.0025}{322.5} \cdot 1350^2 = 4.71\ mm$$

The yielding displacement due to shear is:

$$\Delta_y^{sh} = \frac{V_c}{G \cdot A_v} \cdot L_s = \frac{V_c}{0.4 \cdot E_c \cdot 0.8 \cdot A_g} \cdot L_s$$

The axial load of the column is:

$$N = v \cdot A_g \cdot f_c = 0.2 \cdot 350 \cdot 450 \cdot 20 = 630000\ N$$

The concrete contribution in shear strength is:

$$V_c = \left[\frac{0.5 \cdot \sqrt{f_c}}{L_s/d} \cdot \sqrt{1 + \frac{N}{0.5 \cdot A_g \cdot \sqrt{f_c}}}\right] \cdot 0.8 \cdot A_g$$

$$V_c = \left[\frac{0.5 \cdot \sqrt{20}}{1350/430} \cdot \sqrt{1 + \frac{630000}{0.5 \cdot 450 \cdot 350 \cdot \sqrt{20}}}\right] \cdot 0.8 \cdot 450 \cdot 350 = 149866\ N$$

So, the yielding displacement of the column considering the shear mechanism is:

$$\Delta_y^{sh} = \frac{149866}{0.4 \cdot (5700 \cdot \sqrt{20}) \cdot 0.8 \cdot 450 \cdot 350} \cdot 1350 = 0.16\ mm$$

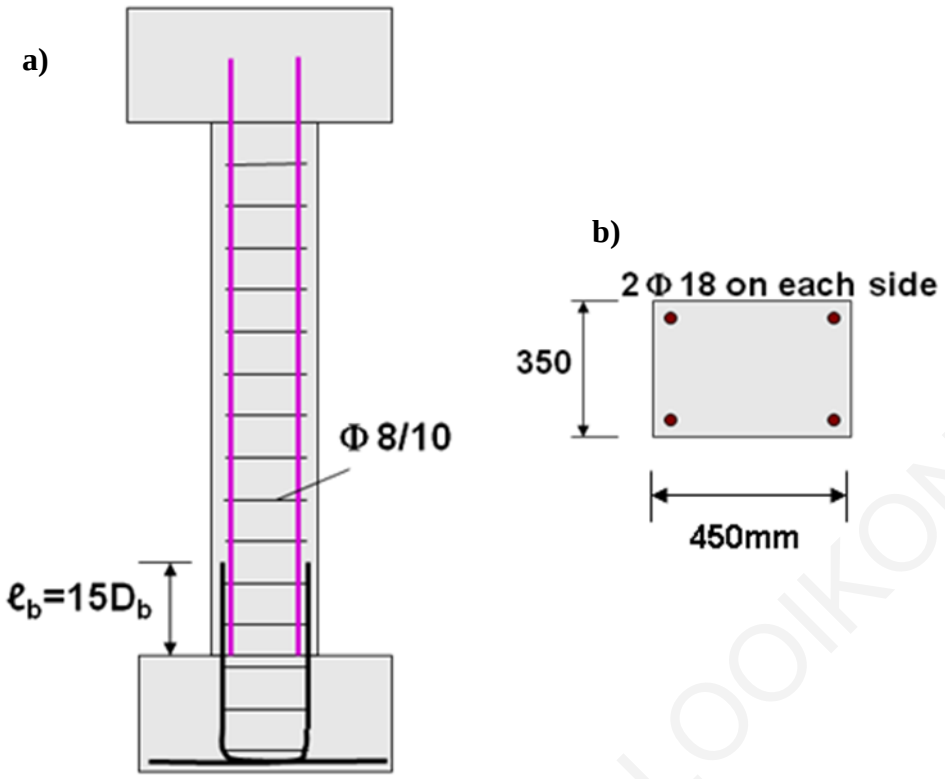

Figure 4.19: a) Example reinforced concrete column under consideration and b) column's rectangular cross section.

The contribution of lap splice in the total yielding displacement is (fib Bulletin No. 24 2003):

$$\Delta_y^{lap} = \frac{\varphi_y \cdot D_b}{8} \cdot \frac{f_y}{f_{b,y}} \cdot L_s = \frac{0.00000775 \cdot 18}{8} \cdot \frac{500}{2 \cdot 1.8 \cdot 1 \cdot \sqrt{\frac{20}{20}}} \cdot 1350 = 3.27\ mm$$

Therefore, the total yielding displacement of the column is:

$$\Delta_y = 2 \cdot \Delta_y^{fl} + 2 \cdot \Delta_y^{sh} + 2 \cdot \Delta_y^{lap} = 2 \cdot 4.71 + 2 \cdot 0.16 + 2 \cdot 3.27 = 16.28\ mm$$

From the calculation of the yielding displacement it may be seen that the applied displacement in the first step of loading is equal to the yielding limit. Therefore, the curvature of critical section of the column is equal to the yielding curvature and the axial deformation of the longitudinal reinforcement is equal to the yielding strain of steel reinforcement:

$$\varphi = \varphi_y = 0.00000775\ mm^{-1}$$

$$\varepsilon_{sy} = 0.0025$$

For the second step of loading, the applied displacement is:

$$\Delta_u = \Delta_u^{fl} + \Delta_u^{sh} + \Delta_u^{lap} = 0.015 \cdot 2700 = 40.5\ mm$$

This displacement is much larger than the yielding displacement, corresponding to a displacement ductility of:

$$\mu_{\Delta} = \frac{\Delta_u}{\Delta_y} = \frac{40.5}{16.28} = 2.5$$

$$\mu_{\Delta} = 2.5$$

An evaluation of the occurrence of brittle failures follows. The shear strength is (Chapter 2):

$$V_{shear} = V_c + V_w$$

The concrete contribution to shear strength according to the ASCE/SEI 41 (2007) is:

$$V_c = k(\mu_{\Delta}) \cdot \left[\frac{0.5 \cdot \sqrt{f_c}}{L_s/d} \cdot \sqrt{1 + \frac{N}{0.5 \cdot A_g \cdot \sqrt{f_c}}}\right] \cdot 0.8 \cdot A_g$$

$$V_c = (-0.1 \cdot 2.5 + 1.2) \cdot 149866 = 142372.7\ N$$

The steel contribution to shear strength according with the same code is:

$$V_w = k(\mu_{\Delta}) \cdot \left[\frac{A_{sw} \cdot f_{yh} \cdot d}{s}\right] = 205334{,}5\ N$$

$$V_{shear} = V_c + V_w = 142372.7 + 205334{,}5 = 347707.2\ N$$

However, as the column has a lap splice at the base, the above calculations should be considered provisional, since the strength of the column owing to the lap splice mechanism could prevail as the dominant mode of failure, thereby precluding the development of the post-yielding strength of the examined column. Therefore, according with Syntzirma and Pantazopoulou 2007, fib Bulletin No. 24 2003, the column shear that can be sustained at the attainment of the lap strength is defined from equilibrium according with:

$$V_{lap} = \frac{min\{F; N_b \cdot A_b \cdot f_y\} \cdot d \cdot (1 - 0.4 \cdot \xi) + N \cdot (0.5 \cdot h - 0.4 \cdot \xi \cdot d)}{L_s}$$

The minimum steel force developed over the lap-spliced zone tensile reinforcement is owing to frictional action (Pardalopoulos et al. 2011):

$$F = \mu_{fr} \cdot L_{lap} \cdot \left(\frac{A_{tr}}{s} \cdot f_{st}\right) = 1.5 \cdot 15 \cdot 18 \cdot \left(\frac{2 \cdot \frac{\pi \cdot 8^2}{4}}{100} \cdot 500\right) = 203575.2\ N$$

$$N_b \cdot A_b \cdot f_y = 2 \cdot \frac{\pi \cdot 18^2}{4} \cdot 500 = 254469\ N$$

Therefore:

$$V_{lap} = \frac{203575.2 \cdot 430 \cdot (1 - 0.4 \cdot 0.25) + 630000 \cdot (0.5 \cdot 450 - 0.4 \cdot 0.25 \cdot 430)}{1350} =$$

$$\boldsymbol{V_{lap} = 143291.56\ N}$$

The yielding flexural strength is:

$$\mathrm{V}_y^{fl} = \frac{M_y^{fl}}{L_s} = \frac{A_{s1} \cdot f_y \cdot 0.85 \cdot d + N \cdot (0.5 \cdot h - 0.4 \cdot \xi \cdot d)}{L_s}$$

$$\mathrm{V}_y^{fl} = \frac{2 \cdot \frac{\pi \cdot 18^2}{4} \cdot 500 \cdot 0.85 \cdot 430 + 630000 \cdot (0.5 \cdot 450 - 0.4 \cdot 0.25 \cdot 430)}{1350} =$$

$$\mathrm{V}_y^{fl} = 153828.5$$

Therefore, according to failure prioritizing the weakest link among the competing response mechanisms is actually the lap-splice development of the reinforcement. This finding suggests that the column failure will take place prior to yielding of longitudinal reinforcement due to failure in the lap splice.

The corresponding flexural moment at the critical section at the instant of estimated lap-splice failure is:

$$M_{lap} = 143291.56 \cdot 1350 = 193443602\ Nmm$$

The column's effective yielding stiffness is:

$$EI_y = \frac{\mathrm{V}_y^{fl} \cdot L_s}{\varphi_y} = \frac{207668421}{0.00000775} = 26795925329787.4\ Nmm^2$$

Therefore, the curvature of the critical section and the strain of the longitudinal reinforcement for this point are:

$$\varphi = \frac{M_{lap}}{EI_y} = \frac{193443602}{26795925329787.4} = 0.0000072\ mm^{-1}$$

$$\varphi = \frac{\varepsilon_s}{d - \xi d} => \varepsilon_s = 0.0000072 \cdot (430 - 0.25 \cdot 430) = 0.0023$$

Finally, the column's stiffness is:

$$k = \frac{12 \cdot EI_y}{h^3} = \frac{12 \cdot 26795925329787.4}{2700^3} = 16336.49\ N/mm$$

and the corresponding displacement at lap-splice failure is:

$$\Delta_{fail} = \frac{V_{lap}}{k} = \frac{143291.56}{16336.49} = 8.77mm$$

This displacement magnitude is less than half the estimated nominal yield displacement of the examined column.

4.5 Summary

The above example illustrates the complexity of the problem when considering substandard construction where basic detailing provisions (e.g. adequate development capacity of lap splices) cannot be guaranteed. Considering a column line, several modes of failure may occur, each one of them being associated with a different type of material failure; to enable prioritizing of these mechanisms so as to identify the one that controls (i.e. the one with the lowest strength), all mechanisms of resistance are expressed by the shear force in the column, at the instant of the material failure that characterizes each specific mechanism. For example, the column shear force that can be sustained at lap-splice failure is obtained from the moment developed in the lap zone, divided by the shear span (approximately half the column height). The flexural moment is obtained from the developed reinforcement force times the internal lever arm. The developed force is a function of the friction that can occur at the interface between the lapped bars, and the normal pressure exerted by the stirrup confinement in the lap zone. Similar procedures are established for all possible alternative mechanisms of resistance. Equation 4.2 illustrates the competition between alternative mechanisms to predominate the response of a column.

Calculation of the deformation capacity associated with the prevailing mechanism requires identification of the prevalent failure mode as pre-requisite. Deformation contributions are clearly not additive in this situation as is generally expected from classical mechanics. In order to find the limiting drift at failure, the effect of loading history, the fraction of drift ratio that is owing to pullout of longitudinal reinforcement from either its anchorage or shear span, and to shear deformations in the plastic hinge regions would need to be clearly defined. This task is the objective of the following two chapters.

5 Rotation Capacity due to Strain Penetration along Reinforcing Bars

5.1 Introduction

The deformation capacity of frame elements comprises contributions of flexural, shear and reinforcement pullout components. The estimation of the available deformation capacity of a column is linked to the length of plastic hinges. Following an implicit assumption that all terms are additive, the flexural component of lateral displacement is obtained from the sum of an elastic component, owing to the flexural deformation occurring along the length of the member, and a plastic component that is practically owing to the inelastic rotation that occurs in the small region near the face of the support where moments may exceed the yielding limit. When comparing these deformation estimates with the experimental evidence from predominantly flexural components, it is found that there is a great disparity between measured and estimated deformation capacities characterized by notable scatter (Syntzirma et al. 2010, Inel et al. 2004). Several attempts to identify the source of inaccuracy have motivated the progress made in that field, not the least the empirical expressions for deformation capacity which are included in EN 1998-3, 2005 that completely bypass the requirement of calculating the plastic hinge length. Another approach, initiated by Priestley et al. (1996) and then followed by several other researchers, and the approach to deformability by EN 1998-1, 2004 estimates the plastic hinge length including the length of yield penetration inside the anchorage (see, for example, the detailed analysis in the book by Priestley Seible and Calvi [1996], and of the fib Bulletin No.24 [2003]).

In new structural design with EN 1998-1 2004, the plastic hinge length is also used in reinforced concrete (RC) seismic detailing in order to determine the region where additional confinement requirements apply, this is apart from its use in seismic assessment to estimate the flexural deformation capacity. Due to its importance in these applications as the key to understanding deformability of members, the plastic hinge has been the subject of many experimental and analytical studies and the expressions derived have been quantified and calibrated against several hundreds of tests on isolated column specimens (Chapter 3). Still, the disconnect between observation and theory persists, and is considered a major roadblock in establishing the performance criteria for many special categories of members (e.g. walls, columns carrying a high axial load, very slender columns, etc.).

In the typical test, a cantilever column fixed at the base and carrying a constant axial load is driven to a protocol of reversed cyclic lateral load displacement history at the top (Chapter 3). Deformation capacity of such members is usually described by the chord rotation that may be sustained by the member prior to loss of its lateral load strength. Apart from the rotation due to flexural curvature that occurs along the length of the member, lumped rotation at the critical section resulting from inelastic strain penetration into the support (e.g. footing) as well as inside the shear span adds up in the reported drift ratios at different levels of performance. This share of deformation is attributed to reinforcement pullout due to the incompatible length change between the bar and the surrounding concrete.

In columns that do not fail by web crushing, pullout rotation increases gradually with imposed drift, claiming a predominant share of the members' deformation capacity near the ultimate limit state. Column deformation capacity at yielding and ultimate may be computed using a variety of models (Pantazopoulou 2003, Inel et. al. 2004, Pantazopoulou et. al. 2010, ASCE/SEI 41 2007, EN 1998-3 2005, Panagiotakos et. al. 2001, Biskinis et. al. 2013). A stick model is a common point of reference to this purpose: The length of the cantilever L_s corresponds to the shear span of an actual frame member under lateral sway; the aspect ratio of the member L_s/h quantifies the intensity of shear force demand in the member. Inelastic activity is assumed to occur within an equivalent "plastic hinge length", ℓ_{pl}, whereas the segment of the member outside ℓ_{pl} is assumed to behave elastically.

Displacements are calculated from flexural curvatures assuming the curvature distributions of Figs. 5.1(a-b), which correspond to development of yielding and post-yielding flexural strengths at the support. The plastic rotation $\theta_{pl}{}^{f}$ developing in the hinge due to flexure is $\theta_{pl}{}^{f}=(\phi_u-\phi_y)\cdot\ell_{pl}$; similarly, the plastic rotation owing to bar pullout from the support is $\theta_{pl}{}^{slip}=\theta_u{}^{slip}-\theta_y{}^{slip}$ (Fig. 5.1c); the total plastic rotation is $\theta_{pl}=\theta_{pl}{}^{f}+\theta_{pl}{}^{slip}$. The corresponding terms are (Fig. 5.1d):

$$\theta_y^{slip}=\frac{s_y}{(d-0.4x_c)}\Big|_{x=0} \quad ; \quad \theta_u^{slip}=\frac{s_u}{(d-0.4x_c)}\Big|_{x=0}$$
$$s_y\approx\varepsilon_y L_{b,min}/2 \quad ; \quad s_u\approx s_y+0.5\cdot(\varepsilon_u+\varepsilon_y)\cdot\lambda_{r,u} \quad ; \tag{5.1}$$
$$L_{b,min}=D_b\cdot f_y/(4f_b^{max}); \quad \lambda_{r,u}=L_b-L_{b,min}$$

where x_c is the depth of compression zone at the critical cross section (here it is assumed to remain constant after yielding) and L_b the total available anchorage length, whereas $L_{b,min}$ is the minimum required anchorage length to yield a typical bar (diameter: D_b), at a yield stress

f_y, considering a uniform bond stress equal to the bond strength of f_b^{max}. Rotation of the critical cross section occurs about the centroid of the compression zone (located at a distance $0.4x_c$ from the extreme compressed fiber based on the equivalent uniform stress block (Whitney 1937). Parameters s_y and s_u are values of reinforcement pullout slip from the support anchorage at yielding and ultimate. Term $\ell_{r,u}$ represents the maximum sustainable penetration of yielding into the anchorage; the maximum reinforcement strain, ε_u, that can be supported by the reinforcement at critical cross section may be estimated assuming that at the extreme, when the anchorage attains its ultimate development capacity the strain distribution along the anchored length is bilinear: $\varepsilon_u = \varepsilon_y + 4(L_b - L_{b,min}) f_b^{res} / (D_b E_{sh})$, where E_{sh} is the hardening modulus of steel. The corresponding maximum and yield flexural curvatures are defined as: $\phi_u = \varepsilon_u / (d - x_c)$ and $\phi_y = \varepsilon_y / (d - x_c)$, whereas the total plastic rotation capacity that may be sustained by the member may be estimated through reverse engineering as (Moehle 1992):

$$\theta_{pl}^{slip} \approx 0.5 \cdot (\varphi_u - \varphi_y) \cdot \lambda_{r,u} \;;\; \theta_{pl}^{f} = (\varphi_u - \varphi_y) \cdot \left(1 - \frac{M_y}{M_u}\right) \cdot L_s \;\Rightarrow$$
$$\theta_{pl} = (\varphi_u - \varphi_y) \cdot \underbrace{0.5 \cdot \lambda_{r,u}}_{(i)} + \underbrace{\alpha \cdot L_s}_{(ii)} \qquad (5.2a)$$

where in Eq. (5.2a) index *(i)* denotes pullout from support and *(ii)* flexure in the shear span. Introducing the concept of the plastic hinge length ℓ_{pl} the plastic rotation capacity is written as:

$$\theta_{pl} \approx (\varphi_u - \varphi_y) \cdot \lambda_{pl} = \phi_{pl} \cdot \lambda_{pl} \quad ; \quad \lambda_{pl} = 0.5 \cdot \lambda_{r,u} + \alpha \cdot L_s \qquad (5.2b)$$

In Eq. (5.2b) α is the strain-hardening ratio of the reinforcement. Empirical equations for the plastic hinge which have prevailed in design Codes (EN 1998-1 2004, EN 1998-3 2005) and in research (Pantazopoulou 2003, Priestley et. al. 1984, Priestley et. al. 1987, Priestley et. al. 1996, Lehman et. al. 1996, Bae, S. et. al. 2008) have the form of Eq. (5.2b):

$$\lambda_{pl} = 0.08 L_s + 0.022 \cdot D_b \cdot f_y \quad ; \quad \lambda_{pl} = 0.1 L_s + 0.17 \cdot h + 0.24 \cdot D_b \cdot f_y / \sqrt{f_c'} \qquad (5.3a)$$

with h being the column sectional depth. (For example, 0.08 and 0.1 are common values for the strain hardening ratio α of common reinforcement, whereas the term proportional to the bar diameter D_b, which represents the strain penetration length within the anchorage, is intended for well-designed anchorages that can easily support strain penetration lengths of $10 \sim 20 \cdot D_b$). The required confined length ℓ_c is obtained from the basic value of ℓ_{pl} by adding

terms to account for the tension shift in the shear span of a member and the increased demands for confinement under high axial loads (Watson et. al. 1994), (γ_c in Eq. (5.3b) is a strength –reduction factor):

$$\lambda_c = \lambda_{pl} + 0.5h \quad ; \quad \frac{\lambda_c}{h} = 1 + 2.8 \cdot \frac{N}{\gamma_c \cdot f_c' A_g} \tag{5.3b}$$

Bae and Bayrak (2008) proposed an alternative expression of ℓ_{pl}, derived from correlation with column experiments under various axial load levels, recognizing explicitly the important variables that control ℓ_{pl}:

$$\frac{\lambda_{pl}}{h} = \left[0.3 \cdot \left(\frac{N}{N_o} \right) + 3 \cdot \left(\frac{A_s}{A_g} \right) - 0.1 \right] \cdot \left(\frac{L_s}{h} \right) + 0.25 \geq 0.25 \tag{5.3c}$$

where h is the column depth, N is the applied axial load, $N_o = 0.85 f_c'(A_g - A_{s,tot}) + f_y A_{s,tot}$, ($f_c'$ is the concrete compressive strength), A_s is the area of tension reinforcement, $A_{s,tot}$ is the total reinforcement area, and A_g the gross area of concrete section.

A significant limitation of the theoretical definition of ℓ_{pl}, as given by Eq. (5.2a), is that it breaks down if the moment-curvature response of the member is elastic – perfectly plastic (a=0), leading to a rather small plastic hinge length. This is counter-intuitive when considering that a necessary accessory to rebar yielding is the localized loss of bond. Thus point-yielding of column reinforcement with no penetration to adjacent areas is physically impossible. In practical applications, to resolve the indeterminacy caused in Eq. (5.2a) due to elastoplasticity (i.e., $M_y = M_u$), ℓ_{pl} is taken as $0.5h$, or Eq. (5.3a) is used directly without reference to the underlying physical model. The apparent inconsistency inherent in the theoretical definition of ℓ_{pl} is partly responsible for the poor correlation of the estimated deformation capacity of flexure-dominated columns with results from experimental databases (Syntzirma et. al. 2007, 2010). An alternative is to explicitly solve for the plastic hinge length by establishing and solving the field equations of bond along the principal reinforcement (in the shear span) of the deformed member under lateral sway, with particular emphasis on the part of the reinforcement that is strained beyond the limit of yielding into the hardening range. This modelling approach is pursued in the present chapter. A unidirectional model of bond is considered as a basis for the evaluation of the longitudinal strain distribution of the primary reinforcement of the column.

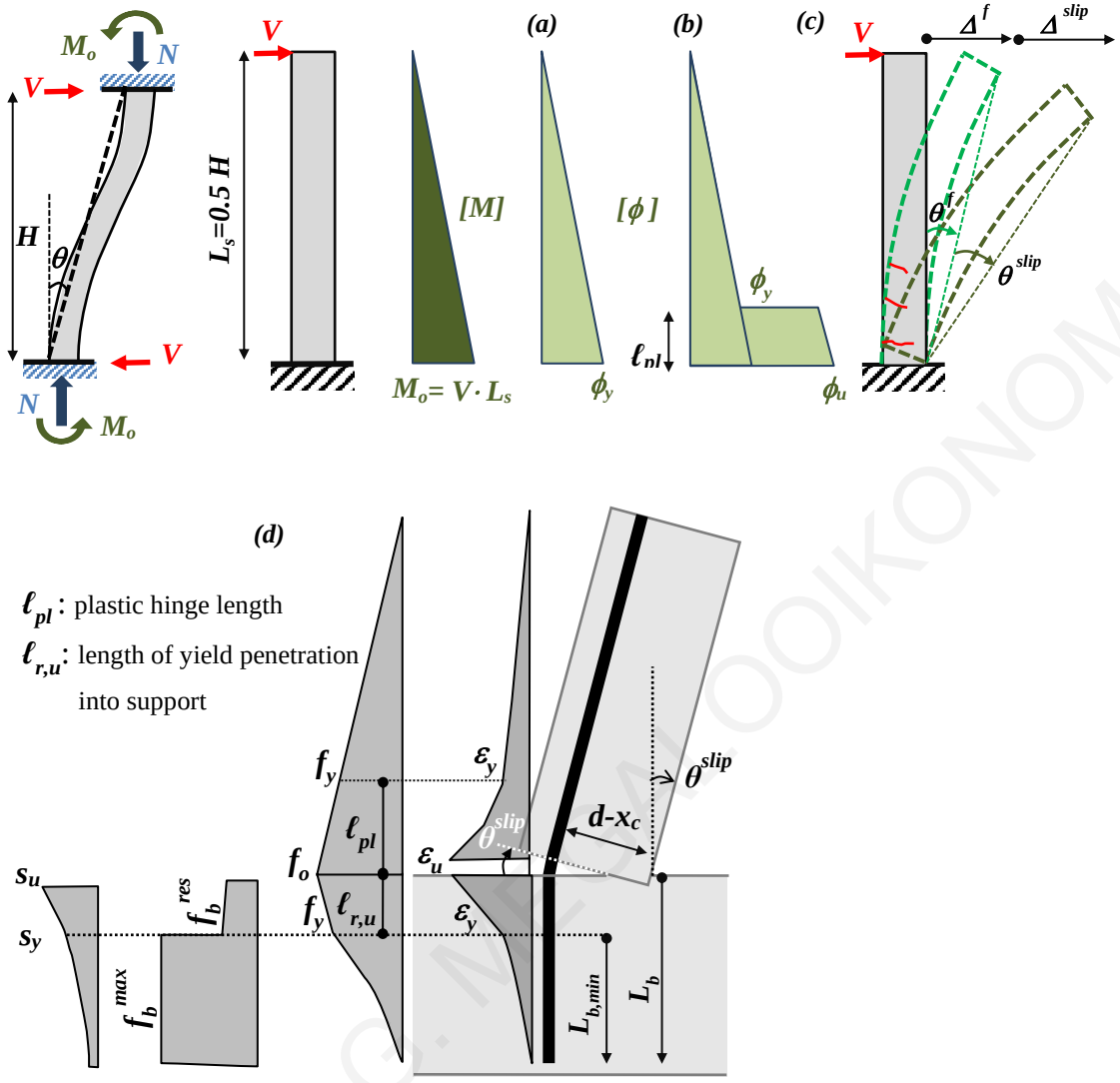

Figure 5.1: Distributions of curvature along the column shear span a) at yielding moment M_y and b) at flexural strength M_u attained at fixed support (M_u>M_y). c) Drift components from curvature along shear span, and from anchorage slip. d) Bar state of stress (& strain) and bond (& slip) along shear span and anchorage.

The processes of sequential crack formation due to tension stiffening, and the subsequent crack opening are explicitly considered. In the analysis, large localized slip magnitudes lead to bond degradation that is accompanied by spread of inelastic strains both in the shear span and in the anchorage. Strain distributions in the span and in the bar anchorage are evaluated using a step by step calculation algorithm; controlling variable is the tension strain magnitude at the critical cross section (support of the cantilever). Through this process disturbed regions are identified in the shear span, where bar strains are controlled by bond development rather than the "plane-sections" assumption. Using this approach, the parametric sensitivities of the plastic hinge length are illustrated and compared with the other

alternatives summarized in the preceding obtained from experimental calibration. Application of the analytical procedure for estimating the plastic hinge length is demonstrated through comparison with column specimens tested under axial load and reversed cyclic lateral drift histories reported in the literature.

5.2 Governing Equations of Bond – Slip Behavior in Concrete

The basic equations that describe force transfer lengthwise from a bar to the surrounding concrete cover through bond are derived from force equilibrium established on an elementary bar segment of length *dx* (Tassios et. al. 1981, Filippou et.al. 1983):

$$df/dx = \left(-4/D_b\right)\cdot f_b \tag{5.4a}$$

where f is the axial stress of the bar; D_b is the bar diameter; f_b is the local bond stress. Furthermore, compatibility between the relative translation of the bar with respect to the surrounding concrete, (s=slip), the axial bar strain ε, and concrete strain ε_c over dx requires that (Tassios et. al. 1981, Filippou et. al. 1983):

$$ds/dx = -\left(\varepsilon - \varepsilon_c\right) \cong \varepsilon \tag{5.4b}$$

For normal concrete, term ε_c is neglected as its tensile value cannot exceed the cracking limit ($\varepsilon_{c,cr} \approx 0.00015$) which is well below the other terms of Eq. (5.4b). Bond stress and slip, and bar stress and strain are related through the material constitutive relationships, $f_b = f_b(s)$ and $f = f(\varepsilon)$. Solution of Eqs. (5.4) is possible though exact integration, resulting in closed-form solutions for the state of stress and strain along the anchorage, through pertinent selection of simple models for the material laws (e.g. piecewise linear relations). This approach has a clear advantage over the numerical solution alternative in that it enables transparent insight into the role of the various design parameters on the behavior of bar

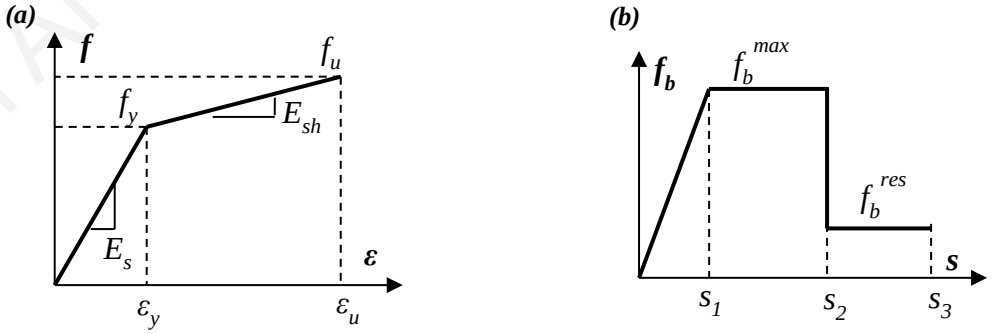

Figure 5.2: (a) Assumed stress-strain law of steel reinforcing bar; (b) Assumed local and average bond slip law.

anchorages and/or lap splices.

Here the reinforcing bar stress-strain relationship is considered elastoplastic with hardening (representing conventional steel reinforcement, Fig. 5.2a). Without loss of generality, and to facilitate derivation of closed-form solutions, a linear elastic, perfectly plastic local bond-slip relationship with residual bond is assumed (Fig. 5.2b). The plateau in the local bond-slip law implies sustained bond strength. This feature is not always manifested in the test data; to be measured it requires redundancy in the anchorage (i.e., availability of longer anchorages to enable force redistribution towards the healthy part of the anchorage before failure). In the assumed law the end of the plateau is marked by abrupt loss of bond strength to the residual value f_b^{res}. (Note that f_b^{res} is taken nonzero only in the case of ribbed steel bars, but not for smooth steel bars.) The last branch represents the residual friction between the concrete cover and the steel bar after failure of the rib interlocking mechanism (Fig. 5.2b).

Strain penetration occurs in the bars beyond the critical section due to the degradation of bond beyond slip limit s_2, that marks the end of the plateau in the local bond-slip law. This stage may be attained in different ways along a bar: (a) for yielding to occur, i.e. constant bar stress ($=f_y$, $df/dx=0$) for a range of values of bar strain $\varepsilon>\varepsilon_y$, bond should be eliminated ($f_b^{res} = 0$); if f_b^{res} is nonzero, then a yielded bar will demonstrate a commensurate amount of strain hardening. (b) If the bar is elastic (e.g. FRP bar), then for large strain levels bar slip values are increased to levels beyond s_2 (Fig. 5.2b): this is marked by debonding and cover splitting of the loaded end of anchorage thereby limiting the development capacity of the reinforcement.

Strain penetration of yielding over a bar anchorage has received some attention, especially with regards to its contribution to rotation capacity of structural members (Bonacci et. al. 1994, Bigaj 1999, Tastani et. al. 2013). But the implications resulting from spreading of inelastic strains in the shear span of a structural member on the development capacity of reinforcement and on member behavior have not yet been described with reference to the mechanics of bond.

Consider a reinforcing bar that spans the deformable length of a structural column, anchored in its footing. An important difference may be traced in the state of stress occurring in the two regions along the bar: within the anchorage stress is controlled by the mechanics of bond, as described by the field equations (Eqs. 5.4). On the other hand, within the shear

span, it is the prevailing notion that bar stress is controlled by flexural theory; i.e. the requirement of plane sections remaining plane at any cross section relates bar strains to flexural moment and axial load through cross sectional equilibrium. This however can be incompatible with the requirements of Equations (5.4). The concept of tension stiffening is used in order to settle this potential conflict between the two antagonistic mechanisms for control of reinforcement strains: a certain nontrivial length ℓ_{Do} is needed, measured from the face of the crack toward the uncracked part of the member until bar strain compatibility with the surrounding concrete cover may be claimed. Thus, the field equations of bond control the segment ℓ_{Do}, whereas the classical theory of bending controls the remaining length. The region over the shear span of a flexural member where bar stresses are controlled by the mechanics of bond (Eqs. 5.4) rather than the mechanics of flexure, is referred to hereon as a "disturbed" region, thereby assigning to this length an alternative interpretation from that used to explain shear dominated response in frame members (MacGregor et. al. 2005). At the same time this alternative significance of the disturbed region underscores the interaction between bond and shear strength (Martin-Pérez et. al. 2001). Clearly, as crack propagates the disturbed zone extends and may spread over the entire length of the member.

5.3 Bond-Slip Distribution along the Anchorage

5.3.1 Bond-Slip Distribution along the Anchorage of a Linear Elastic Bar

Solution of Eq. 5.4 for elastic bars in the anchorage is given in this section; this is valid for the ascending branch of the stress-strain law of steel reinforcing bars, i.e. $\varepsilon \leq \varepsilon_y$. In the case of Fig. 5.3 (a) for the elastic part of the bond slip (i.e., when $s \leq s_1$, bond is linearly related to slip according with: $f_b = (f_b^{max}/s_1) \cdot s$. By substitution in Eqn. (5.4) the differential equation may be solved in closed form. Thus, bar normal strain, slip, and bond stress distributions over the available length of the anchorage [$0 \leq x \leq L_b$] are given by the following equations (Tastani and Pantazopoulou 2013):

$$\varepsilon(x) = \frac{\varepsilon_o}{1-e^{-2\omega L_b}}(e^{-\omega x} - e^{-\omega x - 2\omega L_b}) \leq \varepsilon_y \tag{5.5}$$

$$s(x) = \frac{\varepsilon_o}{\omega(1-e^{-2\omega L_b})}(e^{-\omega x} + e^{\omega x - 2\omega L_b}) \leq s_1 \tag{5.6}$$

$$f_b(x) = (f_b^{max}/s_1) \cdot s(x) \leq f_b^{max} \tag{5.7}$$

where the characteristic property ω is given by : $\omega = [4f_b^{max}/(E_s \cdot D_b \cdot s_1)]^{0.5}$. The variable ε_o is the bar axial strain at the loaded end of the anchorage, and E_s is the modulus of elasticity of the bar in the longitudinal direction. By substituting $x = L_b$ in Eq. 5.6, a nonzero slip value is obtained at the free end of the anchorage $\{i.e,\ s_f = 2\varepsilon_o e^{-\omega L_b}/[\omega(1-e^{-2\omega L_b})] \neq 0\}$ even under very small loads. This finding is consistent with the experimental observations (see for example Tastani 2005).

The bar axial strain at the loaded end, $\varepsilon_o = \varepsilon_{el}^i$, is the limit value beyond which the bond mechanism enters the state of plastification (i.e. yielding of bond) over a length l_p which grows with increasing bar strain at the loaded end, while the bar remains elastic. Therefore the variable ε_{el}^i is directly related to the slip magnitude s_1 in Fig. 5.2 and may be calculated by Eq. 5.6 after substitution of $s(x=0) = s_1$ as follows:

$$\varepsilon_{el}^i = s_1 \omega \frac{1-e^{-2\omega L_b}}{1+e^{-2\omega L_b}} \tag{5.8}$$

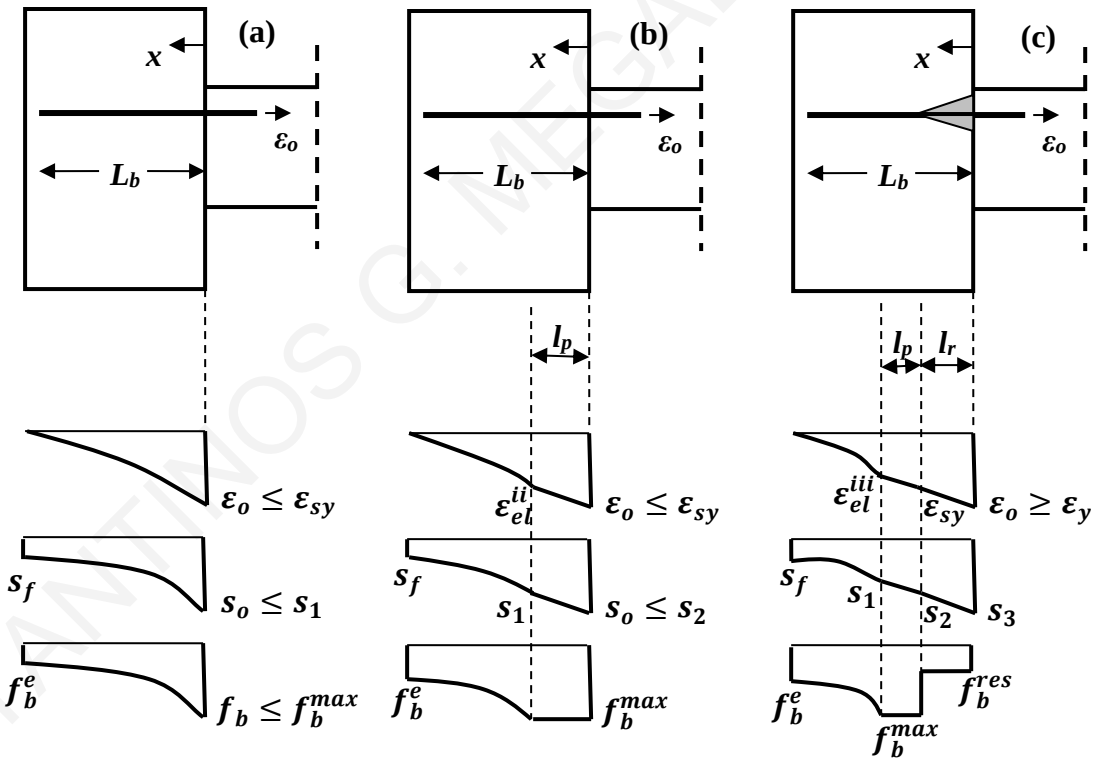

Figure 5.3: (a) Elastic bar response while bond-slip law remains elastic ; (b) Elastic bar response with bond plastification ; (c) plastic (yielded) bar response with bond plastification.

In case the available bond length is sufficient or if transverse confinement acts normal to the contact surface thereby generating secondary strength reserves for the bond

mechanism, then the bar may sustain a strain value higher than ε_{el}^{i} [Fig. 5.3 (b)]. In that case, the maximum bond stress may reach the characteristic strength value f_b^{max}, over a length of bond plastification l_p. The complete solution of Eq. 5.4 over L_b (starting from the loaded end and proceeding toward the end of the anchorage) comprises two segments as follows.

(a) Distributions of bar strain, slip and bond stress over the length l_p (for $0 \le x \le l_p$) are obtained considering that $f_b(s)=f_b^{max}$ = constant (thus the bar stress and strain varies as a linear function of distance over the segment l_p where bond is plastified:

$$\varepsilon(x) = \varepsilon_o - \frac{4 f_b^{\max}}{E_s \cdot D_b} \cdot x \tag{5.9}$$

$$s(x) = s_1 + 0.5\left(l_p - x\right)\left[\varepsilon(x) + \varepsilon_{el}^{ii}\right] \tag{5.10}$$

$$f_b(x) = f_b^{max} \tag{5.11}$$

where, ε_{el}^{ii} is the attenuated value of the bar strain as compared with the ε_o value which occurs at the loaded end. Note that ε_{el}^{ii} now occurs at the end of the bond plastification region, l_p:

$$\varepsilon_{el}^{ii} = \varepsilon_o - \frac{4 f_b^{\max}}{E_s \cdot D_b} \cdot l_p \tag{5.12}$$

For the distributions of bar strain, slip and bond stress over the remaining anchorage length (which is still in the elastic range), $L_b - l_p$ (for $l_p \le x \le L_b$), these are obtained from the elastic solution Eq. 5.5-5.7 :

$$\varepsilon(x) = \frac{\varepsilon_{el}^{ii}}{1-e^{-2\omega\left(L_b-l_p\right)}}\left(e^{-\omega\left(x-l_p\right)} - e^{\omega\left(x-l_p\right)-2\omega\left(L_b-l_p\right)}\right) \tag{5.13}$$

$$s(x) = \frac{\varepsilon_{el}^{ii}}{\omega\left(1-e^{-2\omega\left(L_b-l_p\right)}\right)}\left(e^{-\omega\left(x-l_p\right)} + e^{\omega\left(x-l_p\right)-2\omega\left(L_b-l_p\right)}\right) \tag{5.14}$$

$$f_b(x) = \left(f_b^{max}/s_1\right) \cdot s(x) \le f_b^{max} \tag{5.15}$$

The length of plastification l_p, is estimated if continuity of strain and slip are enforced at $x = l_p$.

5.3.2 Bond-Slip Distribution along the Anchorage of an Elastoplastic Bar

Solution of Eq. 5.4 for an elastoplastic steel bar is explored only after yielding, because the preceding section fully describes the bar's elastic behavior. The bar strain at the onset of

yielding is denoted by ε_{sy} whereas E_{sh} is the strain hardening modulus of the stress-strain relationship in the postyielding regime.

The last case examined in the present model is depicted in Fig. 5.3c and it concerns yield penetration (spread of strains beyond yielding) in the steel bar inside the anchorage with simultaneous plastification of bond. The length of yield penetration is denoted by l_r. In the segment $(0, l_r)$, the bond stress is equal to f_b^{res}. Also, the distribution of strains is linear, ranging from $\varepsilon(x=0)=\varepsilon_o$ at the loaded end, to the value $\varepsilon(x=l_r)=\varepsilon_{sy}$ at the end of the yielded region (Fig. 5.3c). Slip at each point is obtained from integration of strains from the point considered to the unloaded end of the anchorage.

The strain, slip, and bond stress expressions governing this problem in the three distinct regions are given as follows. Over the debonded length l_r (for $0 \le x \le l_r$) (Eq. 5.16 is obtained from Eq. 5.4 for a constant bond stress f_b^{res}):

$$\varepsilon(x) = \varepsilon_o - \frac{4 f_b^{res}}{E_{sh} D_b} x \tag{5.16}$$

$$s(x) = s_2 + 0.5(l_r - x)\left[\varepsilon(x) + \varepsilon_y\right] \tag{5.17}$$

$$f_b(x) = f_b^{res} \tag{5.18}$$

Over the length l_p where bond has exceeded the plasticity limit (for $l_r \le x \le l_r + l_p$):

$$\varepsilon(x) = \varepsilon_y - \frac{4 f_b^{\max}}{E_s D_b}(x - l_r) \tag{5.19}$$

$$s(x) = s_1 + 0.5\left(l_r + l_p - x\right)\left[\varepsilon(x) + \varepsilon_{el}^{iii}\right] \tag{5.20}$$

$$f_b(x) = f_b^{max} \tag{5.21}$$

Over the remaining bonded length $L_b - l_r - l_p$ (for $l_r + l_p \le x \le L_b$):

$$\varepsilon(x) = \frac{\varepsilon_{el}^{iii}}{1 - e^{-2\omega(L_b - l_p - l_r)}}\left(e^{-\omega(x - l_p - l_r)} - e^{\omega(x - l_p - l_r) - 2\omega(L_b - l_p - l_r)}\right) \tag{5.22}$$

$$s(x) = \frac{\varepsilon_{el}^{iii}}{\omega\left(1 - e^{-2\omega(L_b - l_p - l_r)}\right)}\left(e^{-\omega(x - l_p - l_r)} + e^{\omega(x - l_p - l_r) - 2\omega(L_b - l_p - l_r)}\right) \tag{5.23}$$

where, according with the linear ascending branch of the bond-slip law, it is:

$$f_b(x) = (f_b^{max}/s_1) \cdot s(x) \le f_b^{max} \tag{5.24}$$

In Equation (5.22) term ε_{el}^{iii} is the strain at $x = l_r + l_p$, i.e., the point of transition from elastic to plastic bond stress (Fig. 5.3c) and it is calculated from Equation 5.19.

Thus, yield penetration occurs over the segment l_r of the anchorage where strain exceeds ε_{sy}; this phenomenon is accompanied by a sudden increase of slip (Eq. 5.17) with a commensurate reduction of bond strength to f_b^{res} over the yielded bar length.

5.4 Disturbed Region on Shear Span of a Flexural Member

It was mentioned earlier that spread of inelastic strains occurs on both sides of a critical section (*e.g.* at the base of a column). The process of inelastic strain penetration in the anchorage of a reinforcing bar has been demonstrated in the previous section. This section is dedicated to solving the same problem in the other side of the critical section, that is, over the disturbed region along the shear span of a column. Here the problem is different from that of the anchorage in the type of boundary conditions that may be enforced for the governing differential equation, Eqs. (5.4). The bond-slip law has the same multilinear envelope as in the case of an anchorage, however the bond strength value, f_b^{max}, is a function of the available transverse reinforcement.

5.4.1 Evaluation of Disturbed Length on Crack Initiation

For the stage prior to the occurrence of cracking along the length of the flexural member, the bar strain is estimated from the flexural analysis of the uncracked column cross section (*i.e.* from the moment-curvature analysis, Fig. 5.4a):

$$\varepsilon_{fl}(x) = \phi(x) \cdot y_{s,na}^{gr} \tag{5.25a}$$

This is expressed explicitly as:

$$\varepsilon_{fl} = \frac{M(x)}{E_c \cdot I_g} \cdot y_{cg} - \frac{N}{E_c A_g} \quad ; \quad y_{cg} = \frac{h}{2} - C_{cov} - 0.5D_b \quad ; \quad y_{s,na}^{gr} = y_{cg} - \frac{N}{M} \cdot \frac{I_g}{A_g} \tag{5.25b}$$

where $M(x)$, N (+ for compression) and $\varphi(x)$ are the flexural moment, axial load and flexural curvature acting on the member section at distance x from the support, E_c is the elastic modulus of concrete, I_g and A_g are the moment of inertia and the uncracked cross section area, h is the section height and C_{cov} is the clear cover (Fig. 5.4a). Parameters $y_{c,g}$ and $y_{s,na}^{gr}$ are the distances of the centroid of tension reinforcement to the centroid of the uncracked cross-section and to the neutral axis location, respectively (Fig. 5.4a). The distance to the

neutral axis changes significantly from the initial linear elastic state $y_{s,na}^{gr}$, to the cracked state of a cross section, $y_{s,na}^{cr}$. Generally, the position of the neutral axis may be estimated from equilibrium requirements, both in the uncracked cross sections as well as at the crack locations assuming "plane sections remain plane". From the flexural analysis perspective, when the flexural moment $M(x)$ exceeds the cracking moment, M_{cr}, even by a small amount, then the member may be considered cracked in the neighborhood of x. Although a large region may satisfy this definition, however, cracks occur at discrete locations $x_{cr,i}$. Thus, if an analysis of the cracked cross section is available, the tension reinforcement strains $\varepsilon(x_{cr,i})$ that occur in the crack locations may be calculated from:

$$\varepsilon\left(x_{cr,i}\right)=\varphi\left(x_{cr,i}\right)\cdot y_{s,na}^{cr} \tag{5.26}$$

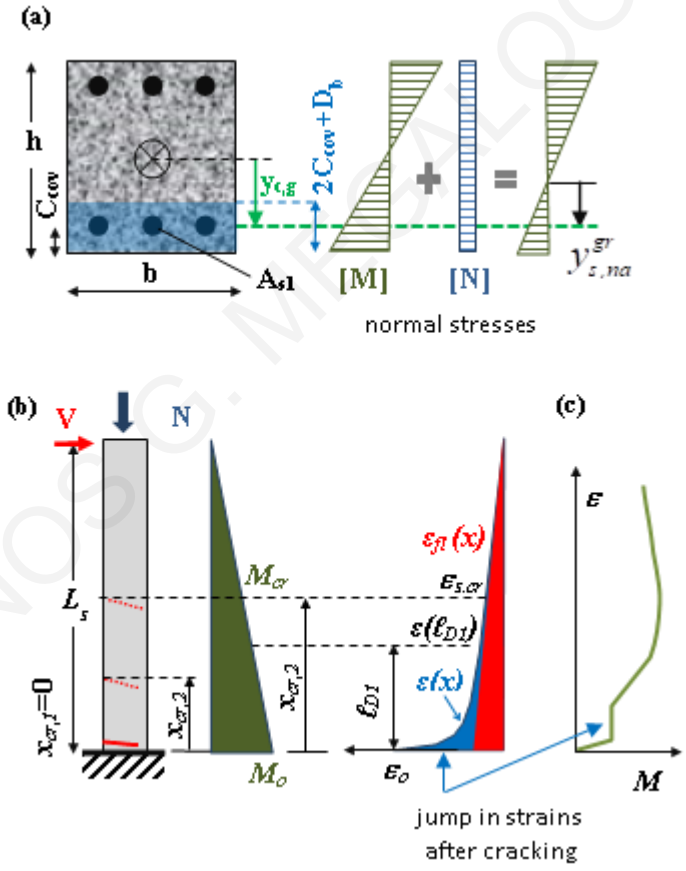

Figure 5.4: Definition of terms: a) Cross sectional flexural analysis. b) Bar strain distribution along the shear span L_s: stage prior to cracking (red); response into the disturbed region ℓ_{D1} (blue). c) Moment - bar strain diagram.

In the segment between successive cracks where moment exceeds the cracking value, bar strains cannot be estimated from flexural analysis as prescribed by Eq. (5.26). Owing to reinforcement slip, the degree of strain compatibility between steel and concrete in these

locations is not well understood, as would be required by the "plane-sections remain plane" assumption, nor can the concrete be considered inert as would happen in a fully cracked tension zone. Because it takes some distance from a crack location before the reinforcement may fully engage its concrete cover in tension again so as to satisfy the conditions of strain compatibility, Eq. (5.26) is invalid even in the region immediately adjacent to the last flexural crack in the shear span, although the flexural moment is below the cracking limit in that region. Bar strain over cracked segments of the member may be estimated from solution of Eq. (5.4). To address all the possible exceptions to the validity of the flexural requirement stated by Eqs. (5.25,5.26), here the term "undisturbed" is used as a qualifier to "un-cracked" in order to refer to sections that also satisfy "the plane sections remaining plane" compatibility requirement. As a corollary, where strains are obtained from solution of the bond equation, the region is "disturbed".

The flexural moment at a distance x from the face of the support is estimated with reference to the flexural moment at the support, M_o (ε_o is the bar tension strain, at $x=0$, Fig. 5.4b):

$$M(x) = M_0 \cdot (1 - x/L_s) \tag{5.27}$$

As the sequence of crack formation is critical for the occurrence of disturbed regions and for the problem of strain penetration that will be subsequently addressed, in the present discussion the static problem represented by Eq. (5.27) will be solved for a gradually increasing value of the support moment, M_o. It is assumed that the characteristic flexural resistance curve (moment-curvature) of any cross section along the shear span (i.e. the moment – curvature and moment – bar strain diagram) is available from classical flexural analysis (plane-sections) for the entire range of response.

For a member with continuous primary reinforcement over the shear span, L_s, the moment distribution that follows Eq. (5.27) will cause first cracking at the face of the support ($x_{cr,1}$=0, Fig. 5.4b). Upon cracking of the tension zone the bar strain experiences a significant jump to maintain equilibrium (Fig. 5.4c). For example, if the cracked section stiffness is about 1/3 of the uncracked value, the bar strain at the critical section is expected to increase threefold by the mere occurrence of the crack even though the moment change from the uncracked to the cracked stage may be imperceptible. Thus suddenly the whole region adjacent to the cracked location becomes "disturbed". Over the length of the disturbed region, ℓ_{D1} (Fig. 5.4b) the reinforcement strain is described by the solution of the bond

equation (Tastani et. al. 2013) i.e.:

$$\varepsilon(x) = C_1 \cdot e^{-\omega x} + C_2 \cdot e^{\omega x}\ ,\ \text{where,}\ \omega = [4f_b^{max}/(E_s \cdot D_b \cdot s_1)]^{0.5} \qquad (5.28)$$

The solution of Eq. (5.28) is valid provided bond is in the elastic range (ascending branch in the bond slip law, Fig. 5.2b). Before the creation of a second crack, the following conditions characterize the end of the disturbed region at $x= \ell_{D1}$:

a) the slope of the bar strain distribution, $\psi=d\varepsilon(x)/dx$, obtained from differentiation of Eq. (5.28), matches that of the strain diagram as would be obtained from Eq. (5.25b):

$$\psi = d\varepsilon(x)/dx = \omega \cdot \left(-C_1 \cdot e^{-\omega \ell_{D1}} + C_2 \cdot e^{\omega \ell_{D1}}\right) = -\left[\underbrace{\left(M_0 \cdot y_{cg}\right)/E_c I_g}_{\varepsilon_{el}^o}\right] \cdot 1/L_s \qquad (5.29a)$$

b) the bar strain $\varepsilon(\ell_{D1})$ satisfies both Equations (5.25b), and (5.28):

$$\varepsilon(\ell_{D1}) = C_1 \cdot e^{-\omega \ell_{D1}} + C_2 \cdot e^{\omega \ell_{D1}} = \varepsilon_{el}^o \cdot (1 - \ell_{D1}/L_s) - N/\left(E_c \cdot A_g\right) \qquad (5.29b)$$

Given the axial load N and the bar strain at the support $\varepsilon(x=0)=\varepsilon_o$ the corresponding moment M_o is obtained from the moment-curvature analysis of the cracked section. A boundary condition of Eq. (5.28) is:

$$\varepsilon(0) = C_1 + C_2 = \varepsilon_o \qquad (5.29c)$$

Unknowns of the system of Eqs. (5.29) are, the disturbed length ℓ_{D1} (Fig. 5.4b), and the coefficients C_1 and C_2. In an algorithm developed to solve Eqs. (5.29) numerically, the controlling parameter is ε_o; required input includes the axial load, N, shear span L_s, the bond-slip characteristic property ω (Eq. 5.28), and the member material and cross-sectional properties. Coefficients C_1, C_2 are obtained from (5.29b) and (5.29c):

$$C_{1,2} = 0.5 \cdot e^{\beta \cdot \omega \ell_{D1}} \left[\varepsilon_{el}^o \cdot \left(1 - \frac{\ell_{D1}}{L_s} + \frac{\beta}{\omega L_s}\right) - N/\left(E_c \cdot A_g\right)\right]$$

where $\beta=1$ for C_1, and $\beta= -1$ for C_2 (5.30)

The value of ℓ_{D1} is determined by solving Eq. (5.29a) after substitution of C_1, C_2.

5.4.2 Formation of Additional Flexural Cracks in the Shear Span

Increasing the reinforcement strain value at the critical section, ε_o, corresponds to a higher flexural moment M_o at the support. Based on Eq. (5.27), the flexural moments exceed the cracking moment up to a distance x_{cr} from the support: $x_{cr} = L_s \cdot \left(1 - M_{cr}/M_o\right)$. But the position of the next crack is not necessarily at x_{cr}; rather, it is controlled by tension stiffening

of the reinforcement.

(a) To determine if the next crack forms within ℓ_{D1}, (Fig. 5.4b) the force transferred through bond to the concrete cover (*i.e.* $E_s A_{s1}[\varepsilon_o - \varepsilon(x)]$) is compared with the tensile resistance of the effective area of concrete cover engaged in tension (*i.e.* $f_{ct} A_{c.eff}$, EN 1992-1-1 2004)

$$\left[(E_s \cdot A_{s1})/(f_{ct} \cdot A_{c.eff})\right] \cdot [\varepsilon_o - \varepsilon(x)] \geq 1, \quad A_{c.eff} = b \cdot (2C_{cov} + D_b) - A_{s1} \qquad (5.31)$$

where, A_{s1} is the area of the tensile reinforcement, $A_{c.eff}$ is the area of concrete effectively engaged in tension (shaded area around A_{s1} in Fig. 5.4a), f_{ct} is the tensile concrete strength, and b is the width of the section of the column (Fig. 5.4a). The lowest value of $x=x_{cr,2} < \ell_{D1}$ that satisfies Eq. (5.31) determines the location of the next crack; otherwise no further cracking is possible within ℓ_{D1} as long as the reinforcement remains elastic.

(b) Alternatively, the next possible crack location, $x_{cr,2} \geq \ell_{D1}$ in the undisturbed region (Fig. 5.4b) is also evaluated from Eq. (5.25b) (here, $\varepsilon_{c.cr}$ is the cracking concrete strain):

$$\varepsilon(x) = \varepsilon_{el}^{o}(1 - x/L_s) - N/(E_c \cdot A_g) = \varepsilon_{c.cr} \Rightarrow x_{cr,2} = L_s \cdot \left[1 - \varepsilon_{c.cr}/\varepsilon_{el}^{o} - N/(E_c A_g\, \varepsilon_{el}^{o})\right] \qquad (5.32)$$

Slip in the disturbed region is obtained from integration of bar strains (from x=0 to $x= \ell_{D1}$).

$$s(x) = \frac{1}{\omega}(C_1 \cdot e^{-\omega x} - C_2 \cdot e^{\omega x}) + C \qquad (5.33)$$

The constant of integration, C is obtained from the requirement of compatibility of strains in the concrete and reinforcement at the end of the disturbed zone, $x=\ell_{D1}$ where the local slip is zero ($s(\ell_{D1})$=0). After localization of the second crack at $x_{cr,2}$, the next step of the solution is the determination of the new disturbed region ℓ_{D2} (along with the updated values of the constants C_1, C_2). This initiates from the crack location $x_{cr,2}$ and extends towards the span until the requirements of slope coincidence and continuity are reached, at coordinate $x_{cr,2} + \ell_{D2}$ in Eqns. (5.29a-b) (Fig. 5.5a). In using the closed form expression of Eq. (5.28), the value of x is substituted by the value x-$x_{cr,2}$; this solution is valid for $x \subseteq [x_{cr,2}, x_{cr,2}+\ell_{D2}]$). The bar strain $\varepsilon_{cr,2}$ at the location of the second crack (Fig. 5.5a) is the outcome of the flexural analysis of the cracked section and corresponds to the moment at that location according to Eq. (5.27) for $x=x_{cr,2}$. In the search of the new disturbed region, an additional requirement is that slip at the location $x_{cr,2}$ should not exceed the limit s_1 in Eq. (5.33) (where x is substituted by x-$x_{cr,2}$),securing that bond is still elastic inside ℓ_{D2} (Fig. 5.5a).

This process is repeated following the gradual increase in the value of bar strain ε_o at the support, until no additional primary cracks can be identified. This point corresponds to stabilization of cracking, and it generally occurs at a strain value in the critical section that is less than the strain at yielding, $\varepsilon_o^{stbl} < \varepsilon_y$. From this stage and until failure of the structural member, for the sake of simplicity of the mathematical problem, the so called *total disturbed region* ℓ_{Do} is defined as the total distance measured from the support to the end of the disturbed region of the last (and remotest) crack that was formed prior to stabilization, $\ell_{D,n}$ (Fig. 5.5b). Since bond development controls the total disturbed region, from that point onwards the field equations (Eq. (5.4)) are solved in ℓ_{Do} ignoring the presence of intermediate discrete cracks or the flexural moment requirements, since the "plane sections" assumption is not valid anywhere over this entire region; upon further increase of the bar strain at the support, the ℓ_{Do} length may increase further as the disturbed zone penetrates towards the tip of the cantilever column.

Following cracking stabilization and beyond yielding of the steel bar ($\varepsilon_o > \varepsilon_y$), the yielded segment of the disturbed region undergoes simultaneous degradation of bond. Thus, of the total length ℓ_{Do}, there is a segment l_r where yielding penetrates and spreads with increasing value of ε_o (Fig. 5.5b). Owing to bar yielding, bar strains increase over l_r without a commensurate increase of stress: this means that bond must have degraded to zero as a consequence of Eq. (5.4a), since $df/dx=0$ and thus $f_b=0$. This segment may be considered debonded. Even if the yield-plateau is neglected, and the bar stress-strain diagram is considered bilinear with some hardening (Fig. 5.2a), it is clear that the small hardening slope may only be supported by the residual bond strength – in other words in order for a bar to yield, it must have slipped beyond the limit s_2 in the bond - slip law (Fig. 5.2b). Limit s_2 is not an intrinsic property of the bar–concrete interface as it is generally assumed by Design Codes (*fib* Model Code 2010), but rather, it depends on the available bonded length (Tastani et. al. 2013).

Solution for the distributions of strain, slip and the state of bond over the disturbed region ℓ_{Do} of the shear span of a column under lateral sway follows that obtained when considering yield penetration in a bar anchorage (Section 5.3). Here, the disturbed region ℓ_{Do} comprises the sequence of the following segments (Fig. 5.5b): the yield penetration length l_r (immediately adjacent to the support), the bond plastification length l_p (i.e. the length where the bar is elastic but bond is constant and equal to the value at the plateau of the bond slip law f_b^{max}); Bar axial stress and bond stress are elastic in the tail length of the

disturbed region. The solution of the bond equations for the different segments is given below:

For $0 \le x \le l_r$: $\varepsilon(x) = \varepsilon_o - \frac{4f_b^{res}}{E_{sh}D_b}x$; $f_b(x) = f_b^{res}$ (5.34a)

$$s(x) = s_2 + 0.5(l_r - x)[\varepsilon(x) + \varepsilon_y] \rightarrow x=0: \; s_o=s_2+0.5\cdot l_r\cdot(\varepsilon_o+\varepsilon_y) \quad (5.34b)$$

For $l_r \le x \le l_r + l_p$: $\varepsilon(x) = \varepsilon_y - \frac{4f_b^{max}}{E_sD_b}(x - l_r)$; $f_b(x) = f_b^{max}$ (5.35a)

$$s(x) = s_1 + 0.5(l_r + l_p - x)[\varepsilon(x) + \varepsilon_{el}^3] \rightarrow x=l_r: \; s_2=s_1+0.5\cdot l_p\cdot(\varepsilon_y+\varepsilon_{el}^3) \quad (5.35b)$$

$$\varepsilon_{el}^3 = \varepsilon_y - \frac{4f_b^{max}}{E_sD_b}l_p \quad (5.35c)$$

For $l_r + l_p \le x \le \ell_{Do}$:

$$\varepsilon(x) = C_{1t}\cdot e^{-\omega(x-l_p-l_r)} + C_{2t}\cdot e^{\omega(x-l_p-l_r)} \qquad f_b(x) = \frac{f_b^{max}}{s_1}\cdot s(x) \quad (5.36a)$$

$$s(x) = \frac{1}{\omega}\left(C_{1t}\cdot e^{-\omega(x-l_p-l_r)} - C_{2t}\cdot e^{\omega(x-l_p-l_r)}\right) + C_t \quad (5.36b)$$

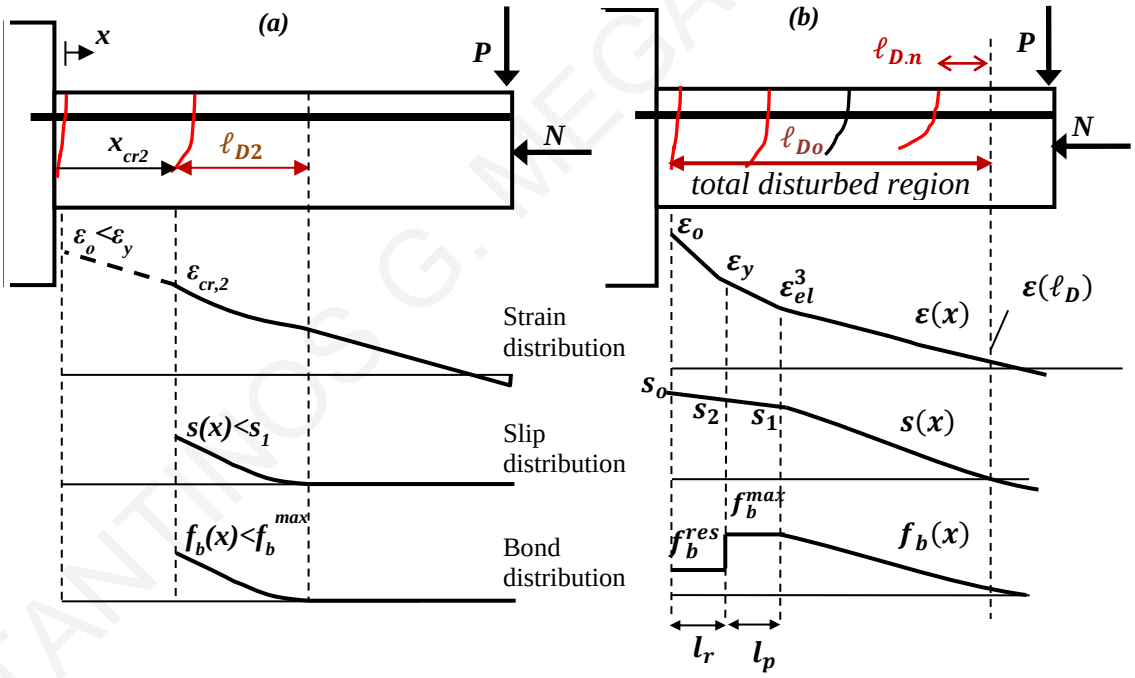

Figure 5.5: a) Disturbed region ℓ_{D2} after formation of the 2nd crack. b) Total disturbed region ℓ_{Do} after stabilization of cracking. Plastic hinge in (b): includes yield penetration length l_r.

Unknowns ℓ_{Do}, C_{1t}, C_{2t} and the constant of integration C_t are obtained from boundary conditions at $x = \ell_{Do}$ (namely slope and strain continuity and slip compatibility - zero relative displacement) between strain distributions obtained from the bond development equation and from flexural analysis. Therefore reinforcement slip is: at $x=l_r+l_p$, $s(x)=s_1$; at $x = \ell_{Do}$,

$s(\ell_{Do})=0$ (i.e., no slip). The following system of boundary conditions is therefore established:

a) Slope continuity of the strain distributions at $x = \ell_{Do}$:

$$\omega \cdot \left(-C_{1t} \cdot e^{-\omega(\ell_{Do}-l_r-l_p)} + C_{2t} \cdot e^{\omega(\ell_{Do}-l_r-l_p)}\right) = -\left[\underbrace{\left(M_0 \cdot y_{cg}\right)/E_c I_g}_{\varepsilon_{el}^o}\right] \cdot 1/L_s \quad (5.37a)$$

b) Continuity of strains at $x = \ell_{Do}$:

$$\varepsilon(\ell_{Do}) = C_{1t} \cdot e^{-\omega(\ell_{Do}-l_r-l_p)} + C_{2t} \cdot e^{\omega(\ell_{Do}-l_r-l_p)} = \varepsilon_{el}^o \cdot (1 - \ell_{Do}/L_s) - N/\left(E_c \cdot A_g\right) \quad (5.37b)$$

c) Continuity of slip at $x=l_r+l_p$:

$$s \cdot \left(l_r + l_p\right) = \frac{1}{\omega}(C_{1t} - C_{2t}) + C_t = s_1 \quad (5.37c)$$

d) Continuity of strain at $x=l_r+l_p$:

$$\varepsilon\left(l_r + l_p\right) = C_{1t} + C_{2t} = \varepsilon_{el}^3 \quad (5.37d)$$

The length of yield penetration l_r (Eq. 5.38) may be estimated considering the continuity of strain at $x=l_r$ (in Eq. (5.34a)).

$$l_r = (\varepsilon_o - \varepsilon_y) \cdot \frac{E_{sh} D_b}{4 f_b^{res}} \quad (5.38)$$

Equation (5.38) for the yield penetration length (which defines the plastic hinge) has two interesting implications: first, it is a strain-based criterion for the spread of yielding in the shear span, as opposed to the stress-based definition given by Eqn. (5.2b); there the coefficient a refers to the flexural overstrength normalized by the yielding moment. A second more subtle point is the observation that the plastic hinge length is influenced by several parameters indirectly, through the determining effect that these have on f_b^{res}. For example the presence of axial load on a member that undergoes cyclic displacement reversals weakens the cover over a larger portion of the shear span length leading to cover delamination due to excessive compressive strains; upon reversal of load, the crushed cover cannot support significant bond action for the reinforcement when it is stressed in tension, leading to a reduced value of f_b^{res}, which in turn causes increased penetration depth for columns carrying a higher axial load; this is consistent with experimental reports (Watson et. al. 1994, Bae et. al. 2008).

5.4.3 Proposed Algorithm

The following algorithm (Fig. 5.6) is established in order to define the locations of primary cracks and bar strain, slip and bond distribution along the shear span L_s of a laterally loaded reinforced concrete column as well as the yield penetration length:

Initial Data: Using standard section analysis obtain M-ϕ and M-ε diagrams (or better a unified diagram M-ϕ -ε) given N for the typical section of the reinforced concrete column studied.

1st Step: Select value of bar strain, $\varepsilon_o^{(1)}=\varepsilon_o$, after crack formation at the support (Eqs. 5.25,5.27).

2nd Step: Find the corresponding moment, M_o at the support, from moment-bar strain diagram. Solve for the length of the disturbed region ℓ_{D1} emanating from the first crack (Eqs. 5.27-5.30).

3rd Step: Increase strain at critical section to $\varepsilon_o^{(2)} = \varepsilon_o^{(1)} + \Delta\varepsilon_o$. Find the location $x_{cr,2}$ of the second crack. Check if second crack will occur: (a) inside ℓ_{D1} according to Eq. (5.31), or (b) in the undisturbed region L_s- ℓ_{D1}, according to Eq. (5.32).

4th Step: (a) If next crack forms within $\ell_{D1,}$ repeat Step 3 for $\varepsilon_o^{(3)} = \varepsilon_o^{(2)} + \Delta\varepsilon_o$. (b) Otherwise, find the new distrurbed region ℓ_{D2} that extends beyond $x_{cr,2}$.

5th Step: Find total disturbed length, $\ell_{Do}=x_{cr,2}+ \ell_{D2}$

6th Step: Solve for $\varepsilon(x)$, $s(x)$, $f(x)$, $f_b(x)$ for $x_{cr,2}\leq x\leq \ell_{Do}$ from Eqs. (5.28, 5.29, 5.30, 5.33) (Fig. 5.5a). In this phase of the solution and up to stabilization of cracking elastic bond is assumed in ℓ_{D2} (Fig. 5.5a). Thus the distributions can be described by the Eqs. (5.36) after substituting l_r=0 and l_p=0. For L_s-ℓ_{Do}<x<L_s, (elastic column) Eqs. (5.25,5.27) are used.

7th Step: Repeat steps 2 to 6 for $\varepsilon_o^{(i)} = \varepsilon_o^{(i-1)} + \Delta\varepsilon_o$ until stabilization of cracking (i.e., no more primary cracks can develop: $\varepsilon_o^{stbl} = \varepsilon_o^{(i)}$). Final length of disturbed zone is obtained from the n^{th} increment using this procedure: $\ell_{Do}=x_{cr,n}+ \ell_{D,n}$.

8th Step: Increase $\varepsilon_o^{(i)} = \varepsilon_o^{(i-1)} + \Delta\varepsilon_o > \varepsilon_o^{stbl}$. Solve for one continuous disturbed region $\ell_{Do} \geq x_{cr,n}+ \ell_{D,n}$ allowing for bond plastification and debonding as well as bar yielding (anchorage solution) up to either (a) ε_o exhausting the ultimate strain of the M-ε diagram, or (b) ℓ_{Do} exceeding the available development length of the bar in the shear span, taken here as (L_s+h_{hook}), where h_{hook} refers to the bent length of a hooked anchorage (according with *fib*

Model Code (2010) the contribution of a hook to the strength of an anchored bar is $50A_b f_b^{max}$, which corresponds to an additional anchored length, $\Delta L_b = h_{hook} = 12.5D_b$). If (b) controls, continue beyond that point for higher strains using the anchorage solution presented in Section 5.3 for the entire length ℓ_{Do}.

9th Step: The last converged value of l_r in the shear span (Fig. 5.5b) is added to the corresponding yield penetration length into the anchorage (Section 5.3) resulting in the definition of the total plastic hinge length ℓ_{pl}.

5.5 Numerical Examples

In the context of the present chapter, the length of plastic hinge is by definition the length of yield penetration (thus $\ell_{pl}=l_r$), occurring from the critical section towards both the shear span and the anchorage; physically it refers to the extent of the region where nonlinear reinforcing strains occur, and it may be used to calculate the inelastic rotation capacity of the column. The solution algorithm developed is applied in this section in order to establish the parametric sensitivities of the estimated plastic hinge to the important design parameters. It is also used to correlate the behaviour of the plastic hinge spread in three published column tests that were conducted to illustrate the effect of axial load on the length of the plastic hinge region (Saatcioglu et.al. 1989, Bae et.al. 2008).

The three column experiments studied in the chapter are specimens U3 (Saatcioglu et.al. 1989), S17-3UT and S24-4UT (Bae et.al. 2008). Column specimens were tested as cantilevers, simulating half a clear column length under lateral sway such as would occur during an earthquake with cross section detailing as shown in Fig. 5.7a. Column U3 is analysed in detail and results are summarized in Table 5.1, whereas results of S17-3UT and S24-4UT are directly included in Table 5.1 for easy correlation.

5.5.1 Column U3 (Saatcioglu et.al. 1989)

The specimen had a 350 mm square cross section reinforced with eight evenly distributed longitudinal reinforcing bars of D_b=25mm and stirrups of $D_{b,st}$=10mm spaced at 75mm o.c. (on centers) and clear cover C_{cov}=32.5mm (i.e., d=350-45=305mm), see Fig. 5.7a. Concrete strength was f_c'=34.8MPa. Longitudinal steel yielding strength was 430MPa with a 5% hardening. Stirrup yield strength was 470MPa.

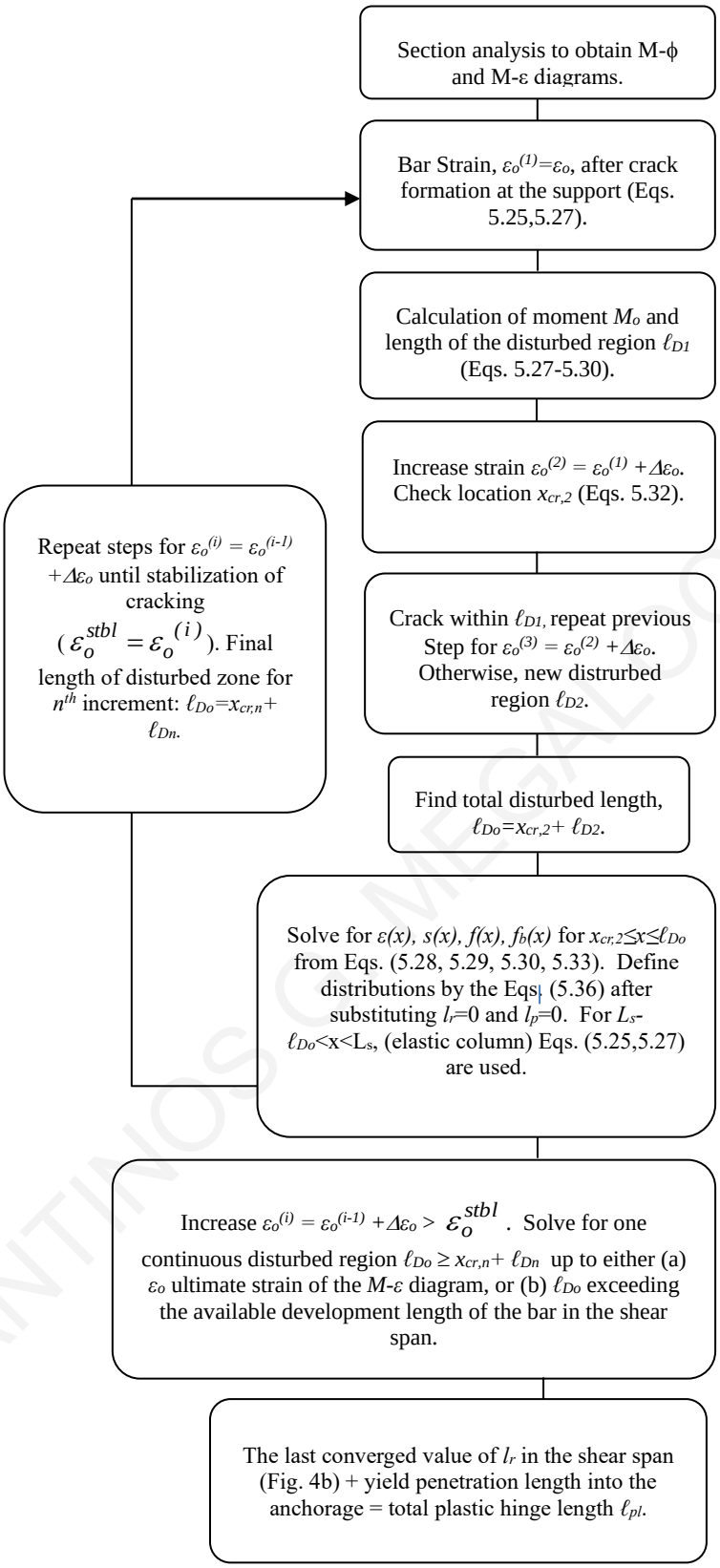

Figure 5.6: a Flow-chart of the established algorithm for the definition of the bond state in the disturbed region of the shear span as well as of the plastic hinge length.

Table 5.1: Summary of the analyzed experiments (units: mm, MPa)

	Experimental details			Analysis		
Test ID	$\nu=N/(f_c' bd)$	Column geometry	Reinforcement	Anchorage	Shear span	Column deformation at ultimate
U3	0.16 f_c'=34.8	Square section h=350, C_{cov}=32.5 d=305, Sh. span, L_s=1000	Long: 8 evenly distributed bars, D_b=25, f_y=430 $E_{sh}=5\%E_s$ Trans: 10@75 $f_{y,st}$=470	$f_b^{max}=1.25\sqrt{f_c'}=7.40$ s_1=0.2 L_b =812 $s_u^{anch}(x=0)$=2.33 $l_{r,u}$ =313	f_b^{max} =7.2, f_b^{res}= 1.44, s_1=0.2 $\ell_{Do}^{max}=L_s+12.5D_b$=1313 l_r =319 ε_u=0.0095, ϕ_u=4.7x10^{-5} x_c= 103, $s_u^{span}(x=0)$=2.36	Total ℓ_{pl}: $\ell_{pl}=l_{r,u}+l_r$ =632mm=1.8h DR=450mm=1.3h θ_u^{slip}=0.018 $\theta_u{}^f=\theta_y{}^f+\theta_{pl}{}^f$=0.015 θ_u=0.033 / θ_u^{exp}=0.027
S17-3UT	0.5 f_c'=43.4	Square section h=440, C_{cov}=27 d=405, Shear span, L_s=3049	Long: 12 evenly distributed bars, D_b=15.9, f_y=496 $E_{sh}=5\%E_s$ Trans: 9.5@86 $f_{y,st}$=496	$f_b^{max}=1.25\sqrt{f_c'}=8.23$ s_1=0.2 L_b =890 $s_u^{anch}(x=0)$=1.50 $l_{r,u}$ =177	$f_{b,w/cov}^{max}$ =11.49MPa $f_{b,wo/cov}^{max}$ =5.40MPa $f_b^{res}=20\%$ f_b^{max}=1.1MPa, s_1=0.2 $\ell_{Do}^{max}=L_s+12.5D_b$=3248 l_r =271 ε_u=0.01, ϕ_u=5.9x10^{-5} x_c= 236, $s_u^{span}(x=0)$=2.30	Total ℓ_{pl}: $\ell_{pl}=l_{r,u}+l_r$ =448mm=h DR=450mm=h θ_u^{slip}=0.012 $\theta_u{}^f$=0.029 θ_u=0.041 / θ_u^{exp}=0.032

S24-4UT	0.2 f_c'=36.5	Square section h=610, C_{cov}=49 d=550, Shear span, L_s=3049	Long: 12 evenly distributed bars, D_b=22.2, f_y=400, E_{sh}=1%E_s Trans: 9.5@152 $f_{y,st}$=455	f_b^{max}=1.25$\sqrt{f_c'}$=7.55s_1 =0.2 L_b =890 $s_u^{anch}(x=0)$=0.98 $l_{r,u}$ =80	$f_{b,w/cov}^{max}$ =8.85MPa $f_{b,wo/cov}^{max}$ =2.0MPa f_b^{res}=20% f_b^{max}=0.4 MPa, s_1=0.2 ℓ_{Do}^{max}=L_s+12.5D_b=3327 l_r =301 ε_u=0.013, ϕ_u=3.9x10^{-5} x_c= 217, $s_u^{span}(x=0)$=3.52	Total ℓ_{pl}: ℓ_{pl} =$l_{r,u}$ + l_r =380mm=0.6h DR=350mm=0.57h θ_u^{slip}=0.01 θ_u^{f}=0.017 θ_u=0.027 / θ_u^{exp}=0.033

Note: Test U3 by Saatcioglu et.al. 1989 and tests S17-3UT, S24-4UT by Bae et. al. 2008; DR= Damaged Region

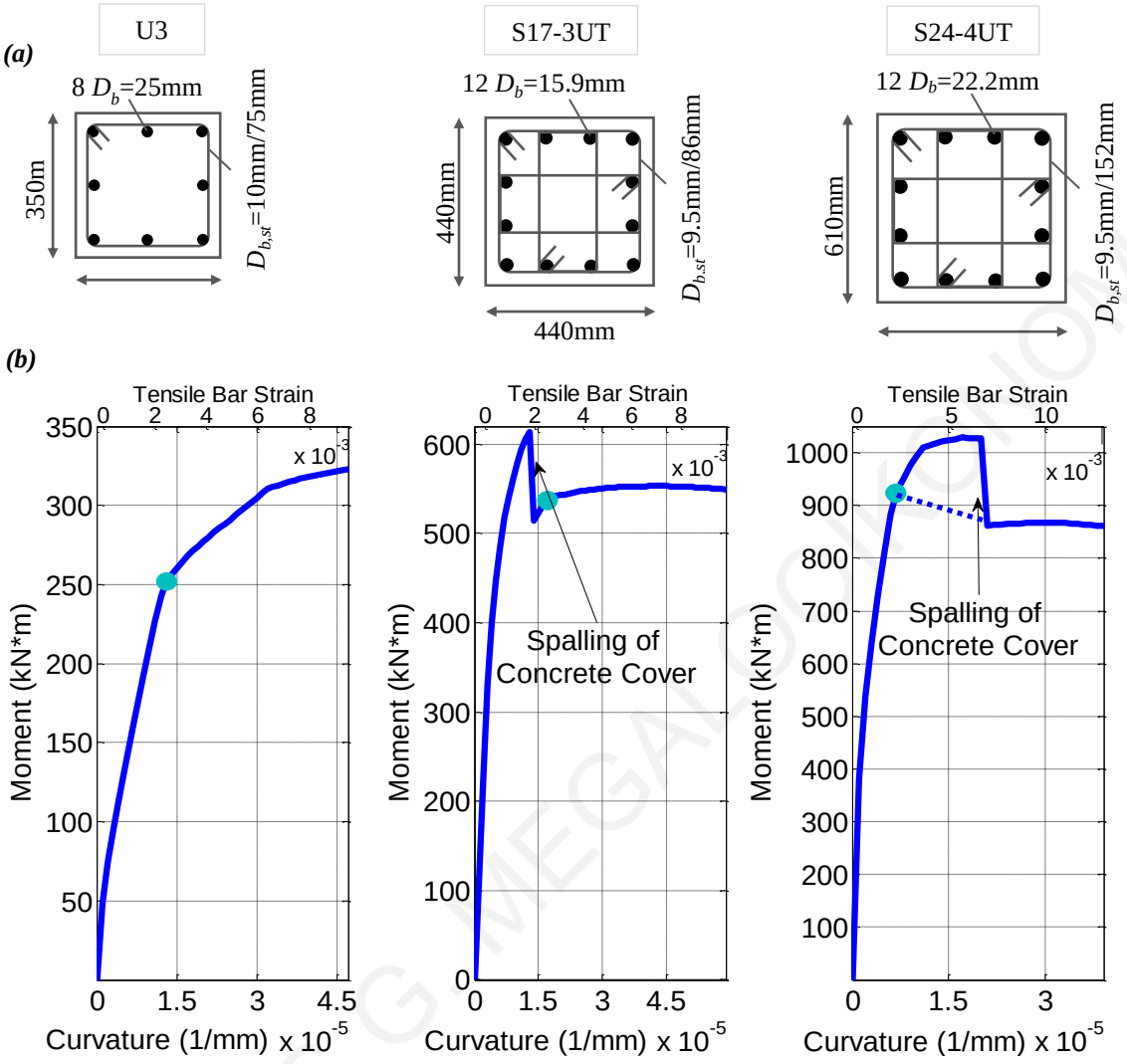

Figure 5.7: Specimens U3, S17-3UT and S24-4UT a) cross section details, b) moment - curvature - tensile bar strain diagrams.

Column shear span was L_s=1.0m and the axial load ratio [$\nu=N/(f_c' bd)$] was 0.16. Figure 5.7b plots the unified M-ϕ-ε relationship obtained for this axial load using fiber section analysis with the modified Kent & Park model for confined concrete (Scott et. al. 1982); a Hognestad-type parabola was used to model the compression stress-strain response of unconfined concrete (Hognestad 1951). A bilinear stress-strain curve with 5% hardening was used to model longitudinal reinforcement (Fig. 5.2a). Bond strength was taken equal to $f_b^{max}=1.25\sqrt{f_c'}$ (7.4MPa) for the anchorage (anchorage with hook with equivalent straight length of L_b=800mm, *fib* Model Code 2010).For the shear span the bond strength is calculated using a frictional model (Tastani et.al. 2010) that accounts for separate contributions of the cover concrete and stirrups according to:

$$f_b^{max} = \frac{2\mu_{fr}}{\pi D_b}\left(2C_{cov}\cdot f_{ct} + 0.33\frac{A_{st}f_{y,st}}{N_b\cdot s}\right) \tag{5.39}$$

where N_b is the number of tension bars (or pairs of tension spliced bars if reinforcement is spliced) laterally restrained by the transverse pressure exerted in the form of confinement by the stirrups, C_{cov} is the clear concrete cover, A_{st} is the area of stirrup legs enclosing the N_b bars (i.e., the total area of legs crossing the splitting plane), s is the stirrup spacing along the member length, μ_{fr} is coefficient of friction, f_{ct} is the concrete tensile strength and $f_{y,st}$ is the yielding strength of stirrups. Therefore the maximum bond strength for the shear span is 7.2MPa when considering the contribution of the cover, which drops to 2.75MPa after cover delamination (for the present example: μ_{fr}=1, $f_{ct} = 0.33\sqrt{f_c'}$, $N_b = 3$). Due to the reversed cyclic nature of the displacement history, cover on the tension reinforcement is assumed to have delaminated or split if during the opposite direction of loading the compressive strain has attained the limit value of 0.003; this is used also in all other examples considered herein. The residual bond strength f_b^{res} is defined as 20% of the maximum bond strength and parameter s_1 = 0.2mm; s_2 mainly depends on the anchorage length which is equal to the shear span if the latter is transmitted to total disturbed region. For the present problem, s_2 is found equal to 0.5mm at the ultimate state of reinforcement (see Fig. 5.8b). After evaluation of the process of crack formation according with the proposed algorithm, the resulting distribution of strains is illustrated in Fig. 5.8. Note that stabilization of cracking occurred before yielding of the tensile bars (just after formation of the 4th crack). Ultimate strain corresponded to a disturbed region extending over the entire length of the column shear span including an equivalent additional length equal to $12.5D_b$ (313 mm) –thus $\ell_{Do}^{max}=L_s+12.5D_b$– in order to account for the end detail of reinforcement at the tip of the column being welded on a steel plate (this additional length is the anchorage length equivalent of a T-headed anchorage according to *fib* Model Code 2010 – here this is a conservative estimate). The red dashed curve in Fig. 5.8d plots the bar strain distribution that results from plane sections analysis; there is marked deviation from the distribution controlled by the bond action in the most stressed part of the shear span.

From Fig. 5.8 it is seen that the yield penetration length over the shear span at the last step of the calculation was 319mm ($0.91h$ or $0.32L_s$) whereas the corresponding pullout slip was $s_u^{span}(x=0)$=2.36mm. When including the yield penetration in the footing

as is intended in the formal definition of ℓ_{pl} (Eq. 5.2b) - the total plastic hinge length is 632mm. (Note that the yield penetration length inside the footing is 313mm or $0.029D_bf_y$ and the corresponding slip is $s_u^{anch}(x=0)$=2.33mm.) Figure 5.9a compares this value with the empirical estimates of Eqs. (5.3a); the easy estimate of *0.5d* is also noted. Also included is the result of the classical definition of plastic hinge length $(1-M_y/M_u)L_s$.

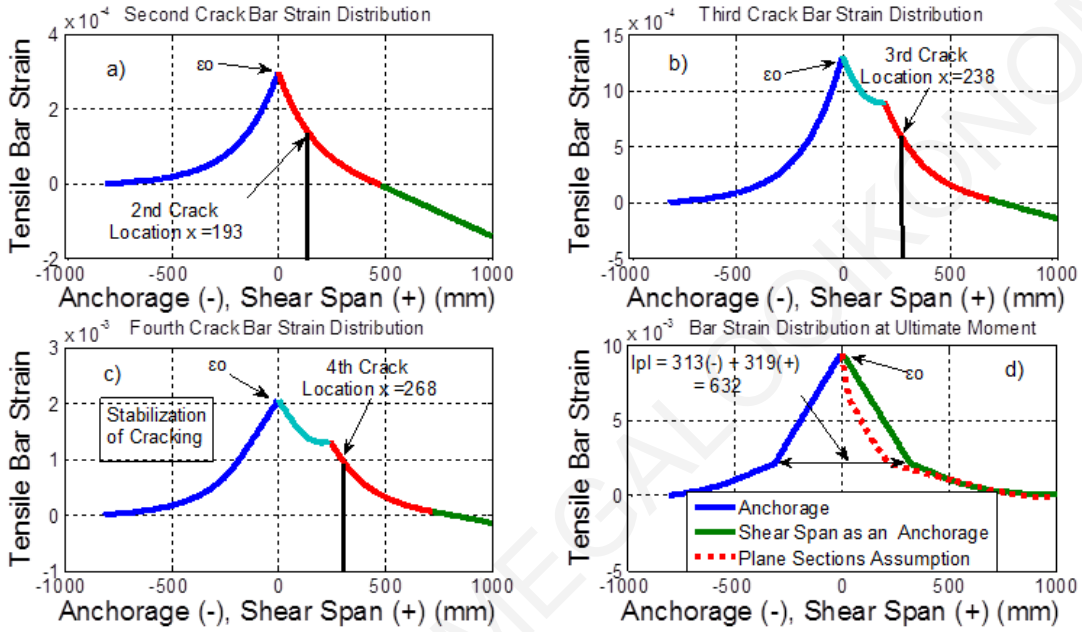

Figure 5.8: Column U3 (a), (b) (c) tensile bar strain distributions along the anchorage (blue curves) and the shear span (cyan-red-green curves). Location of estimated successive cracks is indicated until crack stabilization. d) Strain state of reinforcement at ultimate, where ℓ_{pl} is calculated.

For comparison it is noted (red dashed line in Fig. 5.8a) that cover delamination extended over 520mm measured from the face of the support, according with the experimental report of specimen U3 (Saatcioglu et.al. 1989). Figure 5.9b presents the slip distribution lengthwise the bar reinforcement, from where values at critical section are used next for the calculation of drift components. The rotation components θ^{slip} and θ^{f} occurring at the critical section of the specimen at yielding and in the ultimate limit state are estimated according with Eqs. (5.1) and (5.2) by also adding the contribution from the anchorage (Section 5.3); here the theoretical ultimate point corresponds to the attainment of the maximum supportable disturbed length, $\ell_{Do}^{max}=L_s+12.5D_b$=1313mm as described in the preceding. Thus, Eq. (5.1) is modified as follows:

$$\theta_y^{slip} = \underbrace{\frac{s_y^{span}}{d-0.4x_c}}_{shear\ span}|x=0 + \underbrace{\frac{s_y^{anch}}{d-0.4x_c}}_{anchorage}|x=0; \theta_u^{slip} = \underbrace{\frac{s_u^{span}}{d-0.4x_c}}_{shear\ span}|x=0 + \underbrace{\frac{s_u^{anch}}{d-0.4x_c}}_{anchorage}|x=0 \quad (5.40)$$

The values $s_y(x=0)$ and $s_u(x=0)$ are the contributions to slip at the base of the column resulting from pullout from the anchorage as well as from the shear span. For the analytical estimations of specimen U3, the compression zone depth was (Fig. 5.7b, ε_u=0.0095 and ϕ_u=4.7x10^{-5}mm^{-1}) x_c= 103mm (i.e., $d-0.4x_c$=ή 305-41=264mm) and from Eq. (5.40) the drift capacity owing to pullout slip was estimated as: θ_u^{slip}=2.36⁄264+2.33⁄264=0.018rad. Using ℓ_r=319mm, the ultimate rotation of the column due to flexure was: $\theta_u^f=\theta_y^f+\theta_{pl}^f$ where $\theta_y^f=\phi_y \cdot L_s/3$(see also Eq.(5.2b)):$\theta_u^f$=1/3·0.000013·1000+(0.000047-0.000013)·319=0.015rad. Term θ_u^{slip} accounts for 55% of the total rotation capacity of the RC column (0.018+0.015=0.033rad). The experimental reported tip displacement at maximum moment (268kNm) was 35mm corresponding to a rotation of 0.035rad.

5.5.2 Column S17-3UT (Bae et.al. 2008)

The geometry of the column is summarized in Table 5.1 and depicted in Fig. 5.7a. The main bars were welded on a steel plate for the application of the load at the tip of the column. This was taken into account in the analysis by including a length of 12.5D_b (=199mm) as effective extension of the available development length in the shear span. Figure 5.7b depicts the results of the moment – curvature - strain analysis. It is evident that cover spalling occurs relatively early at a stage corresponding to bar yielding. For the shear span the maximum and the post-cover delamination values for bond strength were estimated from Eq. (5.39) as $f_{b,w/cov}^{max}$=11.49MPa and $f_{b,wo/cov}^{max}$=5.40MPa (indices *w/cov* and *wo/cov* correspond to the inclusion or not of the cover contribution). The process of detecting the crack formation and the corresponding strain distribution for the column are presented in Fig. 5.10. Stabilization of cracking occurred before yielding of the tensile bars. Moreover, after spalling of concrete cover, the contribution of the latter to bond strength was neglected (thus f_b^{max}= $f_{b,wo/cov}^{max}$ =5.40MPa).

As is evident from Fig. 5.10d the maximum sustained yield penetration length based on the proposed procedure is 271mm (0.66h or 0.09L_s) in the shear span and inside the footing it is 177mm (or 0.022$D_b f_y$). Reported damage extended over a distance of

450mm from the base of the column (see experimental reference, red dashed line in Fig. 5.9a). Figure 5.9a presents the correlation of the analytical estimation with the empirical results and Fig. 5.9b the analytically estimated slip distribution lengthwise along the bar reinforcement at ultimate strain.

The rotation of the column at ultimate moment due to slippage θ_u^{slip} (Eqs. (5.40 a,b)) is θ_u^{slip}=2.30⁄311+1.5⁄311=0.012rad whereas the ultimate rotation of the column due to flexure (using ℓ_r= 271mm) is: θ_u^{flex}=1/3·0.000017·3049+(0.000059-0.000017) ·271=0.029 rad. Thus the total drift is estimated as 0.041rad. The experimental curvature corresponding to 20% drop in lateral load capacity (this point was defined on the lateral load lateral displacement envelope after correction for the P-Δ effects), was $7x10^{-5}mm^{-1}$ (at the 6th level of cycling) and the associated drift was 0.032rad.

5.5.3 Column S24-4UT (Bae et.al. 2008)

Table 5.1 and Fig. 5.7a depict the geometric characteristics of the column specimen. As in the previous example, the effective development length of the longitudinal bars in the shear span was extended by $12.5D_b$ (= 278mm) to account for welding of main reinforcement on a steel plate attached to the point load setup. Figure 5.7b plots the calculated moment – curvature - strain diagram, indicating also the onset of cover delamination (beyond that point bond strength is reduced due to elimination of the cover contribution in Eq. 5.39). For the shear span f_b^{max} was $f_{b,w/cov}^{max}$=8.85MPa and $f_{b,wo/cov}^{max}$= 2.0MPa (with and without the cover contribution). The process of crack formation and the resulting bar strain distributions as calculated using the proposed algorithm are shown in Fig. 5.11.

From Fig. 5.11 it is shown that yield penetration length at maximum strain value ε_u =0.013 is l_r=301mm (=0.5h or 0.1L_s) in the shear span. Adding the length of yield penetration in the footing (i.e. 80mm or $0.01D_bf_y$) the plastic hinge length is estimated at 380mm. Figure 5.9a presents the correlation of the analytical estimation with the empirical results and the reported damage into the shear span, extending up to a distance of 350mm. Figure 5.9b shows the estimated slip distribution lengthwise the bar reinforcement at ultimate strain.

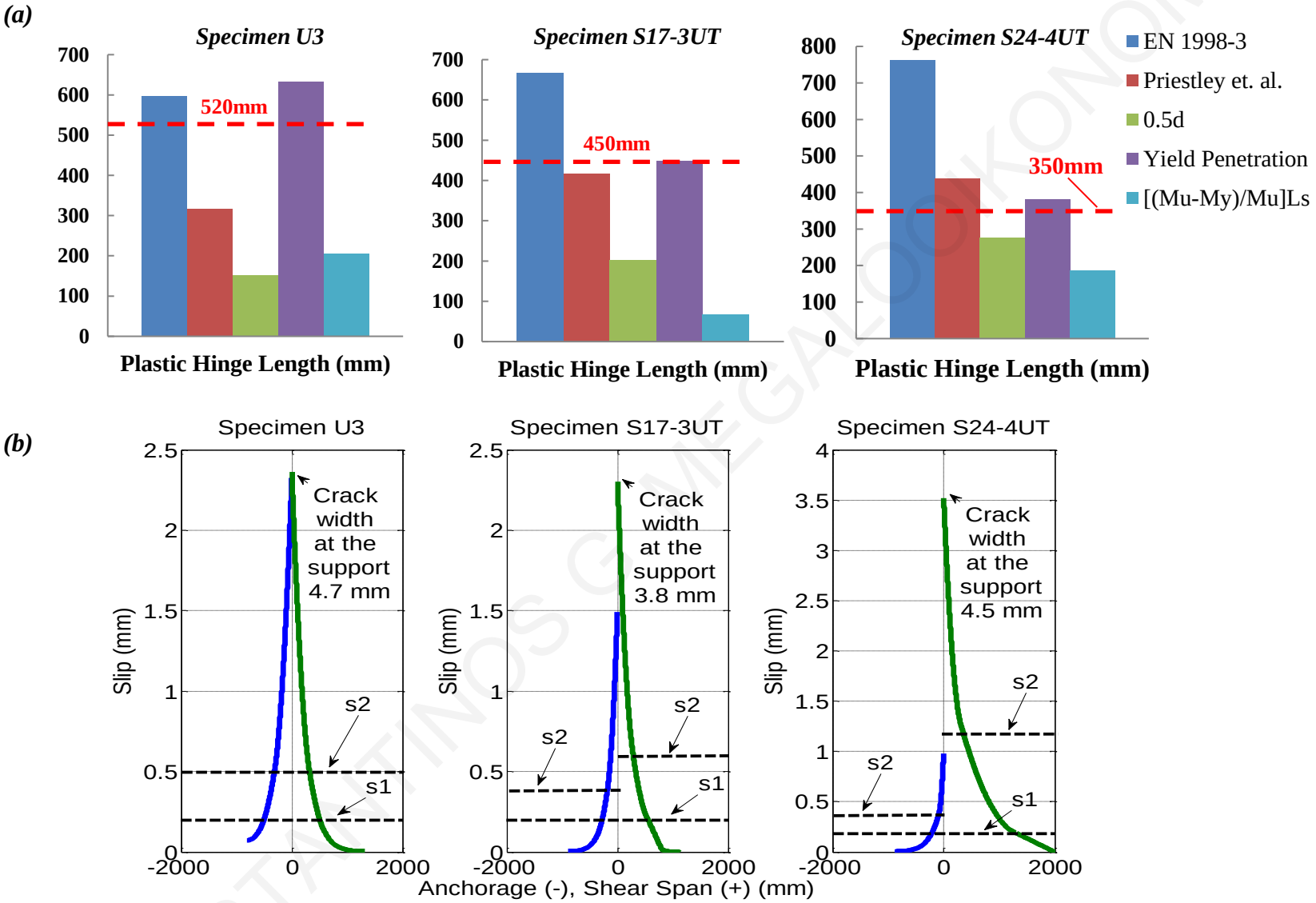

Figure 5.9: For specimens U3, S17-3UT and S24-4UT a) analytical calculation of the plastic hinge length ℓ_{pl} (purple bar) and its correlation with the design equations and b) slip distributions along the bar length at ultimate strain (where ℓ_{pl} is calculated).

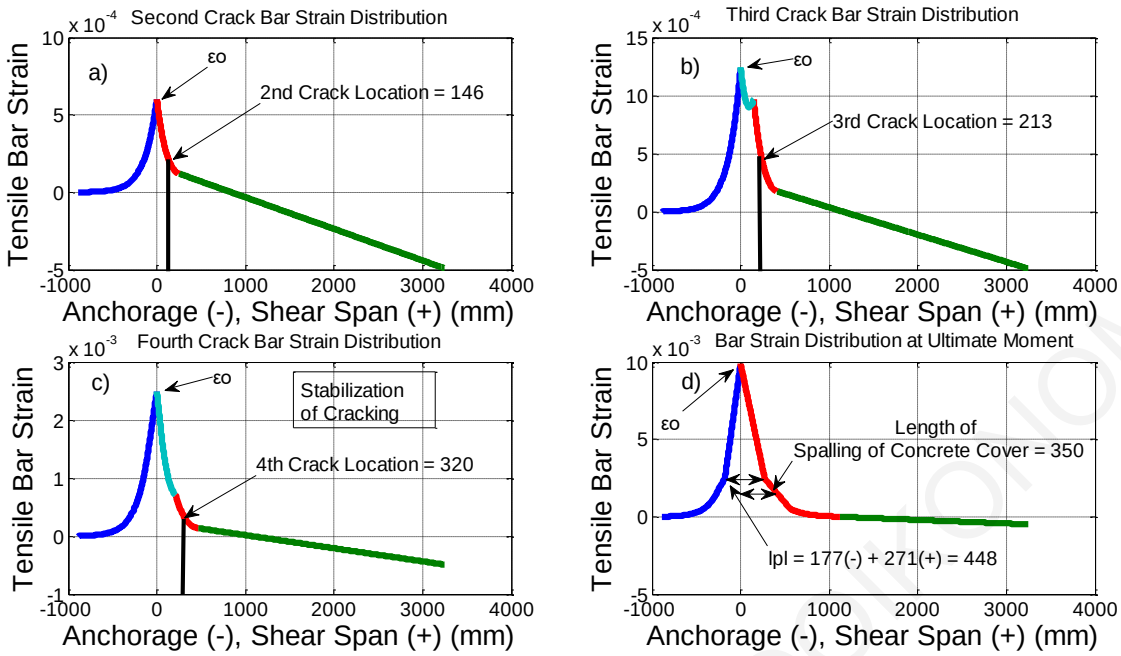

Figure 5.10: Column S17-3UT: (a), (b) (c) tensile bar strain distributions along the anchorage (blue) and shear span (cyan-red-green curves). Location of estimated successive cracks is indicated until crack stabilization. d) Strain state of reinforcement at ultimate, where ℓ_{pl} is calculated.

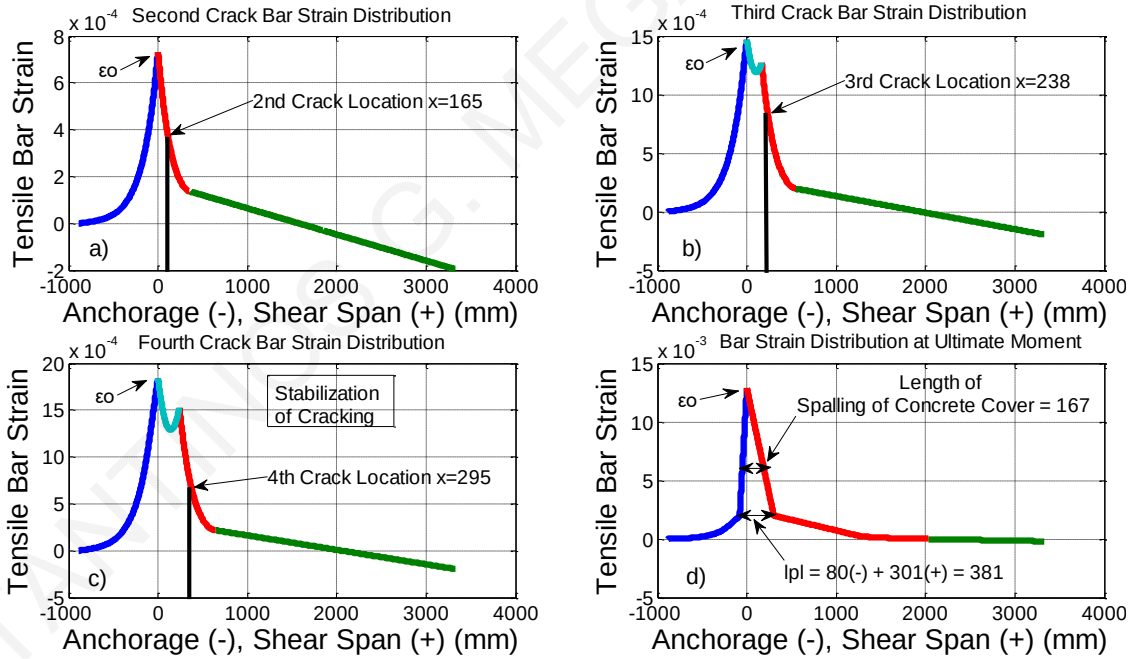

Figure 5.11: Column S24-4UT: (a), (b) (c) tensile bar strain distributions in the anchorage (blue) and the shear span (cyan-red-green curves). Location of estimated successive cracks is indicated until crack stabilization. d) Strain state of reinforcement at ultimate, where ℓ_{pl} is calculated.

Column rotation capacity at the ultimate moment was estimated as follows: from slip, θ_u^{slip}=3.52⁄463+ 0.98⁄463=0.01rad and due to flexure θ_u^{flex}=1/3 0.000007·3049+(0.000039-

0.000007)·301=0.017rad (in total 0.027rad). The experimental reported drift ratio at to 20% net loss of lateral load strength was 0.033rad (after correction of the result for the P-Δ effect); therefore the experimental total rotation of 0.033rad was approximated adequately by the estimated analytical value of 0.027.

5.6 Parametric Investigation

The parametric sensitivity of the proposed solution for the plastic hinge length is investigated in this section considering as a point of reference specimen U3 examined in the preceding section. Parameters considered, reference values, and ranges of parameters thereof are listed in Table 5.2; in each case one parameter is varied at a time keeping the reference values for all other variables (so the possible interaction effects between variables have not been considered in conducting the sensitivity analysis). Consistent with the original definition of the plastic hinge length (Eq. 5.2b) the strain hardening ratio of the reinforcement E_{sh} effectively increases the plastic hinge length (Table 5.2). Similarly, a reduction of the residual bond strength f_b^{res} leads to further increase of the plastic hinge length (Table 5.2). It should be noted that the yield penetration length in the anchorage is included in the plastic hinge length.

The location of the cracks is affected by variable ω that defines the elastic bond according to Eq. (5.28). Decreasing the slip limit s_1 and increasing the value of average bond strength f_b^{max} both led to consolidation of the cracks closer to the critical section at the base of the column (before stabilization of cracking), as evident in Table 5.2. In all analytical cases presented in Table 5.2 the first crack appears always at the base of the column ($x_{1,cr}$=0), whereas in some of the experiments severe cracking occurred about 50mm above the footing owing to the restraint provided by the footing, particularly when the drift history was applied by means of rotating that block while keeping the tip of the cantilever specimen stationary (e.g. Bae et. al. 2008).

In the previous section three specimens with different aspect ratios (L_s/d) and axial load ratios [$v=N/(f_c bd)$] have been considered. The corresponding values for (L_s/d) and v were, (3, 0.16), (7, 0.5), and (5, 0.2) respectively. Based on Bae et. al. 2008 the two parameters have a simultaneous effect on the extent of ℓ_{pl}, and a degree of interaction (i.e., the effect of L_s/d is pronounced only in the presence of high axial load ratio) (Tables 5.2,5.3). To illustrate the sensitivity of the proposed approach in reproducing the experimental trend,

a second reference point is introduced in the parametric study, namely the case of specimen U3 but with an axial load ratio of ν=0.5 (Table 5.3).

Figure 5.12a displays the influence of the variables on the normalized plastic hinge length (ℓ_{pl}/h, vertical axis) of the reference specimen, and on the associated development capacity of the reinforcement (in terms of tensile strain, ε_s, in the horizontal axis) of the critical cross section. Each curve in this diagram is read as follows:

- Reducing the bond strength f_b^{max} (with associated $f_b^{res}=20\%f_b^{max}$) gradually from 7 to 3MPa (red arrow next to the brown curve pointing down) results in the increase of the plastic hinge length attained at a lower bar strain capacity.
- Increasing the normalized axial load v (red arrow next to blue curve pointing up) lowers the strain capacity and the associated plastic hinge length.
- Reducing the hardening modulus E_{sh} (red arrow next to green curve pointing down) decreases the plastic hinge length (as it is implied by Eq. (5.38)) and increases the strain.
- Reducing the bar size D_b (red arrow next to grey curve pointing down) decreases the hinge length (as it is also implied by Eq. (5.38)) and increases the strain.

The hinge length is relatively insensitive to L_s/h at low axial loads, i.e., at v=0.15 all points coincide with the reference point (intersection of all curves; i.e. for L_s/h= 2, 3 and 4, the ℓ_{pl}/h is 1.8 and the associated strain is 0.017).

Table 5.2: Parametric Investigation – Properties similar to specimen U3 (units: mm, MPa)

Parameter	$\nu=N/(f_c' bd)$		
	$=0.15$	$=0.3$	$=0.5$
Plastic Hinge Length	1.8h	1.3h	0.9h
Parameter	$f_b^{max}=3$	$f_b^{max}=5$	$f_b^{max}=7$
Plastic Hinge Length	3.1h	2.2h	1.8h
Parameter	$f_b^{res}=1$	$f_b^{res}=2$	$f_b^{res}=3$
Plastic Hinge Length	2.2h	1.6h	1.3h
Parameter	$E_{sh}=1\%E_s$	$E_{sh}=2.5\%E_s$	$E_{sh}=5\%E_s$
Plastic Hinge Length	0.4h	0.9h	1.8h

Parameter	L_s=2h	L_s=3h	L_s=4h
Plastic Hinge Length	1.8h	1.8h	1.8h
Parameter		D_b=18	
Plastic Hinge Length		1.4h	

Table 5.3: Parametric Investigation – Axial load ratio equal to 0.5 (units: mm, MPa)

Ideal reference case:	*ν=N/(f_c'bd) = 0.5; all other characteristics are those of U3*		
Parameter	f_b^{max} = 3	f_b^{max} = 5	f_b^{max} = 7
Plastic Hinge Length	1.6h	1.1h	0.9h
Parameter	f_b^{res} = 1	f_b^{res} = 2	f_b^{res} = 3
Plastic Hinge Length	1.1h	0.8h	0.7h
Parameter	E_{sh}=1%E_s	E_{sh}=2.5%E_s	E_{sh}=5%E_s
Plastic Hinge Length	0.1h	0.4h	0.9h
Parameter	L_s=2h	L_s=3h	L_s=4h
Plastic Hinge Length	0.9h	0.9h	0.9h
Parameter		D_b=18	
Plastic Hinge Length		0.7h	

The presence of axial load on a member undergoing cyclic displacement reversals weakens the cover over a larger portion of the shear span length speeding up cover delamination due to excessive compressive strains. Upon reversal of load, the crushed cover cannot support significant bond action for the reinforcement when the latter is stressed in tension, leading to a reduced value of f_b^{max} (it is sustained only by the stirrups) and to demise of f_b^{res} (less than half of the bar perimeter is in contact with concrete with implications on residual friction). These in turn cause increased penetration depth for columns carrying a higher axial load. Fig. 5.12b depicts the effect of the studied variables on the plastic hinge length under higher axial load (v=0.5); in the reference case term f_b^{max} was reduced from

7.2MPa to 2.75 after cover loss. The following may conclude:

- Reducing bond strength f_b^{max} from 7 to 3MPa (brown curve in Fig. 5.12b) results in increased plastic hinge length, attained at a higher bar strain.
- Reducing the residual bond strength f_b^{res} (orange curve in Fig. 5.12b) increases the hinge length and lowers the associated strain capacity.
- Lower hardening modulus E_{sh} (green curve in Fig. 5.12b) results in lower hinge length and strain.
- Reduced bar size D_b (grey curve in Fig. 5.12b) lowers the hinge length and the strain capacity.

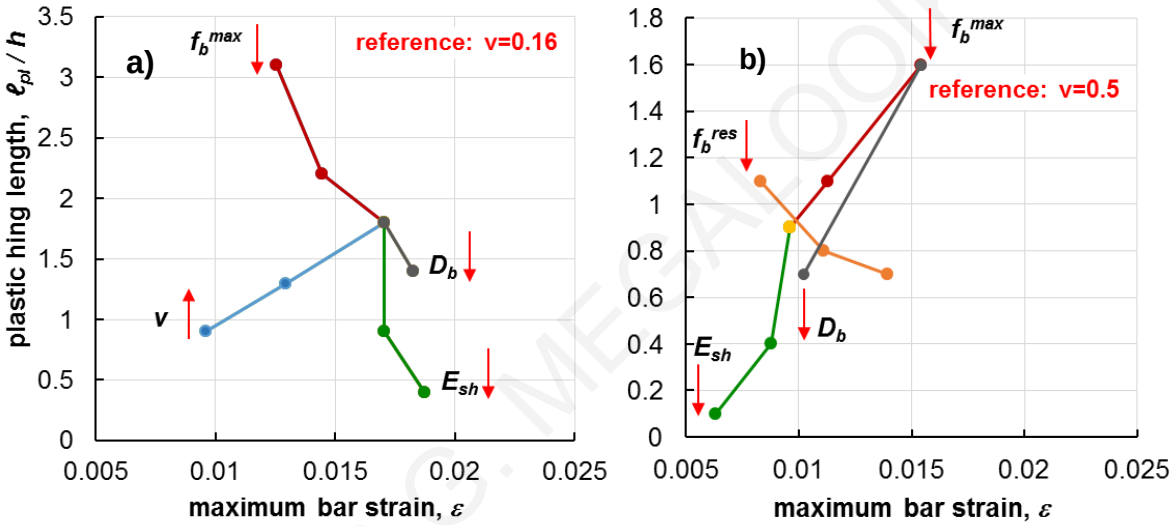

Figure 5.12: Sensitivity analysis of the normalized plastic hinge length ℓ_{pl}/h versus the associated reinforcement maximum tensile strain ε_s for a) low and b) high axial load.

The mechanism by which the axial load ratio affects the damaged region is by accelerating and spreading delamination of the cover in the compression zone of the laterally swaying column. This was already evident in the M-ϕ-ε relationships of Fig. 5.7. To study this parametric trend consider the cross section of Fig. 5.13a. Cover delamination is assumed to occur when the compressive strain at the level of compression reinforcement reaches the limit of 0.004 (term $\xi=x_c/d$ is the normalized compression zone and $\xi'=d_2/d$ defines the position of the compression reinforcement as per the extreme fiber). In this case, from cross section analysis, the strain of the tensile reinforcement ε_o is given by Eq. (5.41).

$$\varepsilon_o = 0.004 \cdot \frac{1-\xi}{\xi - \xi'} \tag{5.41}$$

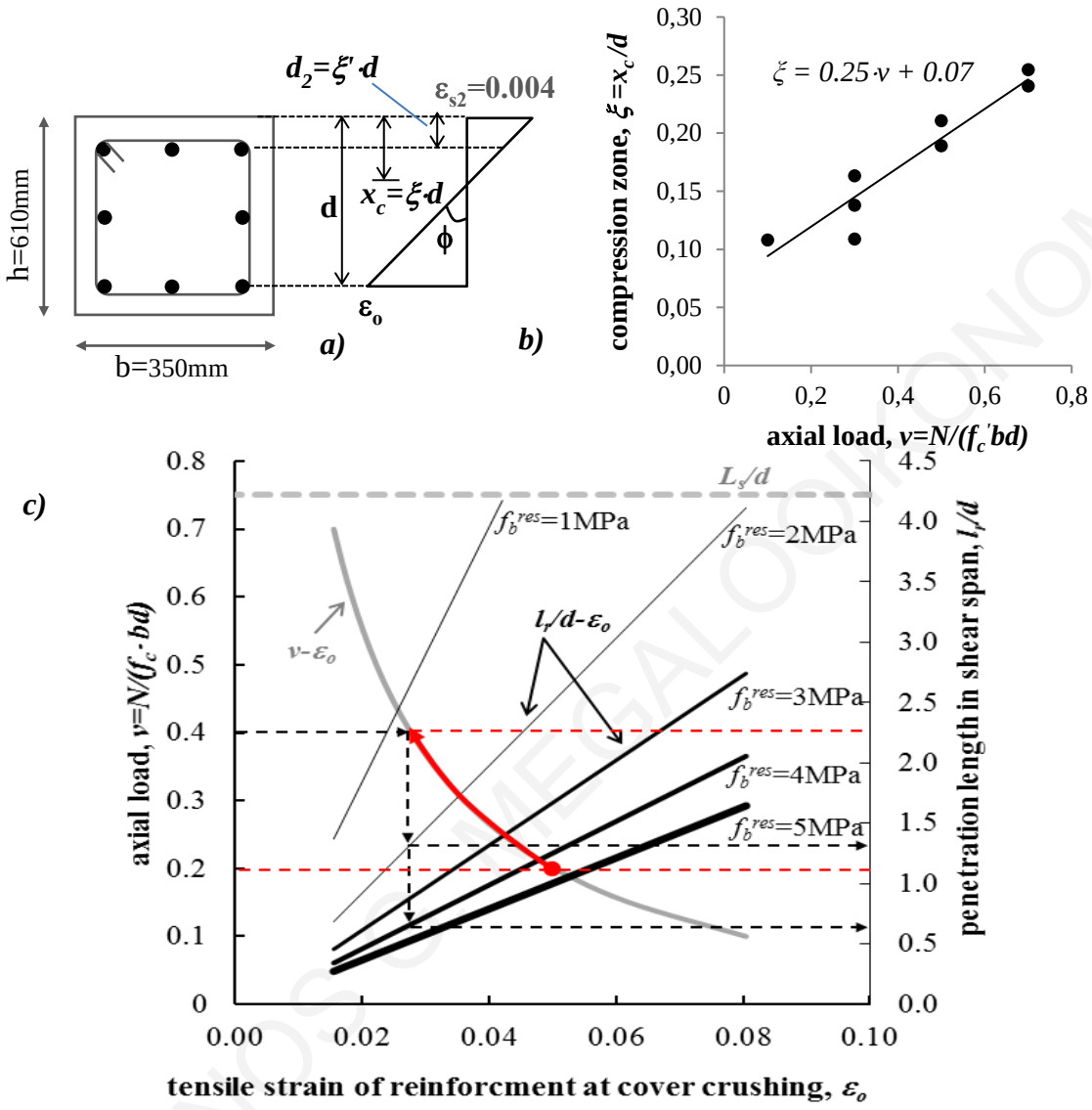

Figure 5.13: a) Strain state of cross section at cover crushing. b) The influence of axial load on compression zone based on data from [16]. c) A unified diagram ν – l_r/d - ε_o for the influence of axial load, residual bond strength and tensile bar strain on yield penetration length into shear span.

For the needs of the parametric investigation the relationship between ν and ε_o is established using experimental evidence: the column test series conducted by Watson et. al. 1994 included specimens with various axial load ratios ranging from ν=0.1 to 0.6. Based on the reported test results, the relation between axial load ν and normalized compression zone depth ξ is estimated as, ξ=0.25ν+0.07 (Fig. 5.13b). Thus, given the applied axial load ν, the

normalized compression zone depth of the cross section is estimated, ξ (from Fig. 5.13a); then, the corresponding strain in the tension reinforcement at the critical section, ε_o, is obtained from Eq. (5.41).

This is substituted in Eq. (5.38) to define the yield penetration length into the shear span, using different intensities of average residual bond strength depending on the magnitude of axial load (lower residual bond strength for higher axial load to reflect the effect of delaminated cover over a broader region). This procedure is visualized in the combined diagram of Figure 5.13c, where curves of v - ε_o (grey curve) and l_r/d - ε_o (black curves, where the thicker the curve the higher the f_b^{res} is) are simultaneously plotted (note: the horizontal grey dashed line drawn at the upper part of Fig. 5.13c defines the available column aspect ratio, L_s/d which serves as the ultimate limit for possible penetration). This diagram may be used to illustrate two aspects of the parametric sensitivity of the problem: a) the increase of axial load for example from 0.2 to 0.4 (following the red arrow) results in reduction of the strain capacity of the cross section (from 0.05 to 0.027) along with diminishing of the f_b^{res} (crossing from the thicker to the thinner curve, i.e. from 4 to near 1MPa) as well as an increase of the extent of the plastic hinge length in the shear span (i.e. from 1.1 to 2.3d, where d is the effective depth of the cross section, see the red dashed horizontal lines). b) the unified diagram v - l_r/d - ε_o can be used in design: given the axial load and the aspect ratio of the member, the strain capacity of the cross section and the corresponding plastic hinge length are uniquely defined, leading to proper assessment of the members' available deformation capacity. The extent and intensity of damage may be effectively reduced through confinement as a higher value of the residual bond strength may be supported (see the black dashed paths in Fig. 5.13c).

6 PHAETHON: FEM Simulation of Shear on RC Columns

6.1 Introduction

The correlation of experimental responses and results obtained from the inelastic flexural analysis of column elements with a dominant shear component had already highlighted the limitations of the underlying assumptions of the later approach, when used beyond their scope of application. Shear is a persistent problem in analysis and assessment because by the mere rotation of the principal directions away from the parallel and normal to a cross section, complicates convergence to solutions that satisfy equilibrium, particularly in the inelastic range. The debate on acceptable methods for calculation of shear strength still persists in the literature as illustrated in Chapter 2; issues such as the effective area participating in shear action and the size effect remain open [Tureyen and Frosch 2003]. On the other hand, it appears that shear strength, although estimated as a cross sectional property, really depends on the overall member response.

Even the most advanced stage of development on seismic design and assessment to date requires some kind of nonlinear analysis - either static or dynamic. Such investigations are mostly carried out using frame elements with different levels of approximation. Two main approaches are mostly used, classified as lumped-plasticity and distributed-inelasticity models. The limitation of lumped plasticity elements is that inelastic deformations take place at predetermined locations in the ends of the element. Another, in many respects more serious limitation, is the fact that lumped plasticity elements require calibration of their parameters against the response of an actual or ideal frame element under idealized loading conditions. This is necessary, because the response of concentrated plasticity elements derives from the moment–rotation relation of their components. In an actual frame element, the end moment–rotation relation results from the integration of the section response (see for example Chapter 3). This can be achieved directly with elements of distributed inelasticity (Filippou and Fenves 2004, Mergos and Kappos, 2008). For the latter approach, the so-called fiber beam elements (Fig. 6.1) provide results that seem to be particularly appropriate for studying the behavior of reinforced concrete (RC) structures under reversed cyclic loads: moment-axial force (M-N) coupling is readily taken into account, as well as the interaction between concrete and steel in the section. Whereas a few fiber beam-column elements have been developed with good capability of reproducing axial force and flexure effects, on the other

hand, the coupling between the effects of normal and shear forces is not straightforward and hence only a few modelling strategies have accounted for, and were fully implemented up till now (Ceresa et al., 2007).

A common framework, appropriate for the analysis of beam-column elements, is the Euler-Bernoulli approach. The fundamental kinematic assumption is that cross-sections remain plain and normal to the deformed longitudinal axis. The engineering beam theory reproduces the response of a beam under combined axial force and bending moments, while shear forces are recovered from a static equilibrium; the effects of shear on beam's deformation are neglected. Where the effects of tangential stresses are important for the element deformation (i.e. in a beam-columns joint or in the column/wall plastic hinge length), more refined theories like the Timoshenko beam theory may be used for modeling the member deformation response.

In the development of a nonlinear frame element, two main approaches have been used, namely the displacement-based (stiffness) approach and the force-based (flexibility) approach (see Chapter 3). The flexibility-based frame element gives the exact solutions for non-linear analysis of frame structures using force interpolation functions that strictly satisfy element equilibrium, and impose the compatibility conditions. Accordingly, this approach allows the overcoming of some limitations of the stiffness approach. In particular, the nonlinear analysis becomes independent of the displacement approximation, it requires fewer elements for the representation of the non-linear behaviour and, above all, in the case of a Timoshenko element or exact-beam theory-element, it avoids the well-known shear-locking problem (a sharp increase in the element stiffness which results in far fewer deformations for the element than expected) (Hughes, 2000).

A pre-requisite for incorporating the Timoshenko beam theory (i.e. accounting for shear) into the fiber approach that was detailed in Chapter 3, is the use of pertinent constitutive relationships. This includes fiber beam-column elements using smeared cracking models. According to this approach, cracked concrete is simulated as a continuous medium with anisotropic characteristics. In general, these models are referred to as "smeared cracking approaches" since cracking is modelled as a distributed effect with directionality. These approaches are particularly suitable for sectional analysis.

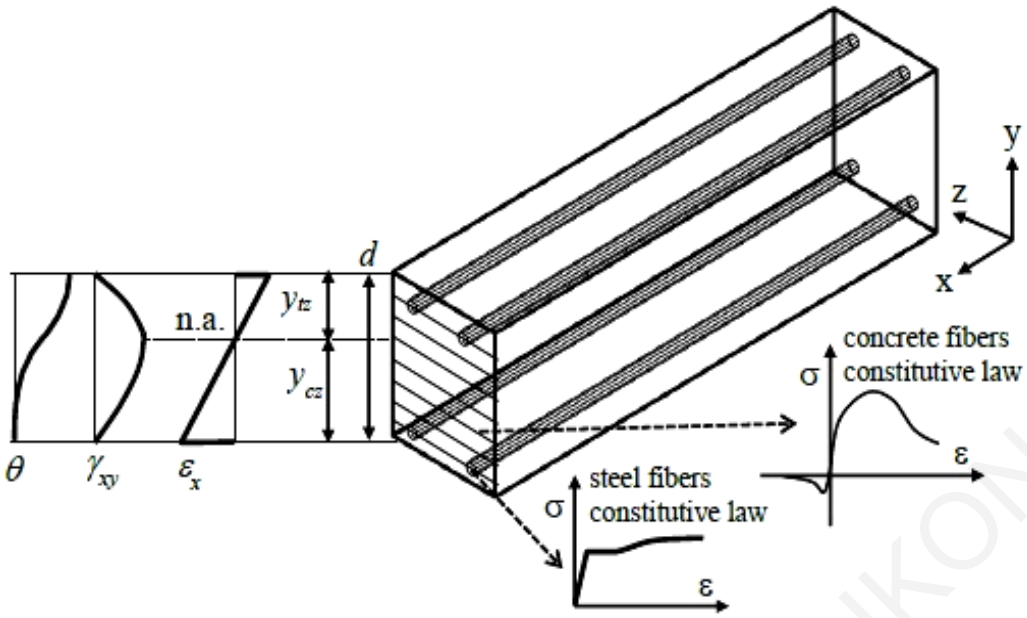

Figure 6.1: Fiber Element Scheme – definitions.

6.2 RC Sectional Model Based on Modified Compression Field Theory (MCFT)

Since the end of 1970s, a considerable amount of experimental and analytical research has been conducted with the aim of developing analytical procedures capable of estimating the load-deformation response of reinforced concrete elements loaded in shear (Ceresa et al., 2008). At the University of Toronto, Collins developed a procedure called the compression field theory (CFT) in 1978 (Collins, 1978). In 1981, a competition was held to predict the load-deformation response of four reinforced concrete panels tested at the University of Toronto (Collins et al., 1985), where leading researchers from around the world entered predictions based on various constitutive approaches. The results indicated that the most highly developed level in analytical modelling at the time was far from satisfactory. Generally, the models were not able to adequately estimate the ultimate strength, the failure mode or the load-deformation response of the panels. Most of the entrants used constitutive theories developed from tests conducted on plain concrete specimens; these do not account effectively for the modification of the properties of concrete after cracking, that is owing to the interaction between the concrete and steel that governs the response of reinforced concrete structures. In an effort to determine more realistic relationships for cracked reinforced concrete, Vecchio and Collins (1982) tested a series of RC panels. From these tests, the modified compression field theory (MCFT) (Vecchio & Collins, 1986) was

calibrated by including stress-strain relationships for cracked reinforced concrete under plane stress conditions.

An RC element is homogenized and is treated as anisotropic elastic material shown in Fig.6.2. Consider an elementary panel under constant plane stress, of uniform thickness, containing a rectangular grid of well distributed reinforcement. Loads acting on the element's edge planes are assumed to consist of uniform membrane stresses, i.e., axial stresses n_x, n_y and uniform shear stresses τ_{xy}. The deformed shape is defined by the strain tensor for plane stresses:

$$\begin{bmatrix} \varepsilon_x & \gamma_{xy}/2 & 0 \\ \gamma_{xy}/2 & \varepsilon_y & 0 \\ 0 & 0 & \varepsilon_z \end{bmatrix} \tag{6.1}$$

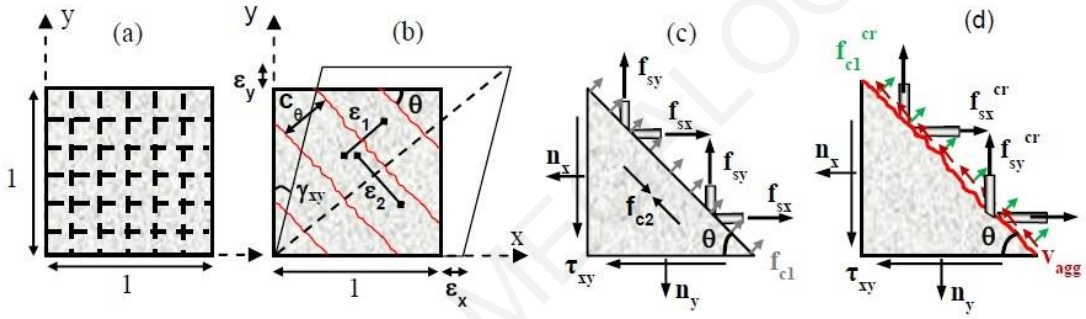

Figure 6.2: a) RC smeared-cracking membrane element, b) average strains (C_θ: spacing of cracks inclined at θ) c) average stresses and d) local stresses

The MCFT utilizes the following assumptions:

- The reinforcement is averaged or smeared throughout the element, i.e. the theory applies only to adequately-detailed members.
- The stresses applied to the element are uniform along edges.
- The total stress state is a function of the total strain state.
- The reinforcement is perfectly bonded to concrete, so that relative displacement due to bond slip between reinforcement and concrete is ignored.
- The shear stress in reinforcement is neglected.
- The principal stresses and principal strain axes are coincident; as a consequence, no deviation between the two is allowed.
- The constitutive relationships for concrete and reinforcement are independent.

- The cracks are smeared and allowed to rotate.

The theory comprises three sets of relationships: compatibility relationships between average strains of concrete and reinforcement, equilibrium relationships between externally applied loads and average stresses in the concrete and reinforcement; and uniaxial stress-strain relationships for cracked concrete along the principal directions and for reinforcement. The constitutive relationships for cracked concrete result from tests of reinforced concrete panels using a purpose-built Panel Element Tester at the University of Toronto. As such, the formulation of the MCFT calibrated with the specific tests conducted in the panel tester, incorporates realistic constitutive models for concrete based on experimentally observed phenomena. While cracks are smeared and the relationships are formulated in terms of average stresses and strains, a critical aspect of the MCFT is the consideration of the local strain and stress conditions at cracks (Fig.6.2d).

6.2.1 Constitutive Model based on MCFT for a Fiber RC Beam

In order to determine the normal and the shear stresses for the *i*-th fiber/layer (σ_x^i, τ_{xy}^i) of a fiber section of a RC beam (Vecchio & Collins, 1988), a bi-axial fiber constitutive model is developed according to the Modified Compression Field Theory (MCFT). The steps and mathematical expressions used to calculate the terms entering equilibrium, compatibility and stress-strain relationships are listed in Table 6.1. For the cross-sectional state-determination the following assumptions were made:

- The longitudinal ε_x and shear γ_{xy} strains are known for each fiber, according to the plane-sections assumption and to a parabolic shear strain distribution along the height of the section with the maximum value $\gamma_{xy.max}$ located on the neutral axis y_{na} (Eq. 6.2, two half-parabolas with the same maximum are met at the point of neutral axis with different starting point, extreme tensile and extreme compressive fiber respectively).

$$\gamma_{xy}(y) = \gamma_{xy.max} \cdot \left[2\left(\frac{y}{y_{na}}\right) - \left(\frac{y}{y_{na}}\right)^2\right] \tag{6.2}$$

- The transversal concrete stress f_{cy} was determined for each fiber from equilibrium conditions (zero normal stress n_y was assumed).
- The logical flow chart of the iterative procedure used is illustrated in Fig. 6.3. The parameter sought is the angle of principal directions assuming coincident principal axes for concrete principal stress and strain. In order to accelerate the convergence of the algorithm to the right value of the angle θ, the initial guess value of the procedure for the

angle of inclination of principal stresses/strains (angle of principal axis *2* with respect to *x*-axis) is determined according to the following equation:

$$\theta(y) = \frac{\pi}{4} \cdot \left(\frac{y}{y_{cz}}\right)^3, \quad 0 < y \le y_{cz}$$
$$\theta(y) = \frac{\pi}{4} + \frac{\pi}{4} \cdot \left[2\left(\frac{y-y_{cz}}{y_{tz}}\right) - \left(\frac{y-y_{cz}}{y_{tz}}\right)^2\right], \quad y_{cz} < y \le d \tag{6.3}$$

where y is the location of the concrete layer/fiber (y : zero reference is the extreme compressive fiber, Fig.6.1), y_{cz} is the depth of the compression zone, y_{tz} is the depth of the tension zone and d is the total depth of the section (i.e., $y_{cz}+y_{tz}=d$, Fig. 6.1).

Figure 6.4 depicts the angle shape function along the height of the section according to the above equation (d =457 mm, y_{cz} = 280 mm similar to Specimen 1 [Sezen & Moehle, 2006]). The solution to the iterative procedure is reached by applying the Regula Falsi root finding a numerical solution (Chabert, 1999).

Table 6.1: Equations embodied in the iterative procedure (Vecchio & Collins, 1988).

$\varepsilon_x = \varepsilon_{cx}$, $\varepsilon_1 = \varepsilon_x + \frac{\gamma_{xy}\cdot\tan(\pi/2-\theta)}{2}$, $\varepsilon_y = \varepsilon_1 - \frac{\gamma_{xy}}{2\cdot\tan(\pi/2-\theta)}$, $\varepsilon_2 = \varepsilon_x + \varepsilon_y - \varepsilon_1$
$f_{c1} = E_c \cdot \varepsilon_1$ for $0 < \varepsilon_1 \le \varepsilon_{cr}$, $f_{c1} = \frac{f_{cr}}{1+\sqrt{200\varepsilon_1}}$ for $\varepsilon_{cr} < \varepsilon_1 \le \varepsilon_{yx}$,
$f_{c2} = f_{c2max} \cdot \left[2\left(\frac{\varepsilon_2}{\varepsilon'_c}\right) - \left(\frac{\varepsilon_2}{\varepsilon'_c}\right)^2\right]$, $\frac{f_{c2max}}{f'_c} = \frac{1}{0.8-0.34\varepsilon_1/\varepsilon'_c} \le 1.0$, $f_{sy} = E_{sy}\varepsilon_y \le f_{yy}$
$f_{cy} = -\rho_y \cdot f_{sy}$, $\tau_{xy} = \frac{f_{cy}-f_{c2}}{\tan(\pi/2-\theta)}$, $f_{cx} = f_{c1} - \tau_{xy} \cdot \tan(\pi/2 - \theta)$, $G_{sec} = \frac{\tau_{xy}}{\gamma_{xy}}$,
$E_{sec} = \frac{f_{cx}}{\varepsilon_x}$,
$theta(\varepsilon_{cx}, \gamma_{xy}) = \tan^{-1}\frac{f_{c1}-f_{cy}}{\tau_{xy}}$
f'_c = Concrete Cylinder Compressive Strength (MPa),
ε'_c = Strain at Concrete Cylinder Compressive Strength,
E_c = Concrete Elastic Modulus (MPa),
f_{cr} = Tensile Concrete Strength (MPa),
ε_{cr} = Cracking Strain at attainment of Tensile Concrete Strength,

ε_{yx} = Yielding Strain of Longitudinal Reinforcement,

E_{sy} =Elastic Modulus of Stirrups (MPa),

f_{yy} = Yielding Strength of Stirrups (MPa),

ρ_y = Stirrup Reinforcement Ratio.

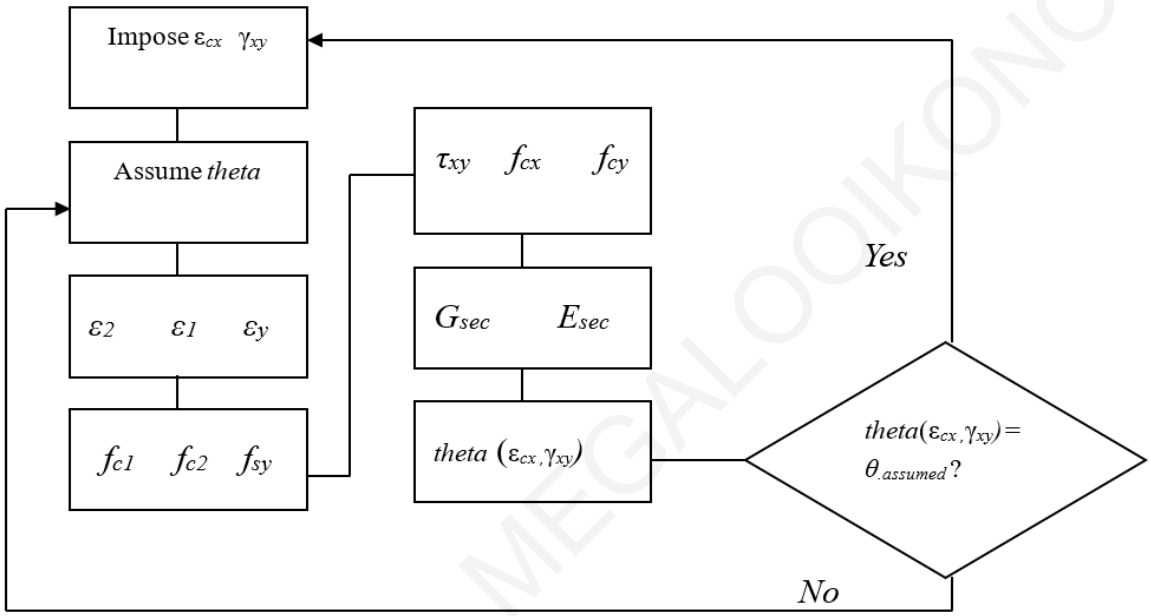

Figure 6.3: Flow Chart of the iterative procedure for each fiber/layer of the section according to MCFT.

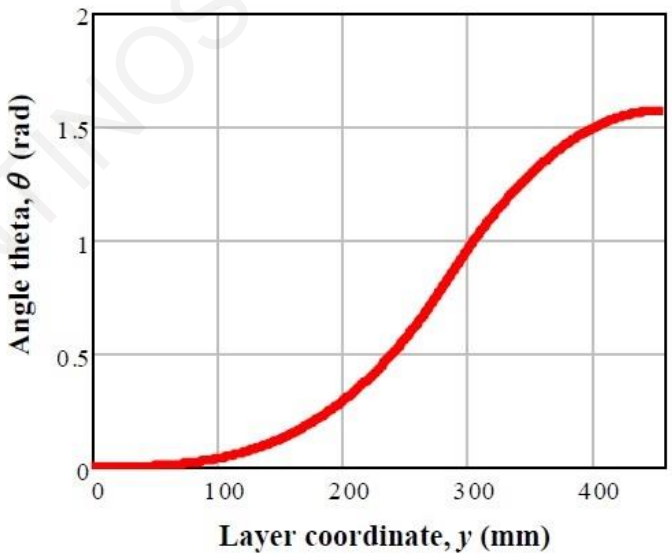

Figure 6.4: Shape function for angle theta *(θ)* of inclination of principal stresses/strains.

6.2.2 Sectional Model

Figure 6.5 depicts a beam element with its degrees of freedom and its displacement/forces in global, local and basic systems of reference. The term "basic" is derived from the system of reference where the rigid body motion of the beam is extracted. Considering now the virtual work principle for the beam element of Fig. 6.5, the Eq. 6.4 can be derived. The external work is done by the end forces (p) on the corresponding displacements (u), whereas the internal work is done by the basic forces (q) on the corresponding deformations (v).

$$\delta u^T p = \delta v^T q \tag{6.4}$$

The internal work of Eq. 5-4 can be derived from the integral of the stress product with the corresponding virtual strains over the element volume V. In many applications of nonlinear structural analysis, the internal work is limited to the internal work of normal stress σ_x and shear stress τ, on the axial strain ε_x and shear strain γ respectively (Filippou and Fenves 2004):

$$\delta v^T q = \int \delta\varepsilon^T \sigma \, dV = \int (\delta\varepsilon_x \, \sigma_x + \delta\gamma \, \tau) dV \tag{6.5}$$

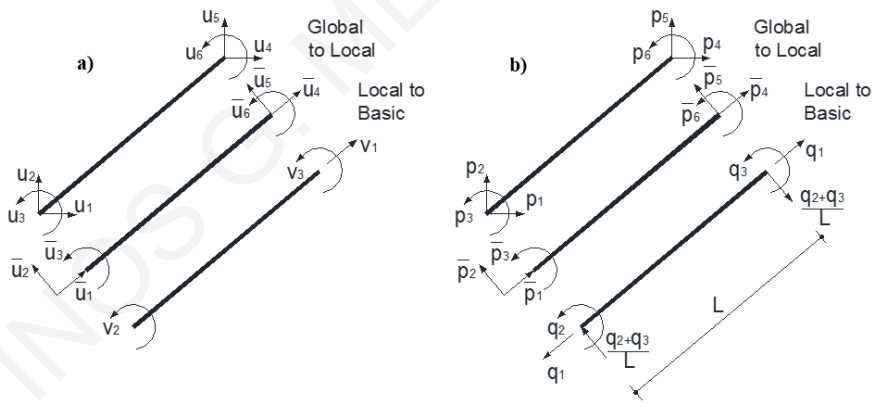

Figure 6.5: Beam a) displacements and b) forces in global, local and basic reference systems.

The strain and stress are functions of the position along the element longitudinal axis x and the position within the cross section specified in local coordinates y (with respect to the height) and z (with respect to the width). Equation 6.5 can be rewritten by substituting the integral over the element volume by integration over the sectional area A at a location x followed by integration over the element length:

$$\delta v^T q = \int (\delta\varepsilon_x \, \sigma_x + \delta\gamma \, \tau) dV = \int [\int (\delta\varepsilon_x \, \sigma_x + \delta\gamma \, \tau \,) dA] \, dx \tag{6.6}$$

The strains at a fiber/layer point of the beam cross section (*2d* case) are related to the sectional deformations as follows (Ceresa et al., 2008):

$$\varepsilon_x(x) = \varepsilon_0 - y_\varepsilon \cdot \varphi(x) \tag{6.7}$$

$$\gamma_{xy}(x) = \gamma_{xy.max} \tag{6.8}$$

where ε_0 is the axial deformation at the center of the coordinate system of the section (center of mass) and y_ε is measured also with reference to this center, $\varphi(x)$ is the curvature of the cross-section and $\gamma_{xy.max}$ is the maximum value of shear strain located on the neutral axis. Therefore, the strains at a material point *m* of the section can be expressed in matrix form as follows:

$$\varepsilon(x, y_\varepsilon) = \begin{Bmatrix} \varepsilon_x \\ \gamma_{xy} \end{Bmatrix} = \begin{bmatrix} 1 & -y_\varepsilon & 0 \\ 0 & 0 & 1 \end{bmatrix} \cdot \begin{Bmatrix} \varepsilon_0 \\ \varphi \\ \gamma_{xy.max} \end{Bmatrix} = B_s(y_\varepsilon) \cdot e(x) \tag{6.9}$$

$$B_s(y_\varepsilon) = \begin{bmatrix} 1 & -y_\varepsilon & 0 \\ 0 & 0 & 1 \end{bmatrix} \tag{6.10}$$

The internal resultant forces at the control section are given by:

$$Axial\ force: \quad N = \int \sigma_x dA \tag{6.11}$$

$$Shear\ force: \quad V = \int \tau_{xy} dA \tag{6.12}$$

$$Bending\ Moment: \quad M = -\int y_\varepsilon \sigma_x dA \tag{6.13}$$

These can be written in matrix form as follows:

$$f_s(x) = \int {B_s}^T(y_\varepsilon) \cdot \sigma(x, y_\varepsilon) dA \tag{6.14}$$

where:

$$f_s(x) = \begin{Bmatrix} N \\ M \\ V \end{Bmatrix}, \; B_s(y_\varepsilon) = \begin{bmatrix} 1 & -y_\varepsilon & 0 \\ 0 & 0 & 1 \end{bmatrix}, \; \sigma(x, y_\varepsilon) = \begin{Bmatrix} \sigma_x \\ \tau_{xy} \end{Bmatrix} \tag{6.15}$$

Taking into account the section discretization into fibers/layers, the total forces on the beam section are easily computed through the summation of the individual fiber contributions:

$$N = \sum_{i=1}^{n.layer} \sigma_x^i A^i \quad , \quad V = \sum_{i=1}^{n.layer} \tau_{xy}^i A^i \quad , \quad M = -\sum_{i=1}^{n.layer} \sigma_x^i {y_\varepsilon}^i A^i \tag{6.16}$$

where A^i is the area of the *i*-th fiber/layer. Normal and shear stress for the *i*-th fiber/layer ($\sigma_x{}^i$, $\tau_{xy}{}^i$) are obtained from the respective strains using a bi-axial fiber constitutive model according to the MCFT (Fig. 6.3, $\sigma_x^i = f_{cx}^i$). In the employed procedure, the section forces are determined based on known sectional deformations; thus, as in the case of the model presented in Chapter 3, for known forces, the iterations are conducted over the values of the deformations within a predefined acceptable tolerance for the force magnitudes.

The procedure for calculating the tangent section stiffness matrix k_s is obtained from differentiation of the section force vector f_s with respect to the section deformation vector e as described also in Chapter 3:

$$k_s = \begin{bmatrix} \frac{\partial f_{s_1}}{\partial e_1} & \frac{\partial f_{s_1}}{\partial e_2} & \frac{\partial f_{s_1}}{\partial e_3} \\ \frac{\partial f_{s_2}}{\partial e_1} & \frac{\partial f_{s_2}}{\partial e_2} & \frac{\partial f_{s_2}}{\partial e_3} \\ \frac{\partial f_{s_3}}{\partial e_1} & \frac{\partial f_{s_3}}{\partial e_2} & \frac{\partial f_{s_3}}{\partial e_3} \end{bmatrix} \tag{6.17}$$

$$k_s = \frac{\partial f_s}{\partial e} = \int {B_s}^T(y_\varepsilon) \cdot \frac{d\sigma(x,y)}{\partial \varepsilon(x,y)} \cdot \frac{\partial \varepsilon(x,y)}{\partial e} dA = \int {B_s}^T(y_\varepsilon) \cdot \frac{d\sigma(x,y)}{d\varepsilon(x,y)} B_s(y_\varepsilon) dA \tag{6.18}$$

$$\sigma(x, y_\varepsilon) = \begin{Bmatrix} \sigma_x \\ \tau_{xy} \end{Bmatrix} \; \varepsilon(x, y_\varepsilon) = \begin{Bmatrix} \varepsilon_x \\ \gamma_{xy} \end{Bmatrix} \tag{6.19}$$

$$\frac{d\sigma(x,y)}{d\varepsilon(x,y)} = \begin{bmatrix} E_m & 0 \\ 0 & G_m \end{bmatrix} \tag{6.20}$$

where E_m and G_m are the tangent moduli of the stress – strain relations at a point *m* of the section approximated here by E_{sec} and G_{sec} (Table 6.1, Fig. 6.3).

6.3 Embedded Algorithms in Phaethon Software

The simple cantilever column is considered under various load combinations (axial load, moment and shear); this represents the shear-span of an actual column under lateral sway, extending from the support to the point of inflection (i.e. position of zero moment). Although from a statics perspective this is a very simple case, its numerical simulation with all interacting deformation mechanisms is still yet a very challenging task to accomplish. Towards this need and for the case of shear-critical cantilever reinforced concrete columns a computer program was developed to be used as a tool for the study of the mechanics of the nonlinear program (software "Phaethon"). In the following section the algorithms embodied in this Windows application are presented.

6.3.1 Moment – Curvature Algorithm

Through the cross-sectional analysis, the unknown moment M (and the associated axial deformation ε_0) are determined for given number of curvature φ increments, and the unknown shear force V for simultaneous shear strain γ increments, with or without the presence of constant axial load N. The system of equations for section equilibrium is established as follows:

$$\begin{Bmatrix} N - N_r(\varepsilon_0, \varphi, \gamma) = 0 \\ \mathrm{M} - \mathrm{M}_r(\varepsilon_0, \varphi, \gamma) = 0 \\ V - V_r(\varepsilon_0, \varphi, \gamma) = 0 \end{Bmatrix} \tag{6.21}$$

The explicit coupling of the resisting forces is noted. With N, φ and γ given, the first equation is used to solve for ε_0; then this value is substituted along with the given values for φ and γ into the second and third equations, in order to determine M and V. The resisting axial force in the first Eq. 5-21 is expanded with Taylor series and the higher than linear terms are truncated:

$$N - \left[N_r(\varepsilon_{00}, \varphi_0) + \frac{\partial N}{\partial \varepsilon_0}\Delta\varepsilon_0 + \frac{\partial N}{\partial \varphi}\Delta\varphi + \frac{\partial N}{\partial \gamma}\Delta\gamma \right] = 0 \tag{6.22}$$

where the second subscript *0* denotes the initial seed value for the solution. Given the axial force N, the curvature increment $\Delta\varphi$ and the shear strain increment $\Delta\gamma$, the above equation can be solved for $\Delta\varepsilon_0$:

$$\Delta\varepsilon_0 = \left(\frac{\partial N}{\partial \varepsilon_0}\right)^{-1} \cdot \left(N_u - \frac{\partial N}{\partial \varphi}\Delta\varphi - \frac{\partial N}{\partial \gamma}\Delta\gamma \right) \qquad \text{with,} \quad N_u = N - N_r(\varepsilon_{01}, \varphi_1) \tag{6.23}$$

For each step, the numerical solution is distinguished in two main phases: the incrementation phase, which consists of the application of the curvature and shear strain increment, and the convergence phase, where iterations are done to satisfy equilibrium under fixed axial force, curvature and shear strain. The axial force is applied in an initial step under zero curvature and zero shear strain. Therefore, the following algorithm is applied in Phaethon for this task:

Given section geometry and material properties, a value for the axial force N, curvature increment $\Delta\varphi$ and shear strain increment $\Delta\gamma$ (e is the section's strain vector and $\boldsymbol{f_s}$ is the resisting section force vector- see previous Section).

Incrementation Phase: for *k = 1..m*

1. Initial guess $e_0^{(k)} = e^{(k-1)}$ the solution at *k-1* with $e^{(0)} = 0$

2. Determine $f_s^{(k)} = f_s\left(e_0^{(k)}\right)$ and $k_s^{(k)} = k_s\left(e_0^{(k}\right)$ according to previous Section

3. Determine

$$N_u^{(k)} = N - f_{s1}^{(k)} \text{ and } \Delta\varepsilon_0^{(k)} = \left(\frac{\partial N}{\partial \varepsilon_0}\right)^{-1} \cdot \left(N_u^{(k)} - \frac{\partial N}{\partial \varphi}\Delta\varphi - \frac{\partial N}{\partial \gamma}\Delta\gamma\right) \text{ where}$$

$$\frac{\partial N}{\partial \varepsilon_0} = k_{s11}^{(k)}, \quad \frac{\partial N}{\partial \phi} = k_{s12}^{(k)} \text{ and } \frac{\partial N}{\partial \gamma} = k_{s13}^{(k)}$$

4. Update solution $e_1^{(k)} = e_0^{(k)} + \begin{pmatrix} \Delta\varepsilon_0^{(k)} \\ \Delta\varphi \\ \Delta\gamma \end{pmatrix}$

Convergence Phase: Iteration for *i = 1..n* and constant *k* (skip superscript)

1. Determine $f_s = f_s(e_i)$ and $k_s = k_s(e_i)$

2. Determine $N_u = N - f_{s1}$ and $\Delta\varepsilon_0 = \left(\frac{\partial N}{\partial \varepsilon_0}\right)^{-1} \cdot (N_u)$ where $\frac{\partial N}{\partial \varepsilon_0} = k_{s11}$

3. Update solution $e_{i+1} = e_i + \begin{pmatrix} \Delta\varepsilon_0 \\ 0 \\ 0 \end{pmatrix}$

The algorithm returns back to Step 1 of the Convergence Phase, until the error norm satisfies the specified tolerance. Upon convergence, the final state is updated thus determining the bending moment and shear force. At that stage the algorithm returns to Incrementation Phase at Step 1.

6.3.2 Pushover Algorithm

For the calculation of the lateral load resistance curve of a column shear span under lateral sway, pushover analysis is conducted: Considering a cantilever shear-critical RC column in Phaethon, the sectional model (either rectangular or circular) established in the previous Section is employed along with the anchorage model in the footing outlined in Chapter 5. An increasing lateral point load at the tip of the cantilever is applied (Fig. 5-6) and a unique fiber element is assigned to the entire height of the cantilever column with the number of

Gauss-Lobatto integration points selected by the user. The user also selects the analysis step of lateral load V to be applied in the Pushover analysis, and the total number of steps until maximum load is attained. (Note that the Modified Compression Field Theory in the fiber approach as described by Bentz (2000) cannot reproduce the descending branch of shear-critical columns which is why a load-control procedure was selected to be embedded in Phaethon). The maximum load in Phaethon is the load of the last step of convergence of the algorithm in incremental form. It should be highlighted that in reality the shear-critical column's ascending response is followed by a descending branch of progressive failure; however, the proposed algorithm is limited by strength attainment. After peak load, the descending branch of the capacity curve is defined as the line connecting the maximum load point with the point at axial failure; this is quantified in terms of the drift estimate by Elwood and Moehle (2005) and 20% of the attained maximum load as residual load at axial failure.

For each point load at the tip of the cantilever (Fig. 6.6) the corresponding shear force at the assigned column's sections (integration points) is equal to that load (constant shear diagram). The flexural moment at the base of the column, M_0, as well as the moment distribution, are both obtained from the lateral load value (constant shear force). The concentric axial load (tensile or compressive) applied at the tip of the cantilever is also constant throughout the pushover analysis and along the length of the cantilever and therefore each column's section has an axial force value equal to the one applied at the tip. Following this procedure, the vector $\boldsymbol{f_s}$ which is the vector of resisting section forces (see previous Section) should converge to the above defined section forces based on the moment, shear and axial load diagram of the cantilever column under constant axial load and gradually increasing lateral tip point loading.

The following algorithm is applied in Phaethon to achieve this convergence:

Given the externally applied section forces s, i.e. an axial force N, a bending moment M and a shear force V, the equilibrium equation between applied and resisting section forces is set up:

$$s_u(e) = s - f_s(e) = 0 \tag{6.25}$$

The Newton-Raphson algorithm for the solution of the system of three nonlinear equations is:

1. Given the nonlinear equations $s_u(e) = 0$ and a guess of the solution e_0.

2. For $i = 0...n$ determine function value $s_u(e_i)$ and derivatives $k_s(e_i)$ (see previous Section).

3. Determine correction to previous solution estimate, $\Delta e_i = s_u(e_i)/k_s$

4. Update the solution estimate: $e_{i+1} = e_i + \Delta e_i$

Return to Step 2 until the error norm is smaller than specified tolerance. On convergence determine the resisting forces for the final deformations.

It should be highlighted that for the cases of "pure compression" or "pure tension" with the angle of inclination of principal stresses/strains (angle of principal axis 2 with respect to *x*-axis) being zero or $\pi/2$ respectively then no iteration is required, but the fiber state determination is defined from the normal strains, after referring directly to the uniaxial stress strain laws of the materials (previous Section, Table 6.1) without calculating any rotation for the principal axes.

After convergence of the section forces is achieved along the length of the cantilever column to the correct values based on the corresponding forces' diagrams along the element due to the applied tip horizontal and axial load, the axial deformation, curvature and shear strain is determined for each section. Integrating the curvatures (Fig. 6.6) along the shear span of the cantilever column leads to the rotation of the cantilever column due to flexure, which can be easily transformed to lateral displacement due to flexure $\Delta_o{}^f$ by multiplying with the length of the shear span. Integration of the shear strains (Fig. 6.6) by sampling a few sections (positions defined according with Gauss-Lobatto) along the length of the cantilever column (integration points) leads to the lateral displacement $\Delta_o{}^{sh}$ due to the shear distortion mechanism of the cantilever column. Finally, the rotation and the displacement $\Delta_o{}^{sl}$ due to pull-out of the tensile reinforcement (Fig. 6.6) is determined based on the closed-form solution of the governing equation of bond (Tastani and Pantazopoulou (2013)) described also in Chapter 5. All the above simultaneous contributions (flexure, shear and anchorage) are added together to define the total lateral displacement (i.e., $\Delta_o = \Delta_o{}^f + \Delta_o{}^{sh} + \Delta_o{}^{sl}$) of the cantilever column at each lateral load step and to obtain the capacity curve of the column until maximum lateral load (Fig. 6.6).

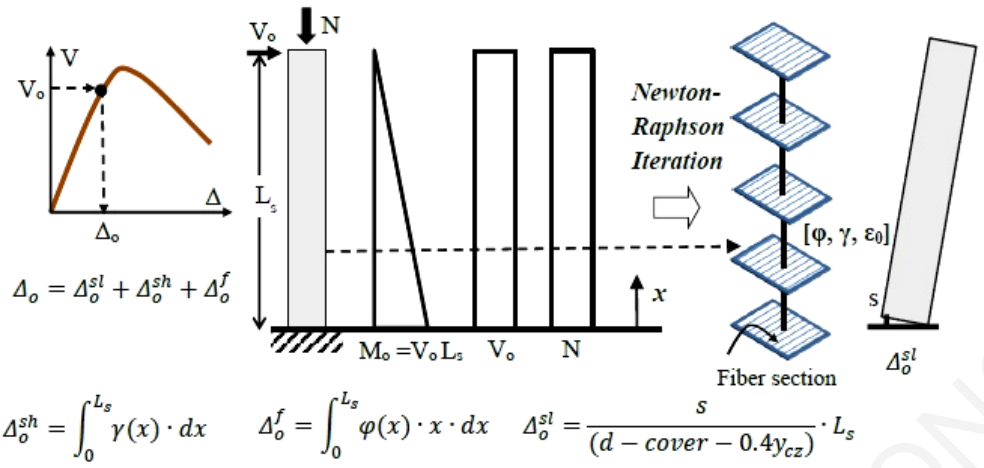

Figure 6.6:. Pushover Analysis in Phaethon.

6.4 Correlation with Experimental Results

This section presents the correlation of the shear-flexure capacity curves obtained from the pushover analysis conducted using Phaethon with the experimental response curves of a number of shear-critical RC columns selected from literature. In the correlation are also included curves obtained from flexural fiber beam/column-based toolbox FEDEAS Lab (see also Chapter 3, Filippou et al, 2004) and from MCFT-based software and dual-section analysis Response 2000 (Bentz, 2000).

The shear capacity degradation curve of RC columns as a function of displacement ductility is approached by EN 1998-3 (2005) and ASCE-SEI 41 (2007) (see also Chapter 2 and Chapter 3) and can be used as the basic criterion in order to detect shear failure before or after flexural yielding depending on the point of intersection with flexural capacity curve (Fig. 6.7). To this end, it is necessary to define the flexural capacity curve based on classic flexural analysis and combine it with the shear capacity curve in order to define the strength and deformation of the RC column at shear failure. This procedure is adopted in this section in order to initially detect whether the columns under study will fail in shear before or after flexural yielding and therefore to judge whether the “Phaethon” tool is suitable.

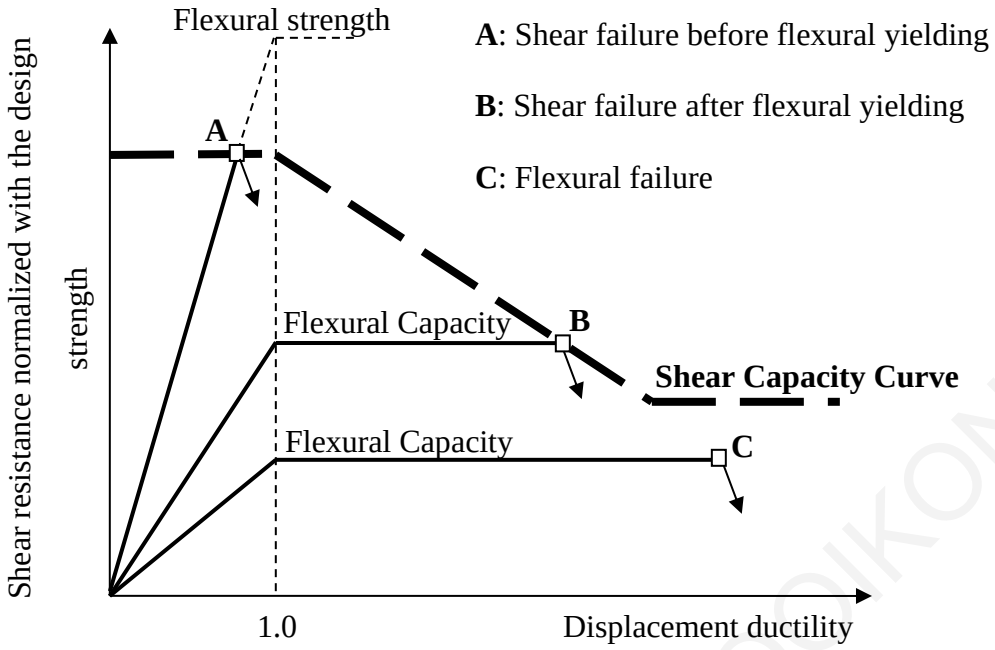

Figure 6.7: Shear strength degradation model adopted by current codes of assessment.

6.4.1 Rectangular Shear-Critical Columns

The first selected rectangular column for comparison is Specimen 1, from the experimental campaign of Sezen and Moehle (2006) that failed in shear after flexural yielding. Its properties are reported in Table 6.2. Figure 6.8 compares the experimental response (in red) with the analytical flexural capacity curve (in blue) and the shear capacity obtained by EN 1998-3 (in green) and by ASCE-SEI 41 (in black) (here the yielding displacement in both shear-strength degradation models is defined by the flexural analysis based on the applied fiber element included in FEDEAS Lab; it can be read from the end of the initial plateau of EN 1998-3 model). The ASCE-SEI 41 estimates a very conservative shear strength value as compared to the yielding strength of this specimen which would be interpreted as premature brittle failure; EN 1998-3 detects the column's shear failure after yielding in terms of strength but at lower displacement compared to the experimental result (i.e. it overestimates the secant to yield stiffness).

Table 6.2: Details of RC columns failed in shear (units: mm, MPa, kN).

Case	Axial Load	Width - Depth or Diameter	Shear Span	Clear Cover	Concrete Strength	Number - Diameter – reinforcing ratio of Longitudinal Bars	Yielding – ultimate Strength of Long. Bars	Yielding Strength - spacing – Diameter –ratio of Transv. Reinf.
Sezen & Moehle (2006) – (Spec. 1) Rectangular cross section	667	457 457	1473	65.13	21.1	8 28.65 0.025	434 645	476 304.8 9.5 0.0025
Lynn et. al. (1996) – (Spec. 3 CMH18) Rectangular cross section	1512	457 457	1473	38.1	27.6	8 31.75 0.03	331 496	400 457 9.5 0.00082
Ang et al. (1989) – (Spec. 19) Circular cross section	432	400	600	18*	34.4	20 16 0.032	436 679	326 80 6 0.0038
Ang et al. (1989) – (Spec. 20) Circular cross section	807	400	700	18*	36.7	20 16 0.032	482 758	326 80 6 0.0038

*: Cover to Ctr. of Hoop Bar

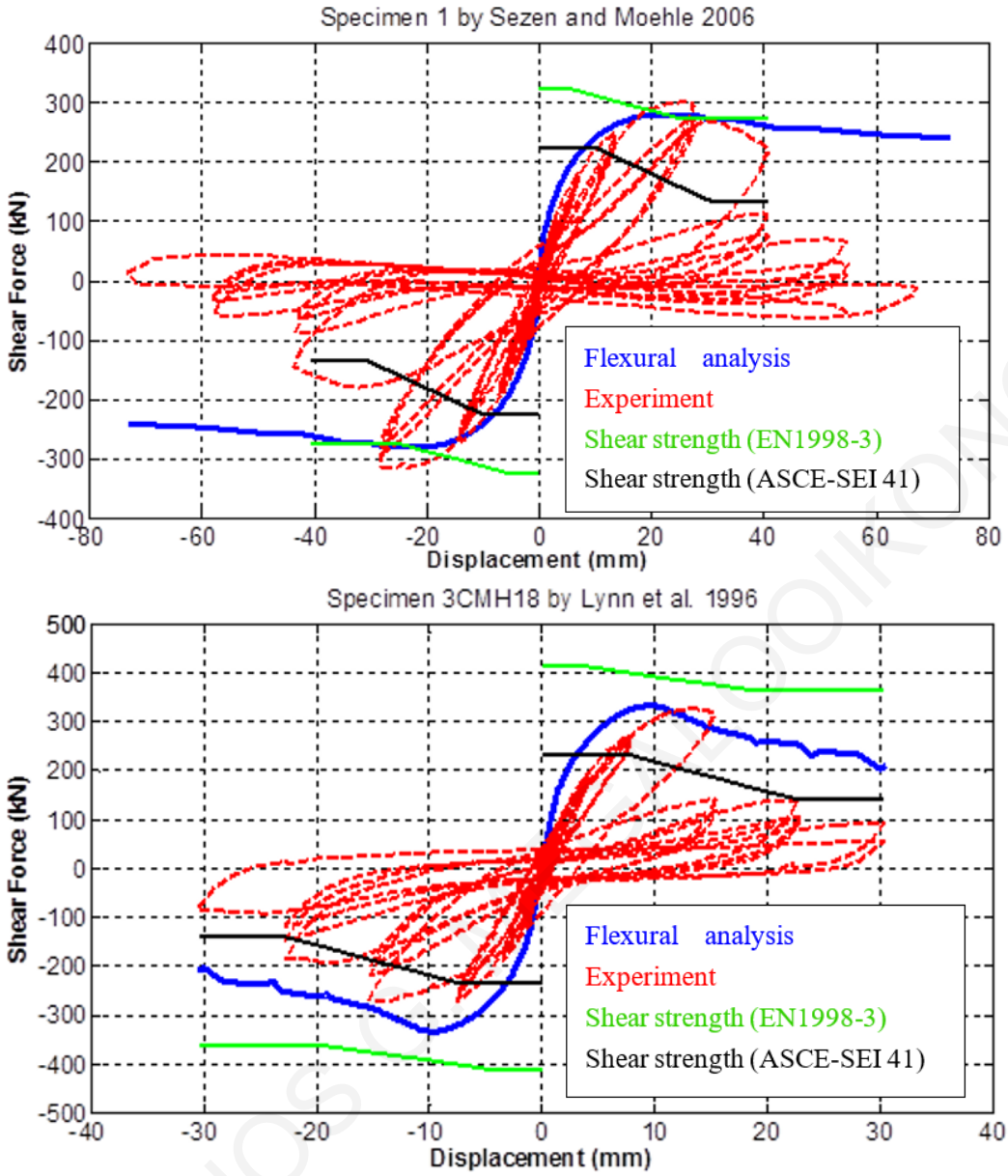

Figure 6.8: Detection of shear-critical rectangular reinforced concrete columns.

As can be seen in Fig. 6.9 the comparison of the capacity curve defined by Phaethon for Specimen 1 (that failed in shear after flexural yielding) until the maximum load, is close to the experimental response but also close to the capacity curves by the other already mentioned software. The deviation of stiffness close to peak load from Phaethon is improved when the displacement component due to pull-out of the tensile reinforcement incorporates the contribution of reinforcement slip from shear span L_s is added (Megalooikonomou et al., 2018, Chapter 5). Figures 6.10 and 6.11 depict the displacement contributions in each pushover analysis step from the various interacting mechanisms as they are defined by Phaethon and they are compared also those measured during the experiment. It is seen that

at the onset of yielding (10 mm total lateral displacement reported by Phaethon) Phaethon gives correctly 62% contribution from flexural deformation, 35% from pull-out and almost 3% from the shear mechanism (which, in this case, is underestimated).

In Fig. 6.8, the degrading shear capacity curve of Eurocode 8 Part 3 (EN 1998-3) doesn't intersect with the flexural capacity curve for the second selected specimen by Lynn et al. (1996). This takes place only with the model of ASCE-SEI 41 almost at the point of yielding at a lower strength and displacement compared to the experimental response.

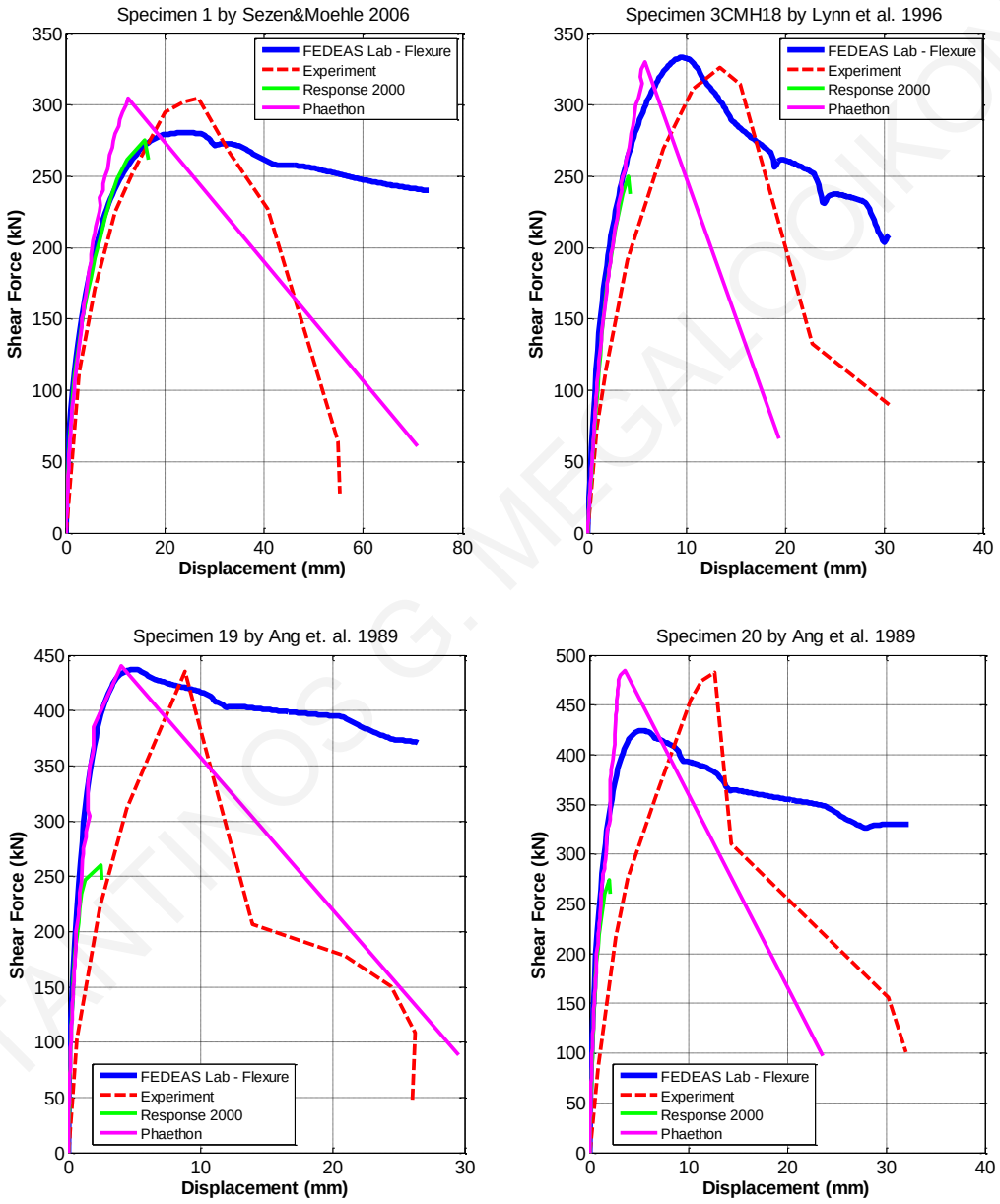

Figure 6.9: Comparison of the capacity curves provided by Phaethon and other software with the experimental responses.

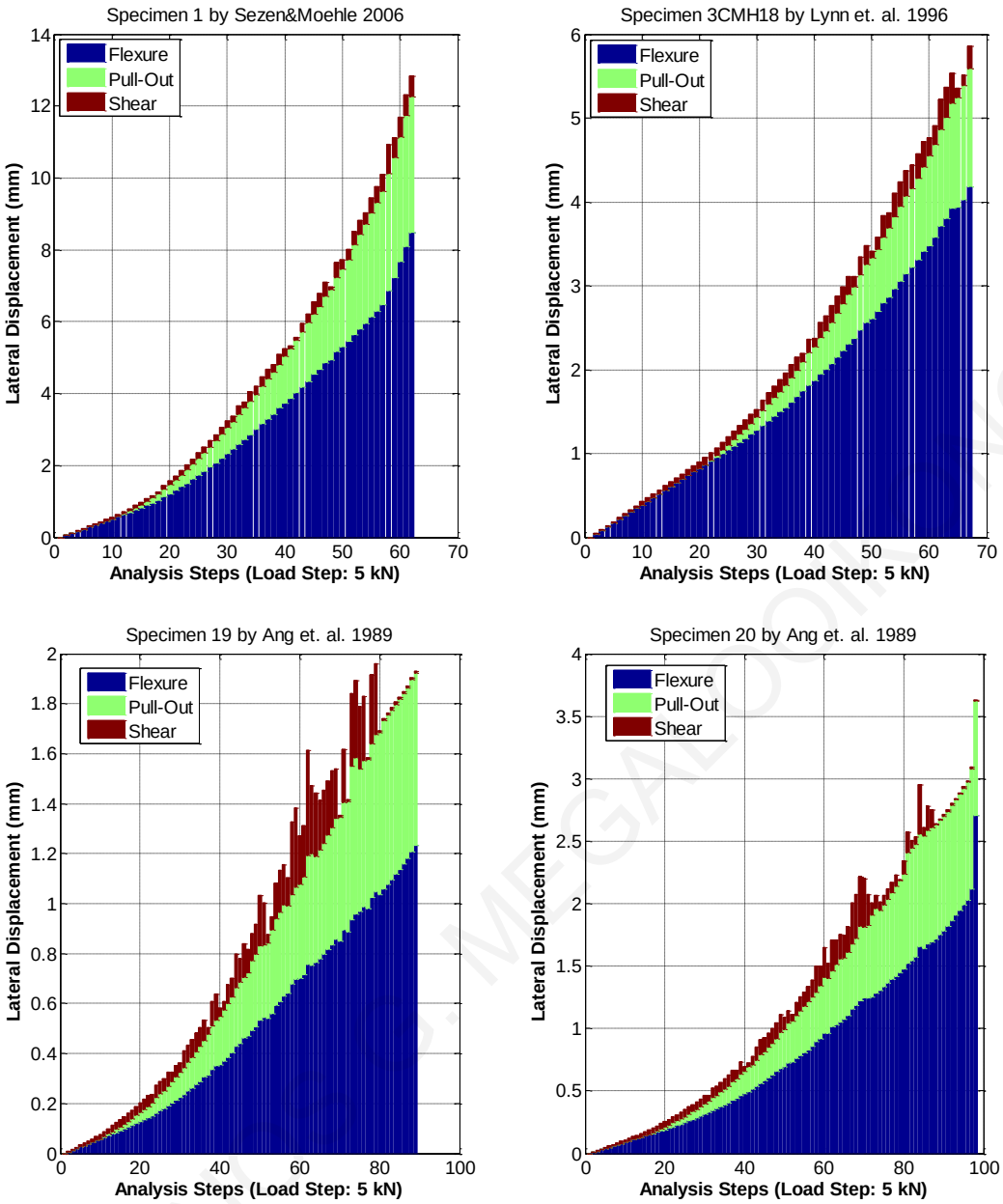

Figure 6.10: Displacement Contributions from various deformation

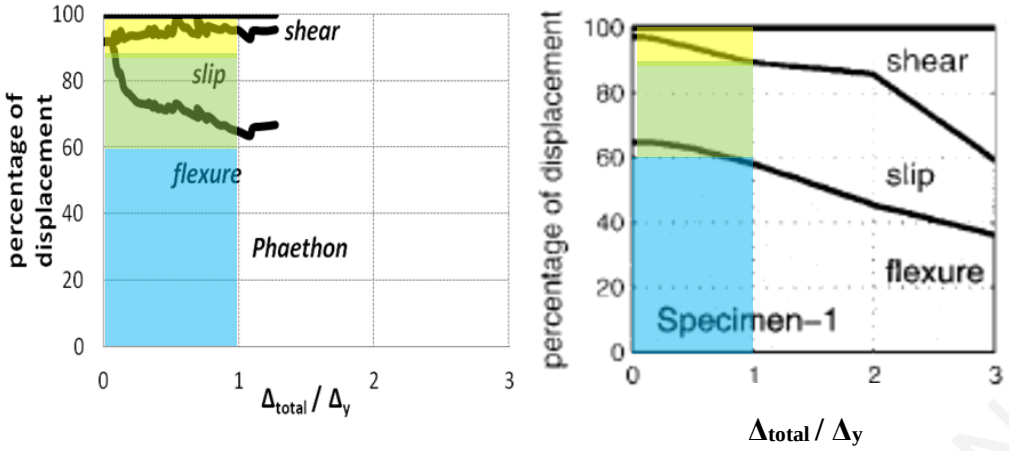

Figure 6.11: Displacement contributions from various deformation mechanisms included in Phaethon (left) for rectangular column compared to the experiment (right) (Sezen and Moehle [2006]).

The second selected rectangular column for comparison is (Spec. 3CMH18) from the experimental campaign of Lynn et al. (1996) that failed in shear before flexural yielding. Its properties are presented in Table 6.2. As can be seen in Fig. 6.9 the comparison until the maximum load is close to the experimental response but also close to the capacity curves by the other already mentioned software. Here, Response 2000 underestimates the specimen's strength and doesn't provide the descending branch of the capacity curve due to shear failure before flexural yielding, while FEDEAS Lab overestimates the response after maximum load is attained since it doesn't consider any shear-flexure interaction mechanism. Phaethon estimates satisfactorily the maximum load as well as the descending branch of the response in this case too. However, in all analytical capacity curves the experimental initial stiffness is overestimated. The axial failure (i.e. collapse as defined by Phaethon) is also reached at a lower displacement compared to the experiment. Finally, Fig. 6.10 depicts the contributions of the various mechanisms of resistance to displacement in each pushover analysis step from the various interacting mechanisms as they are defined by Phaethon. As it can be seen, they are simultaneously increasing with the applied lateral load.

6.4.2 Circular Shear-Critical Columns

The third selected column for comparison is the circular Specimen 19 from the experimental campaign of Ang et al. (1989) that failed in shear before flexural yielding. Its properties are presented in Table 5-2. In Figure 5-12, it can be observed that it is a shear-critical column since both the shear strength degradation models detect shear failure (albeit wrongly, after flexural yielding) at a displacement lower than the corresponding experimental one. The strength at shear failure is better predicted by the model of Eurocode 8 part 3 (EN 1998-3) compared to the alternative of ASCE-SEI 41.

As it can be seen in Figure 6.9 the comparison of the Phaethon response until the maximum load is close to the capacity curves by the other aforementioned software. However, the initial stiffness predicted by Phaethon is higher compared to the experiment although identical to what the other software tools define. Phaethon reproduces well also the maximum load but not the corresponding displacement. The descending branch as defined by Phaethon follows the experimental strength degradation. A closer estimate is obtained for the shear strength by Phaethon as compared to Response 2000. Finally, Fig. 6.10 depicts the contributions to displacement in each pushover analysis step, from the various interacting mechanisms as they are defined by Phaethon. As can be observed from the figure, deformation components are increasing with the applied lateral load, and here, owing to the aspect ratio of the circular column, (short column), the contribution of shear deformation is significant.

The fourth selected column for comparison is the circular Specimen 20 from the experimental campaign of Ang et al. in 1989 that failed in shear after flexural yielding. Its properties are presented in Table 6.2. In Figure 6.12, it can be observed that it is a shear-critical column since both the shear strength degradation models detect shear failure after yielding at a displacement lower than the corresponding experimental one. The strength at shear failure is better predicted by the model of Eurocode 8 part 3 compared to the alternative of ASCE-SEI 41.

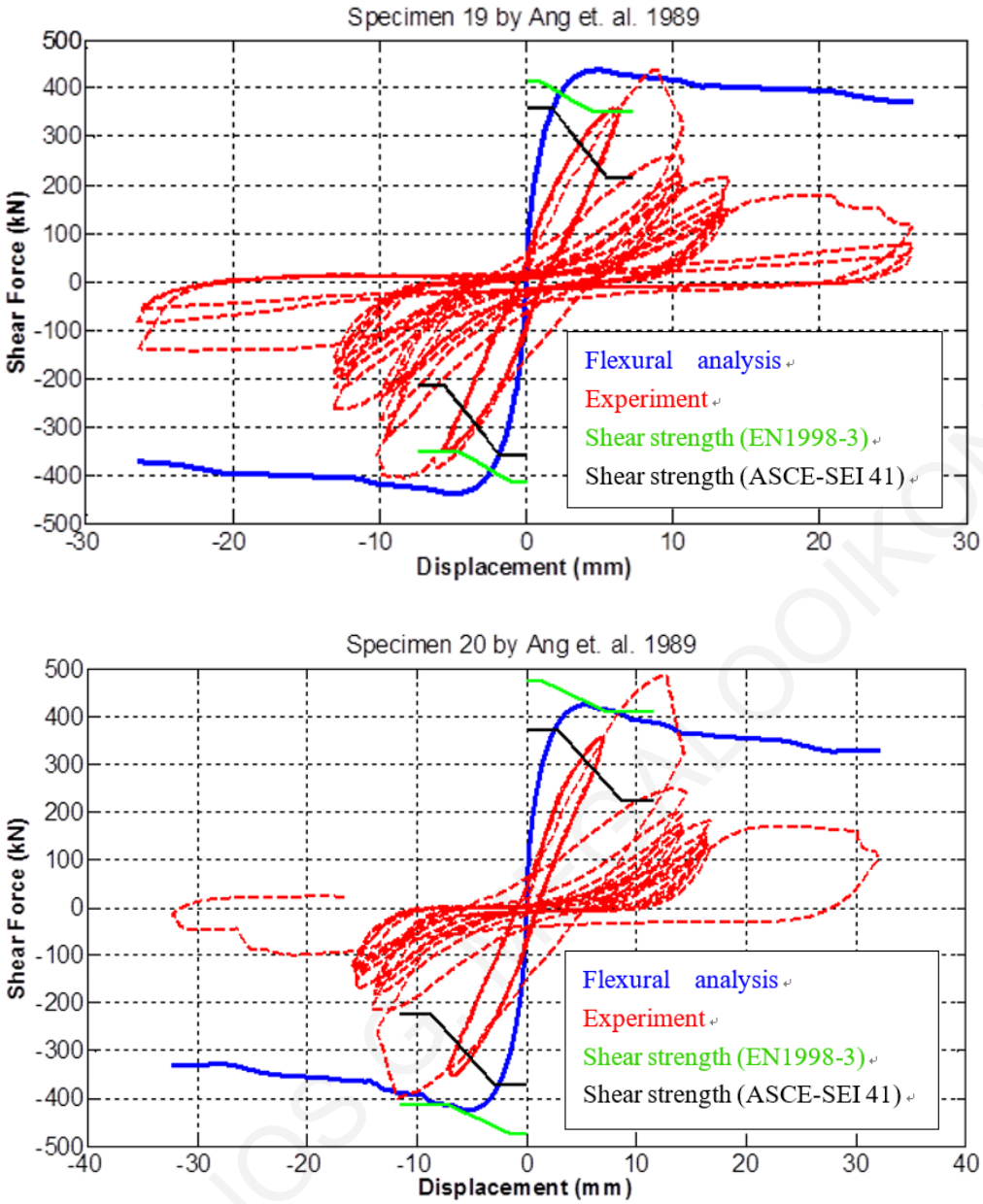

Figure 6.12: Detection of shear-critical circular reinforced concrete columns.

As may be seen in Figure 6.9 the comparison of the Phaethon response until the maximum load is close to the capacity curves by Response 2000; shear strength estimation is better approximated by Phaethon. However, the initial stiffness predicted by Phaethon is higher compared to the experiment although identical to what the other software tools define. Phaethon also captures well the maximum load but not the corresponding displacement. The descending branch as defined by Phaethon follows the experimental strength degradation. The axial failure (i.e. collapse as defined by Phaethon) is reached at a lower displacement compared to the experiment. Finally, Figure 6.10 depicts the displacement contributions in

each pushover analysis step from the various interacting mechanisms as they are defined by Phaethon. As may be noticed by the values of shear strain contribution, convergence of the algorithm at higher displacement levels was rather slow and sometimes erratic. Values were filtered by a tolerance criterion in order to maintain stability and convergence of the analysis.

6.5 Parametric Investigation

The parametric sensitivity of the developed software on the produced capacity curve is investigated in this section, considering as a point of reference Specimen 1 by Sezen and Moehle (2006), examined in the preceding section. Parameters considered are the discretization sensitivity of the force-based fiber element of the cantilever column and the effect of axial load, stirrup spacing and shear span length on the produced pushover curve; in each case one parameter at a time is varied, while keeping the reference values for all other variables (so the possible interaction effects between variables have not been considered in conducting the sensitivity analysis).

In Figure 6.13 the effect on the pushover curve of different number of Gauss-Lobatto integration points [Ele(Number)IP] can be observed along the element, as well as the number of integration points/layers of the Midpoint integration rule along the section [Sec(Number)L]. As expected, by increasing the number of Midpoint layers and Gauss-Lobatto integration points the capacity curve stabilizes, converging to the final result. Deviation from the final result is evident only where fewer integration points both at the section level, and along the element length have been used.

As may be observed in Figure 6.14, by increasing the compressive axial load (here it is given in normalized form) the shear strength of the column under study is correctly increasing and the deformability of the column is decreasing reaching lower displacements at maximum load (shear failure) and at point of axial failure (collapse). The effect of stirrup spacing for a given shear-critical column on the stiffness of the resistance curve produced by Phaethon was negligible but the displacement at axial failure (collapse) was decreasing as the spacing of stirrups was increased. Reducing the shear span of the cantilever column (Figure 6.15) correctly reproduces a more shear-dominant and less deformable reinforced concrete column both at maximum load (shear failure) but also at the point of axial failure (collapse).

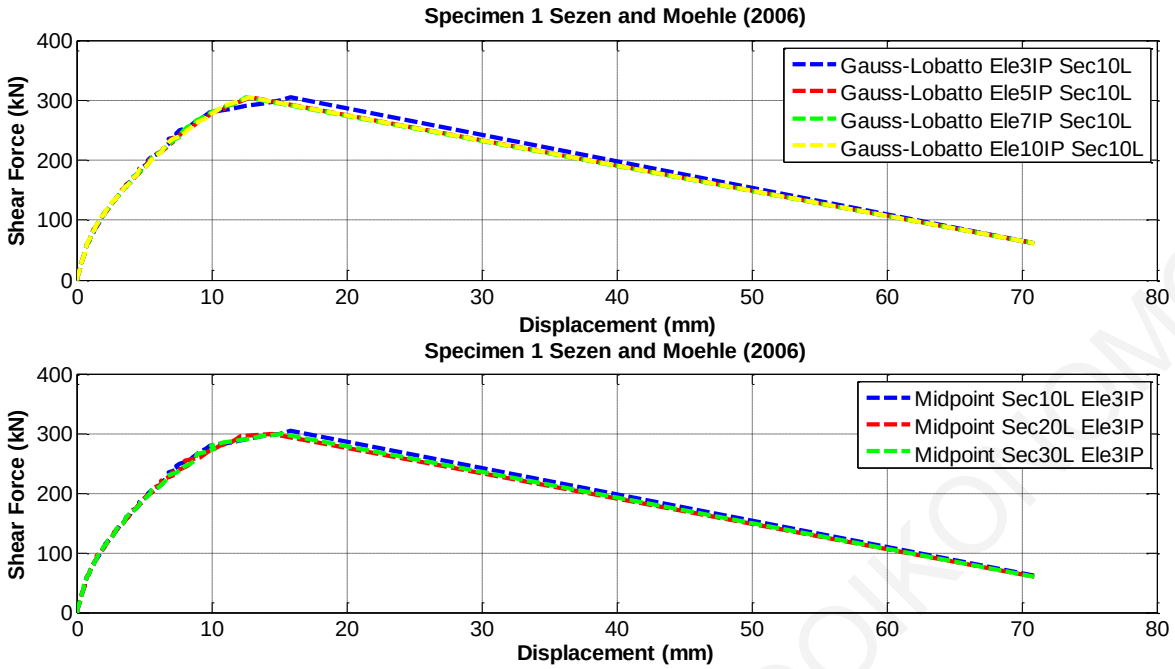

Figure 6.13: Discretization sensitivity along fiber section and element of the capacity curve provided by Phaethon.

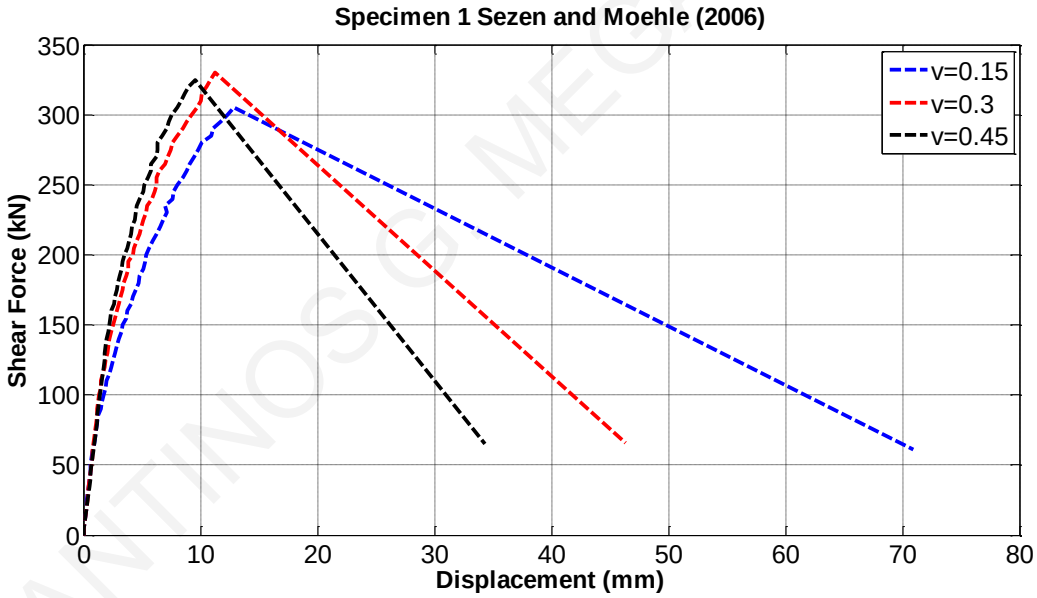

Figure 6.14: Effect of axial load on capacity curve provided by Phaethon.

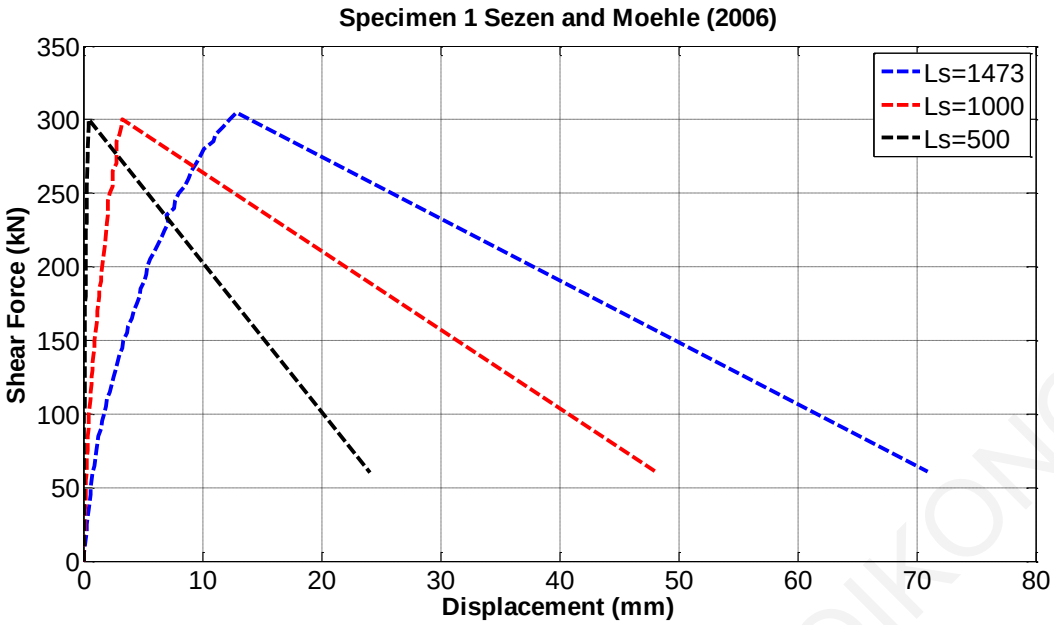

Figure 6.15: Effect of shear span on capacity curve provided by Phaethon.

The Phaethon software installation file may be downloaded freely from the following web address: http://bigeconomy.gr/en/phaethon-en/.

7 Analytical Stress-Strain Model for FRP-Confined Rectangular RC Columns

7.1 Introduction

It was discussed in Chapter 5 that the rotation or drift capacity of a laterally swaying column is quantified by the rotation of the deformed member from its chord in the displaced position. Several different sources of local deformation contribute to the member rotation from its chord, such as, flexural curvature and shear distortion occurring along the shear span, as well as rotation at the support due to reinforcement pullout from the anchorage and crack opening. In swaying columns, the most significant crack often occurs at the column base, where the moment is maximum (Saatcioglu and Ozcebe, 1989, Priestley et al. 1996, Syntzirma et al. 2010). The crack width at that location is a result of bilateral reinforcement slip, both from the column and from the foundation (Chapter 5). The critical flexural crack facilitates rotation of the column about the cross-section's neutral axis. The cracked cross section, which acts as a pole, experiences a local increase of compression strains on account of the fact that the solid compression zone cannot penetrate into the solid footing. Therefore, the required slip has to be accommodated by shortening of the column in the compression zone region. This corresponds to a local compression strain increase, which accelerates spalling of the unconfined cover (Syntzirma et al. 2010). Based on the experimental evidence from wall testing, it appears that this type of slip-flexure interaction inevitably leads to cover spalling within the range of relatively small ductility demands. In order to prevent this premature failure FRP confining jackets has been recommended as a remedy solution.

Confining wraps or jackets to rehabilitate and strengthen existing substandard RC columns such as those described in the present thesis has proven to be an efficient technique for seismic retrofit of structures. The existing literature has an abundance of research works on modelling of circular reinforced concrete columns confined with FRP wraps. The compressive behaviour of concrete cylinders externally confined with FRP under axial loads has been extensively studied nowadays. Numerous stress-strain models have been established during the last three decades. Some of these studies (Vitzileou *et al.*, 2008; Rousakis *et al.*, 2012; Jiang and Wu, 2012; Ozbakkaloglu *et al.*, 2013; Rousakis and Tourtouras, 2015; Hany *et al.*, 2016; Ozbakkaloglu *et al.*, 2016; Farahmandpour *et al.*, 2017) concentrated on modelling the conditions during failure of FRP-confined concrete, including

the ultimate compressive strength and the corresponding ultimate axial strain. Other studies simulate and describe the overall behaviour of the stress-strain curve of FRP-Confined concrete under compression (Hosotani *et al.* 1997; Samaan *et. al*., 1998; Spoelstra and Monti, 1999; Lam and Teng, 2003; Yu *et al.*, 2010a; Yu *et al.*, 2010b; Wang *et al.*, 2011; Ozbakkaloglu *et al.*, 2013; Eid and Paultre, 2017; Fahmy *et al.*, 2017; Ismail *et al.*, 2017). The available stress-strain models in literature have been grouped into two categories by Lam and Teng (2003): (a) design-oriented models and (b) analysis-oriented models. Design-oriented models provide the stress-strain behaviour using closed-form equations, while analysis-oriented models achieve that by an incremental numerical procedure. Such an analysis-oriented model for FRP-confined circular RC columns can be found in Megalooikonomou *et al.* (2012) and Papavasileiou and Megalooikonomou, (2015). The advantage of analysis-oriented models over design-oriented models is their computing versatility. Moreover, they can be easily integrated to a structural analysis software such as Phaethon, where they can be incorporated in the fiber analysis of complete structural components. To the author's knowledge, such an analysis-oriented model for rectangular FRP-confined columns is not yet available. The proposed model was developed with the intention to be integrated in existing structural software such as OpenSees (2006). Furthermore, the approach of this model is unique. While other available models intend to capture the stress-strain behaviour of FRP-confined concrete, the proposed model intends to simulate effectively the axial and lateral strain and, consequently, simulate the stress-strain behaviour. The confining stress occurs as a reaction to the developed strain. This way, in addition to simulating the stress-strain behaviour, the proposed model also yields the lateral dilation, which is not explicitly calculated in available models.

Literature on the modelling of rectangular section FRP-confined RC columns is more limited. While existing studies (Teng *et al.*, 2002; Lam and Teng, 2003; Teng and Lam, 2004; Piscesa *et al.*, 2018) have verified that FRP confinement can substantially enhance both the compressive strength, ductility and energy dissipation of confined concrete in circular-section RC columns, the same method has been found to be much less effective for rectangular RC columns (Mirmiran *et al.*, 1998; Rochette and Labossiere, 2000; Lam and Teng, 2003; Megalooikonomou, 2007; Karabinis *et al.*, 2008; De Luca *et al.* 2011). Corner rounding is recommended overall to enhance the confinement effectiveness in a rectangular RC column and to reduce the detrimental effect of sharp corners on the performance of FRP jackets which causes their rupture in relatively low strain (Lam and Teng, 2003).

The main difference between the two RC column section cases is that in circular sections the confinement is uniform, while the same does not apply on rectangular sections (Mander *et al.* 1988). In the later, concrete is non-uniformly confined, so the effectiveness of the confinement is substantially reduced.

As illustrated in Fig. 7.1, the imposed axial load on a circular section causes radial dilation (*i.e.* uniform strain) on the confining elements so the pressure applied by the jacket to the concrete as a reaction to its dilation is uniform as well. Hence, the stress-state developed in a circular section is uniform. In rectangular sections the confining element develops a concentration of stresses at the corners, where FRP develops its peak stress. Along the sides, its confining effectiveness is reduced as it does not have enough stiffness to fully restrain the dilation of the concrete column. Thus, a non-uniform confining stress-state is developed in the concrete section.

Previous modelling approaches concentrated mainly on dividing the rectangular section in a confined and an unconfined area (Fig. 7.1), based on the concept of possible arching effect (e.g. EN1998-3, Fig. A1). Then, the confined area is considered to be in a state of uniform biaxial confinement, as in the circular cross sections, thus allowing the use of formulas defined for circular FRP-confined elements. The unconfined part is considered to be unaffected.

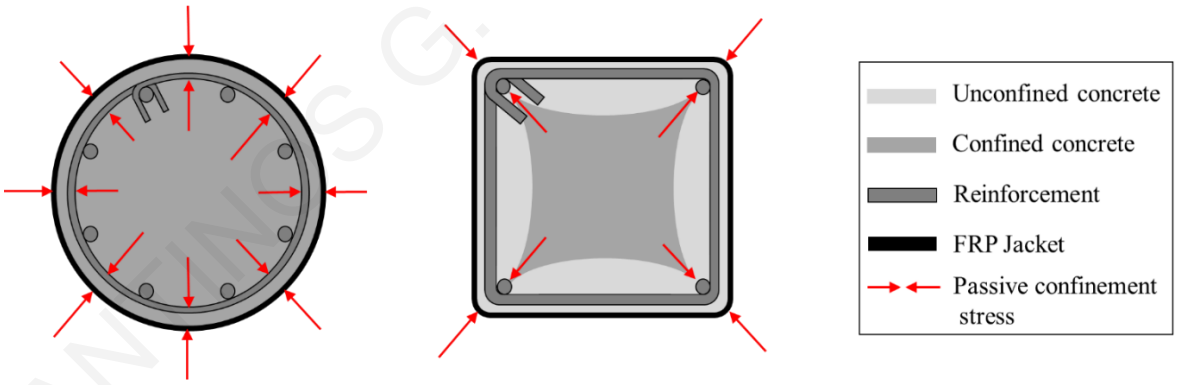

Figure 7.1: Confining mechanisms for circular and rectangular sections.

Considering all the above remarks, an iterative procedure was developed in this research study based on the results of a 3D FEM analysis performed by the author which indicates that the arching effect is not an accurate representation of the actual state of stress in the FRP-confined column cross-section. The unconfined areas shown in Fig. 7.1 are indeed partially confined and they contribute to the overall capacity of the section until they reach their maximum strength which is significantly reduced compared to that of the

confined areas. The analytical procedure employs a system of 'generalized' springs, well-known stress-strain laws and a failure criterion to model the resultant response of the FRP-confined rectangular cross section columns under axial load.

7.2 Numerical Analysis (Finite Element Model)

Figure 7.2 depicts the cross-section of an experimentally tested FRP-confined square concrete specimen under concentric load and the final concrete state along with the effective concrete core after FRP failure at the corner at the end of the experiment (Campione and Miraglia, 2003). Uneven damage can be observed throughout the section. Two different regions can be identified having different confining stress states. To determine the confining stresses and define the confined and unconfined regions in a rectangular section, a 3D Finite Element Model was developed in SAP 2000 (CSI, 2016). The model consists of a square concrete section 200x200 mm (Fig. 7.2) with rounded corners. Solid elements are used to model concrete in the section. The FRP wrap is modelled using shell elements applied on the solid elements in the perimeter. A typical slice with thickness 10mm was simulated. The CFRP wrap was modeled using an orthotropic material model with Young's modulus $3.61 \cdot 10^5$MPa. The confined concrete was modeled with a 'concrete' material with f_{ck} = 17MPa. The applied axial displacement on the FEM model was increased until the lateral strain at the slice was equal to the maximum lateral strain at a cylindrical specimen, when it reaches the maximum strength. The maximum axial displacement was defined so that the lateral strain developed in the slice is equal to that an unconfined cylindrical specimen at the ultimate stress. The FEM results were plotted in three-dimensional graphs (Fig. 7.3) to allow further study of the stress field. Verification of the results yielded by the FEM model against experimental results is available in Teng *et al.* (2015).

Graphs in Fig. 7.3 depict various stress fields in a quadrant of this square section. Stresses near the rounded corner are not shown since they represent local stress state. In Fig.7.3a and 7.3b, the normal stresses parallel to the diagonals (SD1 and SD2) are presented, while in Figs. 7.3c and 7.3d normal stresses parallel to the section's sides (SO1 and SO2) are shown. Stresses parallel to the diagonal of the rounded corner, are increased near the corner, but moving inwards to the centre of the section they reduce significantly (Megalooikonomou, 2007; Nistico and Monti, 2014). Figure 7.3 also illustrates that the stresses perpendicular to the rounder corner, the diagonal direction and close to the sides have much lower values compared to those parallel to rounded corner diagonal, while

towards the centre they both become almost equal. This confirms that close to the centre the confinement stress state is similar to the axisymmetric states of stress seen in circular sections. It is apparent from the plots of the stress field parallel to the orthogonal directions (Fig.7.3c & 7.3d) that some confining stresses are present along the side, while in the central part of the perpendicular side they are close to zero, as the confining device has minimal flexural stiffness.

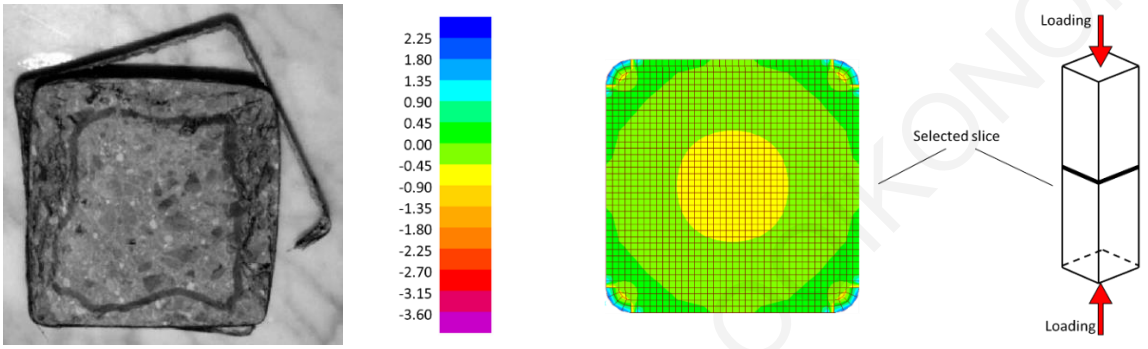

(a) **(b)**

Figure 7.2: Cross-section of a short square column: (a) experiment (Campione and Miraglia, 2003), (b) FEM model.

Based on the aforementioned, the following main remarks can be made:

- No unconfined concrete regions are observed, as assumed in many models. The parts near the edges are confined due to forces coming from the corners and moving parallel to the edges.
- The confining forces near the perimeter have strong directionality (uniaxial confinement). On the contrary, near the centre the state seems to be more uniform (axisymmetric confinement).

Accepting some tolerance, the regions where a biaxial and a uniaxial confinement exist can thoroughly be defined based on the ratio of the principal stresses of the two perpendicular directions in the joints of the FEM. Regarding the stress output in SAP 2000 (CSI, 2016), it is noted that the direction of the middle principal stress (Smid) is perpendicular to the maximum (Smax) and minimum (Smin) principal directions.

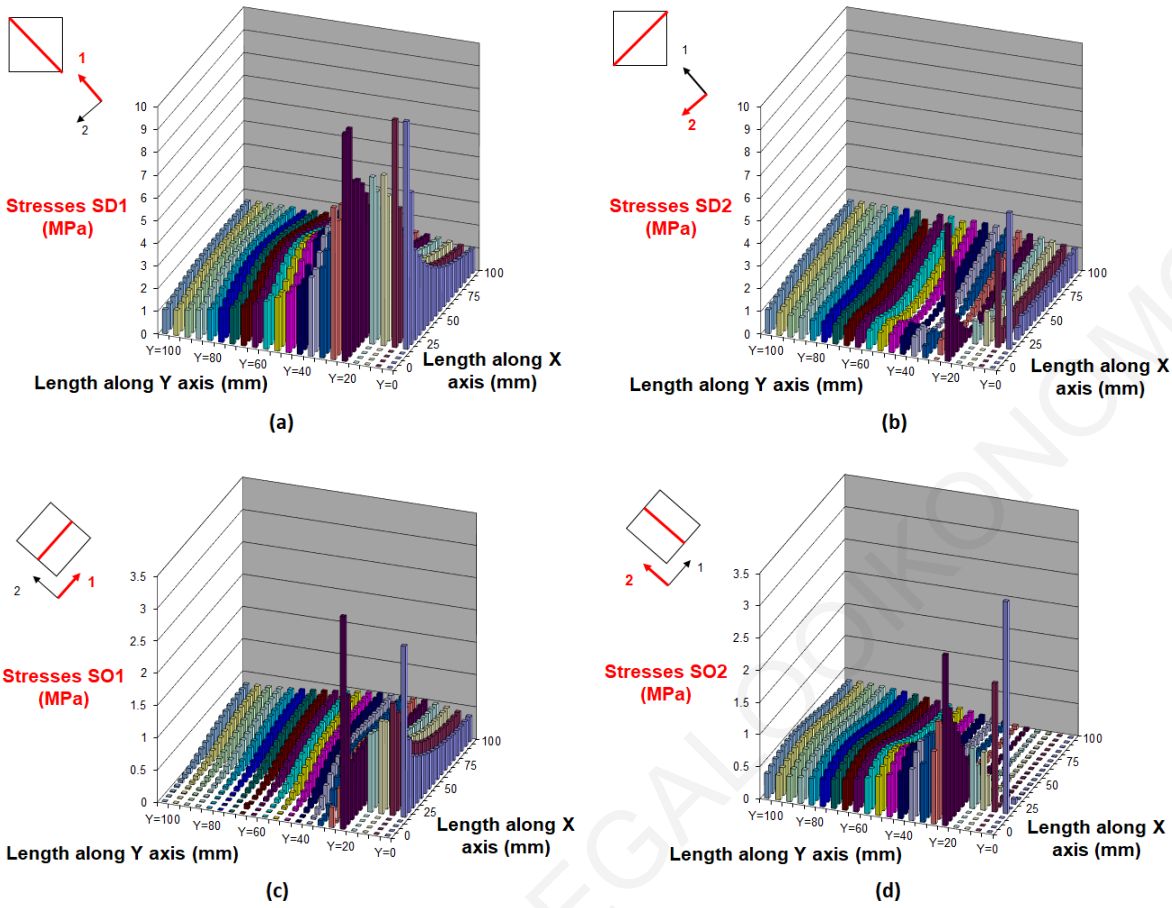

Figure 7.3: Confining stresses in a quartile of a square section 200×200mm: along diagonal (a,b) and orthogonal (c,d) direction. The round corner stresses are not included.

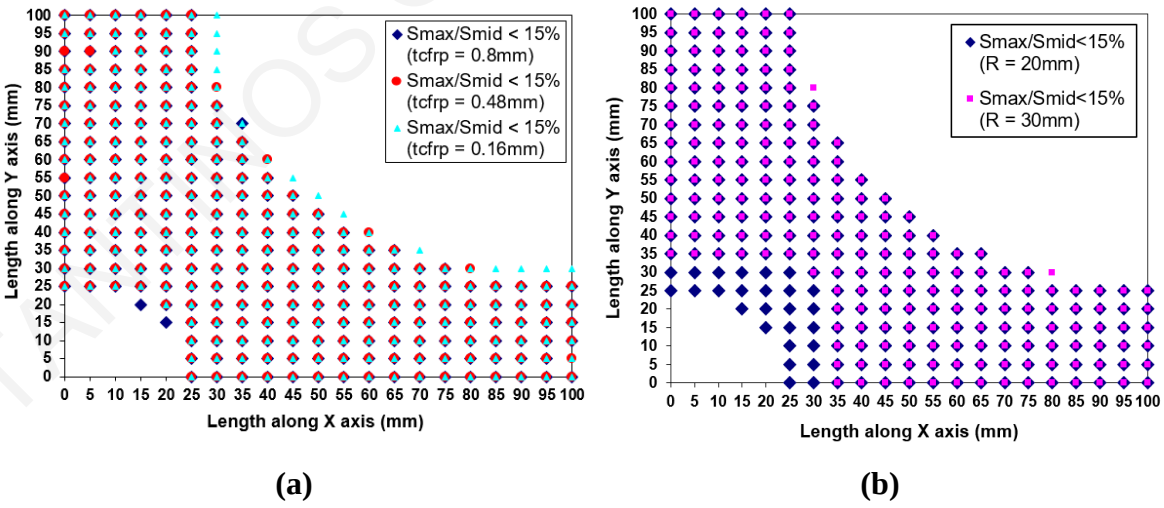

Figure 7.4: Uniaxially and biaxially confined regions: (a) different thicknesses of FRP jacket, (b) different radii of rounded corner.

For a specific tolerance (*i.e.* the ratio of the confining stresses (S_{max}/S_{mid}) is less than 15%), the width of the biaxial stress state region is independent of the stiffness of the FRP

(Fig. 7.4). The radius of the rounded corner affects more the diagonal dimension of this region, while parallel to the sides the width remains the same (Fig. 7.4). Unlike reinforced concrete, where the spacing of stirrups allows for such regions to develop, not only on the concrete cover but also between two consecutive stirrups, FRP-confined members are totally inside the FRP wrap. Due to the FRP's non-infinite stiffness, the FRP wrap can deform laterally to the cross-section. A finite slice of the FRP wrap performs as a cantilever beam with its ends at the rounded corners of the concrete section. The larger the deformation might get (*i.e.* a weaker FRP slice), the smaller the stress applied by the FRP on the confined concrete core is. No matter how small it might get, there is always stress applied on the concrete, so it does not perform as unconfined-concrete. The model considers the confinement pressure to be the same around the column. Hence, the smaller the side which this pressure is distributed on, the more effective the confinement provided. This leads to the conclusion that, unlike unconfined concrete, in FRP-confined concrete the part of the section that is under biaxial confinement is not proportional to the relevant side, but proportional to the opposite side. This assumption is confirmed in previous works (Karam and Tabbara, 2005; Megalooikonomou, 2007). Based on these remarks, the width of the uniaxially confined region can be calculated using Eq. 7.1, where *a* and *b* are the width and the depth of a rectangular section accordingly (Fig.7.8a). The dimensions of the regions are then directly related and determined according to this width (Fig.7.10).

$$h_1 = a/8 \quad and \quad h_2 = b/8 \qquad \text{(Eq. 7.1)}$$

The equations used in the proposed model was initially developed based on results yielded by modelling square FRP-confined concrete columns. Having assessed its effectiveness in modelling square columns, its applicability on rectangular columns was also assessed against experimental results and found to be adequate for a simplified analytical model.

7.3 Simplified Mechanical Model

A simplified mechanical model which describes the stress-strain behaviour of a rectangular concrete cross-section under concentric load is formulated. A series of 'generalized' springs (Fig. 7.5) is used to describe the confinement mechanism. Compressed concrete expands laterally according to its confinement state. Such expansion activates the passive confining elements. The confining forces are applied to the section corners and transferred along the diagonal. In the proposed model, the contribution of the stirrups is considered to be minimal

and is not taken into account. This refers to cases of old construction where stirrup spacing is adequately large to minimize the confinement contribution.

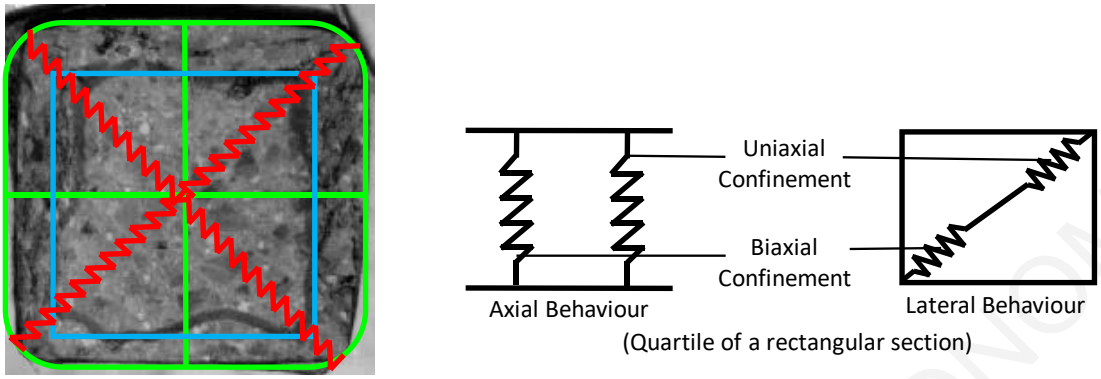

Figure 7.5: FRP-confined rectangular concrete section modelling using 'generalized' springs.

Fig. 7.5 shows the springs used to model the axial and the lateral behavior of the section. Axially, the springs receive the same displacements and their cumulative strength is the summation of the strength of the individual springs (parallel system). Laterally, the springs receive the same force and their displacements are additive (series system).

The 'generalized' springs illustrated in Fig. 7.5 use the constitutive law for concrete proposed by Pantazopoulou and Mills (1995). The model which relates the volumetric strain to the axial strain is shown in Fig. 7.6 (right). In the same figure (left), the corresponding axial stress vs. axial strain is also demonstrated. It is evident that adequate confinement increases the ductility of the RC member which develops considerably larger strain until its stiffness and strength are particularly reduced leading to loss of stability. This is shown in the relationship between volumetric strain ε_v and axial strain ε_c plotted in Fig.7. 6.

The initial slope of the curve (Eq. 7.2, for $\varepsilon_c \leq \varepsilon_l^{lim}$) is characteristic of a perfectly elastic condition. Both curves (for confined and unconfined concrete) deviate from this idealised situation. However, confined concrete develops large volumetric strain reaching much higher axial strain magnitudes than unconfined concrete. Experimentally, in conditions of high confining stress, it has been observed that the ε_V vs. ε_c curve might even remain at negative values of ε_V throughout the test.

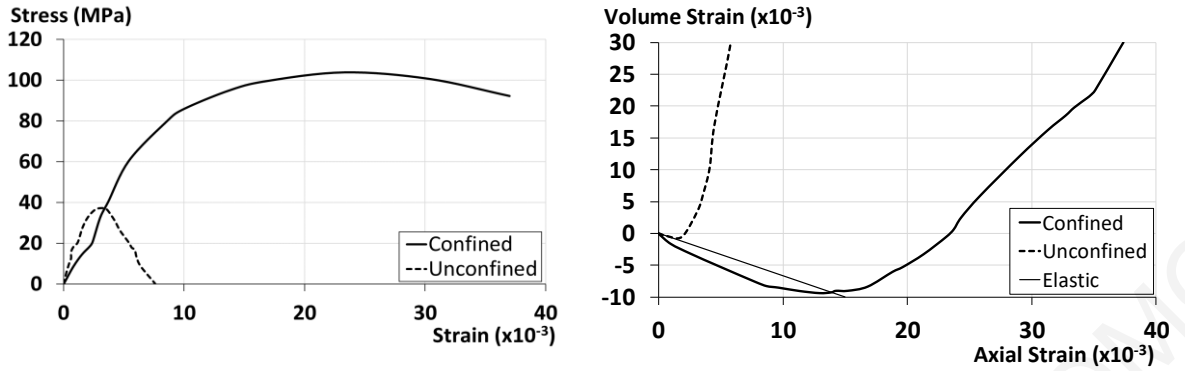

(a) **(b)**

Figure 7.6: Constitutive law for confined concrete (Pantazopoulou and Mills, 1995): (a) stress-strain relationship, (b) volumetric strain- axial strain relationship.

Prior to evident surface cracking, the $\varepsilon_V - \varepsilon_c$ relationship is practically linear, with the lateral strain ε_l being equal to $\nu \cdot \varepsilon_c$ (ν is typically within the range of 0.15 - 0.25). Beyond the limit axial strain ($\varepsilon_c = \varepsilon_{c,lim}$) that corresponds to lateral strains ε_l exceeding the tensile cracking of concrete ε_{cr}, the relationship between ε_V and ε_c shows substantial deviation from the idealized linear response and appears to be well approximated by a parabolic expression. For confined concrete under uniaxial load, the model is:

$$\varepsilon_V = (1-2\nu)\cdot\varepsilon_c \quad \text{for} \quad \varepsilon_c \le \varepsilon_l^{lim} = -\varepsilon_{cr}/\nu$$

$$\varepsilon_V = (1-2\nu)\cdot a_\varepsilon \cdot \varepsilon_{co}\left[\frac{\varepsilon_C}{\alpha_\varepsilon\cdot\varepsilon_{c0}} - b_\varepsilon \cdot \left(\frac{\varepsilon_c - \varepsilon_l^{lim}}{\alpha_\varepsilon\cdot\varepsilon_{c0} - \varepsilon_l^{lim}}\right)^{c_\varepsilon}\right] \text{ for } \varepsilon_c > \varepsilon_l^{lim} \qquad (7.2)$$

The product of $\alpha_\varepsilon \cdot \varepsilon_{co}$ is the compressive axial strain at zero volumetric strain. For standard concrete strength, it is typically observed at axial strain from 2‰ to 3.5‰, *i.e.* at 80% to 100% the strain at peak stress ε_{co}. Coefficient b_ε denotes the degree of passive confinement of concrete. For unconfined concrete loaded uniaxially, b_ε is assigned a value of 1, while smaller values are used as passive confining pressure increases. Coefficients α_ε and c_ε increase for higher strength concrete. Higher values of α_ε are used for higher nominal strength, up to 1, whereas the post peak response becomes more brittle (c_ε tends towards or exceeds 3). The same behaviour (linear and parabolic part) has also been observed in the relationship between volumetric strain and axial stress (Fig.7.7).

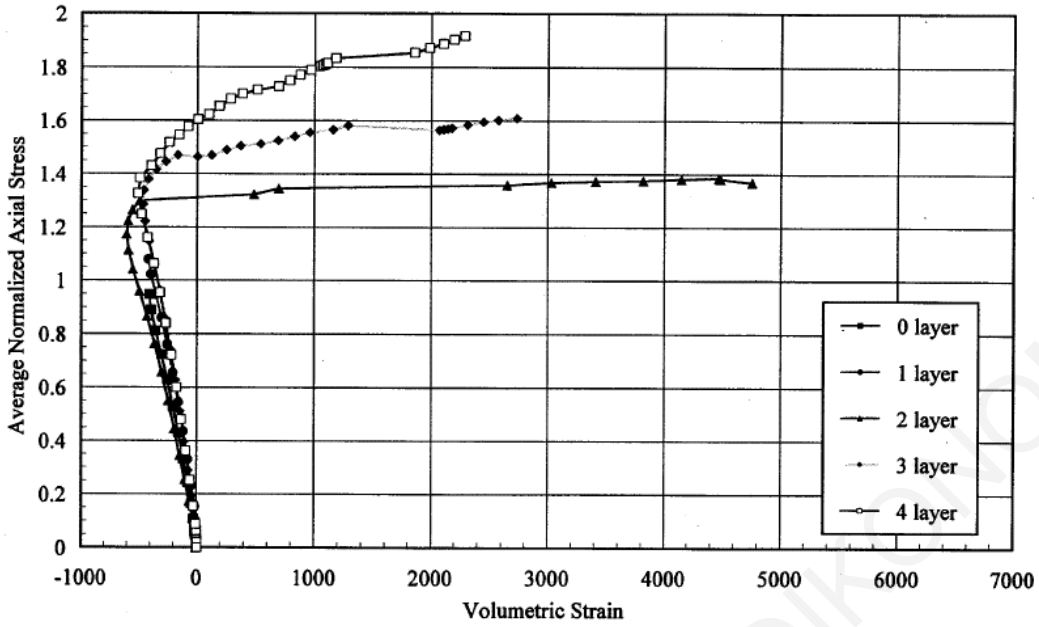

Figure 7.7: Volumetric strain vs. axial stresses (Chaallal et al., 2000).

To comply with the mechanical model of the 'generalized' springs and the regions with varying confinement, this model has been modified to correlate volumetric strain ε_V to axial stress σ_c according to Eq. 7.3 (axial stress in MPa). Initially, change of volume occurs due to elastic contraction and nonlinear compaction (Tastani et al 2013) and is practically linear up to the point of critical stress $\alpha_\sigma \cdot f_{co}$ (unconfined concrete strength, usually α_σ is taken as 0.7). For this axial stress level the Poisson's ratio v remains within the range of 0.15 - 0.25 (here, the initial Young's modulus of concrete is determined as well). At this point, volume change is reversed resulting in volumetric expansion called (near-strength or at-peak-strength) dilatancy. A point can be defined where the compression rate of the specimen is exactly equal to the expansion rate, thus resulting in zero volumetric strain. This point is considered to appear when the ultimate strength of the uniaxially confined region is reached (biaxial stress state, b_σ = 1.2). After the deterioration of this region, the expansion rate increases faster than the compression rate (second order parabola, c_σ = 2) due to reduced effective confinement. The expansion becomes unstable during the crushing phase beyond the ultimate strength.

Based on Fig. 8a, using the value of the volumetric strain ε_V, both area strain (ε_A) and side strains (ε_a *and* ε_b) can be calculated as shown in Eqs. 7.3 to 7.7 (compressive axial strains are taken as negative).

$$\varepsilon_V = -(1-3\nu)\cdot 10^{-4}\cdot \sigma_c \quad \text{for} \quad f_c \le a_\sigma \cdot f_{c0}$$

$$\varepsilon_V = -(1-3\nu)\cdot 10^{-4}\cdot b_\sigma \cdot f_{c0}\cdot \left[\left(\frac{\sigma_c}{b_\sigma \cdot f_{c0}}\right) - \left(\frac{\sigma_c - a_\sigma \cdot f_{c0}}{b_\sigma \cdot f_{c0} - a_\sigma \cdot f_{c0}}\right)^{c_\sigma}\right] \text{ for } \quad f_c > a_\sigma \cdot f_{c0} \qquad \text{(Eq. 7.3)}$$

$$\varepsilon_A = \varepsilon_V - \varepsilon_c \qquad \text{(Eq. 7.4)}$$

$$\varepsilon_A = \frac{\Delta A}{A} = \frac{(a+\Delta a)\cdot(b+\Delta b) - a\cdot b}{a\cdot b} = \frac{(a+\varepsilon_a \cdot a)\cdot(b+\varepsilon_b \cdot b) - a\cdot b}{a\cdot b} = (1+\varepsilon_a)\cdot(1+\varepsilon_b) - 1 \qquad \text{(Eq. 7.5)}$$

$$\frac{\varepsilon_a}{\varepsilon_b} = \frac{\Delta a}{a}\cdot\frac{b}{\Delta b} = \frac{\Delta d\cdot cos\theta \cdot b}{\Delta d\cdot sin\theta \cdot a} = 1 \Rightarrow \varepsilon_{side} = \varepsilon_a = \varepsilon_b \qquad \text{(Eq. 7.6)}$$

$$\varepsilon_A = (1+\varepsilon_{side})^2 - 1 \Rightarrow \varepsilon_{side} = \sqrt{\varepsilon_A + 1} - 1 \qquad \text{(Eq. 7.7)}$$

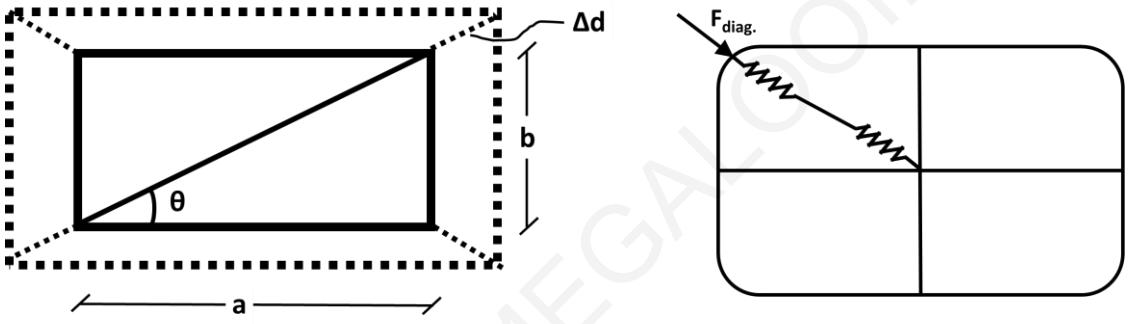

(a) **(b)**

Figure 7.8: (a) Deformed shape of a rectangular section based only on the diagonal lateral deformation, (b) Diagonal force applied to the lateral springs from the corner.

Considering the commonly applied assumption that no friction is developing between the FRP jacket and the concrete surface, the elongation strain of the sides can be assumed equal to the jacket strain. Therefore, the diagonal force of the jacket applied laterally from the corners to the springs in series can be determined by projection (Fig. 8b):

$$F_{diag} = \sqrt{2}\cdot E_i \cdot \varepsilon_{side} \cdot t_j \cdot k_e \qquad \text{(Eq. 7.8)}$$

The coefficient k_e is a confinement efficiency factor by Karam and Tabbara (2005) which takes into account the increasing confinement effectiveness as the corner radius increases and is reduced when the ratio of the larger side to the smaller side of the cross section is increased. Figure 9 shows the considerations made for the definition of this factor.

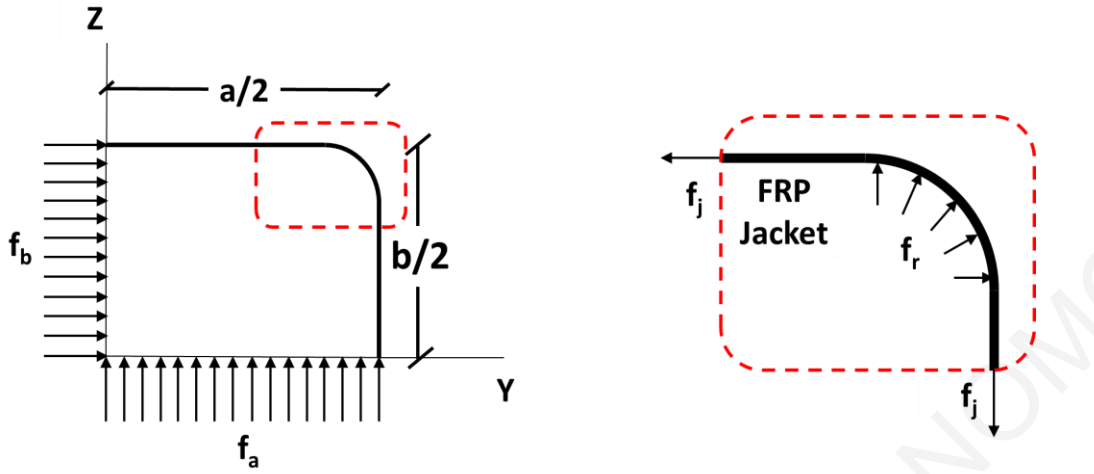

Figure 7.9: Mechanical behaviour for determining the confinement effectiveness factor (Karam and Tabara, 2005).

In Fig. 7.9 (left), a confining FRP wrap is shown acting on a generic rectangular section with long side *a*, a short side *b* and radius of the rounded corner *R*. Concrete is assumed to be subjected to average (uniform) confining stresses at its middle sections with f_a acting along the long side and f_b acting along the short side as illustrated in Fig. 7.9. The relationship between the f_a, f_b and the jacket tensile stress f_j is determined statically (*t* is the thickness of the FRP wrap).

In Fig. 7.9 (right), the FRP wrap is considered to act as a cable around the corner similar to a pulley. Assuming no friction between the FRP jacket and the concrete surface, the relationship between f_j and the confining stress at the corner f_r is also defined statically:

$$t \cdot f_j = \frac{a}{2} \cdot f_a = \frac{b}{2} \cdot f_b \qquad \text{(Eq. 7.9)}$$

$$t \cdot f_j = R \cdot f_r \qquad \text{(Eq.7.10)}$$

Combining Eq. (7.9) and (7.10), the following equation is obtained:

$$\frac{a}{2} \cdot f_a = R \cdot f_r \Rightarrow \frac{f_r}{f_a} = \frac{a}{2R} \qquad \text{(Eq. 7.11)}$$

Hence, the sharper the corner radius is, the higher the confining stress at the corner with respect to the average confining stress inside the cross section. This is supported by finite element analysis results presented by Parvin and Wang (2001) and experimental findings by Parvin and Wang (2002), and Chaallal *et al.* (2003).

Based on the preceding findings, the ratio of the average confinement stress over the maximum confinement stress attained in the cross section can be considered to represent a

geometric confinement effectiveness factor (k_e). In a rectangular section, the maximum confinement stress (f_r) develops at the corners where stress concentration occurs on the jacket due to dilation of concrete. The average confinement stress is the average of the individual stresses f_a and f_b which act at the centre of the section. The confinement effectiveness factor (k_e) can be calculated from:

$$k_e = \frac{f_a + f_b}{2 \cdot f_r} = \frac{R}{a} \cdot \left(1 + \frac{a}{b}\right) \qquad \text{(Eqn. 7.12)}$$

In a circular cross section, this factor is equal to 1, while for a square cross section, it is: $k_e = 2R/a$. For an elongated rectangular cross section with semi-circular ends $b \gg a$ and $2R = a$, the factor k_e tends asymptotically to 0.5, which corresponds to confinement in a single direction in the cross-sectional plane. After the determination of the diagonal force applied to the lateral springs in series from the corners, the lateral pressures for each region may also be calculated, as follows (Fig. 10).

The springs are in series so they develop the same force. For the biaxial stress state region, the force starts from the corners and moves parallel to the sides. Therefore, the confining pressure (assumed uniform) can be determined by the following equation:

$$h = \sqrt{{h_1}^2 + {h_2}^2} \qquad \text{(Eq. 7.13)}$$

$$\sigma_{lateral,biaxial} = F_{diagonal}/h \qquad \text{(Eq. 7.14)}$$

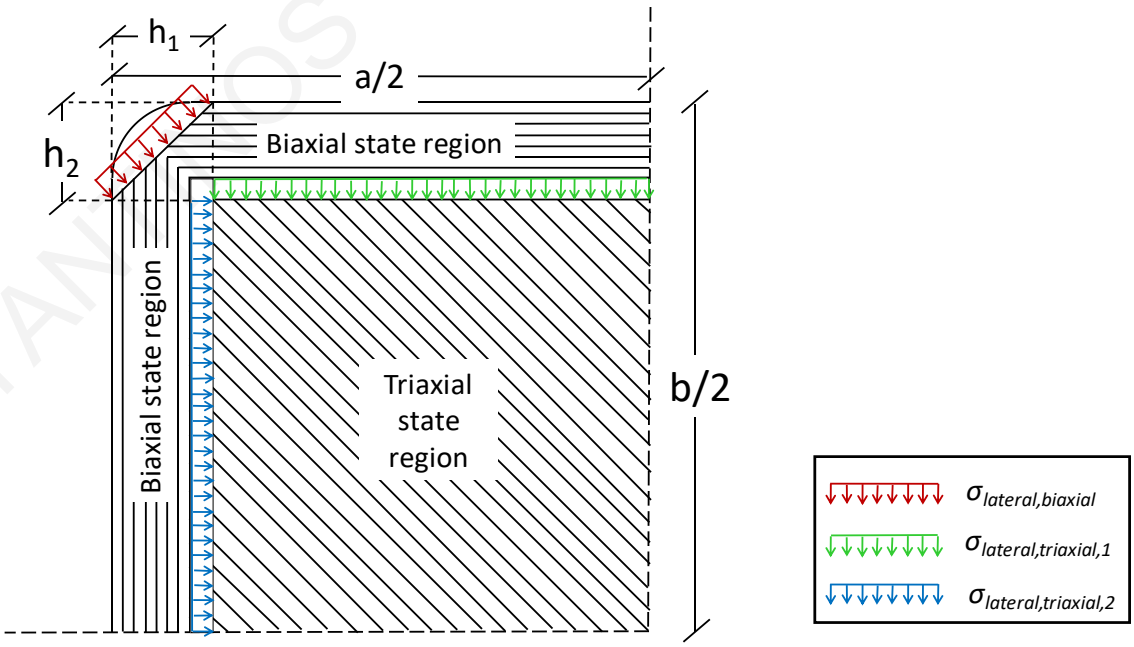

Figure 7.10: Confining pressures in the different regions.

The stress-strain model proposed by Popovics (1973) modified by Mander *et al.* (1988) is used to describe the behaviour of the triaxial stress state region. Based on the lateral pressures calculated according to the Fig. 10 the corresponding axial stress can be determined by the use of a stress-strain model corresponding to the confinement stress state of this region. The equation of the model by Mander *et al.* (1988) for the maximum axial stress σ_{cc} is not used in this case as it describes the performance of uniform biaxial confining pressure. For the region in triaxial stress state, the uniform confining pressures on the sides of the section can be determined based on the geometry of the region (Fig.7.10) as follows:

$$\sigma_{lateral,triaxial,1} = \frac{F_{diag}}{(0.5 \cdot a - h_1)} \quad \text{and} \quad \sigma_{lateral,triaxial,2} = \frac{F_{diag}}{(0.5 \cdot b - h_2)} \qquad \text{(Eqn. 7.15)}$$

To comply with the above modelling of the triaxial stress-state region where the confining pressures are different in the two lateral directions (only in the case of a square section they are the same), a failure criterion where all the lateral confining stress state cases are considered is applied. Specifically, the failure surface by Ottosen (1977) is used (Fig. 11). The latter failure criterion corresponds to a smooth convex failure surface with curved peaks. This surface expands in the negative direction of the hydrostatic axis, while its projection to the deviatoric plane (perpendicular to the hydrostatic axis) changes from nearly triangular tending towards a circular shape as the hydrostatic pressure increases. The behaviour of concrete can be modelled using octahedral normal (hydrostatic) and shear (deviatoric) stresses σ_o and τ_o. Any point in the stress space is described by the coordinates (ξ, ρ, θ), in which ξ is the projection in the hydrostatic axis ($\sigma_1 = \sigma_2 = \sigma_3$) and ($\rho$, θ) are the polar coordinates in the deviatory plane.

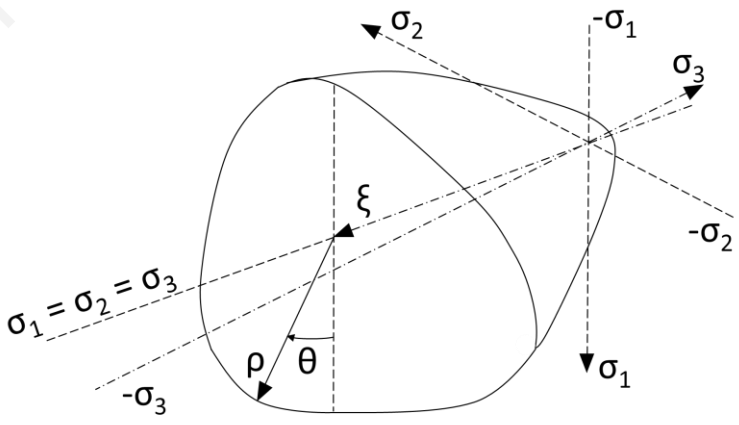

Figure 7.11: Ultimate strength surface by Ottosen (1977).

The following equations describe the failure surface. Having the lateral confining pressures of this region, the value of maximum axial stress $\sigma_{cc,triaxial}$ can be reached through iteration.

$$A \cdot \frac{J_{2\sigma}}{f_{co}^2} + \lambda \cdot \frac{\sqrt{J_{2\sigma}}}{f_{co}} + B \cdot \frac{I_{1\sigma}}{f_{co}} - 1 \geq 0 \quad \text{(Eqn. 7.16)}$$

where:

$$I_{1\sigma} = \sigma_1 + \sigma_2 + \sigma_3 \quad \text{(Eqn. 7.17)}$$

$$\sigma_1 = -\sigma_{cc,triaxial}, \quad \sigma_2 = -\sigma_{lateral,triaxial,1}, \quad \sigma_3 = -\sigma_{lateral,triaxial,2} \quad \text{(Eqn. 7.18)}$$

$$\sigma_0 = \frac{1}{3} \cdot I_{1\sigma} \quad \text{(Eqn. 7.19)}$$

$$J_{2\sigma} = \frac{(\sigma_1-\sigma_0)^2+(\sigma_2-\sigma_0)^2+(\sigma_3-\sigma_0)^2}{2} \quad \text{(Eqn. 7.20)}$$

$$J_{3\sigma} = \frac{(\sigma_1-\sigma_0)^3+(\sigma_2-\sigma_0)^3+(\sigma_3-\sigma_0)^3}{3} \quad \text{(Eqn. 7.21)}$$

$$\lambda = K_1 \cdot cos\left[\frac{1}{3} \cdot cos^{-1}(K_2 \cdot cos3\theta)\right] \quad \text{for } \cos3\theta \geq 0$$

$$\lambda = K_1 \cdot cos\left[\frac{\pi}{3} - \frac{1}{3} \cdot cos^{-1}(-K_2 \cdot cos3\theta)\right] \quad \text{for } \cos3\theta < 0 \quad \text{(Eqn. 7.22)}$$

$$\cos3\theta = \frac{3\sqrt{3}}{2} \cdot \frac{J_{3\sigma}}{J_{2\sigma}^{3/2}} \quad \text{(Eq. 7.23)}$$

The remaining parameters of the model are calibrated by the values proposed in the original work of Ottosen (1977) for different ratios of tensile concrete strength over compressive concrete strength ($k_o = f_{to}/f_{co}$) given in Table 7.1.

Table 7.1: Proposed values for the parameters of the failure criterion by Ottosen (1977).

k_o	A	B	K_1	K_2
0.08	1.8076	4.0962	14.4863	0.9914
0.1	1.2759	3.1962	11.7365	0.9801
0.12	0.9218	2.5969	9.9110	0.9647

Based on the $\sigma_{cc,triaxial}$ determined above, the stress-strain law by Mander *et al*. (1988) is applied. The following equations describe the model's behaviour:

$$\sigma_{c,triaxial} = \frac{\sigma_{cc,triaxial} \cdot x \cdot r}{r-1+x^r} \quad \text{(Eq. 7.24)}$$

$$r = \frac{E_c}{E_c - E_{sec}} \quad \text{(Eq. 7.25)}$$

$$\varepsilon_{cc} = \varepsilon_{co} \cdot \left[1 + 5 \cdot \left(\frac{\sigma_{cc,triaxial}}{f_{c0}} - 1\right)\right] \text{ (Richart } \textit{et al.}\text{, 1928)} \quad \text{(Eq. 7.26)}$$

$$E_{sec} = \frac{\sigma_{cc,triaxial}}{\varepsilon_{cc}} \quad \text{and} \quad x = \frac{\varepsilon_c}{\varepsilon_{cc}} \quad \text{(Eq. 7.27)}$$

The model for concrete under biaxial stress-state by Liu *et al.* (1972) is used for the biaxial stress state region as follows:

$$\sigma_{c,biaxial} = \frac{\varepsilon_c \cdot E_c}{(1-\nu \cdot a_1) \cdot \left[1 + \left(\frac{E_c}{f_{cp} \cdot (1-\nu \cdot a_1)} - \frac{2}{\varepsilon_{cp}+0.005}\right)\varepsilon_c + \left(\frac{\varepsilon_c}{\varepsilon_{cp}+0.005}\right)^2\right]} \quad \text{(Eq. 7.28)}$$

where:

$$a_1 = \frac{\sigma_{lateral,biaxial}}{\sigma_{c,biaxial}} \quad \text{(Eq. 7.29)}$$

$$f_{cp} = \left(1 + \frac{a_1}{1.2-a_1}\right) f_{c0} \quad \text{for} \quad a_1 < 0.2 \quad \text{(Eq. 7.30)}$$

$$f_{cp} = 1.2 f_{c0} \quad \text{for} \quad 0.2 \le a_1 \le 1 \quad \text{(Eq. 7.31)}$$

Note: For $a_1 > 1$, $\sigma_{c,biaxial}$ is constant, equal to $1.2 \cdot f_{c0}$.

$$\varepsilon_{cp,1} = 0.0025 \quad \text{for} \quad a_1 \le 1 \quad \text{(Eq. 7.32)}$$

Based on the areas of the different regions the total averaged axial stress of the cross section can be obtained:

$$A_{biaxial} = (0.5b) \cdot h_1 + (0.5a) \cdot h_2 - h_1 \cdot h_2 \quad \text{(Eqn. 7.33)}$$

$$A_{triaxial} = (0.5b - h_2) \cdot (0.5a - h_1) \quad \text{(Eqn. 7.34)}$$

$$A_{total} = a \cdot b \quad \text{(Eqn. 7.35)}$$

$$\sigma_{c,total} = \frac{4 \cdot A_{biaxial}}{A_{total}} \cdot \sigma_{c,biaxial} + \frac{4 \cdot A_{triaxial}}{A_{total}} \cdot \sigma_{c,triaxial} \quad \text{(Eqn. 7.36)}$$

The proposed model (Fig. 7.12) is implemented through an iterative procedure where an assumed value of axial stress corresponding to an imposed axial strain is brought to convergence. After convergence of the assumed axial stress calculated with the above considerations, the resulting elongation strain through the iterative procedure should be compared to the ultimate rupture strain of the jacketing. It has been observed from

experimental results that the average failure strains of the FRP wraps are of the order of 50-80% of the failure strain of the tensile coupons made from the same material and tested before the application of the material. This actual value of factor k_r (ranging between 50-80%) depends on the type of FRP used (Lam and Teng, 2003).

7.4 Verification of the Analytical Model by Experimental Results

The proposed algorithm's efficiency is assessed by its performance in correlating experimental results obtained in large scale tests conducted on rectangular-section, FRP-confined RC columns (Zeng *et al.*, 2018). The reference experimental study presents results from monotonic tests conducted on nine columns having a cross-section of 435mm in depth and 290mm in width, including eight FRP-confined RC columns and one RC column without FRP jacketing as the control specimen, tested under axial compression. The experimental program examined the sectional corner radius and the FRP jacket thickness as the key test variables. The proposed algorithm was assessed against three of these specimens, *i.e.* the specimens with corner radii 25mm or 45mm and specimens having either one or two layers of Carbon Fiber Reinforced Polymer (CFRP) wrap.

The corner radius of 65mm was not considered in the assessment, since in buildings designed using obsolete design codes the concrete cover thickness is typically small. Hence, a cover of at least 65mm which would allow the formation of the round corners in such a column is highly unlikely to be found. Also, Zeng *et al.* (2018) assessed the effectiveness of material models available in literature against the experimental results. The proposed model does not take into account the contribution of the stirrups, as their spacing is considered to be adequately large to minimize their confinement effect. This is in accordance with the results presented by Zeng *et al.* (2018), where the contribution of the reinforcement is also not taken into account due to the large stirrup spacing. Figure 7.13 shows the correlation of the proposed material model with these experimental results and overall the numerical response can be characterized as satisfactory. The observed deviation can be justified due to the complexity and large variability of the problem under study. It should be noted that for this comparison the iterative procedure was terminated for FRP rupture strain equal to 50% of that of the experimentally tested tensile FRP coupons (Zeng *et al.*, 2018).

A further evaluation of the model's performance under cyclic lateral loading which simulates earthquake loads and simultaneous constant axial compression was also performed. This was achieved by comparison against the experimental tests of FRP-

retrofitted square RC columns performed by Memon and Sheikh, 2005. This experimental study evaluates the effectiveness of Glass Fiber Reinforced Polymer (GFRP) wraps in strengthening deficient and repairing damaged square RC columns. Each of the eight specimens tested, representing columns of buildings and bridges constructed before 1971, consisted of a 305×305×1473mm column connected to a 508×762×813mm stub. Specimens were tested under constant axial compression and cyclic lateral displacement excursions simulating earthquake loads.

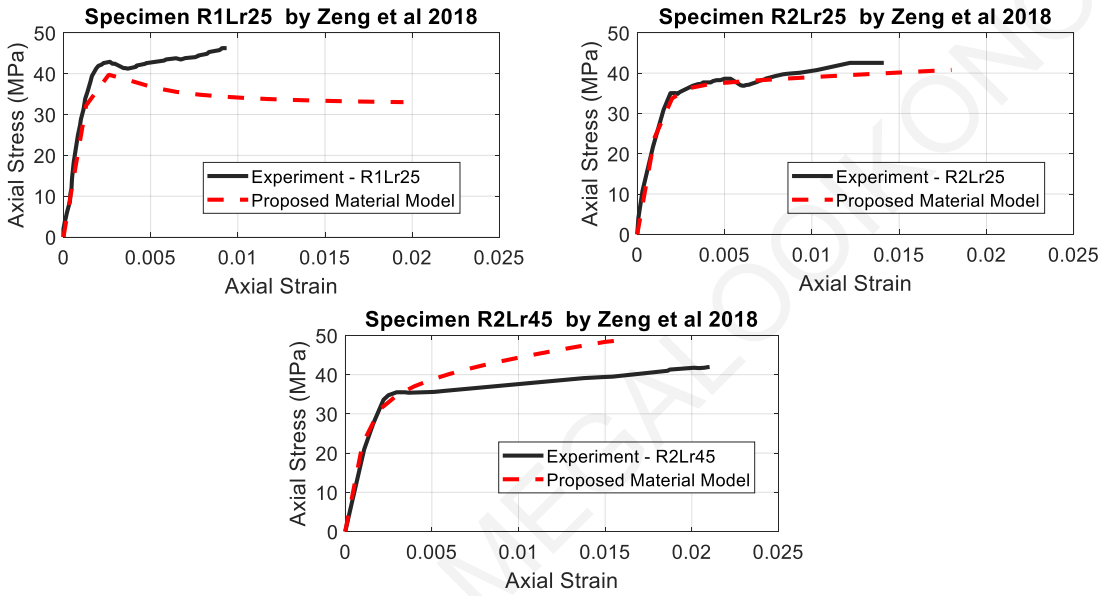

Figure 7.12: Correlation of the proposed material model with experimental results of large-scale CFRP-confined rectangular RC columns under axial compression by Zeng et al. (2018).

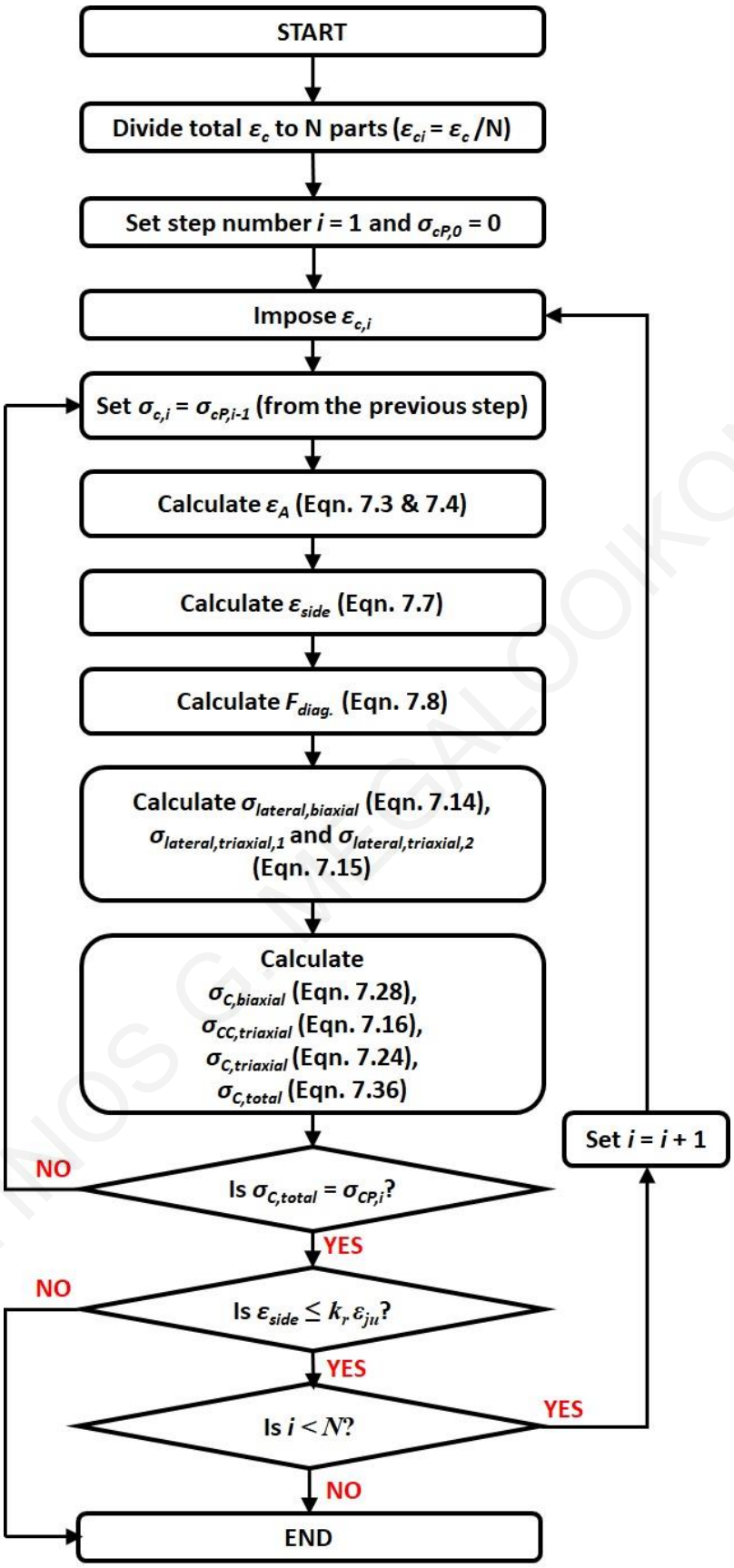

Figure 7.13: Proposed iterative procedure.

The modelling of these FRP-confined square RC columns has been performed using OpenSees (2006). The developed constitutive material law was added to the source code of OpenSees as a uniaxial material, i.e. the 'FRPConfinedConcrete' material. The experimental moment-curvature responses within the plastic hinge regions are reported along with the numerical results in Fig. 7.14. The simulation of the cantilever columns has been applied using a unique fiber beam-column element (Spacone *et al.*, 1996) with force formulation for the entire column, in which the FRP-confined concrete was modelled using the proposed material model with degraded linear unloading/reloading stiffness according to the work of Karsan and Jirsa (1969) and no tensile strength. The constitutive model by Menegotto and Pinto (1973) is used to model the longitudinal steel behaviour. The moment-curvature response of the most critical fiber section of the applied nonlinear fiber element was then reported. It can be seen in Fig. 7.14 that the agreement is close to the experimental one, with some deviation concentrated on the parts of reloading after reversal of the imposed displacement. This difference in response in terms of modelling can be explained based on the way the cracks on the concrete surface are described in the level of the material model. Because the crack is described as a two-event phenomenon (open or closed cracks), when the longitudinal steel reinforcement is in compression and the crack is closing, the concrete contributes to the total strength of the column, creating this deviation in the response. In reality, this case may not occur when lateral dislocation may cause imperfect crack closure.

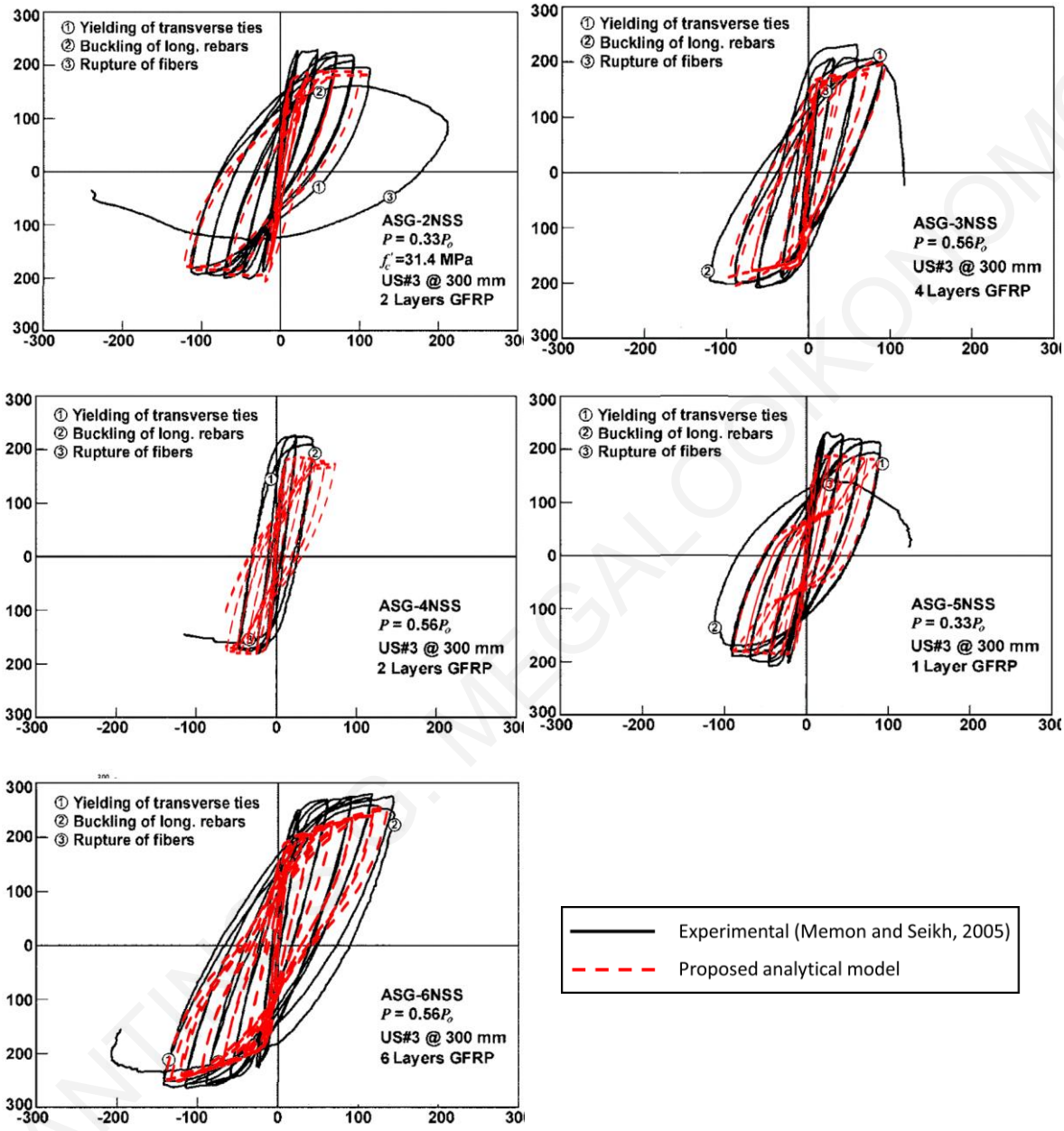

Figure 7.14: Correlation of the proposed material model with experimental results of large-scale GFRP-confined square RC columns under cyclic excitation by Memon and Sheikh (2005) (x-axis: Curvature x10^{-6} (rad/mm), y-axis: Moment (kNm).

7.5 Summary

The column fiber-based element developed in Chapters 3, 5, and 6 in order to model the flexural, shear and pullout slip behavior in the critical zones of columns under lateral sway used the established confinement models to characterize the uniaxial stress of concrete in compression. The work was extended further in the present chapter to also address unconventional confinement development effected by FRP jacketing; the emphasis was placed on rectangular cross sections where variable confinement occurs in the long and short directions of the member cross section. The model was developed from first principles as an extension of a previously developed analytical model for circular columns, after consideration of the variable kinematic restraint to dilation exerted by the confining jacket in subsections of the rectangular section each being affected differently by the jacket confinement depending on the proximity to the corners. The approach developed was calibrated against experimental evidence and a primary finding is that the entire wrapped column cross section is confined, contrary to the established practice that considers an arching action to occur in the intermediate zones of the perimeter of the cross section that effectively reduces confinement performance.

8 CONCLUSIONS

8.1 Summary and Conclusions of the Research

The review of the state of the art regarding interpretation and consistent modeling of reinforced concrete column under lateral loads leaves a lot to be desired: improved response estimation of the behavior of columns that are susceptible to shear failure after flexural yielding; better procedures to estimate shear strength, and the pattern of degradation thereof with increasing displacement ductility; the need to account for reinforcement pullout and its effects on stiffness and deformation capacity; the shape of the hysteresis loops; the detrimental effects of axial load at large displacement limits; the drift capacity of structural elements and the magnitude of deformation (drift ratio) associated with milestone events in the response curve of the column member are open issues that need to be settled before the performance-based assessment framework may be considered complete and dependable.

In this direction, the definition of the deformability of RC columns was reassessed in the present thesis by proposing a new methodology for the determination of plastic hinge length through a consideration of yield penetration effects. It is noted that the plastic hinge is an essential device in mechanics of concrete under seismic action, and is critical in the estimation of drift capacity at the design ultimate limit states. The term strain penetration refers to development of bar strains that do not obey flexural analysis and the plane sections assumption, and it occurs as a result of bond degradation along the length of the reinforcement. Yield penetration is the type of bar strain development that spreads beyond the length where bar yield stress would be predicted to occur from flexural theory.

It was found that yield penetration occurs from the critical section towards both the shear span and the support of columns. The extent of the nonlinear region of the bar is governed by the observation that since bond stress f_b is the slope of the bar stress distribution f_s, thus, where a bar is at the yield plateau no bonding with the surrounding concrete can occur. Thus, yield penetration is synonymous with increased bar pull-out slip contribution to the column lateral drift ratio. Contrary to the fixed design values adopted by codes of assessment, the yield penetration length is actually the only consistent definition of the notion of the plastic hinge length, whereas the latter determines in the practical concrete mechanics, the contribution of pullout rotation to column drift and column stiffness. In order to establish the plastic hinge length in a manner consistent to the above definition, this study

pursued the explicit solution of the field equations of bond over the shear span of a column. Through this approach, the bar strain distributions and the extent of yield penetration from the yielding cross section towards the shear span were resolved and calculated analytically. By obtaining this solution, a consistent definition of plastic hinge length was established, by reference to the state of reinforcement strain (replacing the stress-based definition used previously). The true parametric sensitivities of this design variable for practical use in the seismic assessment of existing structures were illustrated. The numerical result showed good agreement with the experimental evidence and were consistent with the experimental trends supported by test databases, confirming that the plastic hinge length is controlled by the residual bond that may be mobilized along the yielded reinforcement. It was found that at advanced levels of lateral drift the column reinforcement is partially debonded and governed by the solution of the bond equation, thereby behaving as an anchorage over the shear span. Contribution to drift ratio resulting from the strain-definition of the plastic hinge continuously grows with lateral imposed displacement, causing a commensurate reduction of the relative participation of the flexural drift component and causing the yielded region to behave as a pivot. This interaction between flexural and pullout response is responsible for the cover delamination often observed at the toe of structural columns under lateral sway.

In addition, a force-based fiber beam-column element accounting for shear effects and the effect of tension stiffening was developed, in order to provide an analytical test-bed for simulation and improved understanding of experimental cases where testing of reinforced concrete columns actually led to collapse. The developed fiber-element is incorporated in the stand-alone Windows program Phaethon with the user's interface written in C++ programming language code. The latter offers the possibility to obtain the resistance curve for shear-critical reinforced concrete cantilever columns while taking into consideration the shear–flexure interaction mechanism. The procedure also incorporated in the drift capacity estimation of a column; the rotation due to pull-out occurring in the critical section of the column. The software resolves strain, slip and bond distributions along the anchorage length. Comparison with experimental results from the literature verifies the capability of this Windows software tool to assess the strength and deformation indices of shear-critical reinforced concrete columns. Moreover, the moment curvature as well as the shear force – shear strain analysis of the sections of these columns are also possible, all based on the Modified Compression Field Theory. The fiber modelling approach was used to calibrate several column specimens tested under lateral loading and included in an international

database of tests that is curated by the Pacific Earthquake Engineering Research Center. The columns analyzed include all specimens that demonstrated a flexural type response under cyclic displacement reversals (see Chapter 3 and Appendix), as well as columns undergoing shear failure after yielding of primary reinforcement (Chapter 3, and Chapter 6). The effect of fluctuating axial load was also studied as a means of explaining different modes of failure observed in otherwise identical specimens; in the same context the effect of loading history was illustrated to affect the accumulation of member growth due to inelastic strains and the ensuing fulfillment of axial load collapse conditions.

The concept of prioritizing the hierarchy of failure was used in order to decipher the limiting drift capacity and ensuing mode of failure of non-conforming columns with older-type detailing. Alternative modes of failure were considered in order to identify the weakest link of member behavior (from among flexural yielding/concrete crushing due to excessive flexural strains, web cracking/stirrup yielding due to shear failure, exhaustion of reinforcement strain development capacity in poorly confined anchorages and lap splices). Once the weakest mechanism of resistance was identified in old columns, the drift capacity was associated with the development of that particular mechanism, by scaling down the contribution of the other forms of behavior according with the maximum attainable column shear resulting from the prevailing mode of failure. In this manner situations where no plastic rotation capacity could be supported if the member fails prior to flexural yielding were identified, leading to reduced drift ratios as compared to the assessment codes estimations.

Finally, an iterative approach was proposed to model both the axial and lateral stress-strain response of axially loaded FRP-confined rectangular and square reinforced concrete columns. In FRP-confined square or rectangular sections, no unconfined concrete regions are observed, as assumed in many models. These sectors along the sides between adjacent corners are confined from forces coming from the corners and extending parallel to the jacketed sides. Therefore, the areas where arching effect was assumed previously, are found to be in fact partially confined. Thus, two different regions with different stress-states were identified, being uniaxially and biaxially confined. The contribution of each region to the total section strength was modelled as a system of parallel springs, whose axial stresses were taken as additive based on the corresponding constitutive laws for the respective stress states. Similarly, the lateral expansive behavior that occurs along the diagonals of the confined section was represented by a system of springs in series. It was shown that the lateral strains

on both sides of the rectangular sections are equal, regardless of their aspect ratio. The resulting lateral uniform pressures led to the corresponding axial strength of the partially confined regions. The algorithm takes into account all parameters available to designers, such as corner rounding radius, stiffness of the FRP and concrete strength, while it can be easily understood and implemented. Results were found to correlate adequately to recent experimental data obtained from large-scale tests on FRP-confined rectangular RC columns. Finally, the performance of this material model was further investigated by its implementation to the simulation of a series of experimental tests of FRP-retrofitted square RC columns under cyclic lateral loading simulating earthquake loads and simultaneous constant axial compression. Nonlinear fiber element models such as those developed in Chapter 3 and enhanced with the confinement model were implemented in OpenSees ('*FRPConfinedConcrete*') with tensile strength cutoff for the concrete and degraded linear unloading/reloading stiffness in the case of cyclic loadings. The model was found very effective in the modelling of square-section FRP-confined columns under lateral loads. When used in the modelling of rectangular sections the effectiveness of the model was reduced for large aspect ratio of section sides particularly at larger deformations.

8.2 Thesis Contributions

In the course of the thesis a number of findings and innovative concepts were developed. These are considered the important contributions of the work:

- A novel definition was established for the plastic hinge length in flexure-shear members and a methodology was developed for its calculation. The new practical expression for the plastic hinge length proposed refers to the post-yielding strain development capacity of the reinforcement, departing from the established approach that defines the plastic hinge length with reference to reinforcement yield stress.
- A novel closed form solution of bond equations governing the behavior of reinforcement in the shear span of a swaying column was developed considering nonlinearity in the bond-slip law and reinforcement yielding. Tension stiffening effects interfering with the solution of the bond-equation were mathematically described and considered in the solution.
- A Windows-based software was developed for fiber-based, distributed nonlinearity analysis of prismatic frame elements undergoing lateral sway such as would occur

during an earthquake. The program solves the column state of stress under full cyclic load reversals for flexure dominated response conditions.

- The formulation was extended to fiber-type analysis with distributed nonlinearity also considering the exact Timoshenko beam theory whereby shear deformations are explicitly considered in the state determination. Moment, shear and axial load interaction were considered in calculating the resistance curve for a number of different column cases that underwent flexure shear or purely shear dominated mode of failure, and the distinct contributions of the many contributing sources of column deformation (curvature, shear angle, axial elongation, pullout rotation) were illustrated through the developed algorithm.
- The MCFT theory was coupled with a simplifying assumption for the orientation of the principal angles in order to enable fast convergence in the formulation.
- The problem of assessment of older columns with substandard reinforcing details was studied in light of the capacity prioritizing theory which is actually a reverse implementation of capacity design as used in new structures. Through this concept the weakest link of member behavior can be identified. An important finding is that drift capacity of such columns cannot be obtained unconditionally by the contributions of yield and plastic rotation capacities as would be estimated from code expressions, but rather it is dominated by the controlling mode of failure, requiring a case by case examination of the relative strength magnitudes of all the governing response mechanisms.
- A mechanistic model was developed to evaluate the confining effects of FRP jacketing used as a means of retrofitting old columns with a rectangular cross section, in terms of confined concrete stress-strain response. The model illustrated that the arching action effect which is widely accepted in the literature oversimplifies the true nature of the state of confinement in the encased member. Confining forces near the perimeter were found to have strong directionality effects. A novel constitutive approach that accounts for the kinematics of the restrained region was developed and implemented along with the fiber model described in Chapter 3 in OpenSees and is available for public use through this widely accepted simulation platform.
- All developed methodologies correlate adequately to experimental findings.

A new practical expression for the plastic hinge length was derived from first principles. According to this the plastic hinge is dependent on the magnitudes of strain that

exceed yielding over the shear span, which is controlled by the residual frictional bond that can be supported over the yielded portion of the bar including the spread of yield penetration. The expression was validated through comparison of its estimations with the available experimental evidence, the empirical formulae for the plastic hinge length and by exploring its parametric sensitivity to the important design variables. This expression is appropriate for practical implementation to design and it is proposed that it be considered as a critical variable both for seismic design and practical assessment guidelines that could be incorporated in future versions of design and assessment Codes like Eurocodes, particularly with regards to the estimation of deformation capacity of structural members.

8.3 Future Research Priority

The Performance-Based Earthquake Engineering main objective is to define an "acceptable" probability of collapse. Collapse shall be quantified as realistically as possible, using non-linear dynamic analysis which incorporates several suites of ground motions. A comprehensive set of guidelines will form the starting point for addressing the complexity inherent in nonlinear softening response under large displacements and deformations and will contribute to the acceptance of nonlinear response studies in professional practice. The deployment of a new class of column models that account for localized phenomena such as shear and reinforcement pull-out in a consistent iterative element formulation will help minimize the non-convergence issues that arise with the large collection of zero length nonlinear spring and plastic hinge elements currently in use in nonlinear column response simulations. One main future goal based on the present research is to enhance further the developed force-based fiber model using a secant type history-tracking algorithm so as to facilitate convergence and eliminate numerical instabilities associated with tangent stiffness approaches. This would also enable further dissemination of the Timoshenko-beam based fiber element in the OpenSees platform. Another important step would be the development of simple proposals for error-proof estimation of deformation capacities of existing columns according to the procedures developed in this study, to be proposed as alternatives to the current code approaches that are rather complex and difficult to use in practice.

BIBLIOGRAPHY

[1] AASHTO LRFD (2013). "Bridge Design Specifications and Commentary" 3rd Edition, American Association of State Highway Transportation Officials, Washington, D.C, 1264 pp.

[2] Aboutaha, R.S., and Machado, R.I. (1999). "Seismic Resistance of Steel-Tubed High-Strength Reinforced-Concrete Columns." *J. Struct. Eng.*, 125(5), 485-494.

[3] Aboutaha, R.S., Engelhardt, M.D., Jirsa, J.O.: and Kreger, M.E. (1999). "Rehabilitation of Shear Critical Concrete Columns by Use of Rectangular Steel Jackets." *ACI Struct. J.*, 96(1), 68-78.

[4] ACI Committee 318 (2014), "Building Code Requirements for Structural Concrete (ACI 318-14) and Commentary", American Concrete Institute, Farmington Hills, MI. USA

[5] Amitsu, S., Shirai, N., Adachi, H., and Ono, A. (1991). "Deformation of Reinforced Concrete Column with High or Fluctuating Axial Force." *Transactions of the Japan Concrete Institute*, 13.

[6] Ang, B. G., Priestley, M. J. N., and Paulay, T. (1989). "Seismic Shear Strength of Circular Reinforced Concrete Columns". *ACI Structural Journal, 86*(1), 45-59.

[7] Arakawa, T., Arai, Y., Egashira, K., and Fujita, Y. (1982). "Effects of the Rate of Cyclic Loading on the Load-Carrying Capacity and Inelastic Behavior of Reinforced Concrete Columns." *Transactions of the Japan Concrete Institute*, 4.

[8] Arakawa, T., Arai, Y., Mizoguchi, M., and Yoshida, M. (1989). "Shear Resisting Behavior of Short Reinforced Concrete Columns Under Biaxial Bending-Shear." *Transactions of the Japan Concrete Institute,* 11.

[9] Arakawa, T., He, M., Arai, Y., and Mizoguchi, M. (1998). "Shear Resisting Behavior of Reinforced Concrete Columns with Spiral Hoops." Transactions of the Japan Concrete Institute, 10.

[10] ASCE/SEI 41 (2007). Seismic Rehabilitation of Existing Buildings. American Society of Civil Engineers, Reston, VA.

[11] Aschheim, M. and Moehle, J. P. (1992). "Shear Strength and Deformability of RC Bridge Columns Subjected to Inelastic Displacements". Technical Report, UCB/EERC 92/04, University of California, Berkeley, Berkeley, USA.

[12] Atalay, M.B., and Penzien, J. (1975). "The Seismic Behavior of Critical Regions of Reinforced Concrete Components as Influenced by Moment, Shear and Axial Force." Report No. EERC 75-19, University of California, Berkeley, California.

[13] Azizinamini, A., Johal, L. S., Hanson, N. W., Musser, D. W., and Corley, W. G. (1988). "Effects of Transverse Reinforcement on Seismic Performance of Columns – A Partial Parametric Investigation." Project No. CR-9617, Construction Technology Laboratories, Skokie, Illinois.

[14] Bae C., A.M. Mieses and O. Bayrak, 2005, "Inelastic Buckling of Reinforcing Bars", *Journal of Structural Engineering, ASCE,* 131(2), 314-321.

[15] Bae S., and Bayrak O. (2008). "Seismic Performance of Full-Scale Reinforced Concrete Columns". *ACI Structural Journal*; 105(2): 123-133.

[16] Bae, S., and Bayrak O., (2008). Plastic Hinge Length of Reinforced Concrete Columns. *ACI Structural Journal*; 105(3): 291-300.

[17] Baradaran M., Shoraka and K. J. Elwood (2013), "Mechanical Model for Non-Ductile Reinforced Concrete Columns", *Journal of Earthquake Engineering*, Vol.17 (7), pp.937-957.

[18] Barzegar F. and Schnobrich W.C. (1986). "Nonlinear Finite Element Analysis of Reinforced Concrete under Short Term Monotonic Loading" Civil Engineering Studies SRS No. 530, University of Illinois at Urbana, Illinois, USA.

[19] Bayrak O. (1998). "Seismic Performance of Rectilinearly Confined High Strength ConcreteColumns." Doctoral Dissertation. Dept. of Civil Engineering, Univ. of Toronto, Canada.

[20] Bayrak, O., and Sheikh, S. (1996). "Confinement Steel Requirements for High Strength Concrete Columns." Proc. 11th World Conference on Earthquake Engineering, Aculpulco, Mexico,Paper No. 463.

[21] Bentz, E. C. (2000). Sectional Analysis of Reinforced Concrete Members. PhD Thesis, Department of Civil Engineering, University of Toronto, Toronto, Canada.

[22] Bentz, E.C., Vecchio F.J. and Collins, M.P. (2006), "Simplified Modified Compression Field Theory for Calculating Shear Strength of Reinforced Concrete Elements" *ACI Structural Journal*, 103(4), 614-624.

[23] Benzoni G., Ohtaki T., Priestley M.J.N, and Seible F. (1996). "Seismic Performance of Circular Reinforced Concrete Columns under Varying Axial Load", Division of Structural Engineering, University of California, San Diego, La Jolla, California, Report No. SSRP – 96/04.

[24] Berry, M.P., Parrish, M. and Eberhard, M.O. (2004). "PEER Structural Performance Database User's Manual, Version 1.0" Pacific Earthquake Engineering Research Center Report, University of California, Berkeley, 2004 (available at http://nisee.berkeley.edu/spd/).

[25] Bertero, V. V., and E. P. Popov, (1977) "Seismic behaviour of moment-resisting reinforced concrete frames." In Reinforced concrete structures in seismic zones, American Concrete Institute, Special Publication No. 53, pp. 247-292.

[26] Bett, B. J., Klingner, R. E., and Jirsa, J. O. (1985). "Behavior of Strengthened and Repaired Reinforced Concrete Columns Under Cyclic Deformations." PMFSEL Report No. 85-3, Department of Civil Engineering, University of Texas at Austin.

[27] Bigaj A.J. (1999). Structural Dependence of Rotation Capacity of Plastic Hinges in RC Beams and Slabs. PhD Thesis, Faculty of Civil Engineering, Delft University of Technology, Delft, the Netherlands.

[28] Biskinis, D. and Fardis, M. (2013). "Models for FRP-wrapped rectangular RC Columns with Continuous or Lap-Spliced Bars Under Cyclic Lateral Loading". *Engineering Structures*, Elsevier; 57, 199-212.

[29] Bonacci, J. and Marquez, J. (1994). "Tests of Yielding Anchorages under Monotonic Loadings". *Journal of Structural Engineering, ASCE*, 120(3), 987-997.

[30] Braga F., R. Gigliotti and M. Laterza, (2006), "Analytical Stress-Strain Relationship for Concrete Confined by Steel Stirrups and/or FRP Jackets", *Journal of Structural Engineering, ASCE,* 132 (9), 1-15.

[31] Calderone, A.J., Lehman, D.E., and Moehle, J.P. (2000). "Behavior of Reinforced Concrete Bridge Columns Having Varying Aspect Ratios and Varying Lengths of Confinement." Pacific Earthquake Engineering Research Center Report 2000/08, University of California, Berkeley, California.

[32] Campione, G. and Miraglia, N. (2003). Strength and strain capacities of concrete compression members reinforced with FRP. *Cement and Concrete Composites, 25*(1), 31-41.

[33] Carey S.A. and K.A Harries, (2005), "Axial Behavior and Modeling of Confined Small-, Medium-, and Large-Scale Circular Sections with Carbon Fiber-Reinforced Polymer Jackets", *ACI Structural Journal,* 102(4), 596-604.

[34] Celebi, M., and J. Penzien, (l973) "Experimental investigation into the seismic behaviour of critical region of reinforced concrete components as influenced by moment and shear", Earthquake Engineering Research Center, University of California, Berkeley, CA, EERC 73-4.

[35] Ceresa, P., Petrini, L., and Pinho, R. (2007). "Flexure-shear fiber beam-column elements for modeling frame structures under seismic loading-state of the art". *Journal of Earthquake Engineering, 11*, 46–88.

[36] Ceresa, P., Petrini, L., and Pinho, R. (2008). A fibre flexure–shear model for cyclic nonlinear behavior of RC structural elements. Research Report ROSE-2008/07. IUSS Press: Pavia, Italy.

[37] Chaallal, O., Shahawy, M. and Al-Saad, N. (2000). Behaviour of axially loaded short rectangular columns strengthened with CFRP composite wrapping. *FDOT, Structures Research Center, Tallahassee*.

[38] Chaallal, O., Shahawy, M. and Hassan, M. (2003). Performance of axially loaded short rectangular columns strengthened with carbon fiber-reinforced polymer wrapping. *Journal of Composites for Construction, 7*(3), 200-208.

[39] Chai, Y., Priestley, M., and Seible, F. (1991). "Seismic Retrofit of Circular Bridge Columns for Enhanced Flexural Performance." *ACI Structural. Journal,* 88(5), 572-584.

[40] Chasioti S.G., Megalooikonomou K.G. and Pantazopoulou S.J. (2013). "Shear Strength Assessment of Reinforced Concrete Columns," *4th International Conference on Computational Methods in Structural Dynamics and Earthquake Engineering (COMPDYN 2013)*. Kos Island, Greece, June 12 -14.

[41] Chen W.F (1982). "Plasticity in Reinforced Concrete", McGraw-Hill, New York, ISBN: 0070106878.

[42] Cheok, G.S., and Stone, W. C. (1986). "Behavior of 1/6-Scale Model Bridge Columns Subjected to Cycle Inelastic Loading." NBSIR 86-3494, U.S. National Institute of Standards and Technology, Gaithersburg, Maryland.

[43] Code for Structural Interventions (KANEPE) (2011), Organization for Seismic Design and Protection, OASP, in Greek.

[44] Coffman, H. L., Marsh, M. L. and Brown, C. B. (1993). "Seismic Durability of Retrofitted Reinforced-Concrete Columns." *Journal of Structural Engineering, ASCE,* 119(5), 1643-1661.

[45] Collins, M. P. (1978), "Towards a rational theory for RC members in shear". *ASCE Journal of Structural Division,* 104(4), 649-666.

[46] Collins, M. P., Vecchio, F. J., and Mehlhorn, G. (1985). "An international competition to predict the response of reinforced concrete panels". *Canadian Journal of Civil Engineering, 12,* 624-644.

[47] Computers and Structures, Inc. 2016. CSI Analysis Reference Manual. Berkeley, CA: Taylor & Francis.

[48] CSA Committee A23.3 (2004), "Design of Concrete Structures (CSA A23.3-04)," Canadian Standards Association, Mississauga, 214 pp.

[49] Darwin, D. and Pecknold, D. A., (1974) "Inelastic Model for Cyclic Biaxial Loading for Reinforced Concrete," Civil Engineering Studies, Structural Research Series, No. 409, University of Illinois at Urbana-Champaign, Illinois, July.

[50] Davey, B.E. (1975). "Reinforced Concrete Bridge Piers under Seismic Loading." Master of Engineering Report. Civil Engineering Department, University of Canterbury, Christchurch, New Zealand.

[51] De Luca, A., Nardone, F., Matta, F., Nanni, A., Lignola, G. P., and Prota, A. (2010). Structural evaluation of full-scale FRP-confined reinforced concrete columns. *Journal of Composites for Construction, 15*(1), 112-123.

[52] Demers M. and K.W. Neale, (1999), "Confinement of reinforced concrete columns with fibre-reinforced composite sheets—an experimental study", *Canadian Journal of Civil Engineering*, 26, 226–241.

[53] Dhakal P.R. and K. Maekawa, (2002), "Reinforcement Stability and Fracture of Cover Concrete in Reinforced Concrete Members", *Journal of Structural Engineering, ASCE*, 128(10), 1253-1262

[54] DIN 1045 (1972), "Beton und Stahlbetonbau", Bemessung und Ausfuhrung, Deutsches Institut fur Normung, Berlin

[55] DIN 488 (1972), "Reinforcing steels", in english, Deutsches Institut fur Normung, Berlin

[56] Eid, R., and Paultre, P. (2017). Compressive behavior of FRP-confined reinforced concrete columns. *Engineering Structures, 132,* 518-530.

[57] Elwood K., Matamoros A., Wallace J., Lehman D., Heintz J., Mitchell A., Moore M., Valley M., Lowes L., Comartin C., and Moehle J., (2007). "Update to ASCE/SEI 41 Concrete Provisions", *Earthquake Spectra,* 23(3), 493-523.

[58] Elwood K.J. and Moehle J.P. (2008), "Dynamic collapse analysis for a reinforced concrete frame sustaining shear and axial failures", *Earthquake Engineering and Structural Dynamics*, John Wiley & Sons, Vol. 37, pp.991−1012.

[59] Elwood, K. (2002) “Shake Table Tests and Analytical Studies on the Gravity Load Collapse of Reinforced Concrete Frames”. PhD Thesis, University of California, Berkeley, Berkeley, USA.

[60] Elwood, K. J. and Moehle, J. P. (2005) “Drift Capacity of Reinforced Concrete Columns with Light Transverse Reinforcement”, *Earthquake Spectra*, 21, 71-89.

[61] Elwood, K. J. and Moehle, J. P. (2005). Axial Capacity Model for Shear-Damaged Columns. *ACI Structural Journal,* 102(4), 578-587.

[62] EN 1992-1-1 (2004): Eurocode 2: Design of concrete structures – Part 1-1: General rules and rules for buildings, European Committee for Standardization (CEN), Brussels.

[63] EN 1998-1 (2004), Eurocode 8: Design of structures for earthquake resistance – Part 1: General rules seismic actions and rules for buildings, European Committee for Standardization (CEN), Brussels.

[64] EN 1998-3 (2005), Eurocode 8: Design of structures for earthquake resistance -Part 3: Assessment and retrofitting of buildings. European Committee for Standardization (CEN), Brussels.

[65] Esmaeily A. and Xiao Y. (2002). “Seismic Behavior of Bridge Columns Subjected to Various Loading Patterns,” Pacific Earthquake Engineering Research Center Report, University of California, Berkeley, 2002/15.

[66] Eurocode 2, (2005). “Design of Concrete Structures. — Part 1: General Rules and Rules for Buildings”. European Committee for Standardisation. Brussels.

[67] Eurocode 8, (2005). “Design of structures for earthquake resistance − Part 3: Assessment and retrofitting of buildings”, European Committee for Standardisation.

[68] Fahmy, M. F., Ismail, A. M., and Wu, Z. (2017). Numerical Study on the Applicability of Design-Oriented Models of FRP-Confined Concrete for Predicting the Cyclic Response of Circular FRP-Jacketed RC Columns. *Journal of Composites for Construction*, *21*(5), 04017017.

[69] Farahmandpour, C., Dartois, S., Quiertant, M., Berthaud, Y., and Dumontet, H. (2017). A concrete damage–plasticity model for FRP confined columns. *Materials and Structures*, *50*(2), 156.

[70] FEMA 273 (1997), “NEHRP Guidelines for the seismic rehabilitation of buildings”, *Federal Emergency Management Agency*, Washington, D.C., chapter 6.4.4: “Shear and Torsion”.

[71] FEMA 356 (2000), “Prestandard and commentary for the seismic rehabilitation of buildings”, *Federal Emergency Management Agency*, Washington, D.C., chapter 6.4.4: “Shear and Torsion.”

[72] Fenwick R. C., and Davidson B. J. (1995). “Elongation in ductile seismic resistance reinforced concrete frames.” ACI Special Publication SP-157, American Concrete Institute, Detroit, pp.143–170.

[73] Fib Model Code (2010), Chapter 6: Interface Characteristics, Ernst & Sohn Publications, Berlin, Germany, pp.434.

[74] Filip C. Filippou, 1996, "FEDEAS nonlinear static and dynamic analysis from research to practice", Proceedings of the: *Conference on Analysis and Computation, Chicago, IL, USA, 31-42.*

[75] Filippou F.C. and Constantinides M., *FEDEAS Lab – Getting Started Guide and Simulation Examples*, NEESgrid Report 2004-22 and SEMM Report 2004-05, 2004.

[76] Filippou, F. C., and Fenves, G. L. (2004). Methods of analysis for earthquake-resistant structures. In: Bozorgnia Y, Bertero VV (eds) *Earthquake engineering: From engineering seismology to performance-based engineering*. CRC Press, Boca Raton.

[77] Filippou, F., Popov, E., and Bertero, V. (1983). Modeling of R/C joints under cyclic excitations. *Journal of Structural Engineering, ASCE,* 109(11):2666–2684.

[78] Fotopoulou M., G. Thermou and S. J. Pantazopoulou (2011), "Comparative evaluation of displacement based vs. force-based pushover analysis of Seismically deficient R.C. structures", CD-ROM Proceedings, Eurodyn 2011, 8th International Conference on Structural Dynamics, 4-6 July 2011, Leuven, Belgium.

[79] Frosch, R.J. (2009), "Contribution of Concrete to Shear Resistance," *Proceedings of the 2009 ASCE/SEI Structures Congress,* Austin, Texas, USA, April 30- May 2.

[80] Galeota, D.: Giammatteo and M.M., Marino, R. (1996). "Seismic Resistance of High Strength Concrete Columns." *Proceedings of the Eleventh World Conference on Earthquake Engineering*, Disc 3, Paper No. 1390.

[81] Gallardo-Zafra R. and K. Kawashima, 2009, "Analysis of CFRP RC Bridge Columns under Lateral Cyclic Loading, "*Journal of Earthquake Engineering*, 13, 129-154

[82] Ghannoum WM and Moehle JP (2012) "Shake-Table Tests of a Concrete Frame Sustaining Column Axial Failures", *ACI Structural Journal*, 109(3):393-402

[83] Ghee A. B., Priestley M. J. N. and Paulay T (1989) "Seismic Shear Strength of Reinforced Concrete Columns", *ACI Structural Journal*, 86(1):45-59.

[84] Ghee, A. B., Priestley, M.J.N., and Park, R. (1981). "Ductility of Reinforced Concrete Bridge Piers under Seismic Loading." *Report 81-3*, Department of Civil Engineering, University of Canterbury, Christchurch, New Zealand.

[85] Gicev V. and Trifunac M.D. (2006). Non-linear earthquake waves in seven-storey reinforced concrete hotel, Report CE 06-03, Dept. of Civil Eng. Univ. of Southern California, Los Angeles, California

[86] Gil, Amparo; Segura, Javier; Temme, and Nico M. (2007), "§5.3: Gauss quadrature", Numerical Methods for Special Functions, SIAM, ISBN 978-0-89871-634-4

[87] Gill, W. D., Park, R., and Priestley, M.J.N. (1979). "Ductility of Rectangular Reinforced Concrete Columns With Axial Load." Report 79-1, Department of Civil Engineering, University of Canterbury, Christchurch, New Zealand.

[88] Hany, N. F., Hantouche, E. G., and Harajli, M. H. (2016). Finite element modeling of FRP-confined concrete using modified concrete damaged plasticity. *Engineering Structures, 125*, 1-14.

[89] Henry, L., and Mahin, S. A. (1999). "Study of Buckling of Longitudinal Bars in Reinforced Concrete Bridge Columns." Report to the California Department of Transportation.

[90] Hognestad, E. (1951). A Study of Combined Bending and Axial Load in Reinforced Concrete Members. Bulletin No. 399, Engineering Experimental Station, University of Illinois.

[91] Holub C.J. (2009) "Interaction of Variable Axial Load and Shear Effects in RC Bridges", Ph.D. Thesis, University of Illinois at Urbana-Champaign, USA.

[92] Hosotani, M., Kawashima, K. and Hoshikuma, J. (1997). A study on confinement effect of concrete cylinders by carbon fiber sheets. *Non-Metallic (FRP) Reinforcement for Concrete Structures*, *1*, 209-216.

[93] Hughes, T. J. R. (2000). The Finite Element Method: Linear Static and Dynamic Finite Element Analysis, Dover Publications.

[94] Imai, H., and Yamamoto, Y. (1986). "A Study on Causes of Earthquake Damage of Izumi High School Due to Miyagi-Ken-Oki Earthquake in 1978." *Transactions of the Japan Concrete Institute*, 8.

[95] Inel, M., Aschheim, M. and Pantazopoulou, S. (2004). Deformation Indices for Concrete Columns: Predicted vs. Measured. 13thWorld Conf. on Earthquake Engineering, Vancouver, Canada, No. 2397

[96] Ioannou, A.I. and Pantazopoulou, S.J. (2016) Seismic behavior indices of old type reinforced concrete members, ECCOMAS Congress 2016 - Proceedings of the 7th European Congress on Computational Methods in Applied Sciences and Engineering, 3, pp. 5464-5482. 5-10 June, Crete, Greece.

[97] Ioannou, A.I., Pantazopoulou, S.J., Georgiou A and Ilampas R. (2018). Ultimate Behavior (or Limit) States of Reinforced Concrete Columns. In:*18th Pan-Hellenic Conference on Concrete Structures*, Athens, Greece, March, 29-31. (in Greek)

[98] Ismail, A. M., Fahmy, M. F., and Wu, Z. (2017). Simulating the lateral performance of FRP-confined RC circular columns using a new eccentric-based stress-strain model. *Composite Structures*, *180*, 88-104.

[99] Jean-Luc Chabert, ed. (1999) A History of Algorithms: From the Pebble to the Microchip, Berlin: Springer, pp. 86-91.

[100] Jiang, J. F., and Wu, Y. F. (2012). Identification of material parameters for Drucker–Prager plasticity model for FRP confined circular concrete columns. *International Journal of Solids and Structures*, *49*(3-4), 445-456.

[101] Kanda, M., Shirai, N., Adachi, H., and Sato, T. (1988). "Analytical Study on Elasto-Plastic Hysteretic Behaviors of Reinforced Concrete Members." *Transactions of the Japan Concrete Institute*, 10.

[102] Karabinis, A. I., and Kiousis, P. D. (1996). Strength and ductility of rectangular concrete columns: A plasticity approach. *Journal of Structural Engineering*, *122*(3), 267-274.

[103] Karabinis, A. I., Rousakis, T. C., and Manolitsi, G. E. (2008). 3D finite-element analysis of substandard RC columns strengthened by fiber-reinforced polymer sheets. *Journal of Composites for Construction*, *12*(5), 531-540.

[104] Karam, G. and Tabbara, M. (2005). Confinement effectiveness in rectangular concrete columns with fiber reinforced polymer wraps. *Journal of composites for construction*, *9*(5), 388-396.

[105] Karaveziroglou M. (2009), "Strength of Concrete and Steel according to the requirements throughout the years", *16th Hellenic Concrete Conference*, Paphos, Cyprus.

[106] Karsan, I. D. and Jirsa, J. O. (1969). Behavior of concrete under compressive loadings. *Journal of the Structural Division*. 95(12):2543–64.

[107] Kawashima K. (2006), "Seismic Design, Isolation and Retrofit of Bridges", Lecture Notes, ROSE School, IUSS, Pavia, Italy.

[108] Khaloo A., Y. Javid and M. Tazarv, 2008, "Experimental Study of the Internal and External (FRP) Confinement Effect on Performance of Compressive Concrete Members", Proceedings of the: *14th World Conference on Earthquake Engineering (14WCEE), Beijing, China*.

[109] Kim SJ, Holub CJ and Elnashai AS. (2011). "Experimental investigation of the behaviour of RC bridge piers subjected to horizontal and vertical earthquake motion," *Engineering Structures,* 33, 2221-2235

[110] Kono, S., and Watanabe, F. (2000). "Damage Evaluation of Reinforced Concrete Columns Under Multiaxial Cyclic Loadings." The Second U.S.-Japan Workshop on Performance- Based Earthquake Engineering Methodology for Reinfoced Concrete Building Structures, Sapporo, Japan.

[111] Kowalsky, M.J., Priestley, M.J.N., and Seible, F. (1999). "Shear and Flexural Behavior of Lightweight Concrete Bridge Columns in Seismic Regions." *ACI Structural Journal,* 96(1), 136-148.

[112] Kunnath, S., El-Bahy, A., Taylor, A., and Stone, W. (1997). "Cumulative Seismic Damage of Reinforced Concrete Bridge Piers." Technical Report NCEER-97-0006, National Center for Earthquake Engineering Research, Buffalo, New York.

[113] Kupfer, H., Hilsdorf, H. K., and Rusch, H. (1969, August). Behavior of concrete under biaxial stresses. In *ACI Journal* (Vol. 66, No. 8, pp. 656-666).

[114] Lam L. and J.G. Teng, 2004, "Ultimate Condition of Fiber Reinforced Polymer-Confined Concrete", *Journal of Composites for Construction, ASCE,* 8(6), 539-548.

[115] Lam, L., and Teng, J. G. (2003). Design-oriented stress–strain model for FRP-confined concrete. *Construction and building materials, 17*(6-7), 471-489.

[116] Lee J., and Watanabe F. (2003). "Predicting the longitudinal axial strain in the plastic hinge regions of reinforced concrete beams subjected to reversed cyclic loading." *Engineering Structures,* 25(7), pp. 927–939.

[117] Legeron, F., and Paultre, P. (2000). "Behavior of High-Strength Concrete Columns under Cyclic Flexure and Constant Axial Load." *ACI Structural Journal,* 97(4), 591-601.

[118] Lehman, D. E., Lynn, A. C., Aschheim, M. A. and Moehle, J. P. (1996). Evaluation methods for reinforced concrete columns and connections. 11th World Conference on Earthquake Engineering, Acapulco, Mexico, June 23-28, Paper No.673.

[119] Lehman, D.E., and Moehle, J.P. (2000). "Seismic Performance of Well-Confined Concrete Bridge Columns." Pacific Earthquake Engineering Research Center Report 1998/01, University of California, Berkeley, California.

[120] Lim, K. Y., McLean, D. I., and Henley, E. H. (1991). "Moment-Reducing Hinge Details for the Bases of Bridge Columns." Transportation Research Record, No. 1275, Transportation Research Board, Washington, D.C.

[121] Liu, T. C., Nilson, A. H., and Slate, F. O. (1972). Biaxial stress-strain relations for concrete. *Journal of the Structural Division, 98*(5), 1025-1034.

[122] Lynn A.C., Moehle J. P., Mahin S. A., and Holmes W. T. (1996) "Seismic Evaluation of Existing Reinforced Concrete Columns", *Earthquake Spectra,* 12(4): 715-739.

[123] Lynn, A. (1999). "Seismic Evaluation of Existing Reinforced Concrete Building Colums." Ph.D. Thesis, University of California at Berkeley.

[124] Lynn, A. C., Moehle, J. P., Mahin, S. A., and Holmes, W. T. (1996). Seismic Evaluation of Existing Reinforced Concrete Columns. *Earthquake Spectra, 1*2(4), 715-739.

[125] MacGregor, J. and Wight, J. (2005). Reinforced concrete mechanics and design. Pearson Education, Inc., Upper Saddle River, New Jersey, USA. ISBN 0-13-142994-9.

[126] Mandal S., A. Hoskin, and A. Fam, (2005), "Influence of Concrete Strength on Confinement Effectiveness of Fiber-Reinforced Polymer Circular Jackets", *ACI Structural Journal,* 102(3), 383-392.

[127] Mander, J. B., Priestley, M. J. N., and Park, R. (1988). ''Theoretical stress-strain model for confined concrete.'' *Journal of Structural Engineering ASCE,* 114(8), 1804–1826.

[128] Martin-Perez and Pantazopoulou, (2001), "Effect of Bond, Aggregate Interlock and Dowel Action on the Shear-Strength Degradation of Reinforced Concrete", *Engineering Structures, Elsevier,* 23:214-227.

[129] Matamoros, A.B. (1999). "Study of Drift Limits for High-Strength Concrete Columns." Department of Civil Engineering, University of Illinois at Urbana-Champaign.

[130] Matthews, J. G., Mander, J. B., and Bull, D. K. (2004). "Prediction of beam elongation in structural concrete members using a rainflow method." Proc., New Zealand Society of Earthquake Engineering Conf., New Zealand Society for Earthquake Engineering,Wellington, New Zealand.

[131] Matthys S., H. Toutanji K. Audenaert and L.Taerwe (2005), "Axial Load Behavior of Large-Scale Columns Confined with Fiber-Reinforced Polymer Composites", *ACI, Structural Journal,* 102(2), 258-267.

[132] Mazzoni, S., F. Mc Kenna, M. H. Scott, and G. Fenves (2006). The Open System for Earthquake Engineering Simulation (OpenSees) User Command-Language Manual (http://opensees.berkeley.edu/)

[133] McKenna, F. (1997). Object-Oriented Finite Element Programming Frameworks for Analysis, Algorithms and Parallel Computing. Dissertation, University of California, Berkley, Berkley, United States.

[134] Megalooikonomou KG (2018) PHAETHON: Software for Analysis of Shear-Critical Reinforced Concrete Columns, *Modern Applied Science, CCSE,* 12(3), 1-22.

[135] Megalooikonomou KG, Kim KD and Monti G (2007). "Stress-Strain Model for FRP-confined Rectangular RC Sections via an Incremental Procedure". In: *Asia-Pacific Conference on FRP in Structures (APFIS 2007).* Hong Kong China, December 12-14.

[136] Megalooikonomou KG, Monti G. and Santini S., (2011), "Constitutive Model for FRP and Tie – Confined Concrete", Proceedings of the: *3rd International Conference on Computational Methods in Structural Dynamics and Earthquake Engineering (COMPDYN 2011), Corfu, Greece.*

[137] Megalooikonomou KG, Pantazopoulou SJ and Tastani SP (2017). "A Mechanistic Approach in Defining Inelastic Rotation Capacity of RC Columns", *6th International Conference on Computational Methods in Structural Dynamics and Earthquake Engineering (COMPDYN 2017).* Rhodes Island, Greece, June 15 -17.

[138] Megalooikonomou KG, Pantazopoulou SJ and Tastani SP (2017). "Plastic Hinge Length in Columns – Definition through Consideration of Yield Penetration Effects", *16th World Conference on Earthquake Engineering (16WCEE)*, Santiago, Chile, January 9-13.

[139] Megalooikonomou KG, Tastani SP and Pantazopoulou SJ. (2018) "Effect of Yield Penetration on Column Plastic Hinge Length," *Engineering Structures*, 156, 161-174.

[140] Megalooikonomou KG. and Monti G. (2015), "Numerical Modeling of FRP-Retrofitted Circular RC Columns Including Shear." Proceedings of the: *5th International Conference on Computational Methods in Structural Dynamics and Earthquake Engineering* (COMPDYN 2015). Crete, Greece.

[141] Megalooikonomou KG. and Papavasileiou GS (2019). Modeling of FRP-Confinement of Large-Scale Rectangular RC Columns. In: *7th International Conference on Computational Methods in Structural Dynamics and Earthquake Engineering (COMPDYN 2019)*. Crete Island, Greece, June 24 -26.

[142] Megalooikonomou KG., Monti G, Santini S (2012), "Constitutive Model for Fiber Reinforced Polymer- and Tie Confined Concrete." *ACI, Structural Journal*, 109(4), 569-578.

[143] Megalooikonomou KG., Tastani SP and Pantazopoulou SJ (2016). The Effect of Bond on Plastic Hinge Length of Columns – Analytical Solution. In:*17th Pan-Hellenic Conference on Concrete Structures*, Thessaloniki, Greece, November 10-12. (in Greek)

[144] Megalooikonomou, K. G., and Papavasileiou, G. S. (2019). Analytical Stress-Strain Model for FRP-Confined Rectangular RC Columns. Front. *Built Environ*, *5*, 39.

[145] Megalooikonomou. K. G. (2007) Modelling of FRP-Confinement of Rectangular RC Sections, Master Thesis, European School for Advanced Studies in Reduction of Seismic Risk (ROSE School), University of Pavia, Pavia, Italy URL: http://www.roseschool.it/page/202/modelling-of-frp-confinement-of-rectangular-rc-sections.html

[146] Mehrabani R. V. and Sigrist V. (2015), "Elongation of Reinforced Concrete Plastic Hinges Subjected to Reversed Cyclic Loading ", *ASCE, Journal of Structural Engineering*, Vol. 141 (8), pp.1−10.

[147] Memon, M. S. and Sheikh, S. A. (2005). Seismic resistance of square concrete columns retrofitted with glass fiber-reinforced polymer. *ACI structural journal*, *102*(5), 774-783.

[148] Menengotto, M. and Pinto E. (1973). Method of Analysis for Cyclically Loaded Reinforced Concrete Plane Frames Including Changes in Geometry and Nonelastic Behavior of Elements under Combined Normal Force and Bending. In *IABSE Symposium on Resistance and Ultimate Deformability of Structures Acted on by Well-Defined Repeated Loads, Final Report,* Lisbon, Portugal.

[149] Mergos, P. E. and Kappos, A. J. (2008), A distributed shear and flexural flexibility model with shear–flexure interaction for R/C members subjected to seismic loading. *Earthquake Engng. Struct. Dyn.*, 37: 1349-1370.

[150] Mirmiran, A., Shahawy, M., Samaan, M., Echary, H. E., Mastrapa, J. C., and Pico, O. (1998). Effect of column parameters on FRP-confined concrete. *Journal of Composites for construction*, 2(4), 175-185.

[151] Mo, Y.L., and Wang, S.J. (2000). "Seismic Behavior of RC Columns with Various Tie Configurations." *Journal of Structural Engineering*, ASCE. 126(10), 1122-1130.

[152] Moehle, J.P. (1992). "Displacement-Based Design of RC Structures Subjected to Earthquakes." *Earthquake Spectra*; 8(3):403-428.

[153] Monti G. and C. Nuti, 1992, "Nonlinear Cyclic Behavior of Reinforcing Bars Including Buckling", *Journal of Structural Engineering, ASCE*, 118(12), 3268-3284

[154] Monti G. and Megalooikonomou KG., (2009), "Modelling of FRP&Steel Confined Circular RC Sections", Proceedings of the: *9th International Polymer Reinforcement for Concrete Structures (FRPRCS-9),* Sydney, Australia.

[155] Morsch, E. (1922). Der Eisenbetonbau-Seine Theorie und Anwendung, 5th Edition, Vol. 1, Part 1, Wittwer, Stuttgart, Germany.

[156] Mosalam M. K., Talaat M. and Binici B., (2007), "A computational model for reinforced concrete members confined with fiber reinforced polymer lamina : Implementation and experimental validation" *Composites: Part B* ,38 ,598–613

[157] Moyer, M., and Kowalsky, M. (2001). "Influence of Tension Strain on Buckling of Reinforcement in RC Bridge Columns." Department of Civil Engineering, North Carolina State University, Raleigh, North Carolina

[158] Muguruma, H., Watanabe, F., and Komuro, T. (1989). "Applicability of High Strength Concrete to Reinforced Concrete Ductile Column." *Transactions of the Japan Concrete Institute*, 11.

[159] Munro, I.R.M., Park, R., and Priestley, M.J.N. (1976). "Seismic Behaviour of Reinforced Concrete Bridge Piers." Report 76-9, Department of Civil Engineering, University of Canterbury, Christchurch, New Zealand.

[160] Muttoni A., Schwartz J. and Thürlimann B., (1997), "Design of Concrete Structures with Stress Fields", Birkhäuser.

[161] Mwafy A. and Elnashai A. (2008). "Importance of shear assessment of concrete structures detailed to different capacity design requirements", *Engineering Structures*, 30, 1590-1604.

[162] Nagasaka, T. (1982). "Effectiveness of Steel Fiber as Web Reinforcement in Reinforced Concrete Columns." *Transactions of the Japan Concrete Institute*, 4.

[163] Nelson and Jared M. (2000). "Damage Model Calibration for Reinforced Concrete Columns." Master's Thesis, Department of Civil and Environmental Engineering, University of Washington, Seattle.

[164] Ng K. H., Priestley, M.J.N., and Park, R. (1978). "Seismic Behaviour of Circular Reinforced Concrete Bridge Piers." Report 78-14, Department of Civil Engineering, University of Canterbury, Christchurch, New Zealand.

[165] Ngoc Tran C. T., and Li B. (2013), "Ultimate Displacement of Reinforced Concrete Columns with Light Transverse Reinforcement", *Journal of Earthquake Engineering*, 17, 282–300.

[166] Nisticò, N., and Monti, G. (2013). RC square sections confined by FRP: Analytical prediction of peak strength. *Composites Part B: Engineering*, *45*(1), 127-137.

[167] Nosho, K., Stanton, J., and MacRae, G. (1996). "Retrofit of Rectangular Reinforced Concrete Columns using Tonen Forca Tow Sheet Carbon Fiber Wrapping." Report No. SGEM 96-2, Department of Civil Engineering, University of Washington, Seattle.

[168] Ohno, T., and Nishioka, T. (1984). "An Experimental Study on Energy Absorption Capacity of Columns in Reinforced Concrete Structures." *Proceedings of the JSCE, Structural Engineering/Earthquake Engineering,* 1(2).

[169] Ohue, M., Morimoto, H., Fujii, S., and Morita, S. (1985). "The Behavior of R.C. Short Columns Failing in Splitting Bond-Shear Under Dynamic Lateral Loading." *Transactions of the Japan Concrete Institute*, 7.

[170] Otani S. (2006), "Nonlinear Earthquake Response Analysis of Reinforced Concrete Buildings", Lecture Notes, ROSE School, IUSS, Pavia, Italy.

[171] Ottosen, N. S. (1977). A failure criterion for concrete. American Society of Civil Engineers. Engineering Mechanics Division. Journal, 103(4), 527-535.

[172] Ozbakkaloglu, T. and Lim, J. C. (2013). Axial compressive behavior of FRP-confined concrete: Experimental test database and a new design-oriented model. *Composites Part B: Engineering*, 55, 607-634.

[173] Ozbakkaloglu, T., Gholampour, A., and Lim, J. C. (2016). Damage-plasticity model for FRP-confined normal-strength and high-strength concrete. *Journal of Composites for Construction*, *20*(6), 04016053.

[174] Ozbakkaloglu, T., Lim, J. C. and Vincent, T. (2013). FRP-confined concrete in circular sections: Review and assessment of stress–strain models. *Engineering Structures*, 49, 1068-1088.

[175] P. G. Asteris, S. T. Antoniou,D. S. Sophianopoulos and C. Z. Chrysostomou (2011)Mathematical Macromodeling of Infilled Frames: State of the Art", *Journal of Structural Engineering ASCE*,137(12), 1508-1517

[176] Panagiotakos T. B. and Fardis M. N. (2001). Deformations of reinforced concrete members at yielding and ultimate. *ACI Structural Journal;* 98 (2), 135–148.

[177] Pantazopoulou S. J. (2003). Seismic Assessment and Retrofit of Reinforced Concrete Buildings. *fib* Bulletin No. 24 Chapter 4, Case Postale 88, CH-1015, Lausane, Switzerland

[178] Pantazopoulou S. J. and Syntzirma D. V. (2010), "Deformation capacity of lightly reinforced concrete members – Comparative evaluation*", Advances in Performance – Based Earthquake Engineering (ACES workshop)*, Series Geotechnical, Geological, and Earthquake Engineering, Vol.13, Springer.

[179] Pantazopoulou S.J. and R.H. Mills, (1995), "Microstructural Aspects of the Mechanical Response of Plain Concrete", *ACI Materials Journal*, 92(6), 605-616.

[180] Pantazopoulou S.J., (1998), "Detailing for Reinforcement Stability in RC members", *Journal of Structural Engineering, ASCE,* 124(6), 623-632

[181] Pantazopoulou S.J., (2003), Chapter 4 in "Seismic Assessment and Retrofit of Reinforced Concrete Buildings", *fib Bulletin No. 24*, Case Postale 88, CH-1015, Lausanne, Switzerland

[182] Papavasileiou G.S. and Megalooikonomou K.G. (2015, June) Numerical Simulation of FRP-Confined Circular Bridge Piers Using OpenSees, In Proc., *OpenSees Days Italy (OSD), Second International Conference*, University of Salerno, Salerno, Italy.

[183] Pardalopoulos, S. J., Thermou, G. E., and Pantazopoulou, S. J. (2011). Rapid preliminary seismic assessment methodology for non-conforming reinforced concrete buildings. In ECCOMAS Thematic Conference - *COMPDYN 2011: 3rd International Conference on Computational Methods in Structural Dynamics and Earthquake Engineering*: An IACM Special Interest Conference, Programme.

[184] Park H.-G., Yu E.-G. and Choi K.-K. (2012) "Shear-Strength degradation model for RC columns subjected to cyclic loading", *Engineering Structures*, 34, 187-197.

[185] Park R., and Paulay T. (1975). Reinforced Concrete Structures. *J. Wiley & Sons*, N. York, 769pp.

[186] Park, R., and Paulay, T. (1990). "Use of Interlocking Spirals for Transverse Reinforcement in Bridge Columns." Strength and Ductility of Concrete Substructures of Bridges, RRU (Road Research Unit) Bulletin 84, 1, 77-92.

[187] Parvin, A. and Wang, W. (2001). Behavior of FRP jacketed concrete columns under eccentric loading. *Journal of Composites for Construction*, *5*(3), 146-152. DOI:

[188] Parvin, A. and Wang, W. (2002, June). Tests on concrete square columns confined by composite wraps. In *Proc., 3rd International Conf. on Composites in Infrastructure ICCI'02*., San Francisco, USA

[189] Paulay, T., and Priestley, M. J. N., Seismic Design of Reinforced Concrete and Masonry Buildings, *John Wiley and Sons*, New York, 1992, 767 pp.

[190] Paultre, P., Legeron, F., and Mongeau, D. (2001). "Influence of Concrete Strength and Transverse Reinforcement Yield Strength on Behavior of High-Strength Concrete Columns." *ACI Structural Journal*, 98(4), 490-501.

[191] Peng, B. H. H., Dhakal, R. P., Fenwick, R. C., Carr, A. J., and Bull, D. K. (2011). "Elongation of plastic hinges in ductile RC members: Model verification." *J. Adv. Concr. Technol.*, 9(3), pp. 327–338.

[192] Petrovski, J., and Ristic, D. (1984). "Reversed Cyclic Loading Test of Bridge Column Models." Report IZIIZ 84-164, Institute of Earthquake Engineering and Engineering Seismology.

[193] Piscesa, B., Attard, M. M., and Samani, A. K. (2018). 3D Finite element modeling of circular reinforced concrete columns confined with FRP using a plasticity-based formulation. *Composite Structures*, *194*, 478-493.

[194] Pontangaroa, R.T., Priestley, M.J.N., and Park, R. (1979). "Ductility of Spirally Reinforced Concrete Columns Under Seismic Loading." Report 79-8, Department of Civil Engineering, University of Canterbury, Christchurch, New Zealand.

[195] Popovics, S. (1973). A numerical approach to the complete stress-strain curve of concrete. *Cement and concrete research*, *3*(5), 583-599.

[196] Priestley, M. J. N., and Park, R. (1984). "Strength and ductility of bridge substructures." RRU Bull. No. 71, Road Res. Unit, National Roads Board, Wellington, New Zealand.

[197] Priestley, M.J.N., and Benzoni, G. (1996). "Seismic Performance of Circular Columns with Low Longitudinal Reinforcement Ratios." *ACI Structural Journal*, 93(4), 474-485.

[198] Priestley, M.J.N., Seible F., and Calvi M. (1996). Seismic Design and Retrofit of Bridges. J. Wiley & Sons Inc., N. York.

[199] Priestley, M.J.N.; Verma, R.; and Xiao, Y. [1994], "Seismic Shear Strength of Reinforced Concrete Columns," American Society of Civil Engineers, *Journal of Structural Engineering, ASCE* ,120(8), 2310-2329

[200] Pujol, S. (2002). "Drift Capacity of Reinforced Concrete Columns Subjected to Displacement Reversals." PhD Thesis, Purdue University, USA.

[201] Pujol, S., and Ramirez, J.A. and Sozen, M.A. (1999). "Drift capacity of reinforced concrete columns subjected to cyclic shear reversals," Seismic Response of Concrete Bridges, SP-187, *American Concrete Institute*, Farmington Hills, Michigan. pp. 255-274.

[202] Richart, F. E., Brandtzaeg, and Brown, R. L. (1928). *A study of the failure of concrete under combined compressive stresses*. University of Illinois at Urbana Champaign, College of Engineering. Engineering Experiment Station Bulletin No. 185, University of Illinois, Urbana.

[203] Ritter, W. (1899). Die Bauweise Hennebique. Schweizerische Bauzeitung, 33 (7), 59-61.

[204] Rochette, P. and Labossiere, P. (2000). Axial testing of rectangular column models confined with composites. *Journal of composites for construction*, 4(3), 129-136.

[205] Roeder C., Soderstom, and Graph (2001). "Seismic Performance of Pile-Wharf Connections", Pacific Earthquake Engineering Research Center, PEER.

[206] Rousakis T.C., Rakitzis T.D. and Karabinis A.I. (2012): Design - Oriented Strength Model for FRP Confined Concrete Members. *Journal of composites for construction*, 16(6), 615–625.

[207] Rousakis, T. C., and Tourtouras, I. S. (2015). Modeling of passive and active external confinement of RC columns with elastic material. *ZAMM-Journal of Applied Mathematics and Mechanics/Zeitschrift für Angewandte Mathematik und Mechanik*, *95*(10), 1046-1057.

[208] Rousakis, T. C., Karabinis, A. I., Kiousis, P. D., and Tepfers, R. (2008). Analytical modelling of plastic behaviour of uniformly FRP confined concrete members. *Composites Part B: Engineering*, *39*(7-8), 1104-1113.

[209] Saatcioglu M., and Ozcebe G. (1989). Response of Reinforced Concrete Columns to Simulated Seismic Loading. *ACI Structural Journal*, 86(1), 3-12.

[210] Saatcioglu, M., and Baingo, D. (1999). "Circular High-Strength Concrete Columns Under Simulated Seismic Loading." *Journal of Structural Engineering, ASCE,* 125(3), 272-280.

[211] Saatcioglu, M., and Grira, M. (1999). "Confinement of Reinforced Concrete Columns with Welded Reinforcement Grids." *ACI Structural Journal*, 96(1), 29-39.

[212] Sakai, Y., Hibi, J., Otani, S., and Aoyama, H. (1990). "Experimental Study on Flexural Behavior of Reinforced Concrete Columns Using High-Strength Concrete." *Transactions of the Japan Concrete Institute*, 12.

[213] Samaan, M., Mirmiran, A. and Shahawy, M. (1998). Model of concrete confined by fiber composites. *Journal of structural engineering*, 124(9), 1025-1031.

[214] Scott, B.D., Park, R., and Priestley, M.J.N. (1982). Stress-strain behavior of concrete confined by overlapping hoops at low and high strain rates. *American Concrete Institute Journal*, 79, 13-27.

[215] Scott, B.D., Park, R., and Priestley, M.J.N. (1982). Stress-strain behavior of concrete confined by overlapping hoops at low and high strain rates. *American Concrete Institute Journal*, 79, 13-27.

[216] Sezen H. and Moehle JP (2006) "Seismic Tests of Concrete Columns with Light Transverse Reinforcement", *ACI Structural Journal*, 103(6), 842-849.

[217] Sheikh SA and Yao G., 2002, "Seismic Behaviour of Concrete Columns Confined with Steel and Fiber-Reinforced Polymers, "*Structural Journal, ACI*, 99(1), 72-80.

[218] Sherwood, E.G., Bentz, E. and Collins, M.P. (2006) "Evaluation of Shear Design Methods for Large, Lightly-Reinforced Concrete Beams*," Proceedings of the International Conference on Advances in Engineering Structures, Mechanics & Construction*, University of Waterloo, Waterloo, Ontario, Canada, May 14-17, pp. 153-164

[219] Sigrist V. (2011), "Generalized Stress Field Approach for Analysis of Beams in Shear," *ACI Structural Journal*, 108(4), 479-487.

[220] Sigrist, V., Bentz, E., Ruiz F. M., Foster S. and Muttoni A. (2013). Background to the *fib* Model Code 2010 Shear Provisions – Part I: Beams and Slabs. *Structural Concrete Journal,* International Federation for Structural Concrete (*fib*), 14(3), 195-203.

[221] Siryo K. K. (1975). "A seismic Analysis of Building Structural Members: a List of Experimental Results on Deformation Ability of Reinforced Concrete Columns Under Large Deflection (No.2)." Building Research Institute, Ministry of Construction, Japan.

[222] Soesianawati, M.T., Park, R., and Priestley, M.J.N. (1986). "Limited Ductility Design of Reinforced Concrete Columns." Report 86-10, Department of Civil Engineering, University of Canterbury, Christchurch, New Zealand.

[223] Spacone, E., Filippou, F. C. and Taucer, F. F. (1996). Fibre beam–column model for non-linear analysis of R/C frames: Part I. Formulation. *Earthquake Engineering & Structural Dynamics, 25*(7), 711-725.

[224] Spoelstra M.R., and G. Monti, (1999), "FRP-Confined Concrete Model," *Journal of Composites for Construction, ASCE*, 3(3), 143-150.

[225] Sritharan, S., Priestley and M.J.N., Seible F. (1996). "Seismic Response of Column/Cap Beam Tee Connections with Cap Beam Prestressing." Structural Systems Research Project, Report No. ssrp-96/09, University of California, San Diego.

[226] Stone, W. C., and Cheok, G. S. (1989). "Inelastic Behavior of Full-Scale Bridge Columns Subjected to Cyclic Loading." NIST Building Science Series 166, U.S. National Institute of Standards and Technology, Gaithersburg, Maryland.

[227] Sugano, S. (1996). "Seismic Behavior of Reinforced Concrete Columns Which used Ultra-High- Strength Concrete." *Eleventh World Conference on Earthquake Engineering*, Paper No. 1383.

[228] Syntzirma D. V. and Pantazopoulou S. J. (2007), "Deformation Capacity of R.C. Members with Brittle Details under Cyclic Loads", *ACI Special Publication* 236, 1-22.

[229] Syntzirma D. V., Pantazopoulou S. J. and Aschheim M. (2010), "Load history effects on deformation capacity of flexural members limited by bar buckling", *ASCE, Journal of Structural Engineering*, Vol. 136(1), pp.1−11.

[230] Taciroglu E. and Khalili-Tehrani P. (2008), "Older Reinforced Concrete Buildings", The Shake Out Scenario: U.S. Geological Survey Open File Report 2008-1150, California Geological Survey Preliminary Report 25 version 1.0, U.S. Geological Survey Circular 1324 California Geological Survey Special Report 207 version 1.0.

[231] Tanaka, H., and Park, R. (1990). "Effect of Lateral Confining Reinforcement on the Ductile Behavior of Reinforced Concrete Columns." Report 90-2, Department of Civil Engineering, University of Canterbury, Christchurch, New Zealand.

[232] Tassios, T. P. and Yannopoulos, P. J. (1981). Analytical studies onreinforced concrete members under cyclic loading based on bond-slip relationships. *ACI Materials Journal*; 78 (3), 206-216.

[233] Tastani S.P. and Pantazopoulou S.J. (2013). Yield penetration in seismically loaded anchorages: effects on member deformation capacity. *Techno press Earthquake and Structures*; 5(5), 527-552.

[234] Tastani S.P., S.J. Pantazopoulou, D. Zdoumba, V. Plakantaras, and E. Akritidis, (2006), "Limitations of FRP Jacketing in Confining Old – Type Reinforced Concrete Members in Axial Compression," *Journal of Composites for Construction, ASCE,* 10(1), 13-25.

[235] Tastani, S. P., and Pantazopoulou, S. J. (2013). Reinforcement and concrete bond: State determination along the development length. *Journal of Structural Engineering, ASCE, 139*(9), 1567-1581.

[236] Tastani, S. P., Balafas, I., Dervisis A., and S. J. Pantazopoulou, (2013). "Effect of Core Compaction on Deformation Capacity of FRP-Jacketed Concrete", *Construction & Building Materials, Elsevier*, Volume 47, October 2013, Pages 1078-1092.

[237] Tastani, S.P. and Pantazopoulou, S.J. (2010). Direct tension pullout bond test: experimental results. *Journal of Structural Engineering, ASCE*. 136(6): 731-743.

[238] Tastani. S (2005), Conventional and New type Reinforcing Bar – to –Concrete Bond , PhD Thesis, Department of Civil Engineering, Democritus University of Thrace, Xanthi, Greece, (in Greek).

[239] Technical Report, 2001, *Externally bonded FRP reinforcement for RC structures, 14th fib Bulletin, fib,* Lausanne, Switzerland.

[240] Teng JG, Chen JF, Smith ST, and Lam L. (2002) FRP-strengthened RC structures. U.K.: John Wiley and Sons Inc.

[241] Teng, J. G., and Lam, L. (2004). Behavior and modeling of fiber reinforced polymer-confined concrete. *Journal of structural engineering*, *130*(11), 1713-1723.

[242] Teng, J. G., Zeng, J. J., and Chen, J. F. (2015, December). Measurement of axial stress distributions in FRP-confined concrete columns using Tekscan pressure sensors. In *Proceedings of the Joint Conference of FRPRCS-12 & APFIS-2015, Nanjing, China* (pp. 14-16).

[243] Thomsen, J., and Wallace, J. (1994). "Lateral Load Behavior of Reinforced Concrete Columns Constructed Using High-Strength Materials." *ACI Structural Journal*, 91(5), 605-615.

[244] Timoshenko, S., (1953), History of strength of materials, McGraw-Hill New York

[245] Tureyen, A.K. and Frosch, R.J. (2003), "Concrete Shear Strength: Another Perspective," *ACI Structural Journal*, 100(5), 609-615.

[246] Umehara, H., and Jirsa, J.O. (1982). "Shear Strength and Deterioration of Short Reinforced Concrete Columns Under Cyclic Deformations." PMFSEL Report No. 82-3, Department of Civil Engineering, University of Texas at Austin.

[247] Vecchio, F. J., and Collins, M. P. (1982). Response of Reinforced Concrete to In-Plane Shear and Normal Stresses, Publication No. 82-03, Department of Civil Engineering, University of Toronto, Canada.

[248] Vecchio, F. J., and Collins, M. P. (1986). The modified compression field theory for reinforced concrete elements subjected to shear. *ACI Journal Proceedings,* 83(2), 219-231.

[249] Vecchio, F. J., and Collins, M. P. (1988). Predicting the Response of Reinforced Concrete Beams Subjected to Shear Using Modified Compression Field Theory. *ACI Structural Journal*, 85(3), 258-268.

[250] Vintzileou, E. and Panagiotidou, E. (2008). An empirical model for predicting the mechanical properties of FRP-confined concrete. *Construction and Building Materials*, *22*(5), 841-854.

[251] Vu, Nganha D., Priestley, M.J.N., Seible, F., and Benzoni, G. (1998). "Seismic Response of Well Confined Circular Reinforced Concrete Columns with Low Aspect Ratios." Proceedings of the 5th Caltrans Seismic Research Workshop, Sacramento, California.

[252] Wang, Z., Wang, D., Smith, S. T., and Lu, D. (2011). CFRP-confined square RC columns. II: Cyclic axial compression stress-strain model. *Journal of composites for construction*, *16*(2), 161-170.

[253] Watson, S. (1989). "Design of Reinforced Concrete Frames of Limited Ductility." Report 89-4, Department of Civil Engineering, University of Canterbury, Christchurch, New Zealand.

[254] Watson, S., and Park, R. (1989). "Design of Reinforced Concrete Frames of Limited Ductility." Report 89-4, Department of Civil Engineering, University of Canterbury, Christchurch, New Zealand.

[255] Watson, S., and Park, R., (1994), "Simulated Seismic Load Tests on Reinforced Concrete Columns", *Journal of Structural Engineering, ASCE*, 120(6):1825-1849.

[256] Wehbe, N., and Saiidi, M.S., and Sanders, D. (1998). "Confinement of Rectangular Bridge Columns for Moderate Seismic Areas." National Center for Earthquake Engineering Research (NCEER) Bulletin, 12(1).

[257] Whitney, C.S. (1937). Design of Reinforced Concrete Members Under Flexure and Combined Flexure and Direct Compression. *American Concrete Institute Journal*, 33: 483-498.

[258] Wight, J.K., and Sozen, M.A. (1973). "Shear Strength Decay in Reinforced Concrete Columns Subjected to Large Deflection Reversals." Structural Research Series No. 403, Civil Engineering Studies, University of Illinois, Urbana-Champaign.

[259] Wong Y. L., Paulay T, and Priestley M. J. N., (1993) "Response of Circular Reinforced Concrete Columns to Multi-directional Seismic Attack", *ACI Structural Journal*, 90(2), 180-191.

[260] Wong, Y.L., Paulay, T., and Priestley, M.J.N. (1990). "Squat Circular Bridge Piers Under Multi- Directional Seismic Attack." Report 90-4, Department of Civil Engineering, University of Canterbury, Christchurch, New Zealand.

[261] Woods, C. and Matamoros, A.B. (2010). "Effect of longitudinal reinforcement ratio on the failure mechanism of R/C columns most vulnerable to collapse." *9thU.S. National and 10th Canadian Conference on Earthquake Engineering*. No 1636.

[262] Xiao Y., and Yun., H. W. (2002). "Experimental Studies on Full-Scale High-Strength Concrete Columns." *ACI Structural Journal*, 99(2), 199-207.

[263] Xiao, Y., and Martirossyan, A. (1998). "Seismic Performance of High-Strength Concrete Columns." *Journal of Structural Engineering, ASCE*, 124(3), 241-251.

[264] Yavari S., Elwood K. J., Wu C.-L., Lin S.-H., Hwang S.-J., and Moehle J. P. (2013) "Shaking Table Tests on Reinforced Concrete Frames without Seismic Detailing", *ACI Structural Journal*, 110(6), 1001-1011.

[265] Yu, T. T. J. G., Teng, J. G., Wong, Y. L., and Dong, S. L. (2010). Finite element modeling of confined concrete-I: Drucker–Prager type plasticity model. *Engineering Structures*, *32*(3), 665-679.

[266] Yu, T., Teng, J. G., Wong, Y. L., and Dong, S. L. (2010). Finite element modeling of confined concrete-II: Plastic-damage model. *Engineering structures*, *32*(3), 680-691.

[267] Zahn, F.A., Park, R., and Priestley, M.J.N. (1986). "Design of Reinforced Bridge Columns for Strength and Ductility." Report 86-7, Department of Civil Engineering, University of Canterbury, Christchurch, New Zealand.

[268] Zeng, J. J., Lin, G., Teng, J. G. and Li, L. J. (2018). Behavior of large-scale FRP-confined rectangular RC columns under axial compression. *Engineering Structures, 174*, 629-645.

[269] Zeris, C.A. (1986). "Three-Dimensional Nonlinear Response of Reinforced Concrete Buildings. "Ph.D. Thesis, Department of Civil and Environmental Engineering, University of California, Berkeley, California, USA.

[270] Zhou, X., Higashi, Y., Jiang, W., and Shimizu, Y. (1985). "Behavior of Reinforced Concrete Column Under High Axial Load." *Transactions of the Japan Concrete Institute*, 7.

[271] Zhou, X., Satoh, T., Jiang, W., Ono, A., and Shimizo, Y. (1987). "Behavior of Reinforced Concrete Short Column Under High Axial Load." *Transactions of the Japan Concrete Institute*, 9.

APPENDIX A

This is an Appendix for Chapter 3.

Table A.1: Reinforced Concrete Columns with a circular cross section, that failed in flexure.

Specimen ID in Database	Axial Load (KN)	Diameter (mm)	Cover to Ctr. of Hoop Bar (mm)	Shear Span (mm)	Concrete Strength (MPa)	Number of Longitudinal Bars	Diameter of Long. Bars (mm)	Yield Strength of Long. Bars (MPa)	Ultim. Strength of Long. Bars (MPa)	Longitudinal Reinforc. ratio (%)	Hoop Spacing (mm)	Spiral Diameter (mm)	Yielding Strength Spiral (MPa)	Transverse Reinforc. ratio (%)
43	907	400	20	800	38	20	16	423	577	3.2	60	10	300	1.42
45	1813	400	20	800	37	20	16	475	625	3.2	60	10	300	1.42
46	145	307	36	1910	38.8	12	12	240	-	1.83	75	6	240	0.63
47	254	307	36	1910	36.2	12	12	240	-	1.83	75	6	240	0.63
50	151	152	10.2	1140	34.5	8	12.7	448	-	5.57	22	3.7	620	1.45
51	151	152	10.2	570	34.5	8	12.7	448	-	5.57	22	3.7	620	1.45
52	220	152	10.2	570	34.5	8	12.7	448	-	5.57	22	3.7	620	1.45
53	4450	1520	58.7	9140	35.8	25	43	475	-	1.99	89	15.9	493	0.63
54	4450	1520	60.3	4570	34.3	25	43	475	-	1.99	54	19.1	435	1.49
55	120	250	9.9	750	24.1	25	7	446	-	1.98	9	3.1	441	1.41
56	239	250	9.9	750	23.1	25	7	446	-	1.98	9	3.1	441	1.41

57	120	250	9.7	1500	25.4	25	7	446	-	1.98	14	2.7	476	0.68
58	120	250	9.9	750	24.4	25	7	446	-	1.98	9	3.1	441	1.41
59	239	250	9.9	750	24.3	25	7	446	-	1.98	9	3.1	441	1.41
60	120	250	9.7	1500	23.3	25	7	446	-	1.98	14	2.7	476	0.68
93	200	305	14.5	1372	29	21	9.5	448	690	2.04	19	4	434	0.94
94	200	305	14.5	1372	29	21	9.5	448	690	2.04	19	4	434	0.94
95	222	305	14.5	1372	35.5	21	9.5	448	690	2.04	19	4	434	0.94
96	222	305	14.5	1372	35.5	21	9.5	448	690	2.04	19	4	434	0.94
97	222	305	14.5	1372	35.5	21	9.5	448	690	2.04	19	4	434	0.94
98	222	305	14.5	1372	32.8	21	9.5	448	690	2.04	19	4	434	0.94
99	222	305	14.5	1372	32.8	21	9.5	448	690	2.04	19	4	434	0.94
100	222	305	14.5	1372	32.5	21	9.5	448	690	2.04	19	4	434	0.94
101	200	305	14.5	1372	27	21	9.5	448	690	2.04	19	4	434	0.94
102	200	305	14.5	1372	27	21	9.5	448	690	2.04	19	4	434	0.94
103	200	305	14.5	1372	27	21	9.5	448	690	2.04	19	4	434	0.94
106	1780	610	27.76	3660	41.1	20	22.23	455	746	2.66	57	9.5	414	0.89
107	1928	457	24.76	910	38.3	20	15.875	427.5	-	2.41	60	9.5	430.2	1.14

109	970	457	24.76	910	39.4	20	15.875	427.5	-	2.41	60	9.5	430.2	1.14
112	1914	457	26.35	910	35	30	19.05	486.2	-	5.21	40	12.7	434.4	3.04
113	1780	457	30.16	3656	36.6	30	15.875	477	-	3.62	76	9.5	445	0.92
114	1780	457	30.16	3656	40	30	15.875	477	-	3.62	51	6.4	437	0.6
115	1780	457	30.16	3656	38.6	30	15.875	477	-	3.62	76	9.5	445	0.92
116	654	609.6	22.23	2438.4	31	22	15.875	461.965	630	1.49	31.75	6.4	606.76	0.7
117	654	609.6	22.23	4876.8	31	22	15.875	461.965	630	1.49	31.75	6.4	606.76	0.7
118	654	609.6	22.23	6096	31	22	15.875	461.965	630	1.49	31.75	6.4	606.76	0.7
119	654	609.6	22.23	2438.4	31	11	15.875	461.965	630	0.75	31.75	6.4	606.76	0.7
120	654	609.6	22.23	2438.4	31	44	15.875	461.965	630	2.98	31.75	6.4	606.76	0.7
121	912	609.6	28.58	1828.8	34.5	28	19.05	441.28	602	2.73	25.4	6.4	606.76	0.89
122	912	609.6	28.58	4876.8	34.5	28	19.05	441.28	602	2.73	25.4	6.4	606.76	0.89
123	912	609.6	28.58	6096	34.5	28	19.05	441.28	602	2.73	25.4	6.4	606.76	0.89
125	400	600	30.16	1800	34.6	14	22.225	448	739	1.92	97	9.5	431	0.54
126	400	600	30.16	1800	33	14	22.225	461	775	1.92	64	9.5	434	0.81
127	1000	250	13.75	1645	65	8	16	419	-	3.28	50	7.5	1000	1.54
128	1000	250	15.65	1645	65	8	16	419	-	3.28	50	11.3	420	3.49

130	1850	250	14	1645	90	8	16	419	-	3.28	50	8	580	1.75
131	1850	250	15.65	1645	90	8	16	419	-	3.28	100	11.3	420	1.74
132	925	250	13.75	1645	90	8	16	419	-	3.28	50	7.5	1000	1.54
133	1850	250	13.75	1645	90	8	16	419	-	3.28	50	7.5	1000	1.54
141	1308	609.6	22.23	2438.4	37.2	22	15.875	462	-	1.49	31.75	6.4	606.76	0.7
142	654	609.6	22.23	2438.4	37.2	22	15.875	462	-	1.49	63.5	6.4	606.76	0.35
143	1779	609.6	20	3657	32.6	26	19.05	315.1	497.8	2.54	127	6.4	351.6	0.17
157	0	406.4	14.96	1854.2	36.5	12	12.7	458.5	646	1.17	31.75	4.5	691.5	0.53
158	0	406.4	14.96	1854.2	36.5	12	12.7	458.5	646	1.17	31.75	4.5	691.5	0.53

Comparison of Calculated with Experimental Results for Circular Section Columns Dominated by Flexural Response, listed in Table A.1.

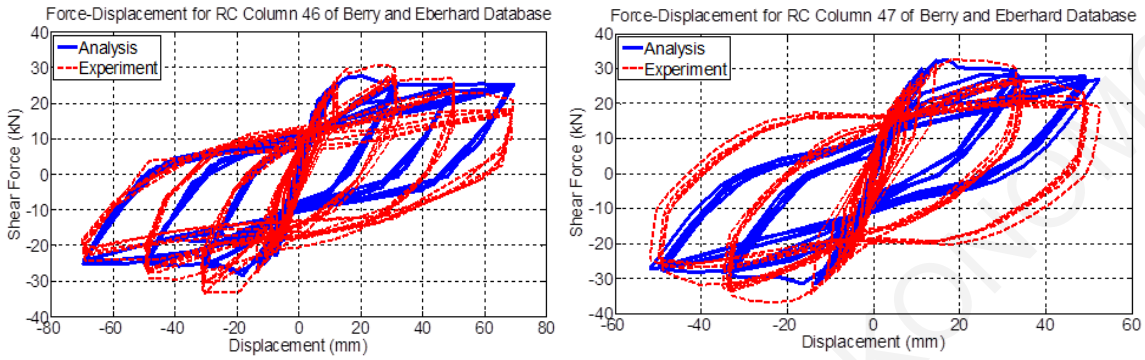

Concrete Model: Scott et al, 1982

Figure A.1: Comparison between numerical and experimental responses of circular columns (ID#46&47) of the database.

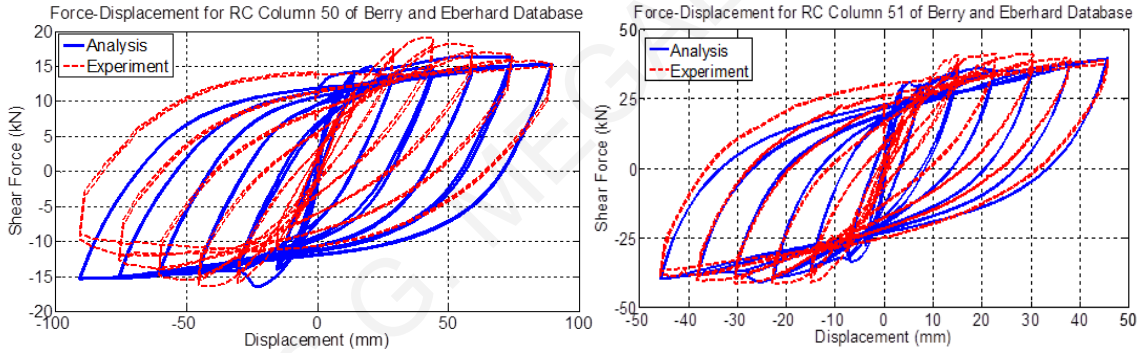

Concrete Model: Scott et al, 1982

Figure A.2: Comparison between numerical and experimental responses of circular columns (ID#50&51) of the database.

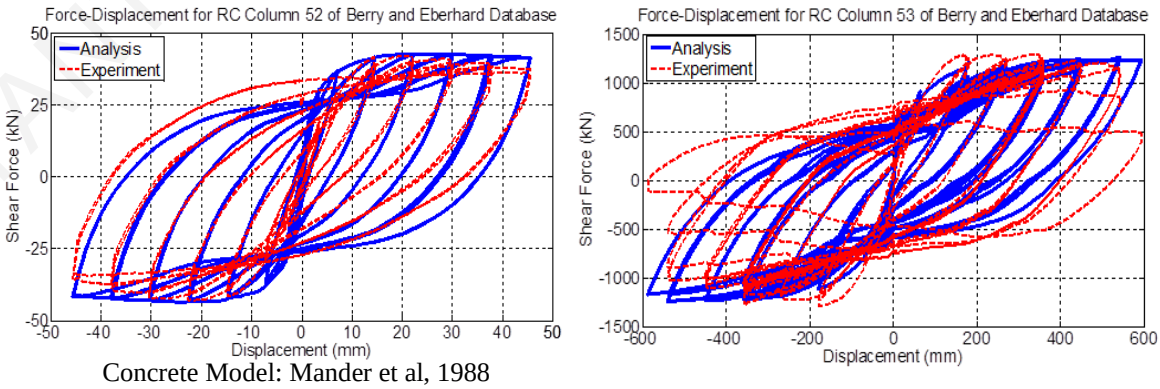

Concrete Model: Mander et al, 1988

Figure A.3: Comparison between numerical and experimental responses of circular columns (ID#52&53) of the database.

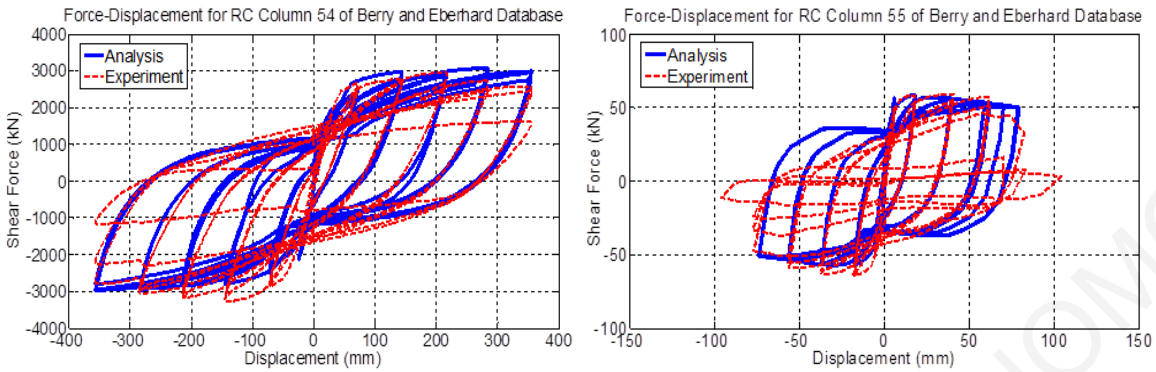

Concrete Model: Mander et al, 1988

Figure A.4: Comparison between numerical and experimental responses of circular columns (ID#54&55) of the database.

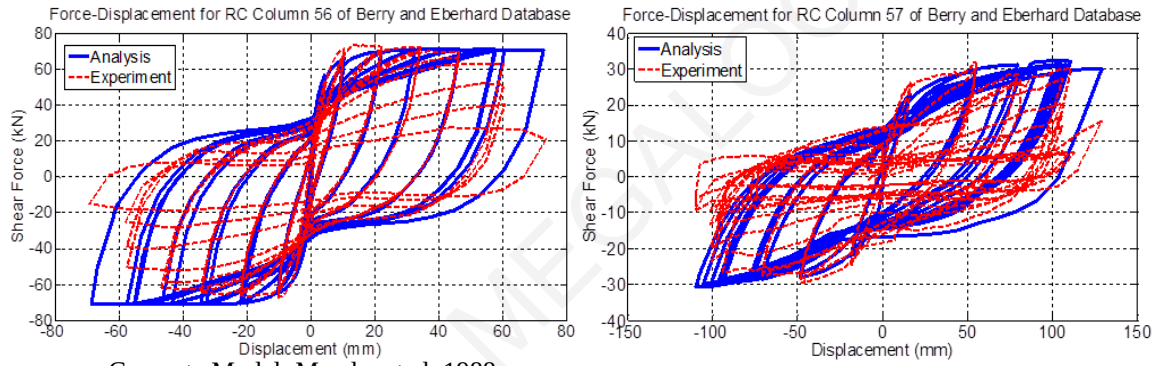

Concrete Model: Mander et al, 1988

Figure A.5: Comparison between numerical and experimental responses of circular columns (ID#56&57) of the database.

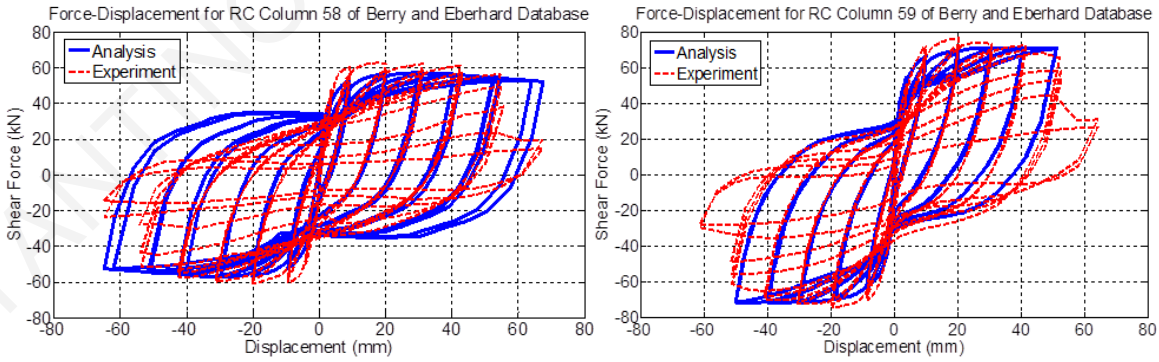

Concrete Model: Mander et al, 1988

Figure A.6: Comparison between numerical and experimental responses of circular columns (ID#58&59) of the database.

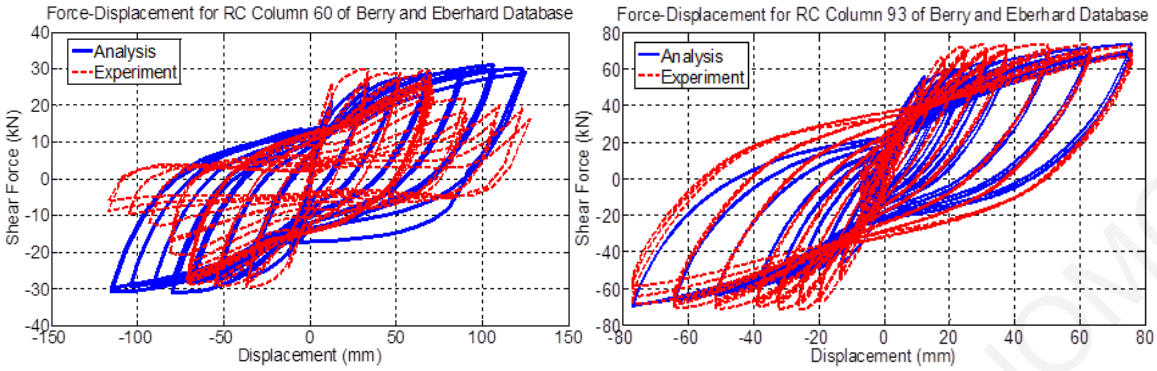

Concrete Model: Mander et al, 1988

Figure A.7: Comparison between numerical and experimental responses of circular columns (ID#60&93) of the database.

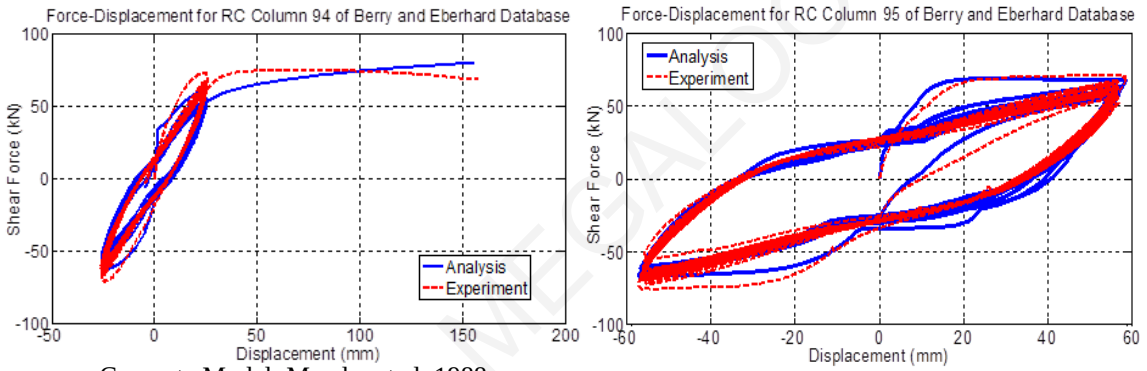

Concrete Model: Mander et al, 1988

Figure A.8: Comparison between numerical and experimental responses of circular columns (ID#94&95) of the database.

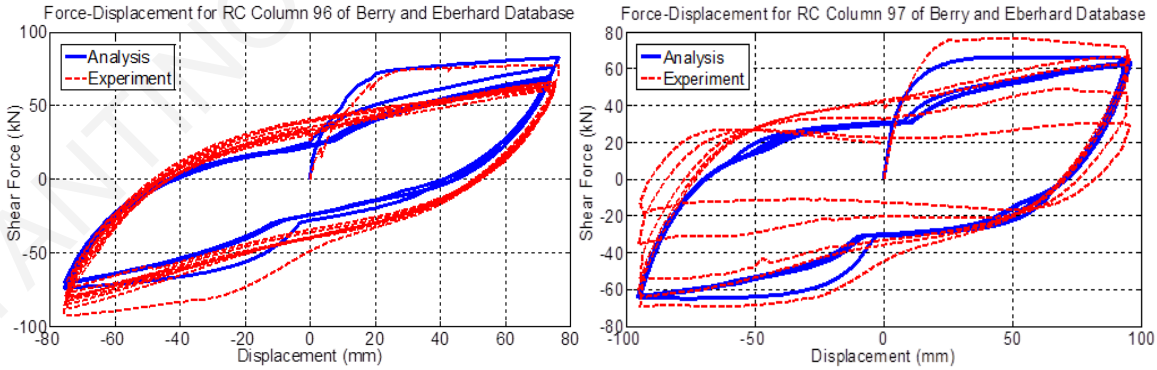

Concrete Model: Mander et al, 1988

Figure A.9: Comparison between numerical and experimental responses of circular columns (ID#96&97) of the database.

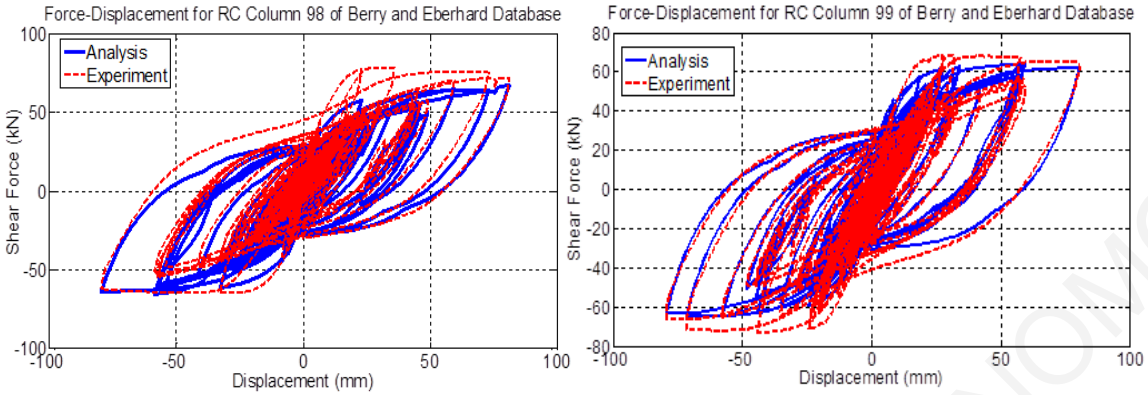

Concrete Model: Mander et al, 1988

Figure A.10: Comparison between numerical and experimental responses of circular columns (ID#98&99) of the database.

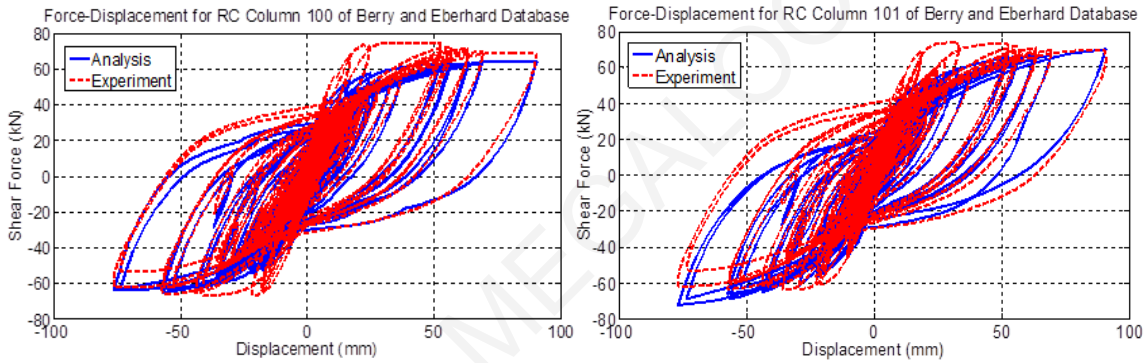

Concrete Model: Mander et al, 1988

Figure A.11: Comparison between numerical and experimental responses of circular columns (ID#100&101) of the database.

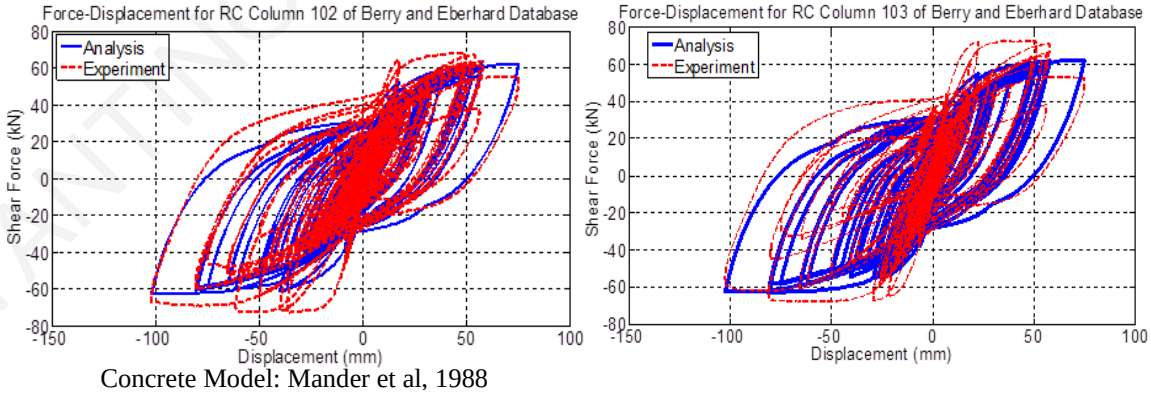

Concrete Model: Mander et al, 1988

Figure A.12: Comparison between numerical and experimental responses of circular columns (ID#102&103) of the database.

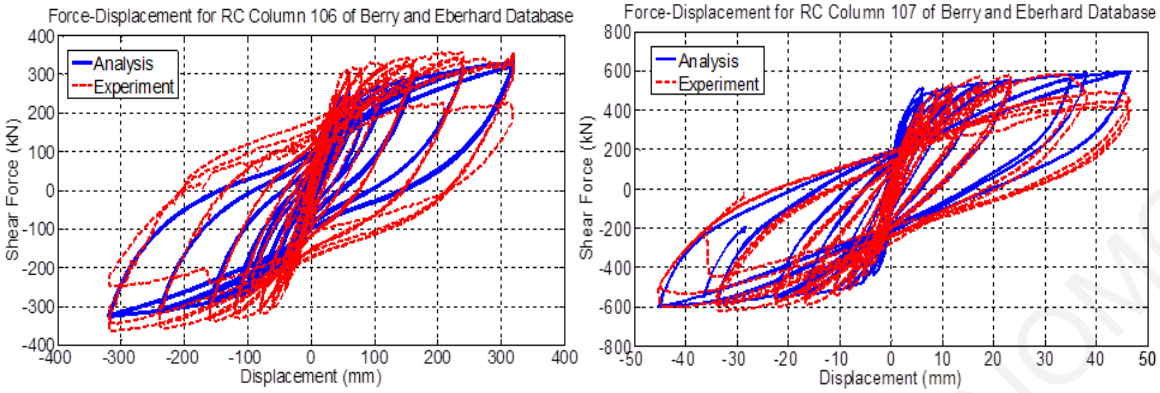

Concrete Model: Mander et al, 1988

Figure A.13: Comparison between numerical and experimental responses of circular columns (ID#106&107) of the database.

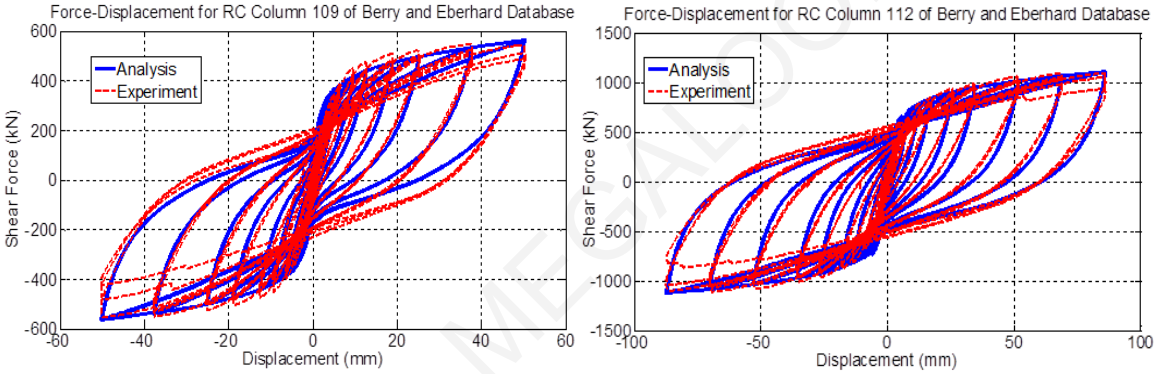

Concrete Model: Mander et al. 1988

Figure A.14: Comparison between numerical and experimental responses of circular columns (ID#109&112) of the database.

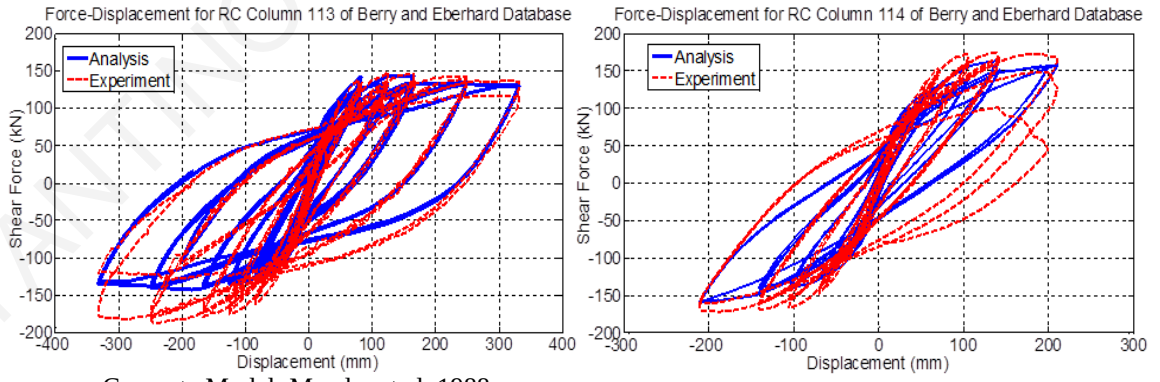

Concrete Model: Mander et al, 1988

Figure A.15: Comparison between numerical and experimental responses of circular columns (ID#113&114) of the database.

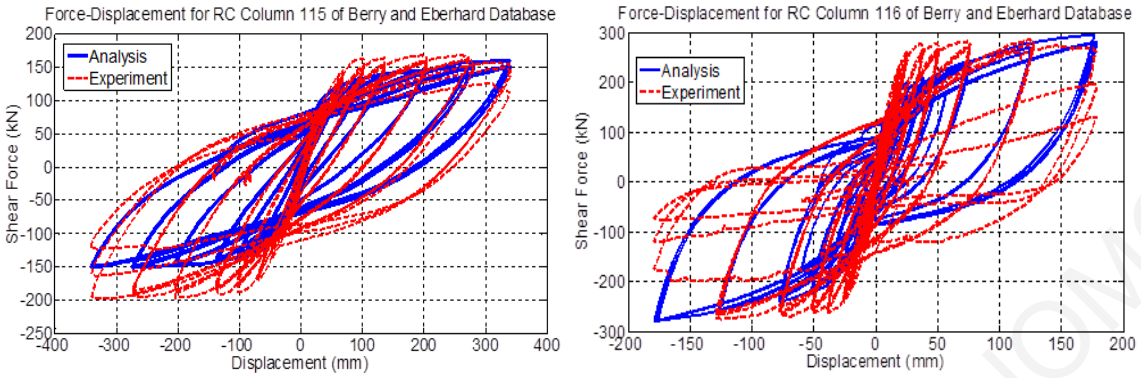

Concrete Model: Mander et al, 1988

Figure A.16: Comparison between numerical and experimental responses of circular columns (ID#115&116) of the database.

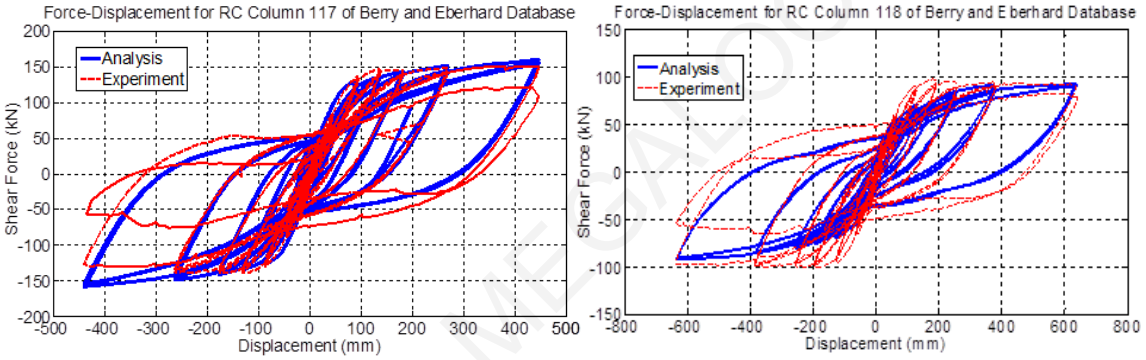

Concrete Model: Mander et al. 1988

Figure A.17: Comparison between numerical and experimental responses of circular columns (ID#117&118) of the database.

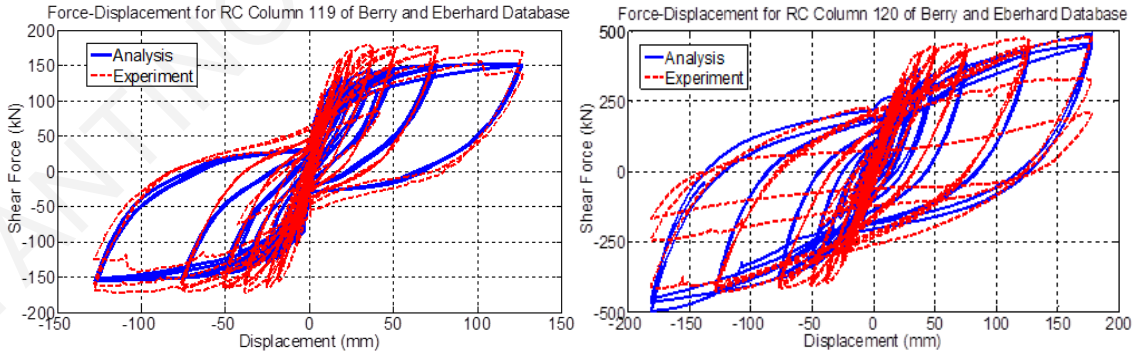

Concrete Model: Mander et al, 1988

Figure A.18: Comparison between numerical and experimental responses of circular columns (ID#119&120) of the database.

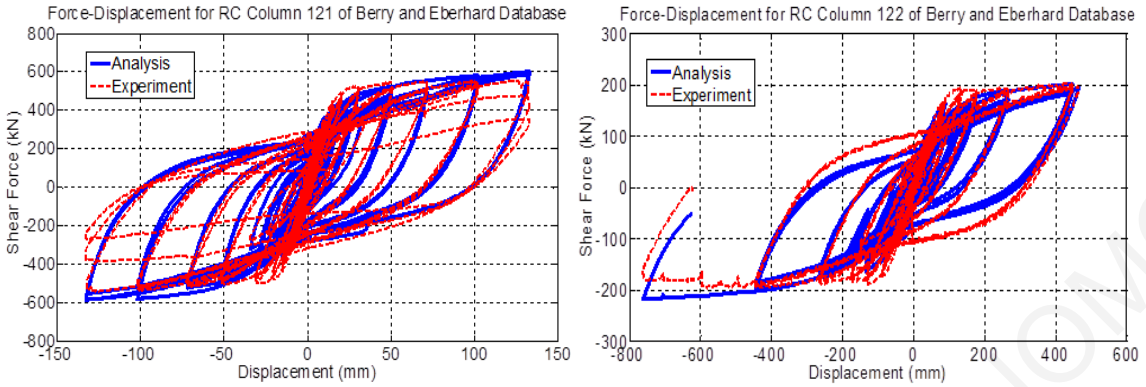

Concrete Model: Mander et al, 1988

Figure A.19: Comparison between numerical and experimental responses of circular columns (ID#121&122) of the database.

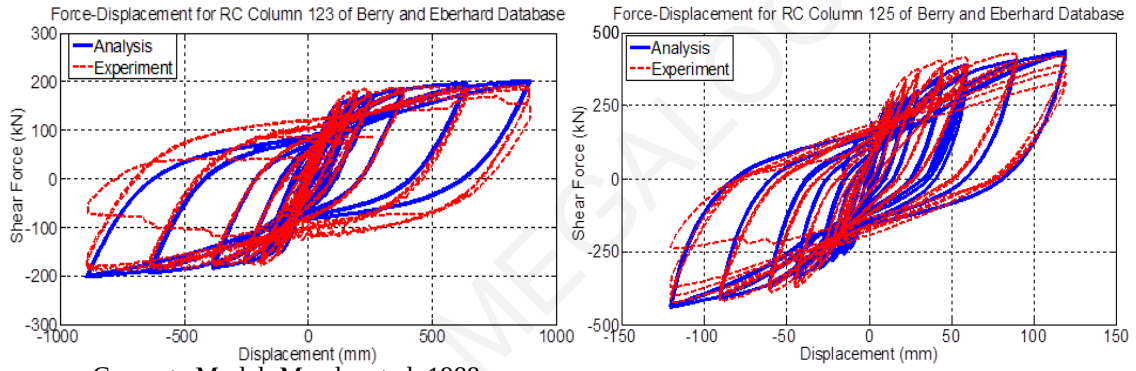

Concrete Model: Mander et al, 1988

Figure A.20: Comparison between numerical and experimental responses of circular columns (ID#123&125) of the database.

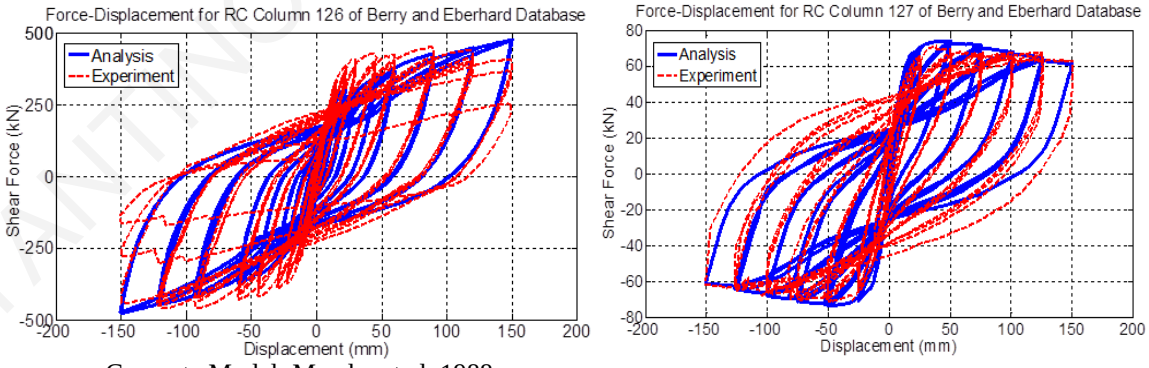

Concrete Model: Mander et al, 1988

Figure A.21: Comparison between numerical and experimental responses of circular columns (ID#126&127) of the database.

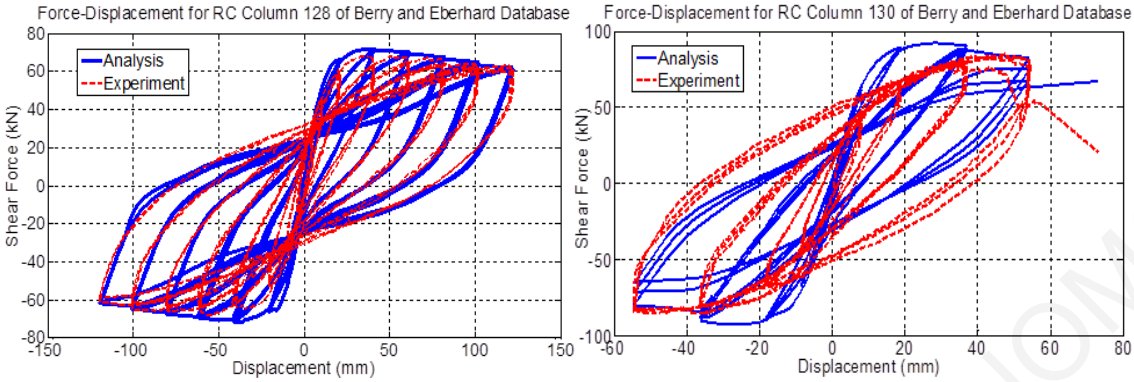

Concrete Model: Mander et al, 1988

Figure A.22: Comparison between numerical and experimental responses of circular columns (ID#128&130) of the database.

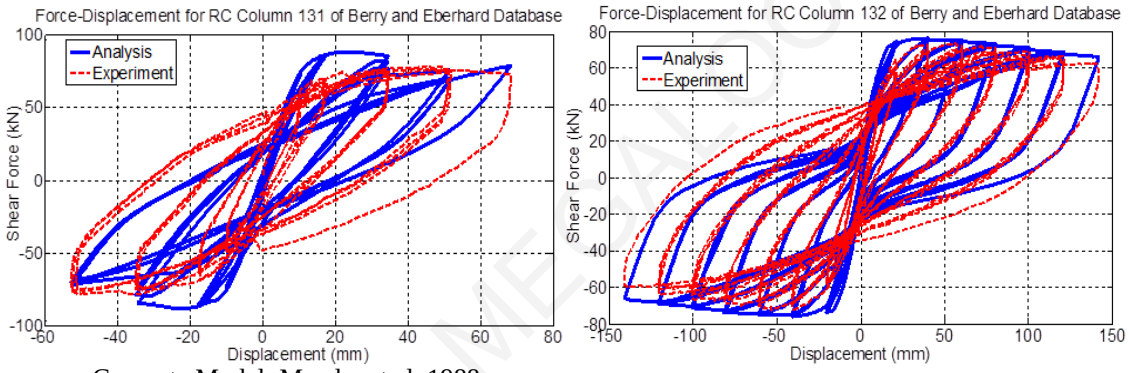

Concrete Model: Mander et al, 1988

Figure A.23: Comparison between numerical and experimental responses of circular columns (ID#131&132) of the database.

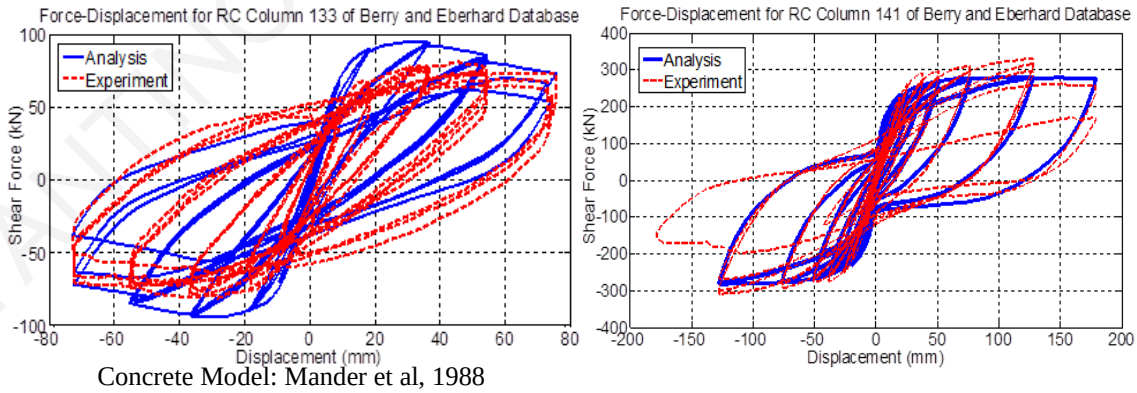

Concrete Model: Mander et al, 1988

Figure A.24: Comparison between numerical and experimental responses of circular columns (ID#133&141) of the database.

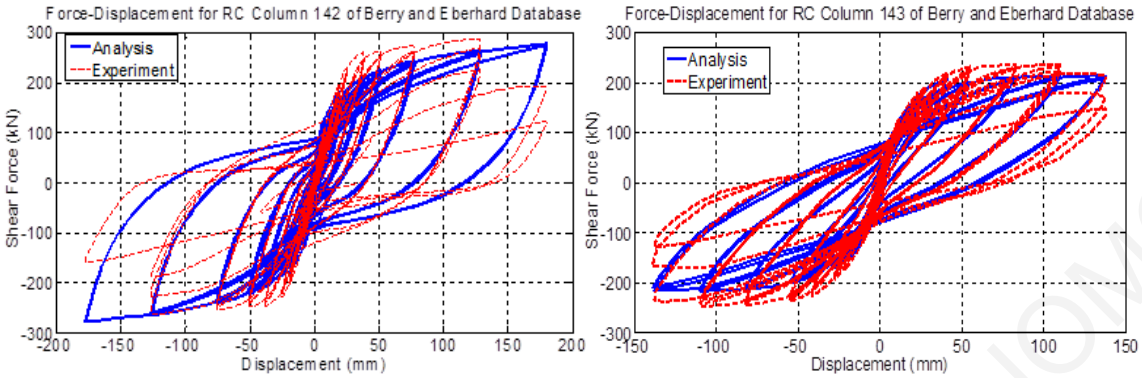

Concrete Model: Mander et al, 1988

Figure A.25: Comparison between numerical and experimental responses of circular columns (ID#142&143) of the database.

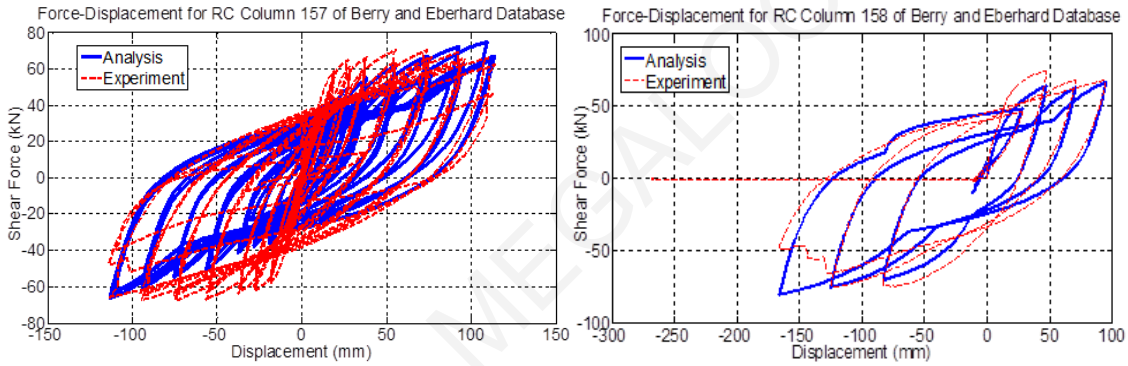

Concrete Model: Mander et al, 1988

Figure A.26: Comparison between numerical and experimental responses of circular columns (ID#157&158) of the database.

Table A.2: Reinforced Concrete Columns with a rectangular cross section, that failed in flexure

SpecimenID in Database	Axial Load (KN)	Width - Depth (mm)	Clear Cover	Shear Span (mm)	Concrete Strength (MPa)	Number of Longitudinal Bars	Diameter of Long. Bars (mm)	Yielding Strength of Long. Bars (MPa)	Ultimate Strength of Long. Bars (MPa)	Longitudinal Reinforcement ratio	Stirrups Spacing (mm)	Diameter of Stirrups (mm)	Stirrups Yielding Strength (MPa)	Transverse Reinforcement ratio
1	1815	550-550	40	1200	23.1	12	24	375	635.6	0.0179	80	10	297	0.015
2	2680	550-550	38	1200	41.4	12	24	375	635.6	0.0179	75	12	316	0.023
3	2719	550-550	40	1200	21.4	12	24	375	635.6	0.0179	75	10	297	0.02
4	4265	550-550	38	1200	23.5	12	24	375	635.6	0.0179	62	12	294	0.035
5	1435	400-400	24.5	1600	23.6	12	16	427	670	0.0151	100	12	320	0.028
6	840	400-400	22.5	1600	25	12	16	427	670	0.0151	90	10	280	0.022
7	744	400-400	13	1600	46.5	12	16	446	702	0.0151	85	7	364	0.0086
8	2112	400-400	13	1600	44	12	16	446	702	0.0151	78	8	360	0.0122
9	2112	400-400	13	1600	44	12	16	446	702	0.0151	91	7	364	0.008
10	1920	400-400	13	1600	40	12	16	446	702	0.0151	94	6	255	0.0057
11	1010	400-400	13	1600	28.3	12	16	440	674	0.0151	117	10	466	0.0156
12	2502	400-400	13	1600	40.1	12	16	440	674	0.0151	92	10	466	0.0199

13	3280	400-400	13	1600	41	12	16	474	633.3	0.0151	81	8	372	0.0066
14	3200	400-400	13	1600	40	12	16	474	633.3	0.0151	96	6	388	0.0032
15	4704	400-400	13	1600	42	12	16	474	633.3	0.0151	96	12	308	0.0126
16	4368	400-400	13	1600	39	12	16	474	633.3	0.0151	77	8	372	0.007
17	4480	400-400	13	1600	40	12	16	474	633.3	0.0151	52	12	308	0.0233
18	819	400-400	40	1600	25.6	8	20	474	721	0.0157	80	12	333	0.0255
19	819	400-400	40	1600	25.6	8	20	474	721	0.0157	80	12	333	0.0255
20	819	400-400	40	1600	25.6	8	20	474	721	0.0157	80	12	333	0.0255
21	819	400-400	40	1600	25.6	8	20	474	721	0.0157	80	12	333	0.0255
22	968	550-550	40	1650	32	12	20	511	675	0.0125	110	12	325	0.017
23	968	550-550	40	1650	32	12	20	511	675	0.0125	110	12	325	0.017
24	2913	550-550	40	1650	32.1	12	20	511	675	0.0125	90	12	325	0.0208
25	2913	550-550	40	1650	32.1	12	20	511	675	0.0125	90	12	325	0.0208
26	646	400-600	24	1784	26.9	10	24	432	-	0.0188	80	12	305	0.0217
27	429	250-250	-	375	20.6	6	9.5	392.8	-	0.0068	32	5.5	323	0.0118
30	127	400-400	31.5	1600	24.8	8	19	362	-	0.0142	100	9	325	0.0032

31	127	400-400	31.5	1600	24.8	8	19	362	-	0.0142	100	9	325	0.0032
32	127	400-400	31.5	1600	24.8	8	19	362	-	0.0142	100	9	325	0.0032
43	432	160-160	12.5	320	21.1	8	10	341	448	0.0222	40	5	559	0.0073
48	184	250-250	35	750	27.9	8	12.7	374	494	0.0162	50	5.5	506	0.0038
49	184	250-250	35	750	27.9	8	12.7	374	494	0.0162	50	5.5	506	0.0038
50	184	250-250	35	750	27.9	8	12.7	374	494	0.0162	50	5.5	506	0.0038
51	184	250-250	35	750	24.8	8	12.7	374	494	0.0162	50	5.5	352	0.0038
52	184	250-250	35	750	27.9	8	12.7	374	494	0.0162	50	5.5	506	0.0038
53	184	250-250	35	750	27.9	8	12.7	374	494	0.0162	50	5.5	506	0.0038
56	1371	200-200	9	500	85.7	12	12.7	399.6	-	0.038	35	6	328.4	0.0161
57	1371	200-200	9	500	85.7	12	12.7	399.6	-	0.038	35	6	792.3	0.0161
58	2156	200-200	9	500	85.7	12	12.7	399.6	-	0.038	35	6	328.4	0.0161
59	2156	200-200	9	500	85.7	12	12.7	399.6	-	0.038	35	6	792.3	0.0161
60	1176	200-200	9	500	115.8	12	12.7	399.6	-	0.038	35	6	328.4	0.0161
61	1176	200-200	9	500	115.8	12	12.7	399.6	-	0.038	35	6	792.3	0.0161
62	1959	200-200	9	500	115.8	12	12.7	399.6	-	0.038	35	6	328.4	0.0161
63	1959	200-200	9	500	115.8	12	12.7	399.6	-	0.038	35	6	792.3	0.0161

66	2176	250-250	23.5	500	99.5	12	12.7	379	571	0.0243	60	5	774	0.005
67	2176	250-250	23.5	500	99.5	12	12.7	379	571	0.0243	40	5	774	0.0075
68	2176	250-250	23.5	500	99.5	12	12.7	379	571	0.0243	60	5.5	344	0.0061
69	2176	250-250	23.5	500	99.5	12	12.7	379	571	0.0243	60	5	1126	0.005
70	2176	250-250	23.5	500	99.5	12	12.7	379	571	0.0243	30	5	774	0.005
71	2176	250-250	23.5	500	99.5	12	12.7	379	571	0.0243	60	7	857	0.005
72	2176	250-250	30.5	500	99.5	4	19	339	512	0.0181	30	5	774	0.005
88	267	305-305	32	1676	29.1	4	22	367	578	0.0163	76	9.5	363	0.0154
89	267	305-305	32	1676	30.7	4	22	367	578	0.0163	127	9.5	363	0.0093
90	267	305-305	32	1676	29.2	4	22	367	578	0.0163	76	9.5	363	0.0154
91	267	305-305	32	1676	27.6	4	22	429	657	0.0163	127	9.5	363	0.0093
92	534	305-305	32	1676	29.4	4	22	429	657	0.0163	76	9.5	392	0.0154
93	534	305-305	32	1676	31.8	4	22	429	657	0.0163	127	9.5	392	0.0093
94	801	305-305	32	1676	33.3	4	22	363	563	0.0163	76	9.5	392	0.0154
95	801	305-305	32	1676	32.4	4	22	363	563	0.0163	127	9.5	392	0.0093
96	801	305-305	32	1676	31	4	22	363	563	0.0163	76	9.5	373	0.0154
97	801	305-305	32	1676	31.8	4	22	363	563	0.0163	127	9.5	373	0.0093

102	1690	457-457	38.1	1372	39.3	8	25.4	439	736	0.0194	102	12.7	454	0.0219
103	2580	457-457	41.3	1372	39.8	8	25.4	439	736	0.0194	102	9.5	616	0.0126
105	600	350-350	22.5	1000	34.8	8	25	430	-	0.0321	75	10	470	0.0169
106	600	350-350	22.5	1000	32	8	25	438	-	0.0321	50	10	470	0.0254
107	600	350-350	26	1000	37.3	8	25	437	-	0.0321	65	6.4	425	0.0195
108	600	350-350	26	1000	39	8	25	437	-	0.0321	65	6.4	425	0.0195
109	1500	250-250	30	1140	80	12	10	531	641	0.0151	150	8	531	0.0122
110	1500	250-250	30	1140	80	12	10	531	641	0.0151	150	8	531	0.0122
111	1000	250-250	30	1140	80	12	10	531	641	0.0151	150	8	531	0.0122
112	1000	250-250	30	1140	80	12	10	531	641	0.0151	150	8	531	0.0122
113	1000	250-250	30	1140	80	12	10	531	641	0.0151	100	8	531	0.0183
114	1500	250-250	30	1140	80	12	10	531	641	0.0151	100	8	531	0.0183
115	1500	250-250	30	1140	80	12	10	531	641	0.0151	100	8	531	0.0183
116	1000	250-250	30	1140	80	12	10	531	641	0.0151	100	8	531	0.0183
117	1000	250-250	30	1140	80	12	10	531	641	0.0151	50	8	531	0.0366
118	1500	250-250	30	1140	80	12	10	531	641	0.0151	50	8	531	0.0366
119	1000	250-250	30	1140	80	12	10	531	641	0.0151	50	8	531	0.0366

120	1500	250-250	30	1140	80	12	10	531	641	0.0151	50	8	531	0.0366
121	1000	250-250	30	1140	80	12	20	430	-	0.0603	150	8	430	0.0122
122	1500	250-250	30	1140	80	12	20	579	677	0.0603	150	8	579	0.0122
123	1500	250-250	30	1140	80	12	20	579	677	0.0603	150	8	579	0.0122
124	1000	250-250	30	1140	80	12	20	579	677	0.0603	150	8	579	0.0122
125	1000	250-250	30	1140	80	12	20	579	677	0.0603	100	8	579	0.0183
126	1000	250-250	30	1140	80	12	20	579	677	0.0603	100	8	579	0.0183
127	1500	250-250	30	1140	80	12	20	579	677	0.0603	100	8	579	0.0183
128	1500	250-250	30	1140	80	12	20	579	677	0.0603	100	8	579	0.0183
129	1000	250-250	30	1140	80	12	20	430	-	0.0603	50	8	430	0.0366
130	1000	250-250	30	1140	80	12	20	430	-	0.0603	50	8	430	0.0366
131	1500	250-250	30	1140	80	12	20	430	-	0.0603	50	8	430	0.0366
132	1500	250-250	30	1140	80	12	20	430	-	0.0603	50	8	430	0.0366
133	615	380-610	28	2335	27.2	18	19.1	448	731	0.0222	110	6	428	0.0037
134	1505	380-610	28	2335	27.2	18	19.1	448	731	0.0222	110	6	428	0.0037
135	601	380-610	25	2335	28.1	18	19.1	448	731	0.0222	83	6	428	0.0048
136	1514	380-610	25	2335	28.1	18	19.1	448	731	0.0222	83	6	428	0.0048

145	489	254-254	13	508	76	8	19.1	510	-	0.0355	51	9.5	510	0.0367
146	979	254-254	13	508	76	8	19.1	510	-	0.0355	51	9.5	510	0.0367
147	534	254-254	13	508	86	8	15.9	510	-	0.0246	51	9.5	510	0.0367
148	1068	254-254	13	508	86	8	15.9	510	-	0.0246	51	9.5	510	0.0367
156	1076	280-280	25.4	2134	40.6	4	15.875	407	659	0.0101	228.6	6.35	351	-
157	3354	305-305	11	1842	72.1	8	19.54	454	700	0.0258	95	15.98	463	0.0315

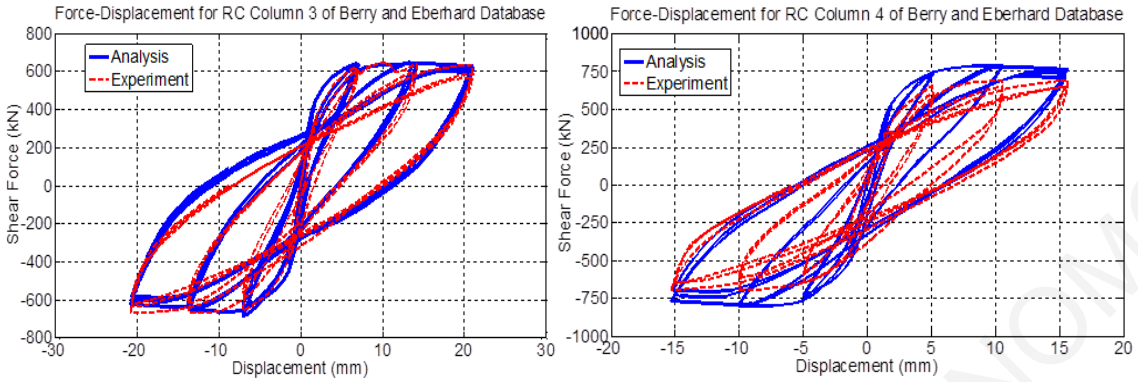

Concrete Model: Mander et al, 1988

Figure A.27: Comparison between numerical and experimental responses of rectangular columns (ID#3&4) of the database.

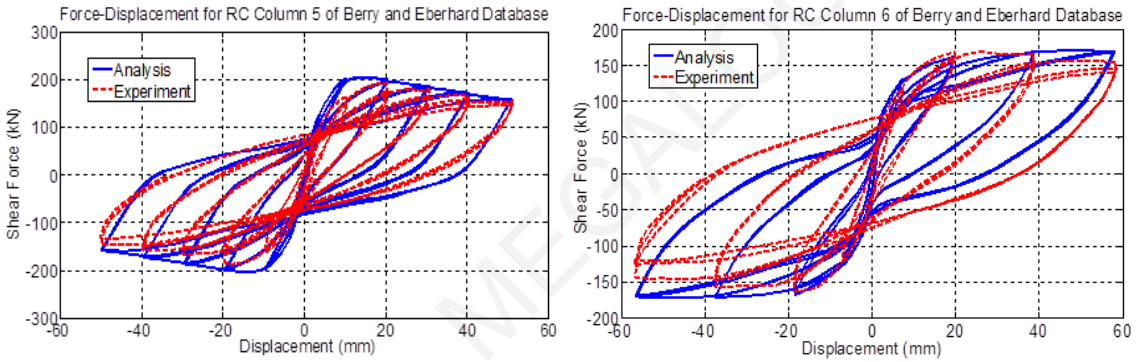

Concrete Model: Mander et al, 1988

Figure A.28: Comparison between numerical and experimental responses of rectangular columns (ID#5&6) of the database.

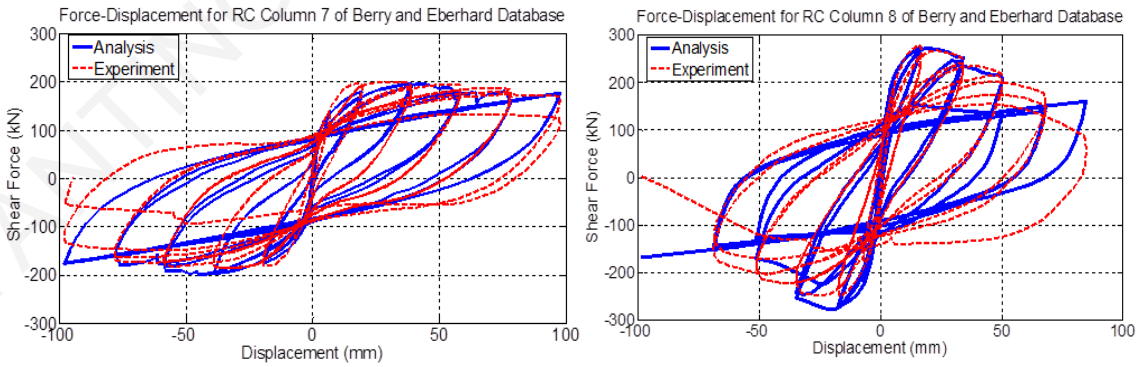

Concrete Model: Mander et al, 1988

Figure A.29: Comparison between numerical and experimental responses of rectangular columns (ID#7&8) of the database.

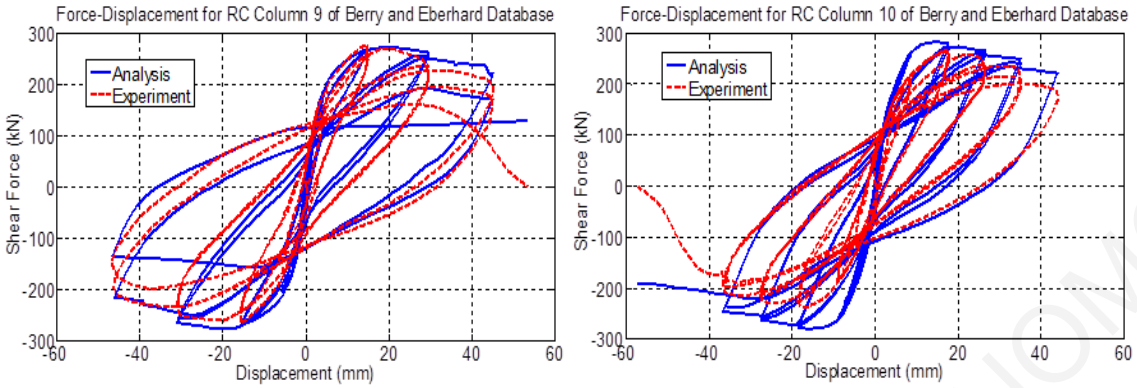

Concrete Model: Mander et al, 1988

Figure A.30: Comparison between numerical and experimental responses of rectangular columns (ID#9&10) of the database.

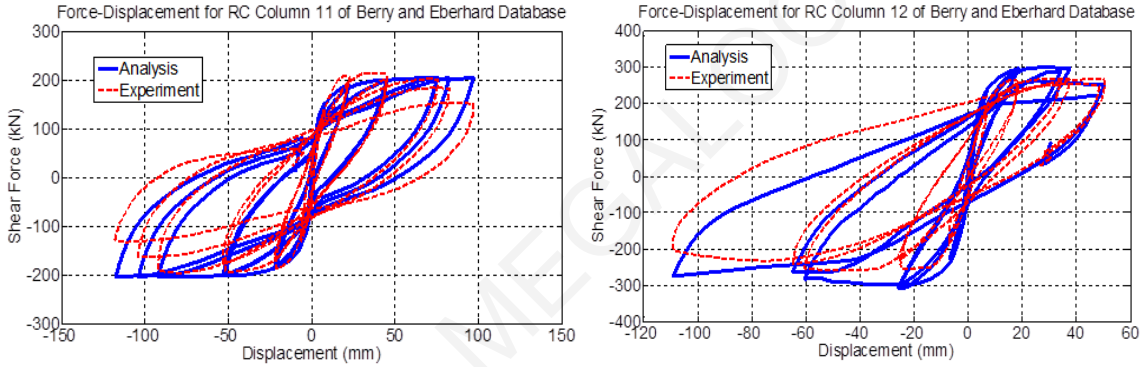

Concrete Model: Mander et al, 1988

Figure A.31: Comparison between numerical and experimental responses of rectangular columns (ID#11&12) of the database.

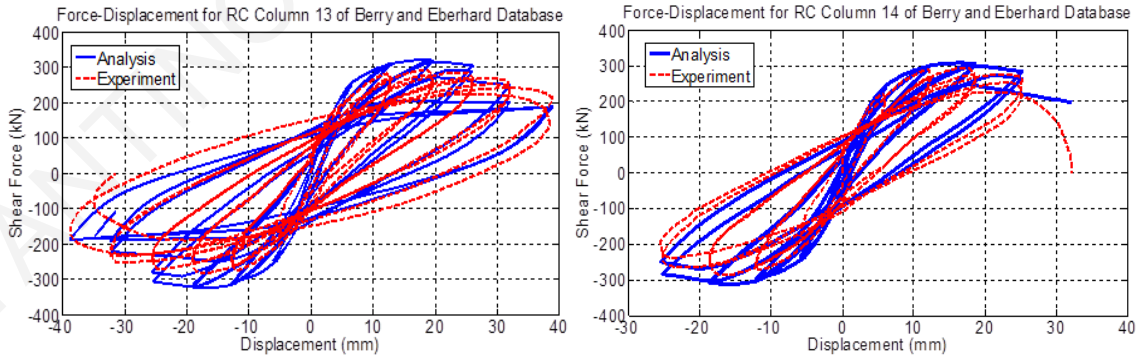

Concrete Model: Mander et al, 1988

Figure A.32: Comparison between numerical and experimental responses of rectangular columns (ID#13&14) of the database.

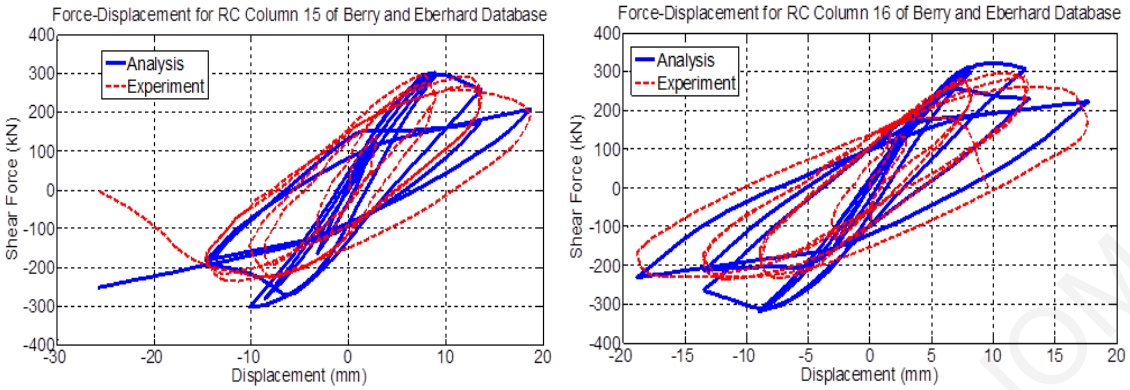

Concrete Model: Mander et al, 1988

Figure A.33: Comparison between numerical and experimental responses of rectangular columns (ID#15&16) of the database.

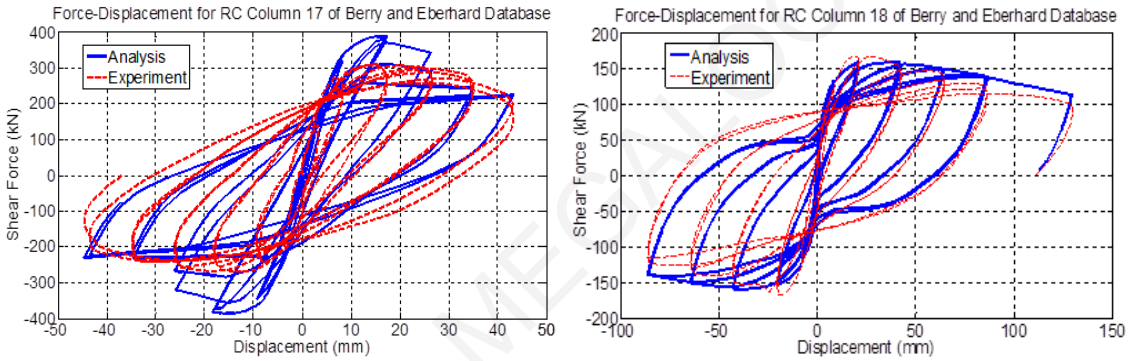

Concrete Model: Mander et al, 1988

Figure A.34: Comparison between numerical and experimental responses of rectangular columns (ID#17&18) of the database.

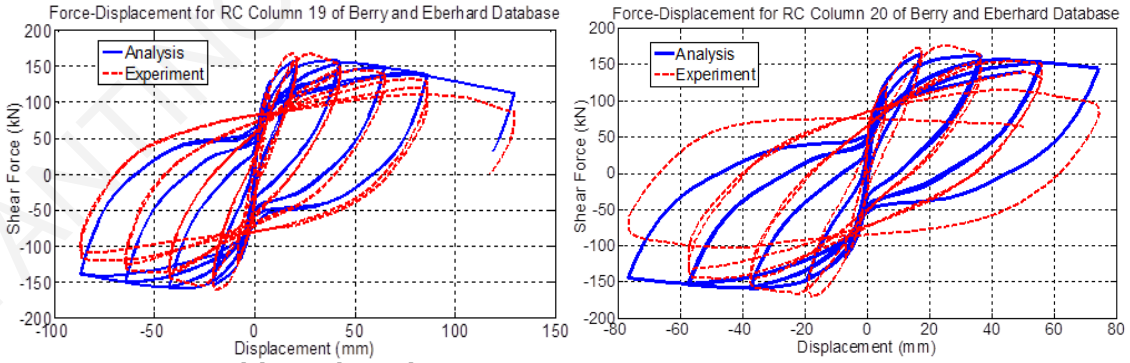

Concrete Model: Mander et al, 1988

Figure A.35: Comparison between numerical and experimental responses of rectangular columns (ID#19&20) of the database.

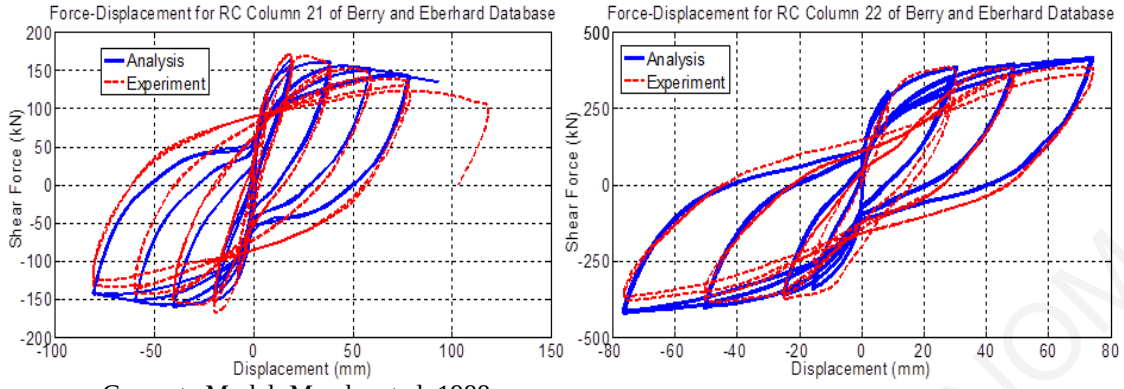

Concrete Model: Mander et al, 1988

Figure A.36: Comparison between numerical and experimental responses of rectangular columns (ID#21&22) of the database.

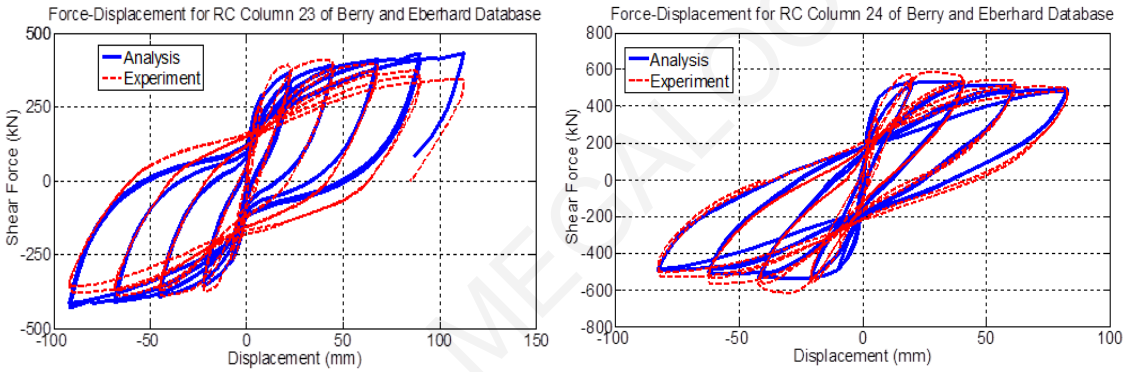

Concrete Model: Mander et al, 1988

Figure A.37: Comparison between numerical and experimental responses of rectangular columns (ID#23&24) of the database.

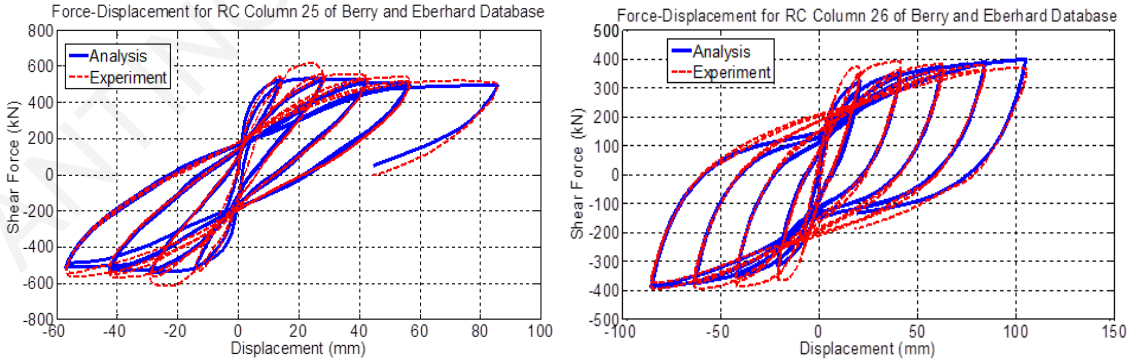

Concrete Model: Mander et al, 1988

Figure A.38: Comparison between numerical and experimental responses of rectangular columns (ID#25&26) of the database.

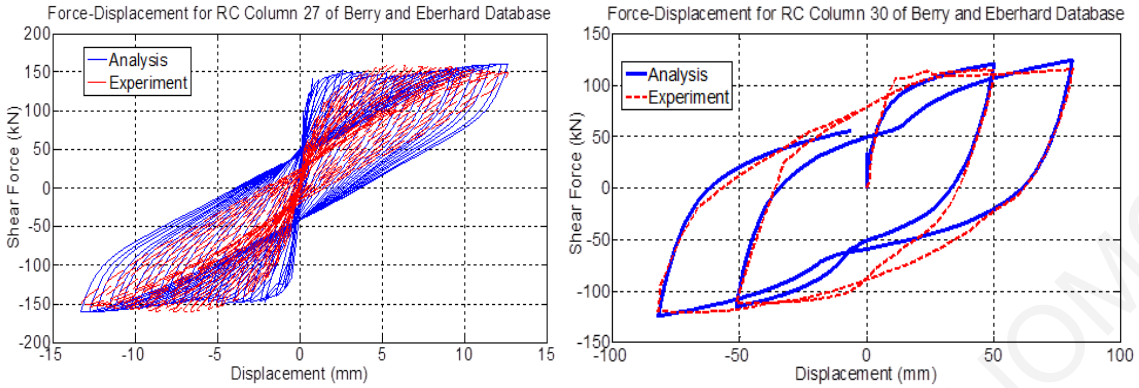

Concrete Model: Mander et al, 1988

Figure A.39: Comparison between numerical and experimental responses of rectangular columns (ID#27&30) of the database.

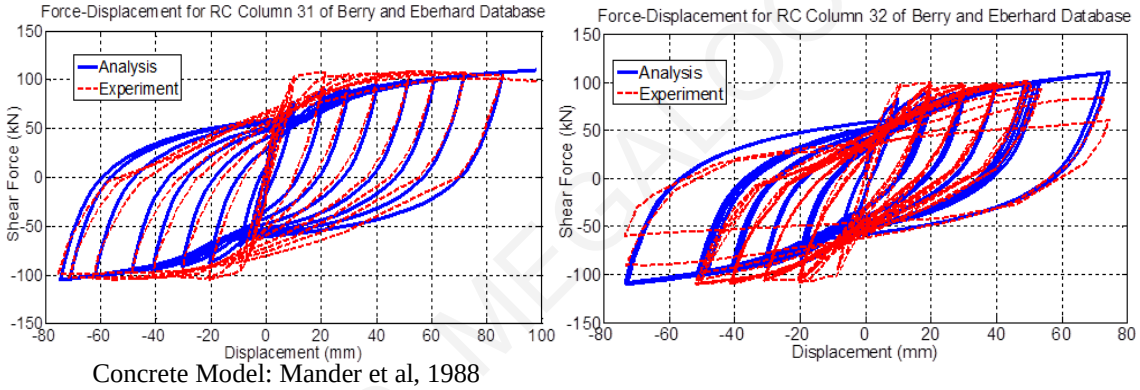

Concrete Model: Mander et al, 1988

Figure A.40: Comparison between numerical and experimental responses of rectangular columns (ID#31&32) of the database.

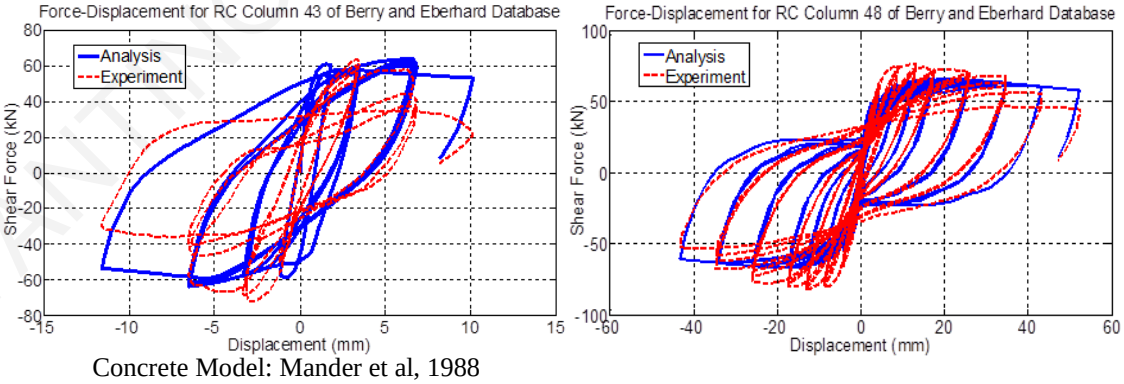

Concrete Model: Mander et al, 1988

Figure A.41: Comparison between numerical and experimental responses of rectangular columns (ID#43&48) of the database.

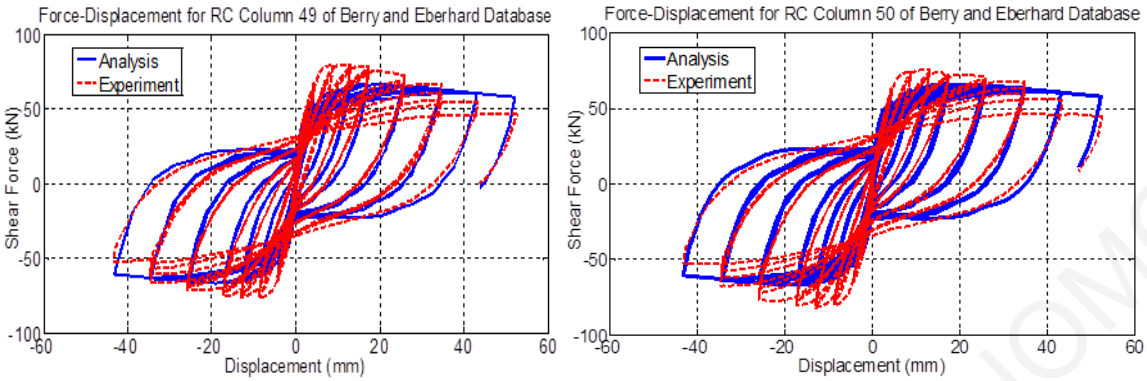

Concrete Model: Mander et al, 1988

Figure A.42: Comparison between numerical and experimental responses of rectangular columns (ID#49&50) of the database.

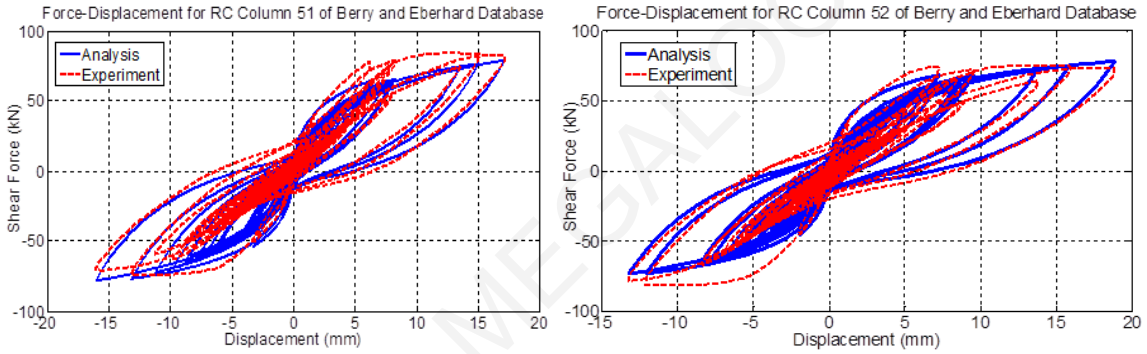

Concrete Model: Mander et al, 1988

Figure A.43: Comparison between numerical and experimental responses of rectangular columns (ID#51&52) of the database.

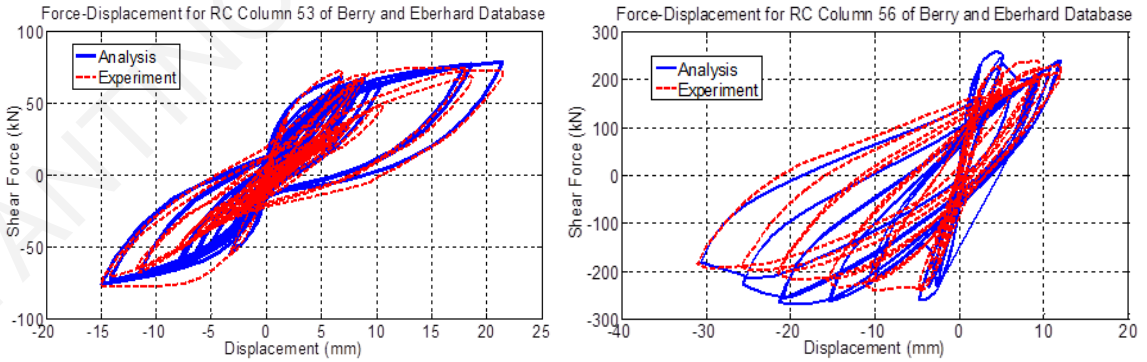

Concrete Model: Mander et al, 1988

Figure A.44: Comparison between numerical and experimental responses of rectangular columns (ID#53&56) of the database.

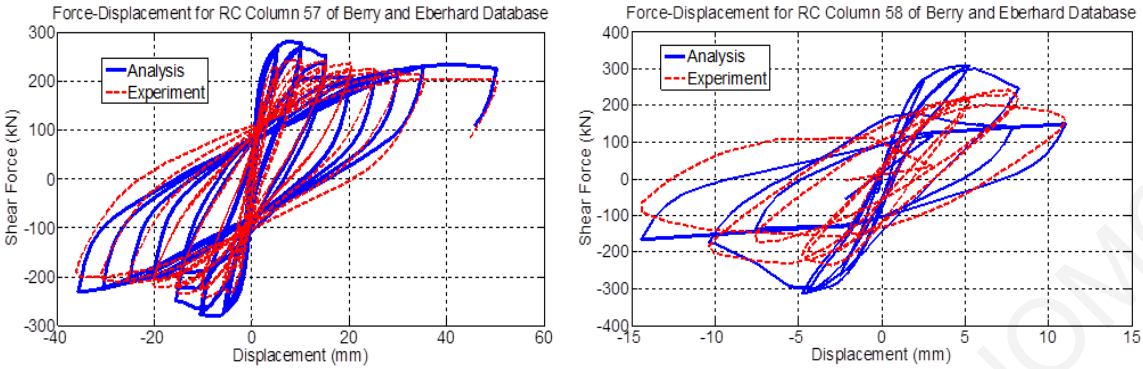

Concrete Model: Mander et al, 1988

Figure A.45: Comparison between numerical and experimental responses of rectangular columns (ID#57&58) of the database.

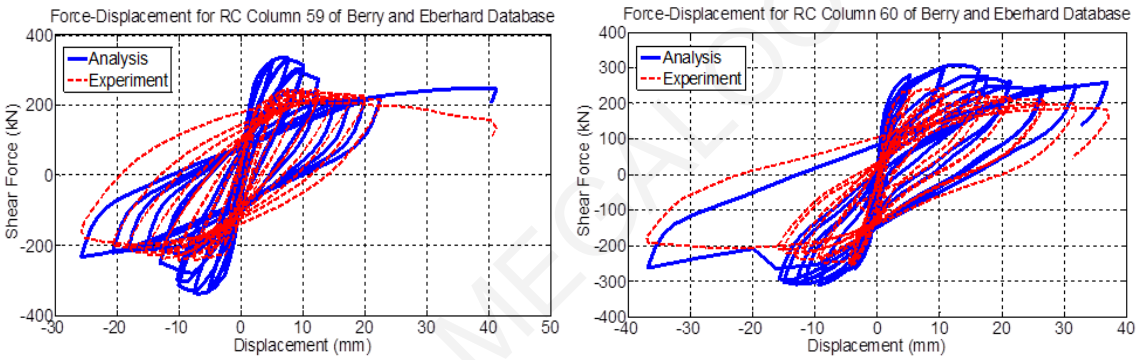

Concrete Model: Mander et al, 1988

Figure A.46: Comparison between numerical and experimental responses of rectangular columns (ID#59&60) of the database.

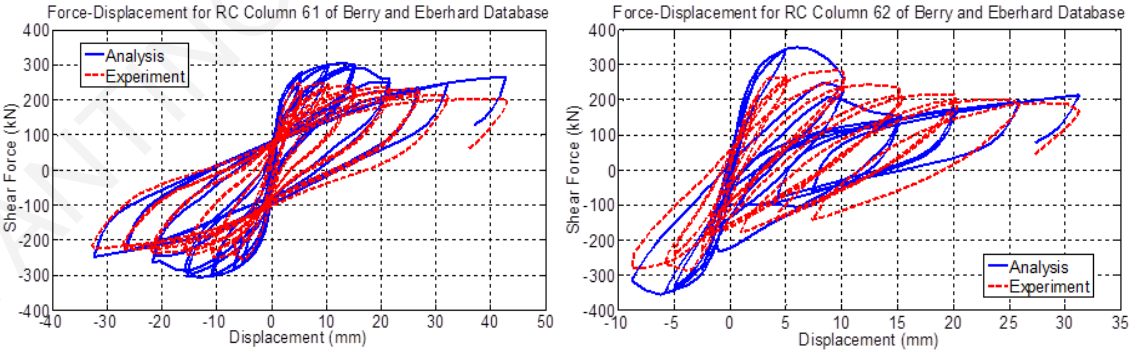

Concrete Model: Mander et al, 1988

Figure A.47: Comparison between numerical and experimental responses of rectangular columns (ID#61&62) of the database.

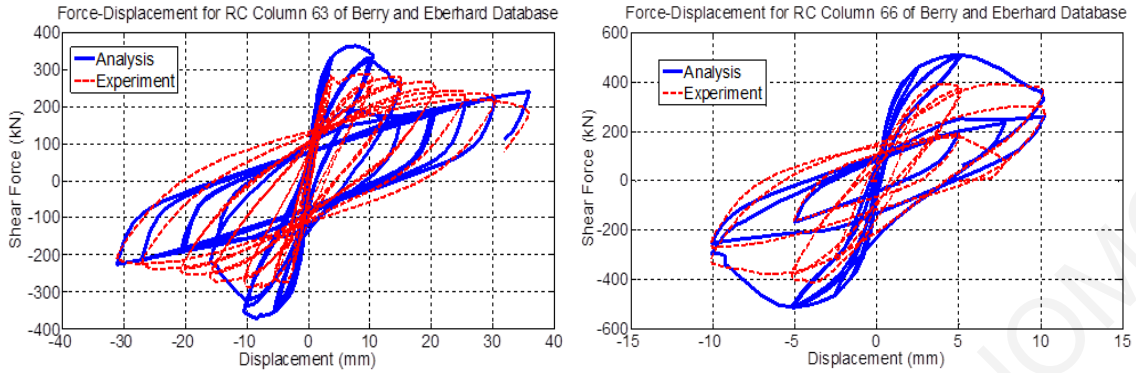

Concrete Model: Mander et al, 1988

Figure A.48: Comparison between numerical and experimental responses of rectangular columns (ID#63&66) of the database.

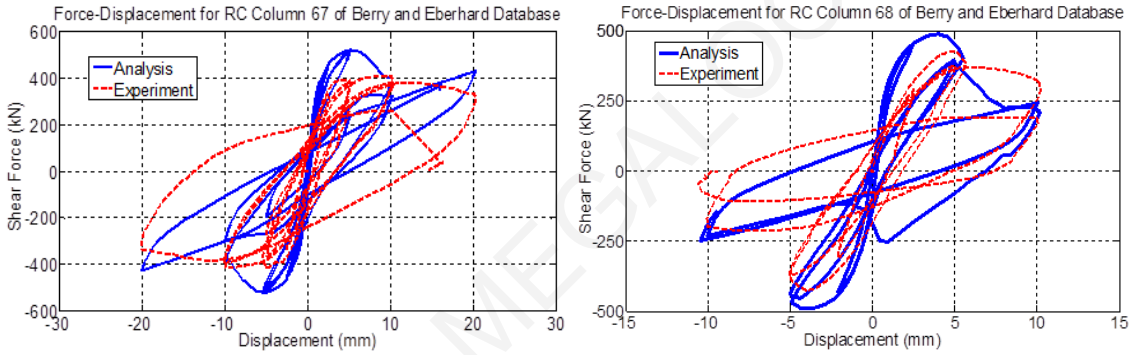

Concrete Model: Mander et al, 1988

Figure A.49: Comparison between numerical and experimental responses of rectangular columns (ID#67&68) of the database.

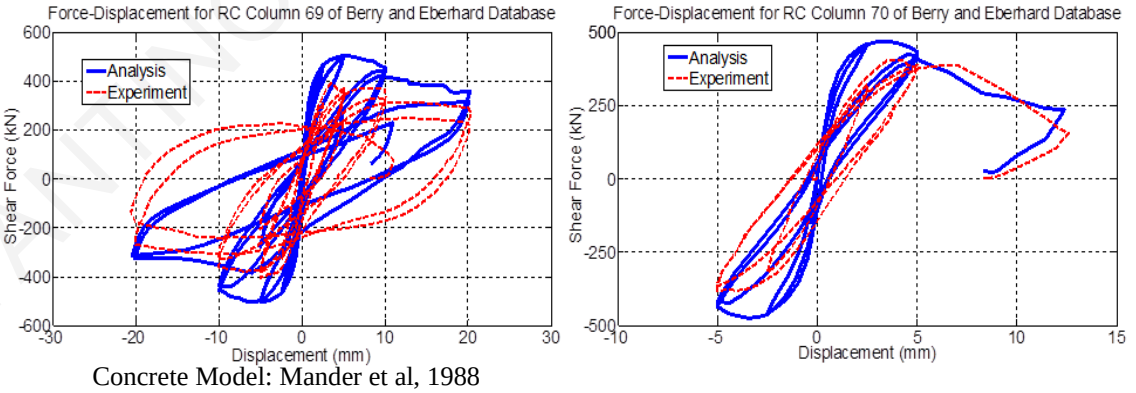

Concrete Model: Mander et al, 1988

Figure A.50: Comparison between numerical and experimental responses of rectangular columns (ID#69&70) of the database.

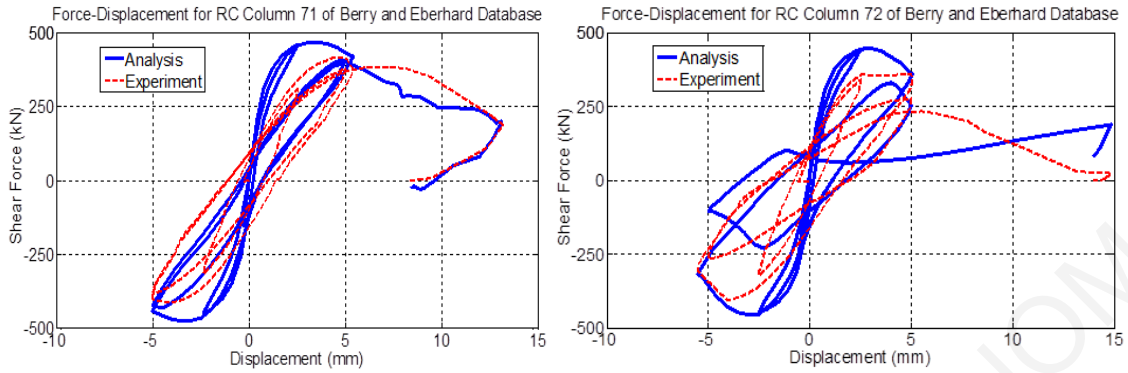

Concrete Model: Mander et al, 1988

Figure A.51: Comparison between numerical and experimental responses of rectangular columns (ID#71&72) of the database.

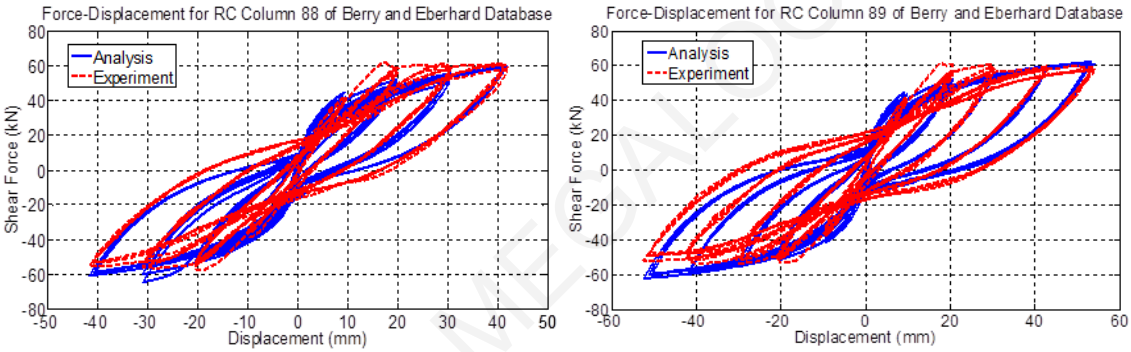

Concrete Model: Mander et al, 1988

Figure A.52: Comparison between numerical and experimental responses of rectangular columns (ID#88&89) of the database.

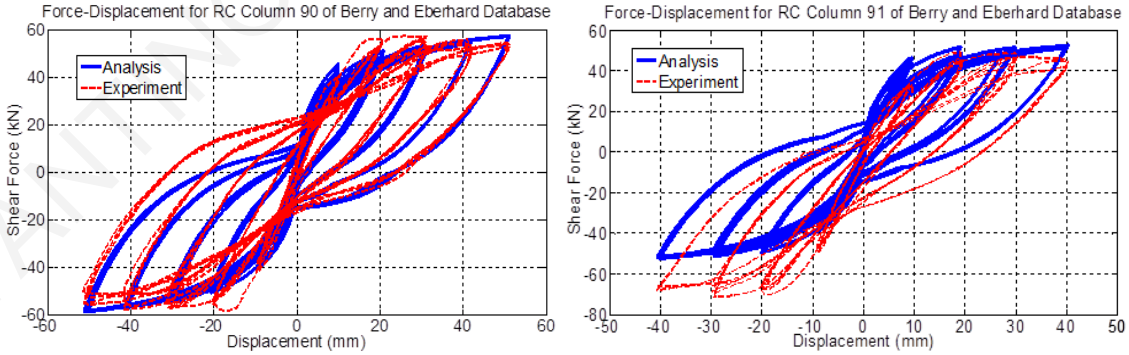

Concrete Model: Mander et al, 1988

Figure A.53: Comparison between numerical and experimental responses of rectangular columns (ID#90&91) of the database.

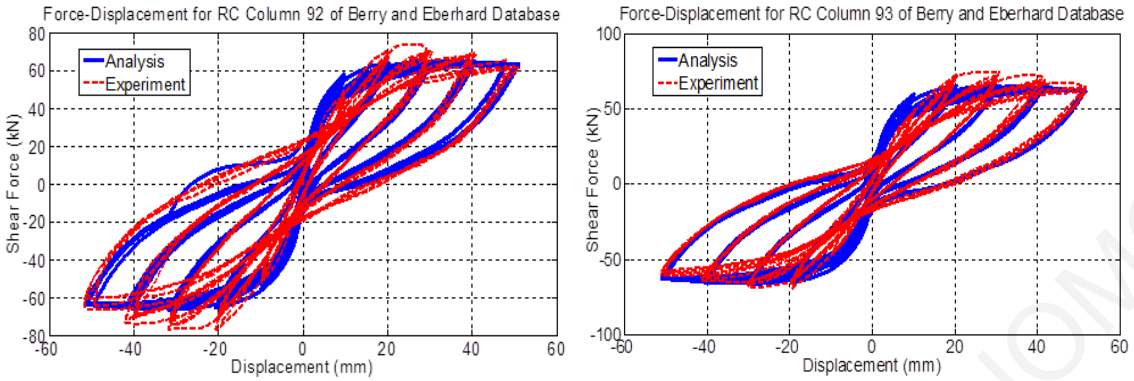

Concrete Model: Mander et al, 1988

Figure A.54: Comparison between numerical and experimental responses of rectangular columns (ID#92&93) of the database.

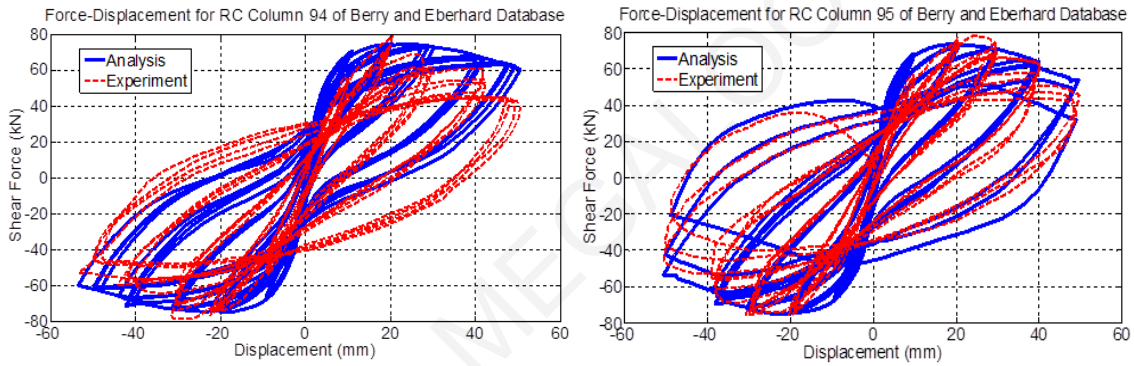

Concrete Model: Mander et al, 1988

Figure A.55: Comparison between numerical and experimental responses of rectangular columns (ID#94&95) of the database.

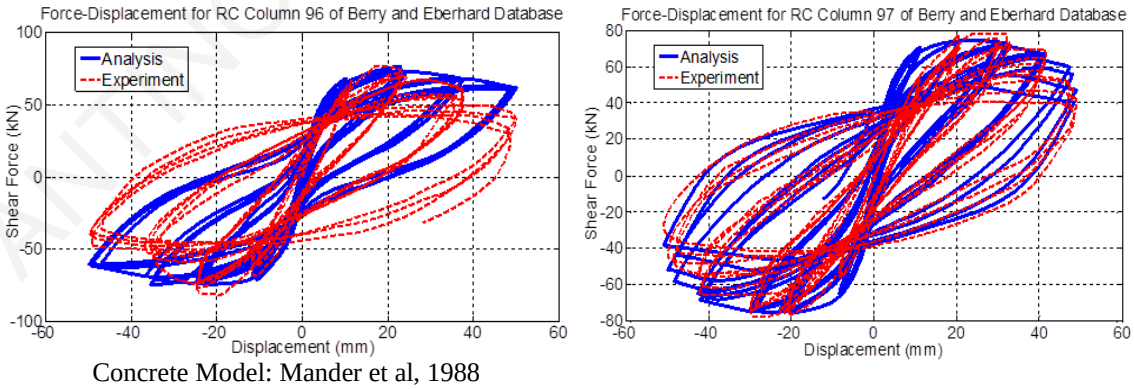

Concrete Model: Mander et al, 1988

Figure A.56: Comparison between numerical and experimental responses of rectangular columns (ID#96&97) of the database.

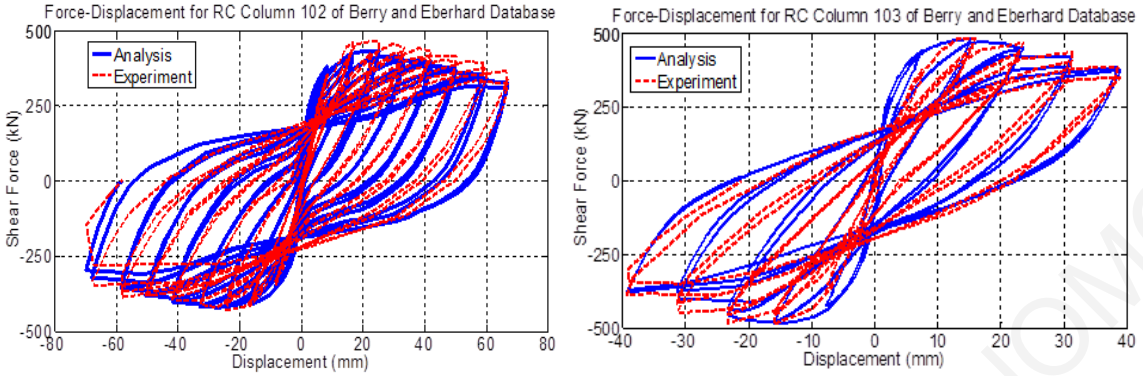

Concrete Model: Mander et al, 1988

Figure A.57: Comparison between numerical and experimental responses of rectangular columns (ID#102&103) of the database.

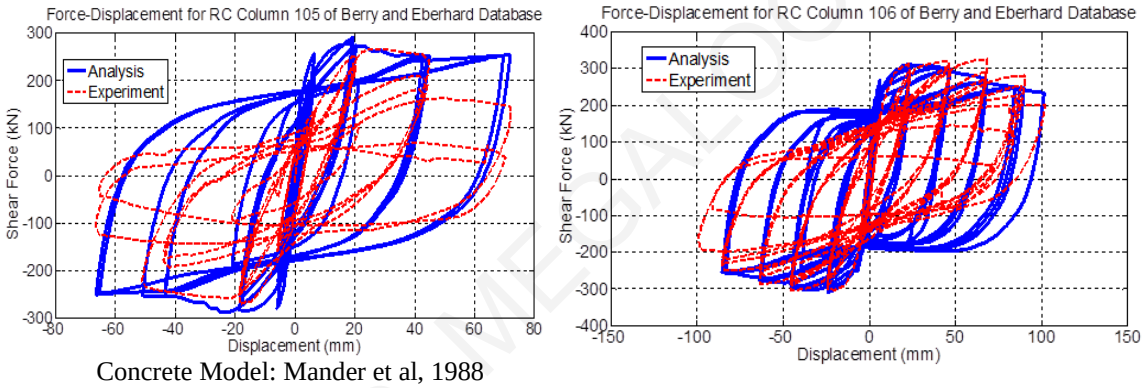

Concrete Model: Mander et al, 1988

Figure A.58: Comparison between numerical and experimental responses of rectangular columns (ID#105&106) of the database.

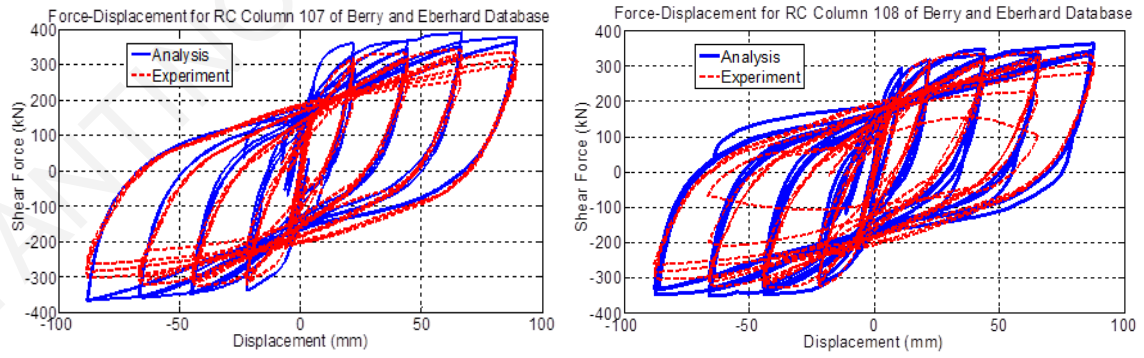

Concrete Model: Mander et al, 1988

Figure A.59: Comparison between numerical and experimental responses of rectangular columns (ID#107&108) of the database.

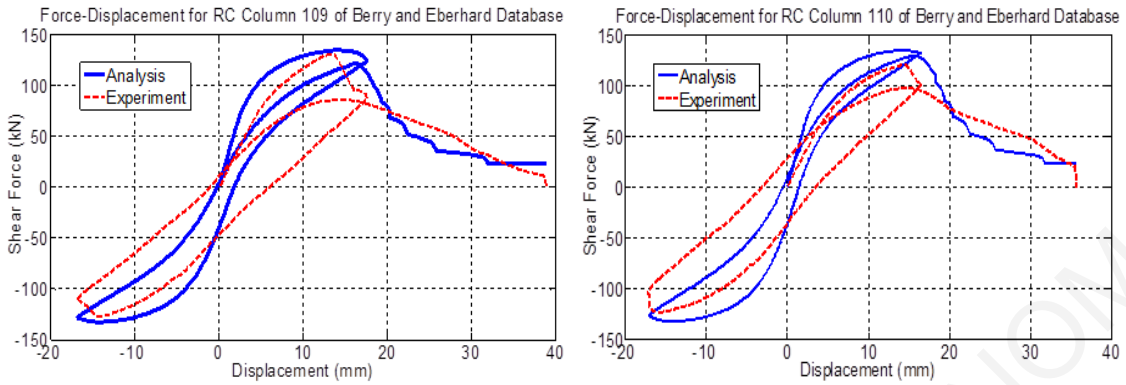

Concrete Model: Mander et al, 1988

Figure A.60: Comparison between numerical and experimental responses of rectangular columns (ID#109&110) of the database.

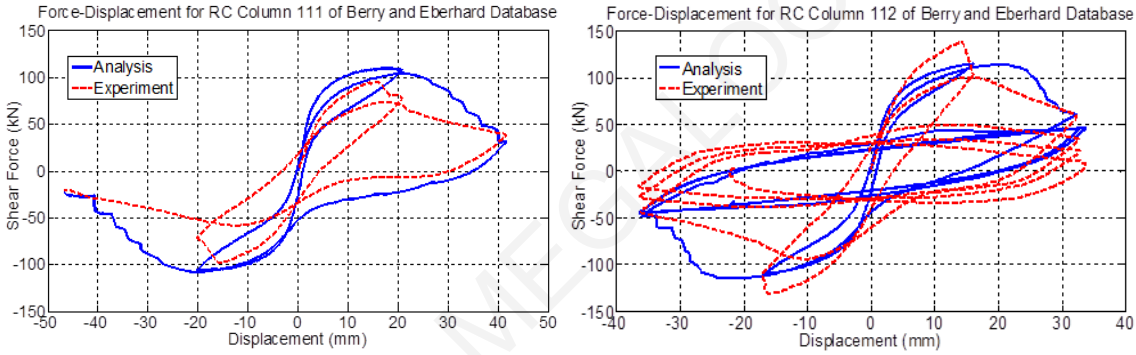

Concrete Model: Mander et al, 1988

Figure A.61: Comparison between numerical and experimental responses of rectangular columns (ID#111&112) of the database.

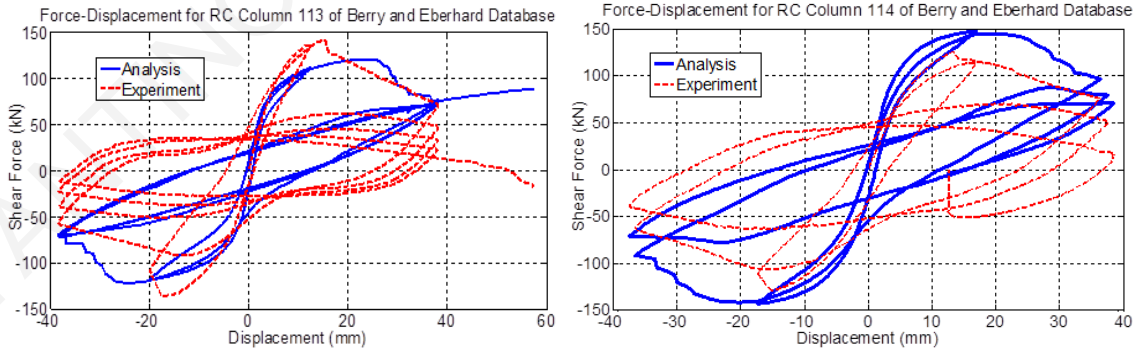

Concrete Model: Mander et al, 1988

Figure A.62: Comparison between numerical and experimental responses of rectangular columns (ID#113&114) of the database.

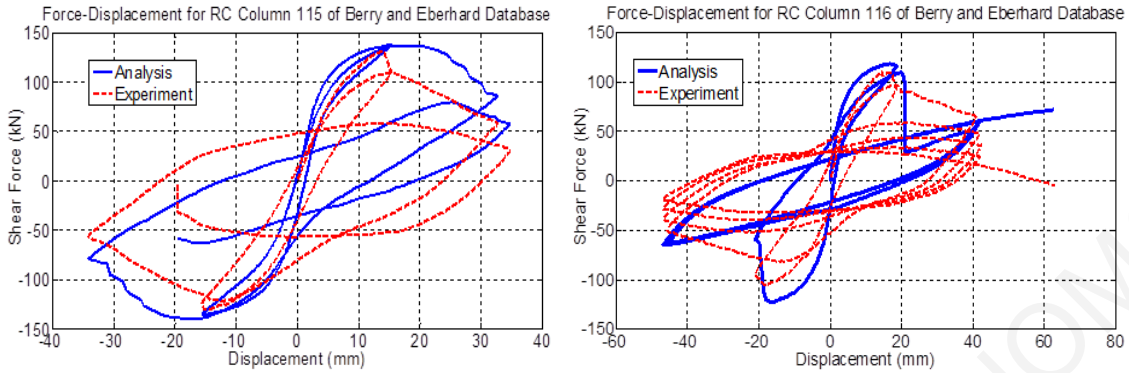

Concrete Model: Mander et al, 1988

Figure A.63: Comparison between numerical and experimental responses of rectangular columns (ID#115&116) of the database.

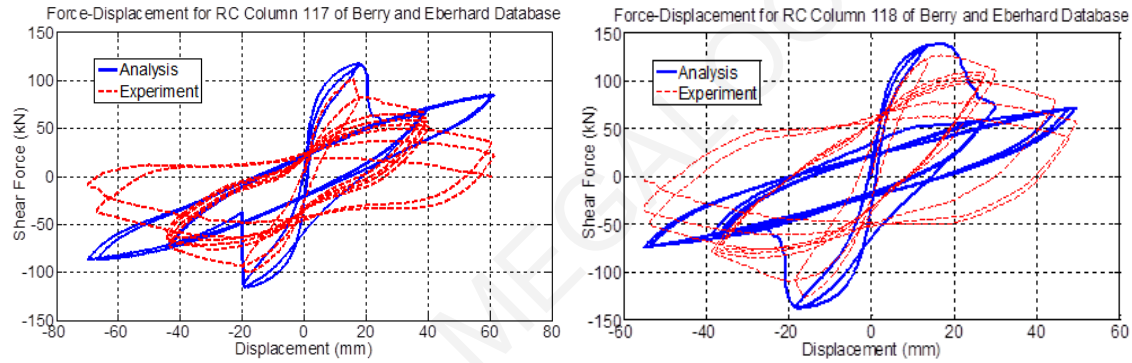

Concrete Model: Mander et al, 1988

Figure A.64: Comparison between numerical and experimental responses of rectangular columns (ID#117&118) of the database.

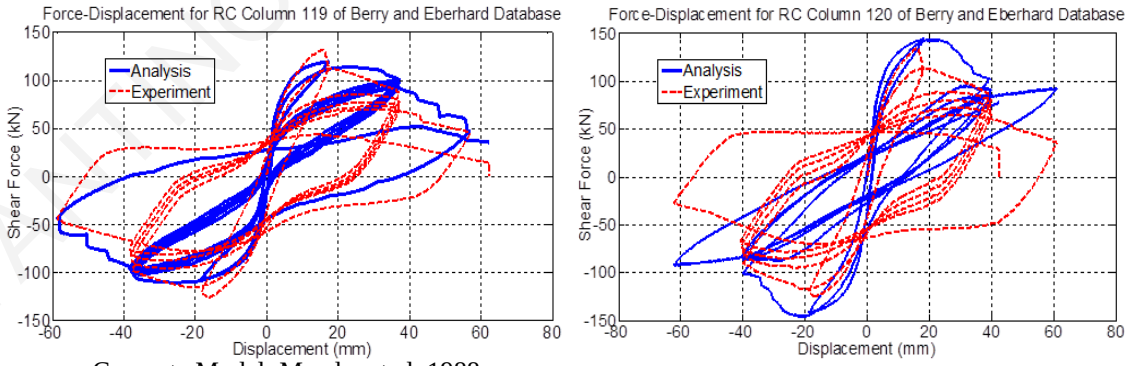

Concrete Model: Mander et al, 1988

Figure A.65: Comparison between numerical and experimental responses of rectangular columns (ID#119&120) of the database.

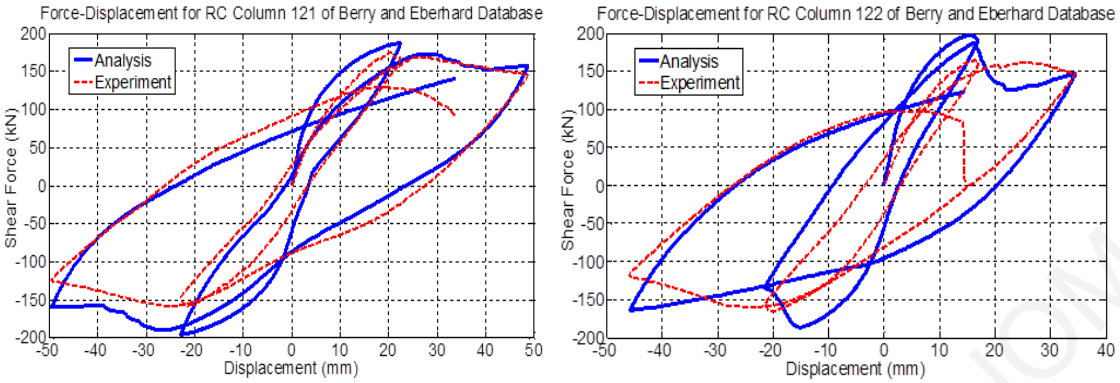

Concrete Model: Mander et al, 1988

Figure A.66: Comparison between numerical and experimental responses of rectangular columns (ID#121&122) of the database.

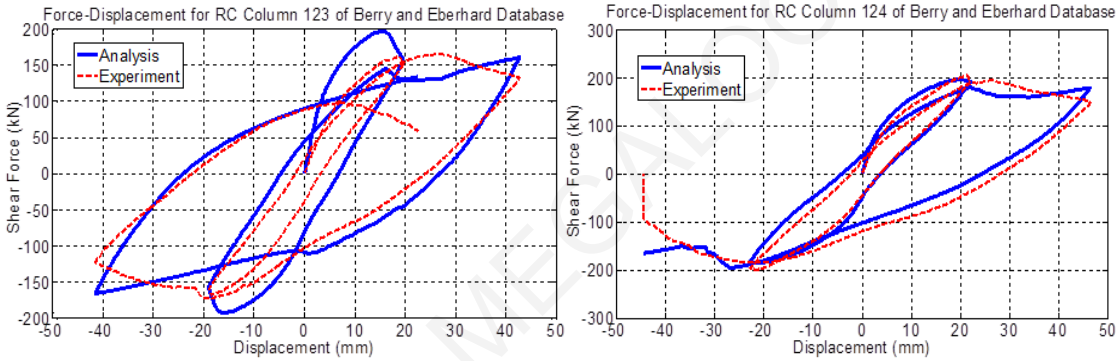

Concrete Model: Mander et al, 1988

Figure A.67: Comparison between numerical and experimental responses of rectangular columns (ID#123&124) of the database.

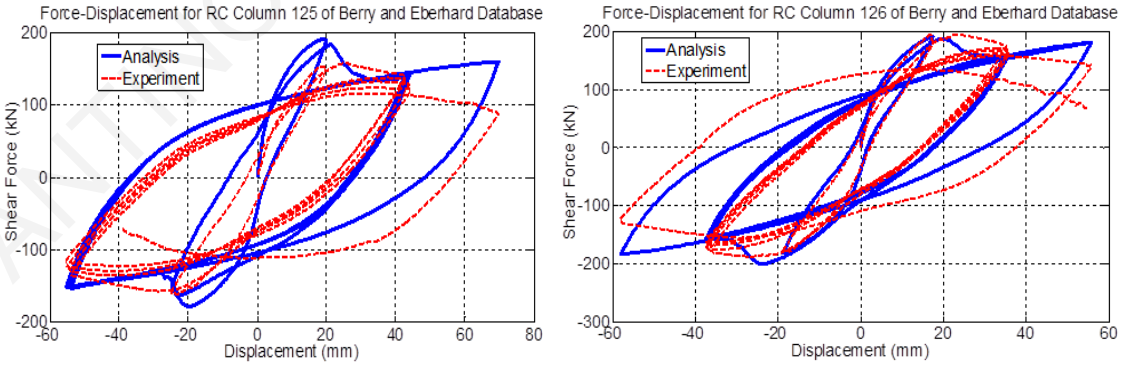

Concrete Model: Mander et al, 1988

Figure A.68: Comparison between numerical and experimental responses of rectangular columns (ID#125&126) of the database.

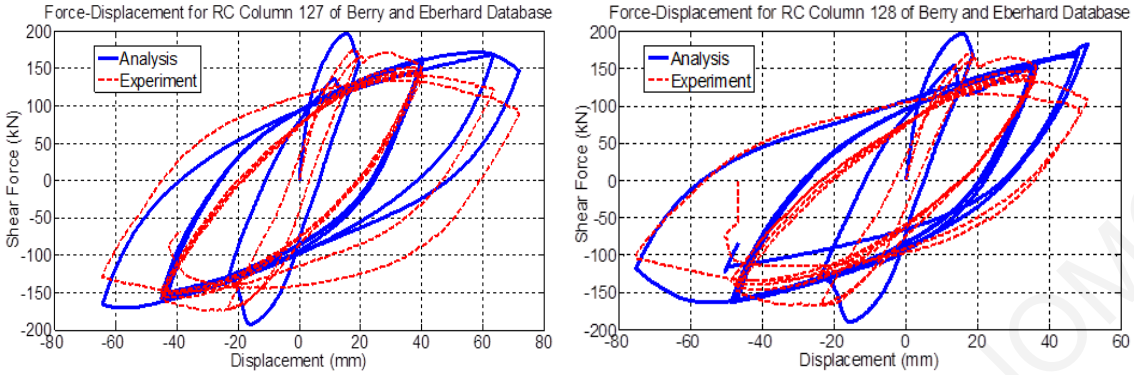

Concrete Model: Mander et al, 1988

Figure A.69: Comparison between numerical and experimental responses of rectangular columns (ID#127&128) of the database.

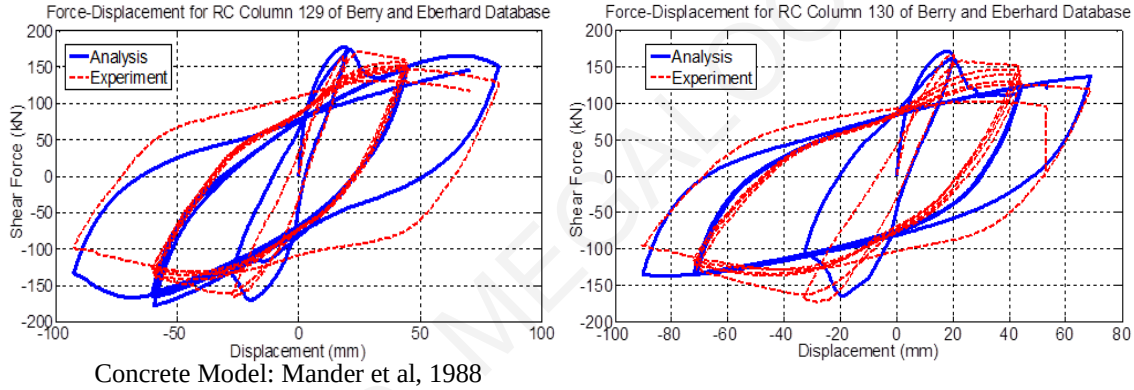

Concrete Model: Mander et al, 1988

Figure A.70: Comparison between numerical and experimental responses of rectangular columns (ID#129&130) of the database.

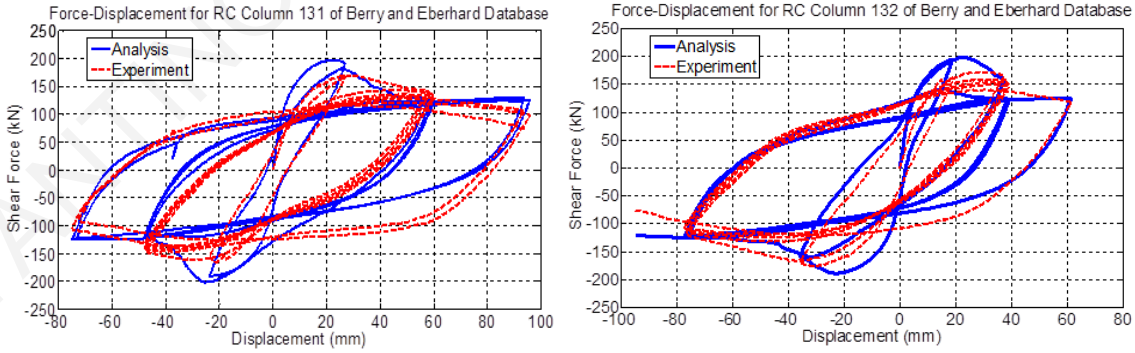

Concrete Model: Mander et al, 1988

Figure A.71: Comparison between numerical and experimental responses of rectangular columns (ID#131&132) of the database.

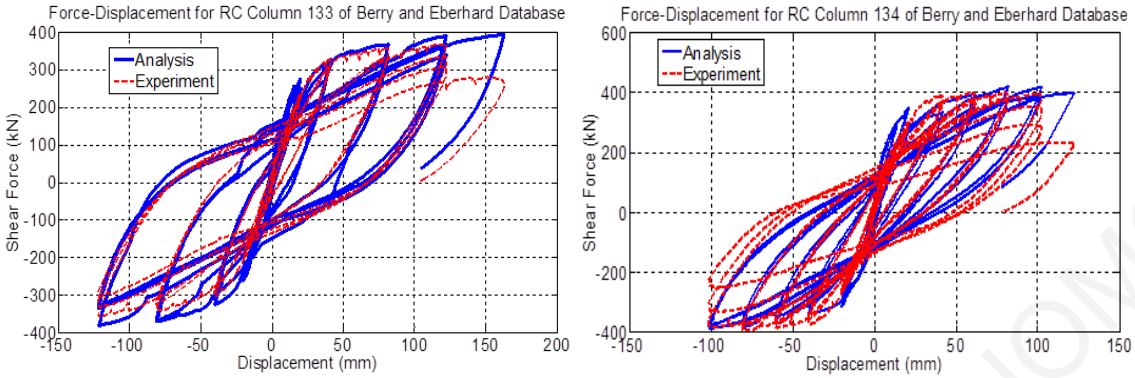

Concrete Model: Mander et al, 1988

Figure A.72: Comparison between numerical and experimental responses of rectangular columns (ID#133&134) of the database.

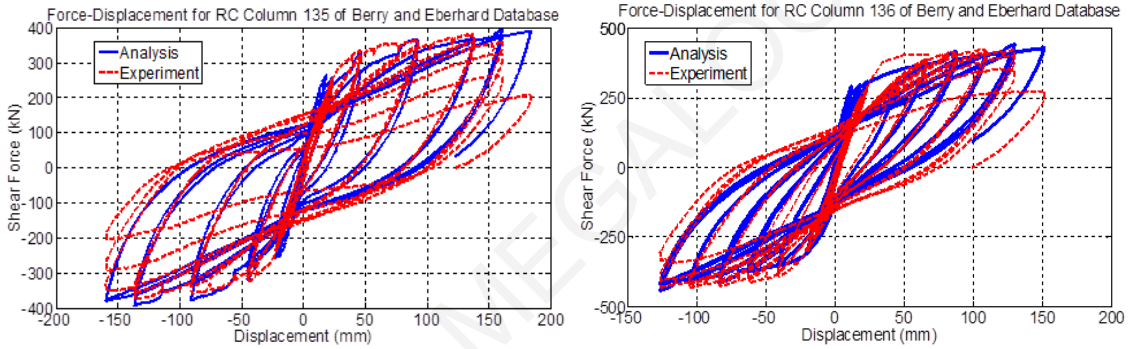

Concrete Model: Mander et al, 1988

Figure A.73: Comparison between numerical and experimental responses of rectangular columns (ID#135&136) of the database.

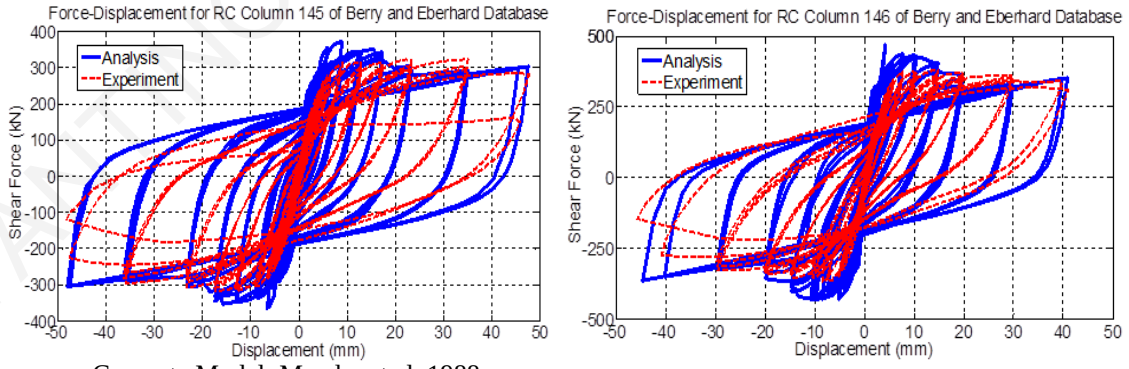

Concrete Model: Mander et al, 1988

Figure A.74: Comparison between numerical and experimental responses of rectangular columns (ID#145&146) of the database.

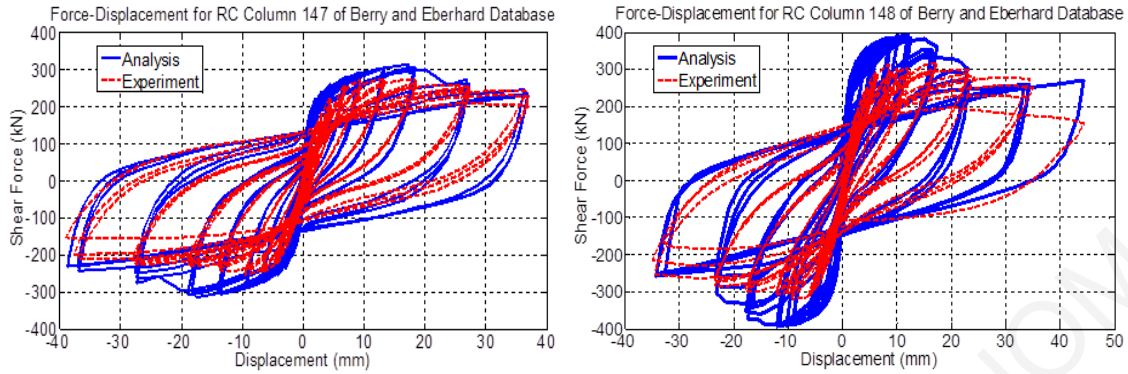

Concrete Model: Mander et al, 1988

Figure A.75: Comparison between numerical and experimental responses of rectangular columns (ID#147&148) of the database.

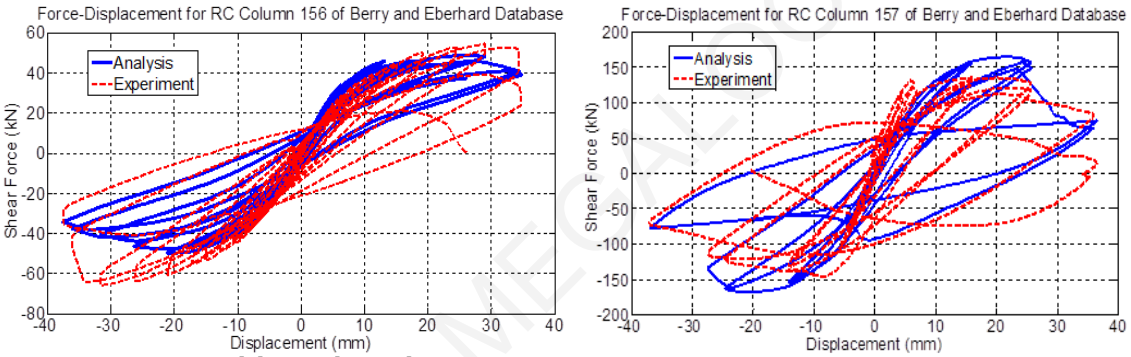

Concrete Model: Mander et al. 1988

Figure A.76: Comparison between numerical and experimental responses of rectangular columns (ID#156&157) of the database.

Table A.3: Reinforced Concrete Columns with a rectangular cross section, that failed in shear.

SpecimenID in Database	Axial Load (KN)	Width - Depth (mm)	Clear Cover (mm)	Shear Span (mm)	Concrete Strength (MPa)	Number of Longitudinal Bars	Diameter of Long. Bars (mm)	Yielding Strength of Long. Bars (MPa)	Ultimate Strength of Long. Bars (MPa)	Longitudinal Reinforcement ratio	Stirrups Spacing (mm)	Diameter of Stirrups (mm)	Stirrups Yielding Strength (MPa)	Transverse Reinforcement ratio
28	147	200-200	12	300	21.6	4	12.7	371	541	0.0127	35	5.5	344	0.0081
29	294	200-200	12	300	21	4	12.7	371	541	0.0127	20	5.5	344	0.0139
33	183	200-200	11	400	32	4	16	369	-	0.0201	50	5.5	316	0.0057
34	183	200-200	12.5	400	29.9	8	13	370	-	0.0265	50	5.5	316	0.0057
38	392	400-500	37	825	27.1	14	22	318	-	0.0266	100	9	336	0.0036
39	406	160-160	12.5	160	19.8	8	10	341	448	0.0222	40	5	559	0.0073
41	406	160-160	12.5	160	19.8	8	10	341	448	0.0222	40	5	559	0.0175
42	432	160-160	12.5	320	21.1	8	10	341	448	0.0222	40	5	559	0.0073
44	486	160-160	12.5	320	21.1	8	10	341	448	0.0222	40	5	559	0.0175
45	517	160-160	12.5	480	28.8	8	10	341	448	0.0222	40	5	559	0.0073
47	517	160-160	12.5	480	28.8	8	10	341	448	0.0222	40	5	559	0.0175

54	190	180-180	10	225	31.8	8	12.7	340	-	0.0313	64.3	4	249	0.0021
55	476	180-180	10	225	33	8	12.7	340	-	0.0313	64.3	4	249	0.0021
64	265	200-200	19	300	25.8	12	9.5	361	533	0.0213	70	6	426	0.0091
65	636	200-200	19	300	25.8	12	9.5	361	533	0.0213	70	6	426	0.0091
73	2632	278-278	28	323	46.3	16	13	441	-	0.0275	52	6	414	0.0089
74	189	152-304	35	876	34.7	4	19	496	835	0.0245	127	6.3	345	0.0033
76	178	152-304	35	876	26.1	4	19	496	835	0.0245	89	6.3	345	0.0048
78	178	152-304	35	876	33.6	4	19	496	835	0.0245	127	6.3	345	0.0033
80	111	152-304	35	876	33.6	4	19	496	835	0.0245	127	6.3	345	0.0033
82	178	152-304	35	876	33.4	4	19	496	835	0.0245	64	6.3	345	0.0067
84	178	152-304	32	876	33.5	4	19	496	835	0.0245	64	9.5	317	0.0147
86	178	152-304	32	876	33.5	4	19	496	835	0.0245	102	9.5	317	0.0092
98	534	230-410	25	455	34.9	10	19	441	745	0.0301	89	6	414	0.0028
99	534	410-230	25	455	34.9	10	19	441	745	0.0301	89	6	414	0.0031
100	1068	230-410	25	455	42	10	19	441	745	0.0301	89	6	414	0.0028
101	288	305-305	25	457	29.9	8	19	462	772	0.0244	210	6	414	0.0026

137	503	457-457	38.1	1473	26.9	8	31.75	330.96	496	0.0303	457.2	9.525	399.91	-
138	503	457-457	38.1	1473	33.1	8	25.4	330.96	496	0.0194	457.2	9.525	399.91	-
139	1512	457-457	38.1	1473	25.5	8	25.4	330.96	496	0.0194	457.2	9.525	399.91	-
140	1512	457-457	38.1	1473	27.6	8	31.75	330.96	496	0.0303	457.2	9.525	399.91	-
141	1512	457-457	38.1	1473	27.6	8	31.75	330.96	496	0.0303	304.8	9.525	399.91	-
142	503	457-457	38.1	1473	26.9	8	31.75	330.96	496	0.0303	457.2	9.525	399.91	-
143	503	457-457	38.1	1473	33.1	8	25.4	330.96	496	0.0194	457.2	9.525	399.91	-
144	1512	457-457	38.1	1473	25.5	8	31.75	330.96	496	0.0303	304.8	9.525	399.91	-
149	534	254-254	13	508	86	8	15.9	510	-	0.0246	51	6.4	449	0.0163
150	1068	254-254	13	508	86	8	15.9	510	-	0.0246	51	6.4	449	0.0163
199	0	914-457	38	1219	21.9	16	25	434	690	0.0188	406.4	9.53	400	-
200	0	457-914	38	1219	16	16	25	434	690	0.0188	406.4	9.53	400	-
212	667	457-457	65.13	1473	21.1	8	28.651	434.37	645	0.0247	304.8	9.525	476	0.0025
213	2669	457-457	65.13	1473	21.1	8	28.651	434.37	645	0.0247	304.8	9.525	476	0.0025
214	667	457-457	65.13	1473	21.8	8	28.651	434.37	645	0.0247	304.8	9.525	476	0.0025

276	507	406-610	22.23	1220	37.9	22	19.05	324	-	0.0253	127	6.35	358.5	-
277	507	406-610	22.23	1220	34.5	22	19.05	469	-	0.0253	127	6.35	324	-
278	507	406-610	22.23	915	32.4	22	19.05	469	-	0.0253	127	6.35	324	-
279	0	305-305	25.4	457.5	34.5	8	19.05	374		0.0245	65.3	6.35	455	-
280	534	305-305	25.4	457.5	30.7	8	19.05	455		0.0245	65.3	6.35	455	-
281	0	152-305	35	876	32	4	19	496	835	0.0245	127	6.3	345	0.0033
283	0	152-305	35	876	25.9	4	19	496	835	0.0245	89	6.3	345	0.0048

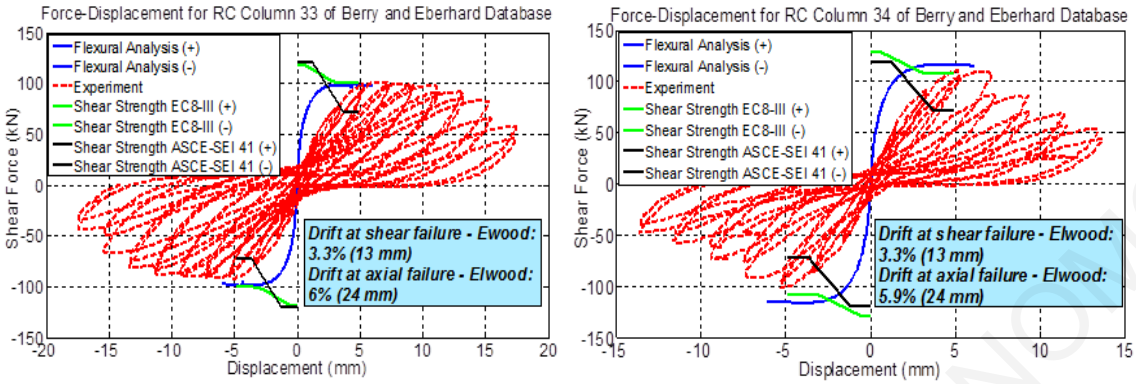

Concrete Model: Mander et al, 1988

Figure A.77: Comparison between numerical and experimental responses of rectangular columns (ID#33&34) of the database.

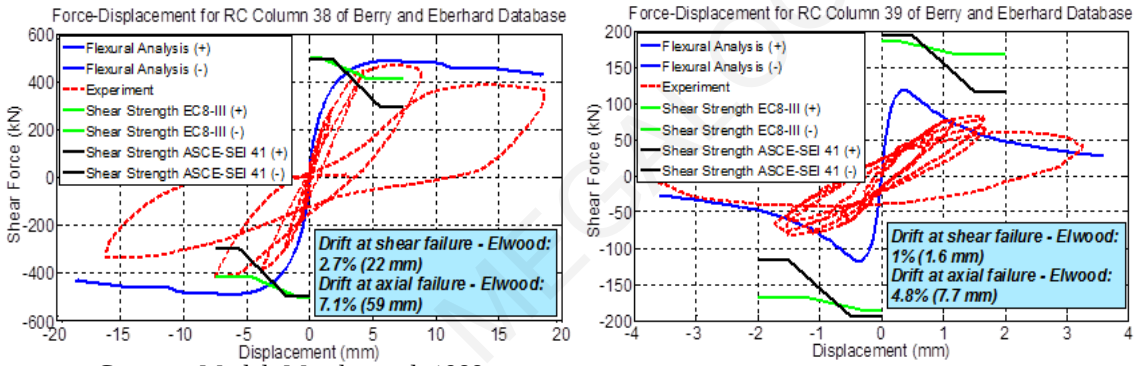

Concrete Model: Mander et al, 1988

Figure A.78: Comparison between numerical and experimental responses of rectangular columns (ID#38&39) of the database.

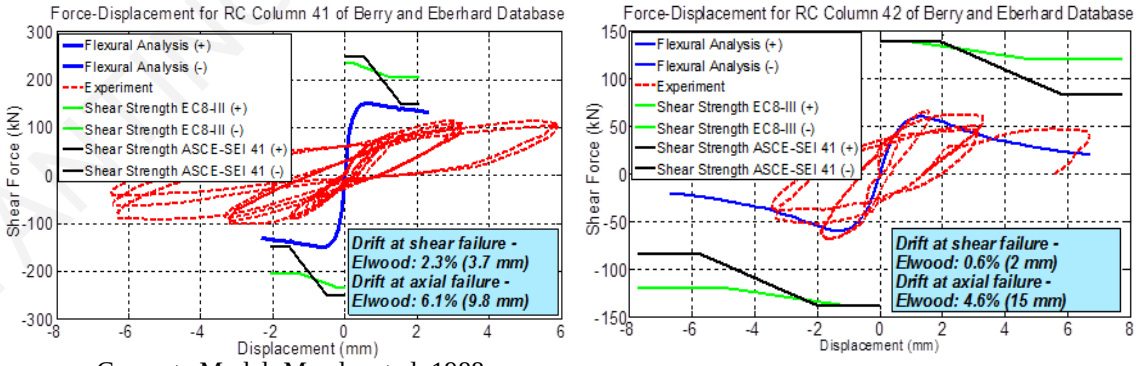

Concrete Model: Mander et al, 1988

Figure A.79: Comparison between numerical and experimental responses of rectangular columns (ID#41&42) of the database.

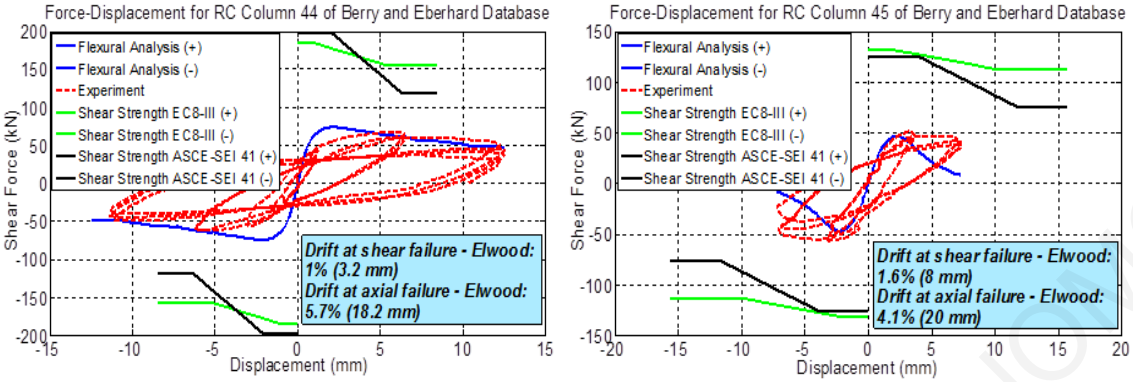

Concrete Model: Mander et al, 1988

Figure A.80: Comparison between numerical and experimental responses of rectangular columns (ID#44&45) of the database.

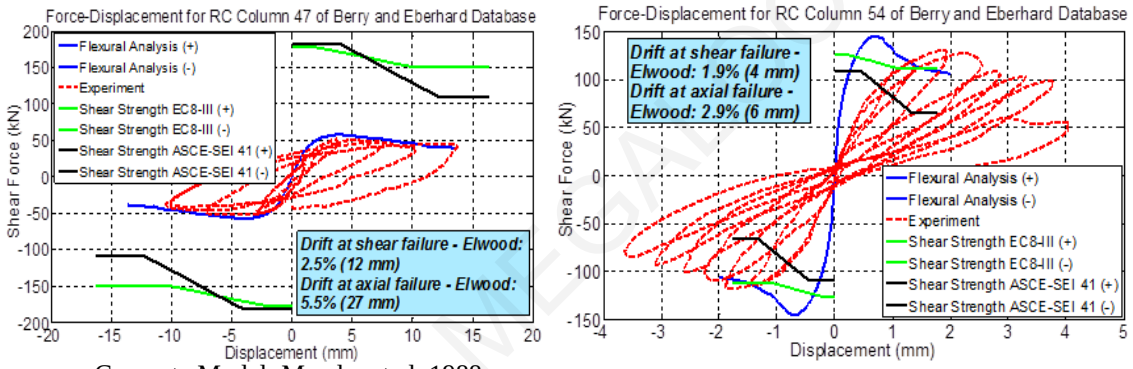

Concrete Model: Mander et al, 1988

Figure A.81: Comparison between numerical and experimental responses of rectangular columns (ID#47&54) of the database.

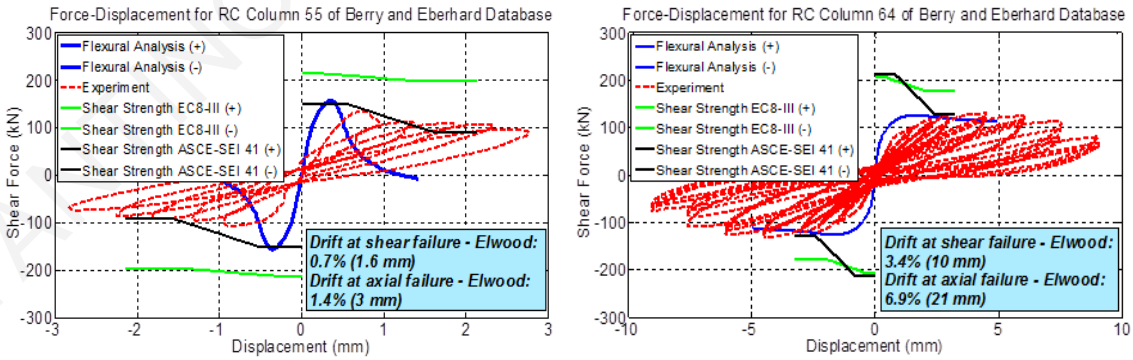

Concrete Model: Mander et al, 1988

Figure A.82: Comparison between numerical and experimental responses of rectangular columns (ID#55&64) of the database.

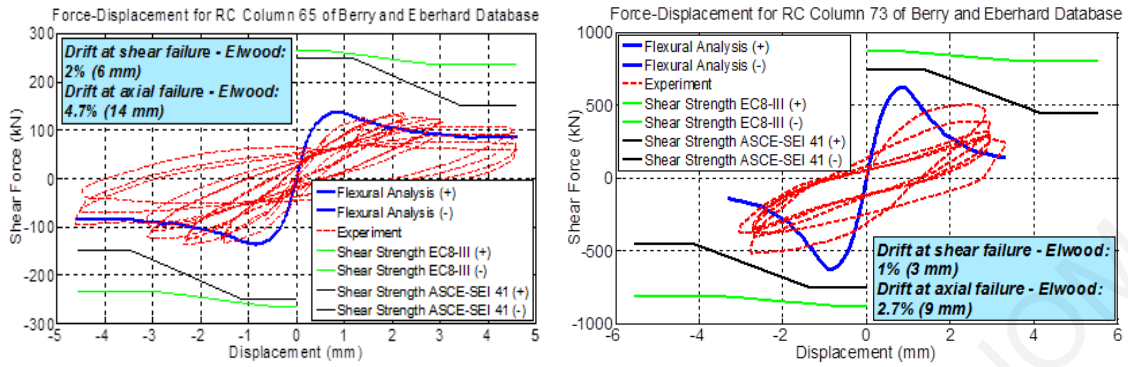

Concrete Model: Mander et al, 1988

Figure A.83: Comparison between numerical and experimental responses of rectangular columns (ID#65&73) of the database.

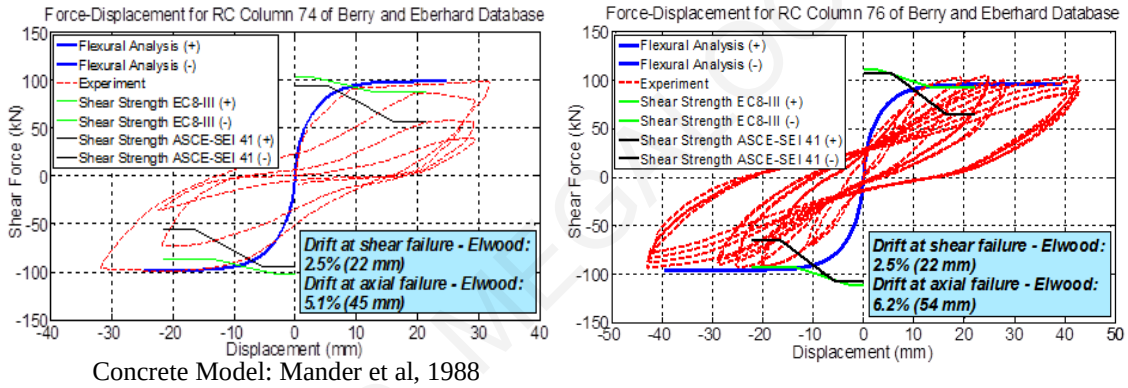

Concrete Model: Mander et al, 1988

Figure A.84: Comparison between numerical and experimental responses of rectangular columns (ID#74&76) of the database.

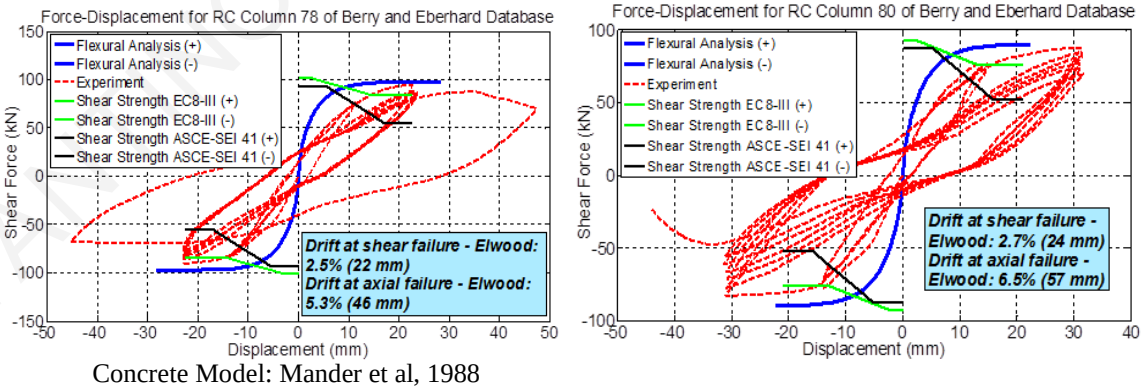

Concrete Model: Mander et al, 1988

Figure A.85: Comparison between numerical and experimental responses of rectangular columns (ID#78&80) of the database.

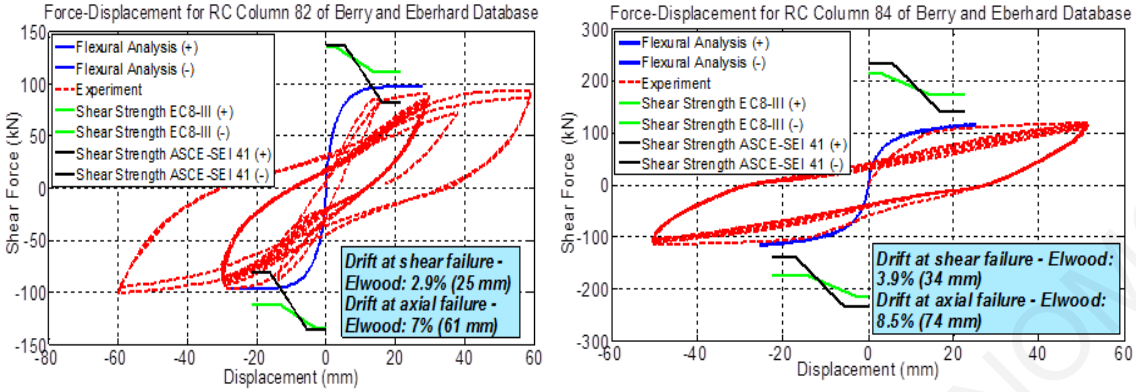

Concrete Model: Mander et al, 1988

Figure A.86: Comparison between numerical and experimental responses of rectangular columns (ID#82&84) of the database.

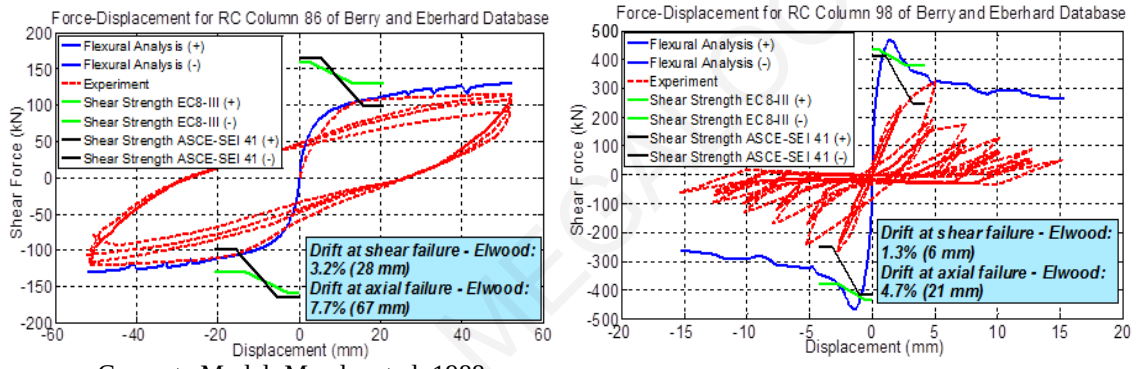

Concrete Model: Mander et al, 1988

Figure A.87: Comparison between numerical and experimental responses of rectangular columns (ID#86&98) of the database.

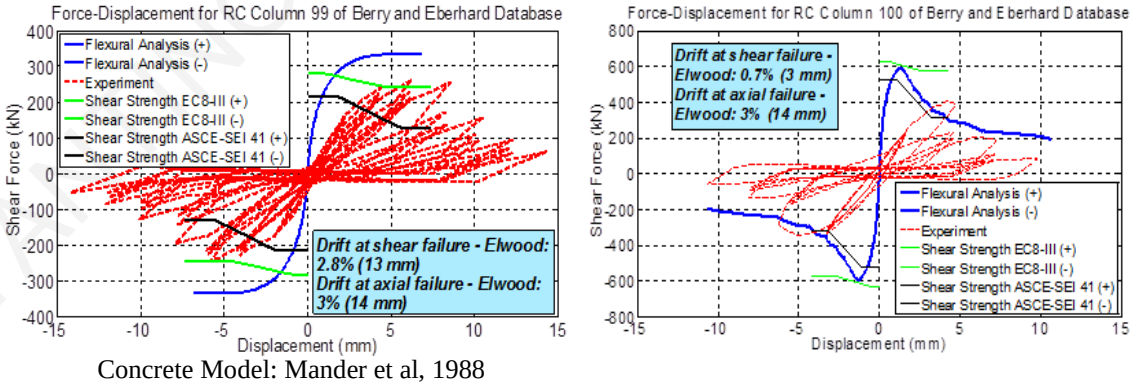

Concrete Model: Mander et al, 1988

Figure A.88: Comparison between numerical and experimental responses of rectangular columns (ID#99&100) of the database.

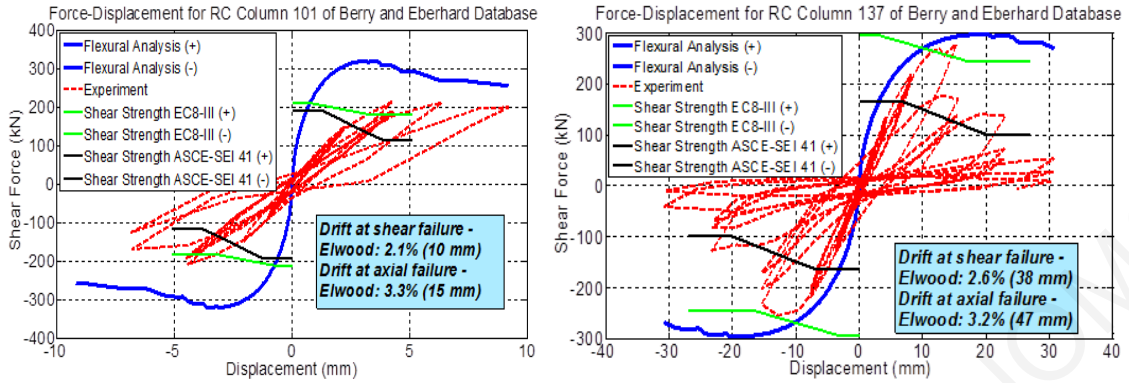

Concrete Model: Mander et al, 1988

Figure A.89: Comparison between numerical and experimental responses of rectangular columns (ID#101&137) of the database.

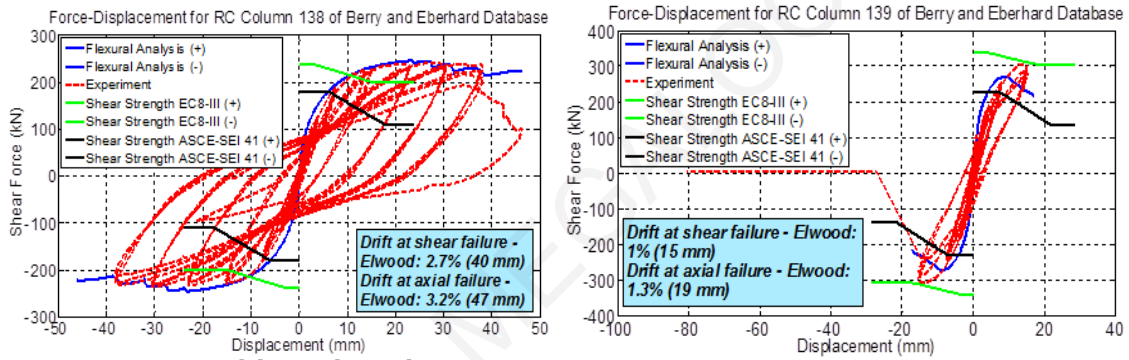

Concrete Model: Mander et al, 1988

Figure A.90: Comparison between numerical and experimental responses of rectangular columns (ID#138&139) of the database.

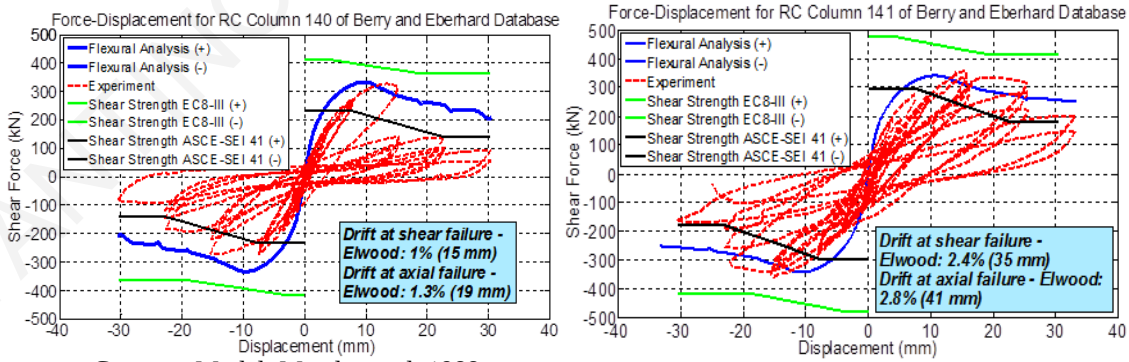

Concrete Model: Mander et al, 1988

Figure A.91: Comparison between numerical and experimental responses of rectangular columns (ID#140&141) of the database.

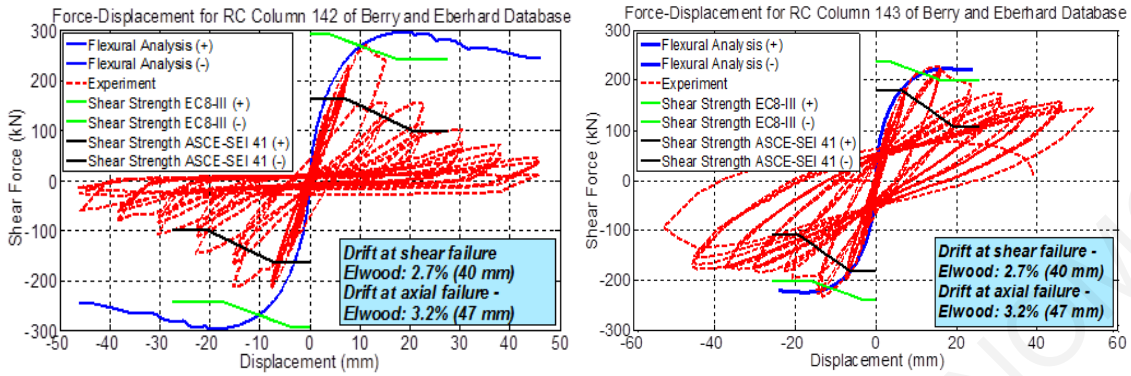

Concrete Model: Mander et al, 1988

Figure A.92: Comparison between numerical and experimental responses of rectangular columns (ID#142&143) of the database.

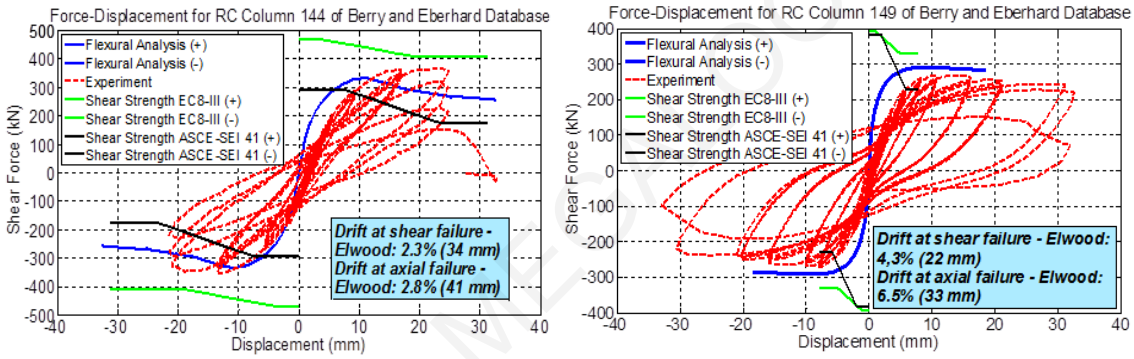

Concrete Model: Mander et al, 1988

Figure A.93.: Comparison between numerical and experimental responses of rectangular columns (ID#144&149) of the database.

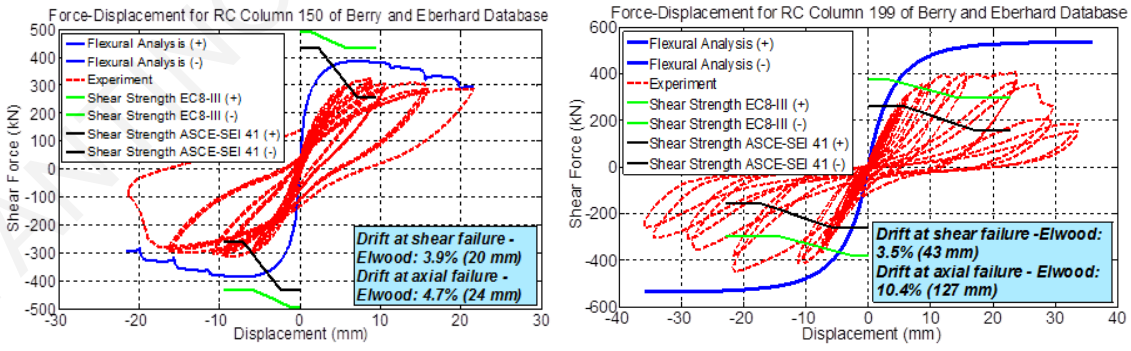

Concrete Model: Mander et al, 1988

Figure A.94: Comparison between numerical and experimental responses of rectangular columns (ID#150&199) of the database.

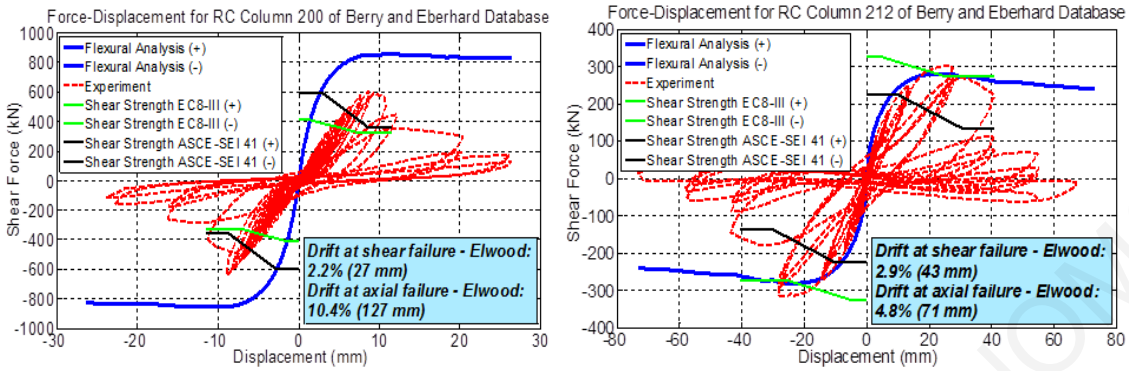

Concrete Model: Mander et al, 1988

Figure A.95: Comparison between numerical and experimental responses of rectangular columns (ID#200&212) of the database.

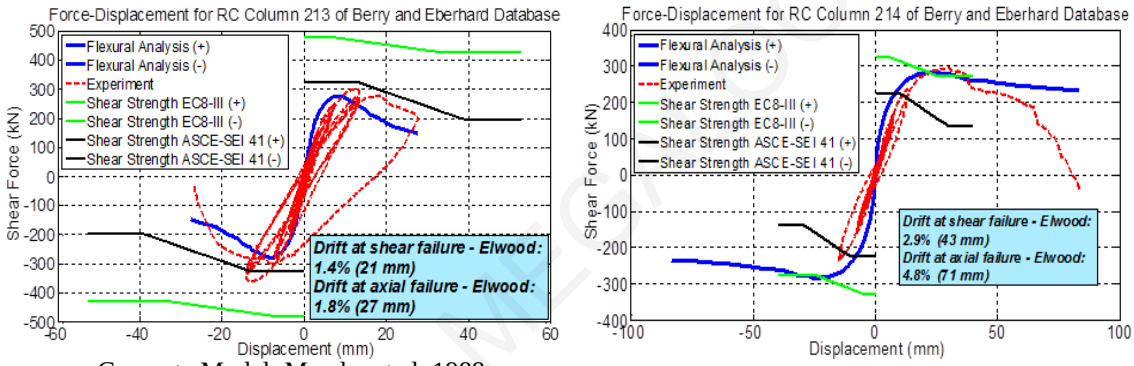

Concrete Model: Mander et al, 1988

Figure A.96: Comparison between numerical and experimental responses of rectangular columns (ID#213&214) of the database.

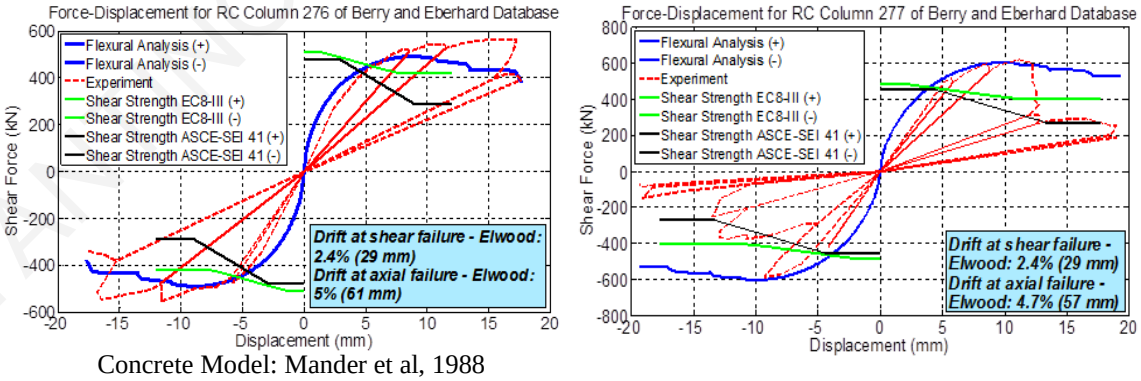

Concrete Model: Mander et al, 1988

Figure A.97: Comparison between numerical and experimental responses of rectangular columns (ID#276&277) of the database.

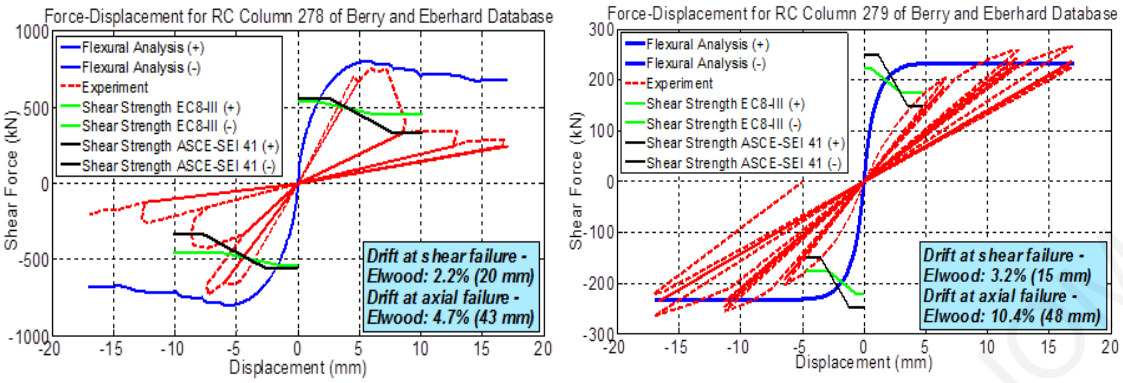

Concrete Model: Mander et al, 1988

Figure A.98: Comparison between numerical and experimental responses of rectangular columns (ID#278&279) of the database.

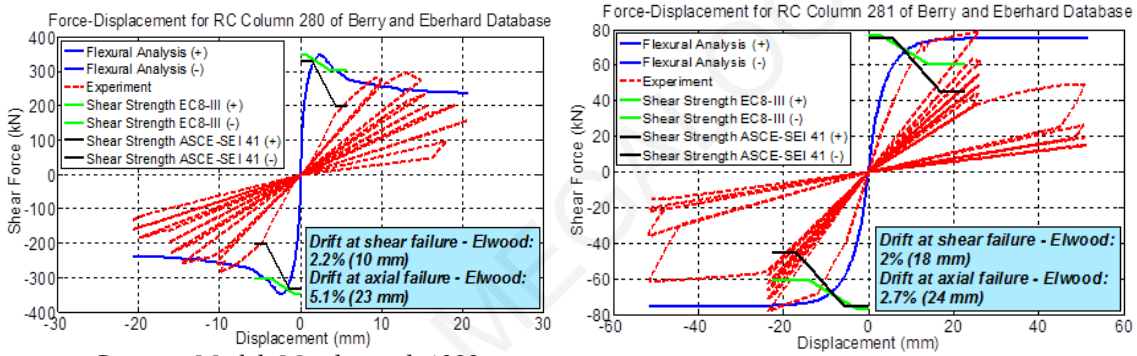

Concrete Model: Mander et al, 1988

Figure A.99: Comparison between numerical and experimental responses of rectangular columns (ID#280&281) of the database.

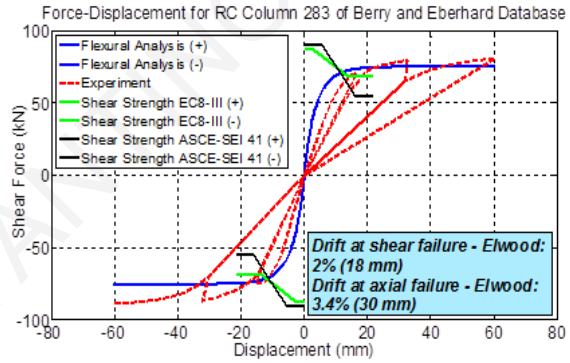

Concrete Model: Mander et al, 1988

Figure A.100.: Comparison between numerical and experimental response of rectangular column (ID#283) of the database.

Table A.4: Reinforced Concrete Columns with a circular cross section, that failed in shear.

SpecimenID in Database	Axial Load (KN)	Diameter	Cover to Ctr. of Hoop Bar	Shear Span (mm)	Concrete Strength (MPa)	Number of Longitudinal Bars	Diameter of Long. Bars (mm)	Yielding Strength of Long. Bars (MPa)	Ultimate Strength of Long. Bars (MPa)	Longitudinal Reinforcement ratio (%)	Hoop Spacing (mm)	Diameter of Spiral (mm)	Yielding Strength Spiral (MPa)	Transverse Reinforcement ratio (%)
14	0	400	18	800	37.5	20	16	436	674	3.2	60	6	328	0.51
15	0	400	18	800	37.2	20	16	296	457	3.2	60	6	328	0.51
16	0	400	18	1000	36	20	16	436	674	3.2	60	6	328	0.51
17	0	400	20	800	30.6	20	16	436	674	3.2	165	10	316	0.51
18	0	400	18	800	31.1	20	16	436	674	3.2	40	6	328	0.76
19	0	400	18	600	30.1	20	16	436	674	3.2	60	6	328	0.51
20	0	400	18	800	29.5	20	16	448	693	3.2	80	6	372	0.38
21	721	400	18	800	28.7	20	16	448	693	3.2	30	6	372	1.02
23	784	400	21	800	31.2	20	16	448	693	3.2	120	12	332	1.02
24	751	400	18	800	29.9	20	16	448	693	3.2	60	6	372	0.51
25	359	400	18	600	28.6	20	16	436	674	3.2	30	6	328	1.02

26	455	400	18	800	36.2	20	16	436	679	3.2	30	6	326	1.02
27	0	400	18	800	33.7	9	24	424	671	3.24	60	6	326	0.51
28	0	400	18	800	34.8	12	16	436	679	1.92	60	6	326	0.51
29	420	400	18	800	33.4	20	16	436	679	3.2	60	6	326	0.51
30	431	400	18	1000	34.3	20	16	436	679	3.2	60	6	326	0.51
31	440	400	18	600	35	20	16	436	674	3.2	60	6	326	0.51
32	432	400	18	600	34.4	20	16	436	679	3.2	80	6	326	0.38
33	807	400	18	700	36.7	20	16	482	758	3.2	80	6	326	0.38
34	0	400	18	800	33.2	20	16	436	679	3.2	80	6	326	0.38
35	0	400	20	800	30.9	20	16	436	679	3.2	220	10	310	0.39
36	0	400	21	800	32.3	20	16	436	679	3.2	160	12	332	0.76
37	0	400	20	800	33.1	20	16	436	679	3.2	110	10	310	0.77
44	1813	400	18	800	37	20	16	475	625	3.2	65	6	340	0.47
48	145	307	36	900	35.9	12	12	240	-	1.83	75	6	240	0.63
49	254	307	36	895	34.4	12	12	240	-	1.83	75	6	240	0.63
104	503	610	15.88	914.5	30	12	12.7	462	-	0.52	76.2	6.4	361	0.28

105	503	610	15.88	914.5	30	24	12.7	462	-	1.04	127	6.4	361	0.17
108	-634	457	24.76	910	39.2	20	15.875	427.5	-	2.41	60	9.5	430.2	1.14
110	850	457	26.35	910	35	30	19.05	468.2	-	5.21	45	12.7	434.4	2.7
111	-490	457	24.76	910	35.2	20	15.875	507.5	-	2.41	80	9.5	448.2	0.85
159	0	406.4	10.44	1047.8	34.7	14	12.7	458.5	646	1.37	171.45	4.5	691.5	0.1
161	0	406.4	10.44	1047.8	35.4	12	12.7	458.5	646	1.17	63.5	4.5	691.5	0.26
163	18.8	609.6	18.63	1219.2	29..8	20	15.875	454	729.6	1.36	101.6	4.9	200	0.13
164	18.8	609.6	18.63	1219.2	26.8	20	15.875	454	729.6	1.36	101.6	4.9	200	0.13
165	18.8	609.6	18.63	1219.2	31.2	20	15.875	437.6	688	1.36	101.6	4.9	200	0.13
166	356	1828.8	57.15	3658	29.6	24	43	508	797	1.33	304.8	12.7	298	0.1
168	0	564	24	1000	39.8	40	13	324.5	-	-	250	9	259.6	0.1

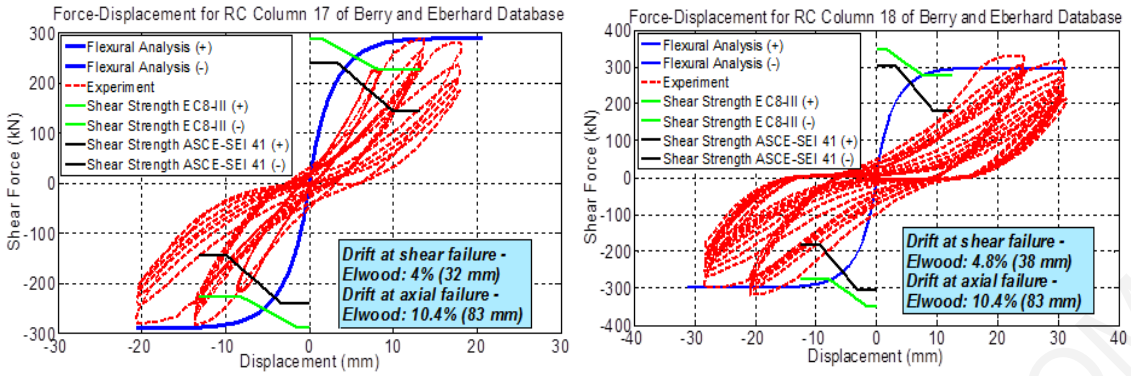

Concrete Model: Mander et al, 1988

Figure A.101: Comparison between numerical and experimental responses of circular columns (ID#17&18) of the database.

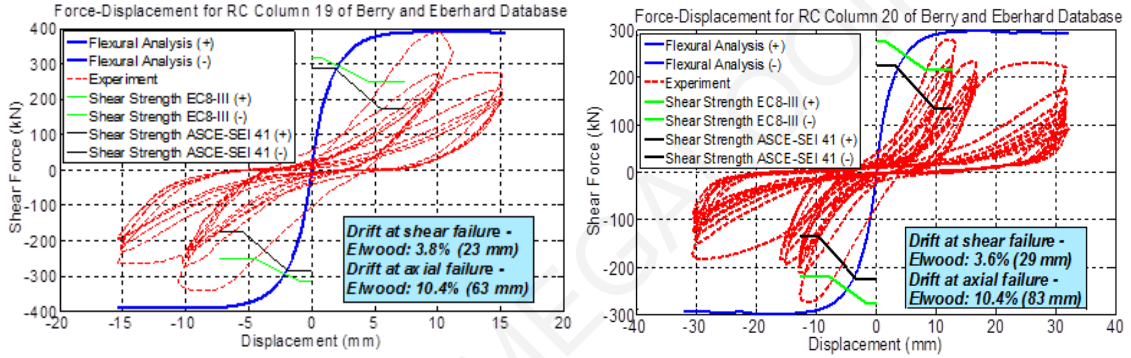

Concrete Model: Mander et al, 1988

Figure A.102: Comparison between numerical and experimental responses of circular columns (ID#19&20) of the database.

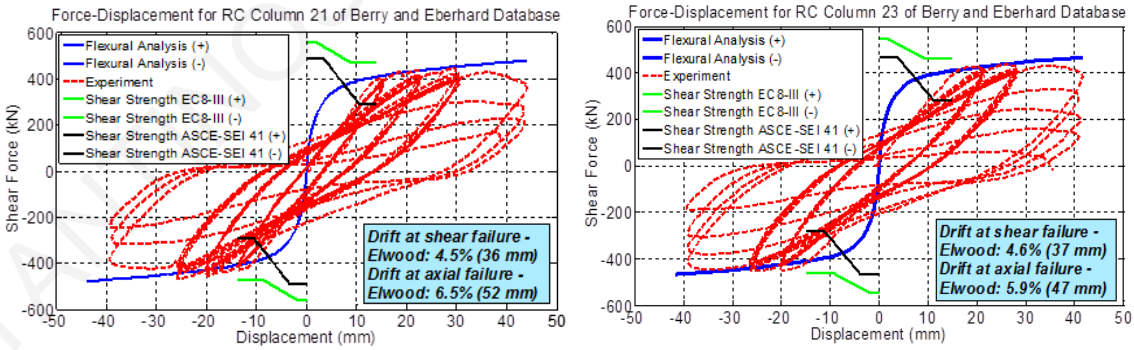

Concrete Model: Mander et al, 1988

Figure A.103: Comparison between numerical and experimental responses of circular columns (ID#21&23) of the database.

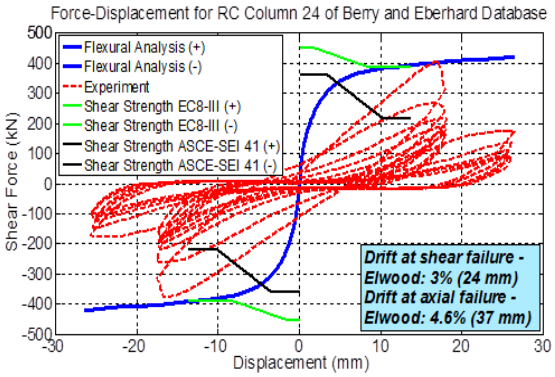

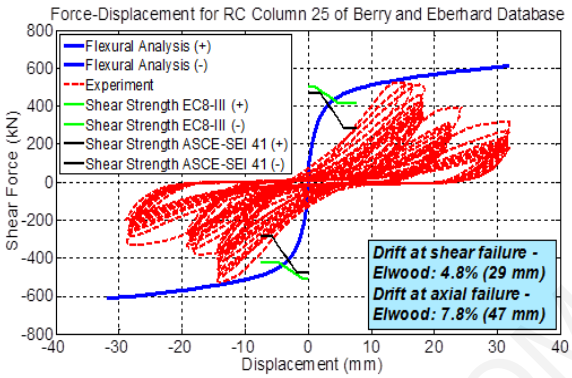

Concrete Model: Mander et al, 1988

Figure A.104: Comparison between numerical and experimental responses of circular columns (ID#24&25) of the database.

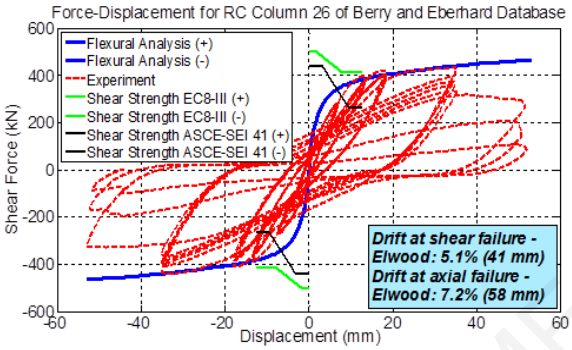

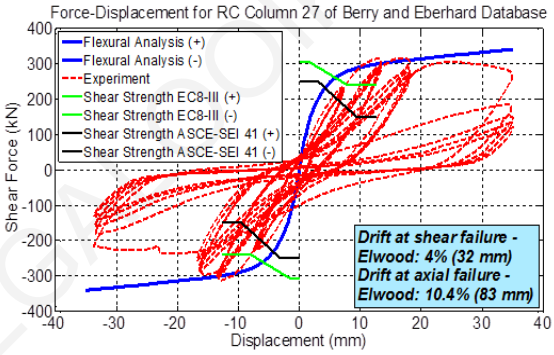

Concrete Model: Mander et al, 1988

Figure A.105: Comparison between numerical and experimental responses of circular columns (ID#26&27) of the database.

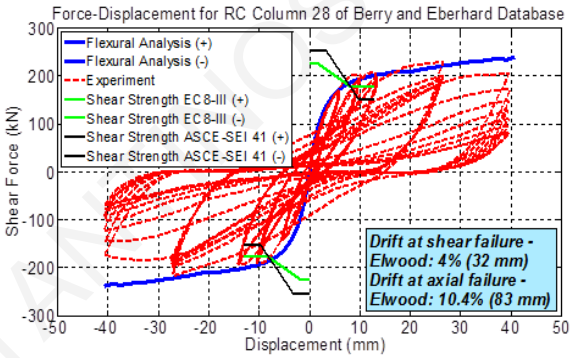

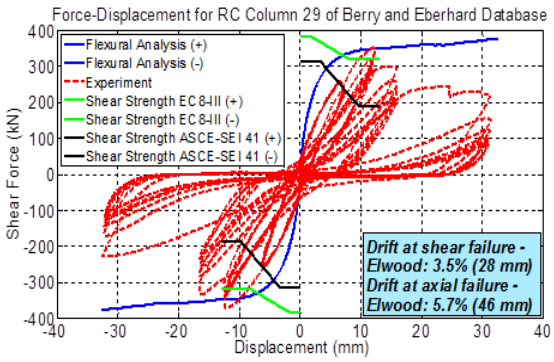

Concrete Model: Mander et al, 1988

Figure A.106: Comparison between numerical and experimental responses of circular columns (ID#28&29) of the database.

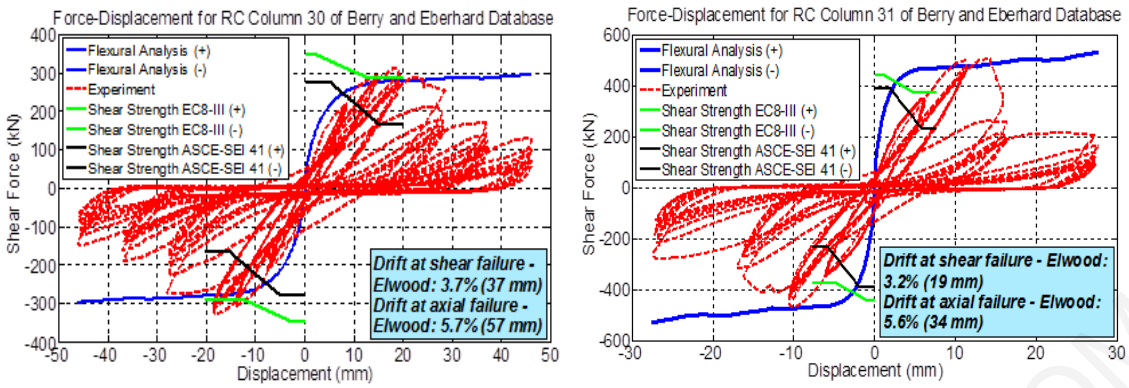

Concrete Model: Mander et al, 1988

Figure A.107: Comparison between numerical and experimental responses of circular columns (ID#30&31) of the database.

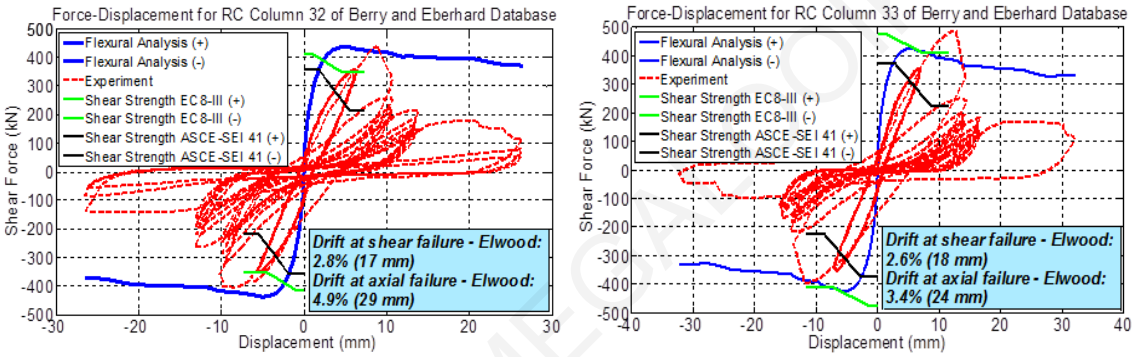

Concrete Model: Mander et al, 1988

Figure A.108: Comparison between numerical and experimental responses of circular columns (ID#32&33) of the database.

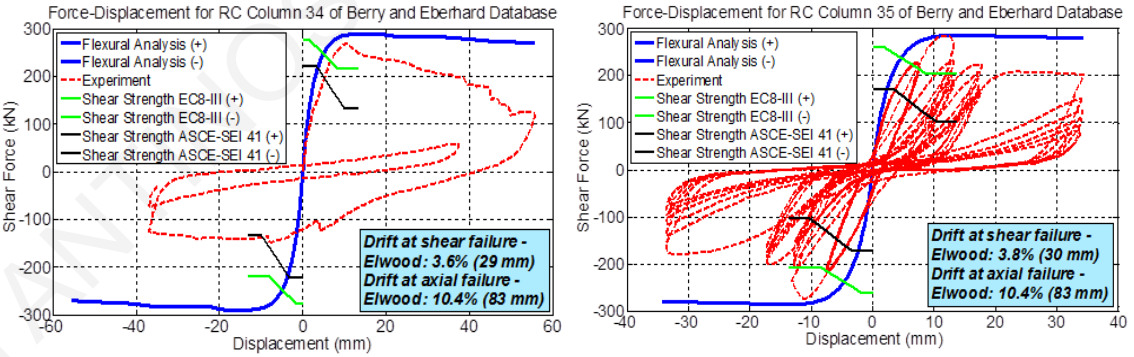

Concrete Model: Mander et al, 1988

Figure A.109: Comparison between numerical and experimental responses of circular columns (ID#34&35) of the database.

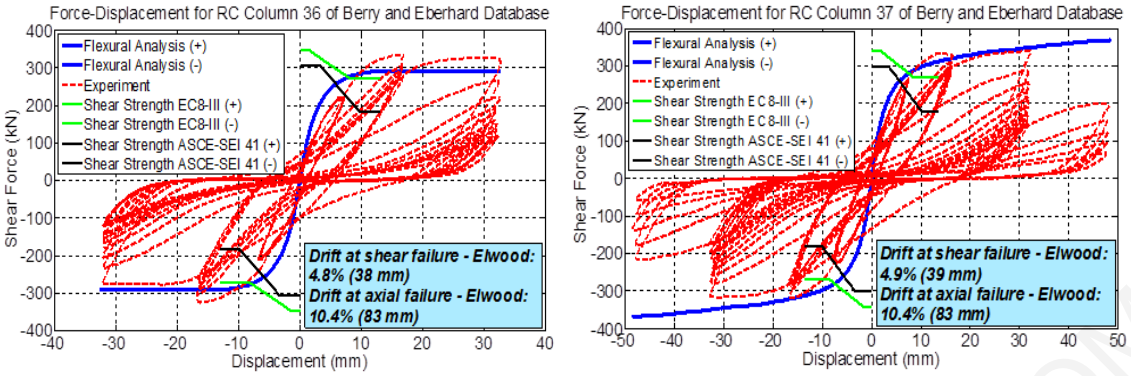

Concrete Model: Mander et al, 1988

Figure A.110: Comparison between numerical and experimental responses of circular columns (ID#36&37) of the database.

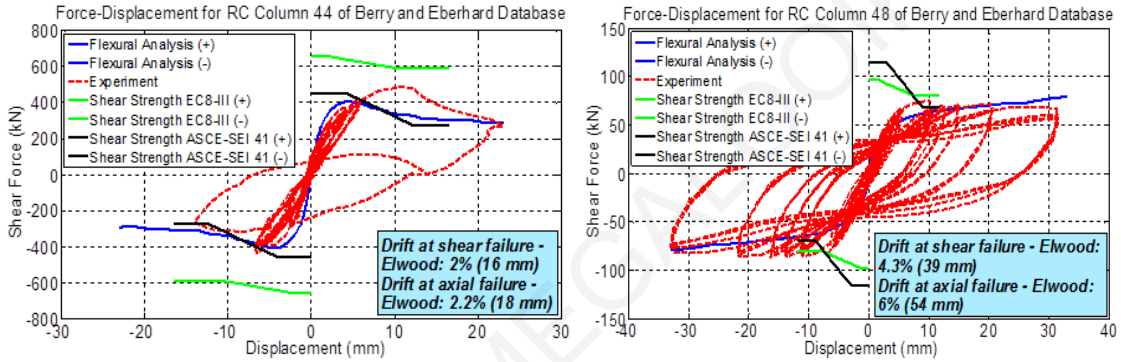

Concrete Model: Mander et al, 1988

Figure A.111: Comparison between numerical and experimental responses of circular columns (ID#44&48) of the database.

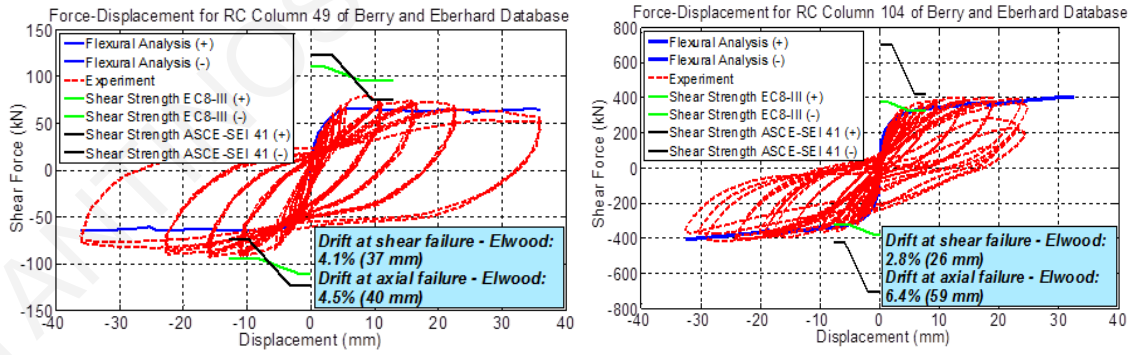

Concrete Model: Mander et al, 1988

Figure A.112: Comparison between numerical and experimental responses of circular columns (ID#49&104) of the database.

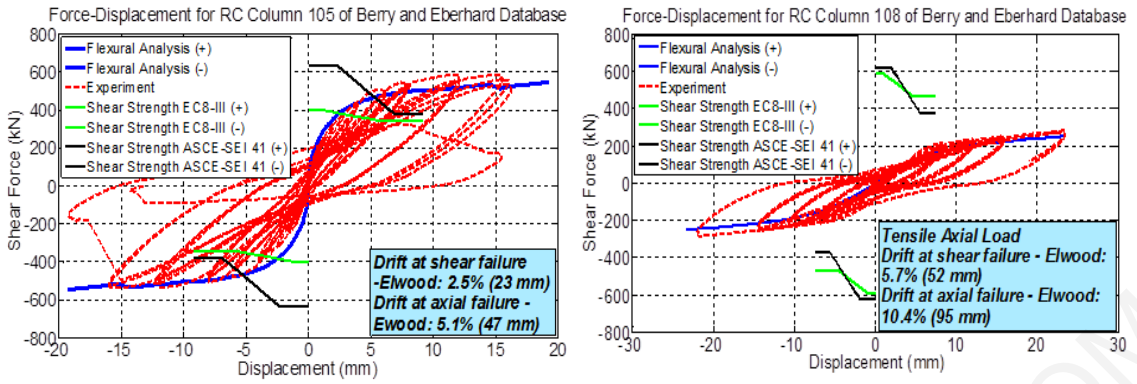

Concrete Model: Mander et al, 1988

Figure A.113: Comparison between numerical and experimental responses of circular columns (ID#105&108) of the database.

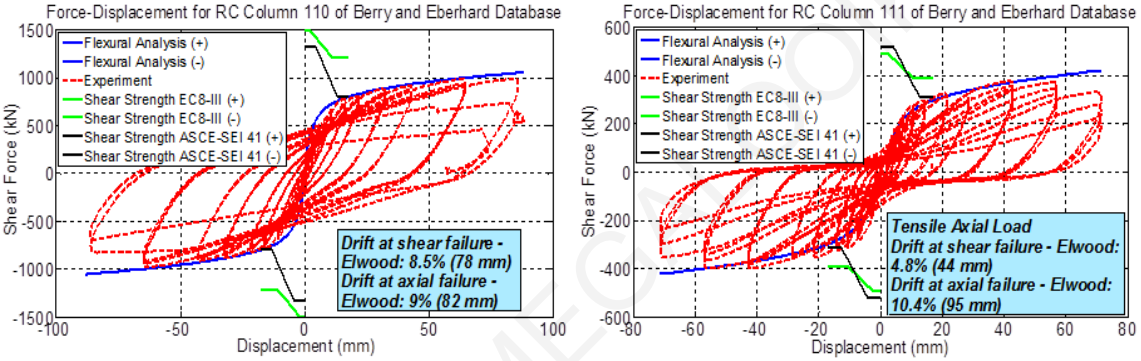

Concrete Model: Mander et al, 1988

Figure A.114: Comparison between numerical and experimental responses of circular columns (ID#110&111) of the database.

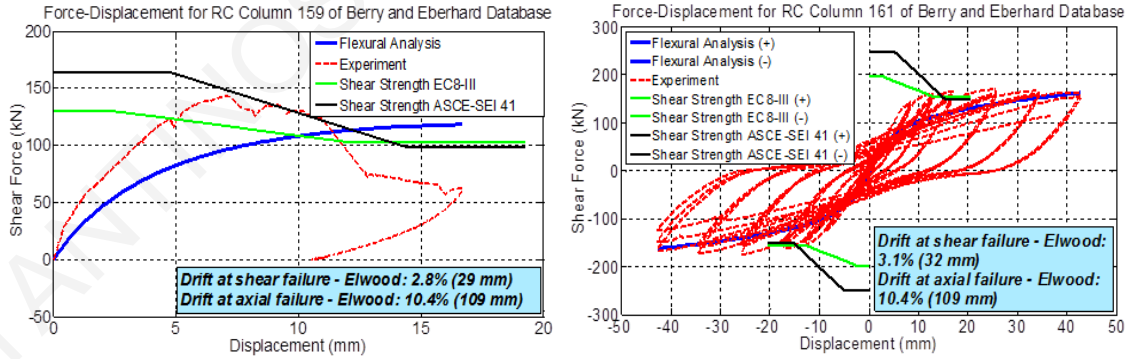

Concrete Model: Mander et al, 1988

Figure A.115: Comparison between numerical and experimental responses of circular columns (ID#159&161) of the database.

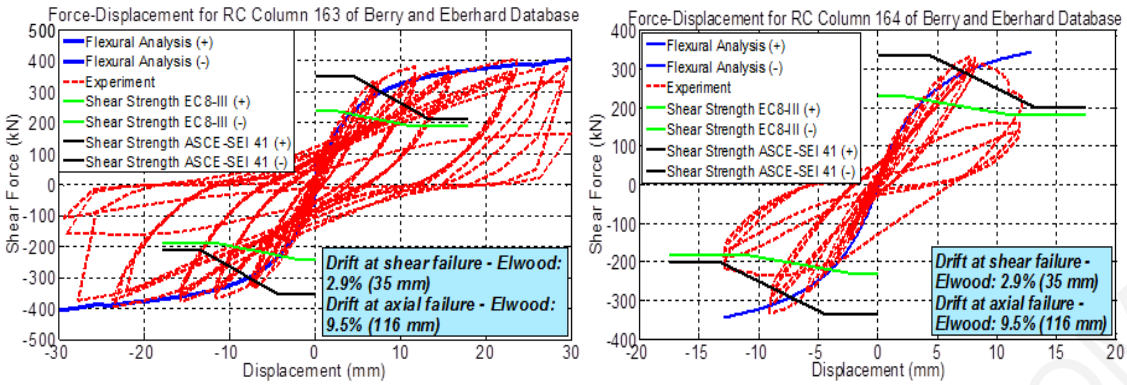

Concrete Model: Mander et al, 1988

Figure A.116: Comparison between numerical and experimental responses of circular columns (ID#163&164) of the database.

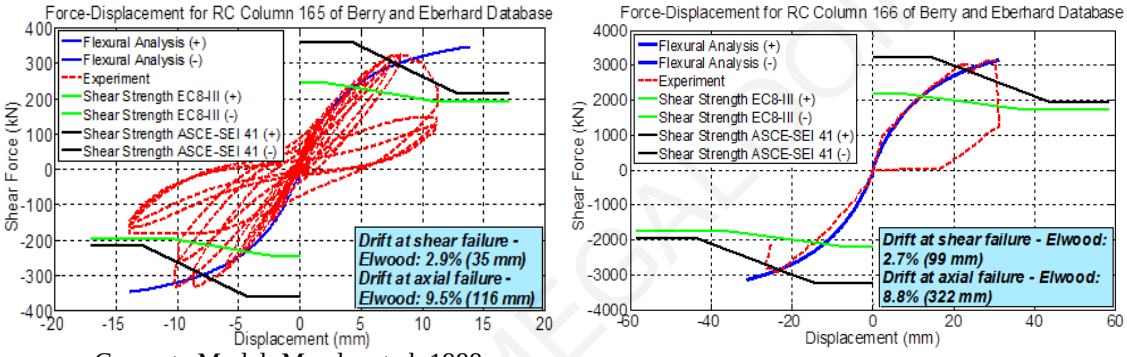

Concrete Model: Mander et al, 1988

Figure A.117: Comparison between numerical and experimental responses of circular columns (ID#165&166) of the database.

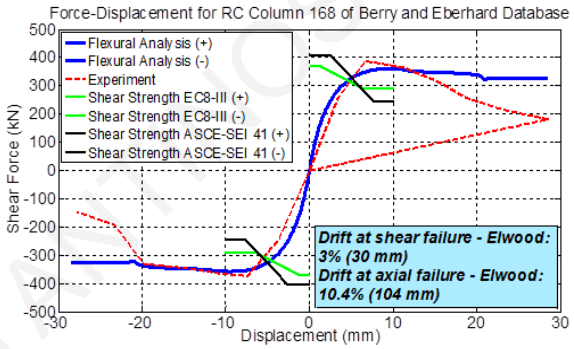

Concrete Model: Mander et al, 1988

Figure A.118: Comparison between numerical and experimental response of circular column (ID#168) of the database.

Table A.5: Reinforced Concrete Columns under variable axial load (Tensile Axial Load is negative).

Specimen ID	Researcher	Diameter or Width - Depth (mm)	Cover to Ctr. of Long. Bar (mm)	Shear Span (mm)	Concrete Strength (MPa)	Number of Longitudinal Bars	Diameter of Long. Bars (mm)	Yielding Strength of Long. Bars (MPa)	Hoop Spacing (mm)	Diameter of Hoop (mm)	Yielding Strength Spiral (MPa)	Mode of failure	Max Axial Load (+/- Lat. Loading) (KN)	Axial Load Case
Specimen No. 2	Y.Xiao	406.4	13	1575	49.3	12	12.5	489.5	32	4.52	468.8	Flexure	-70.45 81.52	tan(47.32°) Lateral Force
Specimen 3	J.P. Moehle	457-457	41.3	1473	20.9	8	28.7	438	305	9.5	476	Shear - Flexure	-250 2670	1110 + 4.67V 1110-5.83V
Specimen ICC	A.S. Elnashai	609.6	25.4	1295.5	43.4	16	25.4	427.5	63.5	9.5	517.1	Shear - Flexure	1112	Constant
Specimen ICT	A.S. Elnashai	609.6	25.4	1295.5	43.4	16	25.4	427.5	63.5	9.5	517.1	Flexure	-222	Constant
VCL1L	A.S Elnashai	60.96	2.54	121.92	31.5	20	2.087	434	8.787	0.884	310	Shear - Flexure	21.24 1.57	Variable Axial Load

VCL1P	A.S Elnashai	60.96	2.54	121.92	31.5	20	2.087	434	8.787	0.884	310	Shear - Axial	25.93 6.12	Variable Axial Load
VCL1U	A.S Elnashai	60.96	2.54	121.92	31.5	20	2.087	434	8.787	0.884	310	Shear - Flexure	16.55 6.1	Variable Axial Load
VTL1L	A.S Elnashai	60.96	2.54	121.92	31.5	20	2.087	434	8.787	0.884	310	Shear - Axial	1.66 24.18	Variable Axial Load
VTL1P	A.S Elnashai	60.96	2.54	121.92	31.5	20	2.087	434	8.787	0.884	310	Shear - Axial	3.24 24.45	Variable Axial Load
VTL1U	A.S Elnashai	60.96	2.54	121.92	31.5	20	2.087	434	8.787	0.884	310	Shear - Axial	5.31 18.85	Variable Axial Load
VCS1P	A.S Elnashai	60.96	2.54	121.92	31.5	20	2.087	434	8.787	0.884	310	Shear - Axial	20.59 0.648	Variable Axial Load
VCS4P	A.S Elnashai	60.96	2.54	121.92	31.5	20	2.087	434	8.787	0.884	310	Shear - Axial	20.59 20.58	Variable Axial Load
VCS8P	A.S Elnashai	60.96	2.54	121.92	31.5	20	2.087	434	8.787	0.884	310	Shear - Axial	13.53 20.69	Variable Axial Load

VCL4P	A.S Elnashai	60.96	2.54	121.92	31.5	20	2.087	434	8.787	0.884	310	Shear - Axial	15.87 24.82	Variable Axial Load
VCL8P	A.S Elnashai	60.96	2.54	121.92	31.5	20	2.087	434	8.787	0.884	310	Shear - Axial	15.8 27.58	Variable Axial Load
VTS1P	A.S Elnashai	60.96	2.54	121.92	31.5	20	2.087	434	8.787	0.884	310	Shear - Flexure	1.95 20.59	Variable Axial Load
VTS4P	A.S Elnashai	60.96	2.54	121.92	31.5	20	2.087	434	8.787	0.884	310	Shear - Axial	17.23 20.77	Variable Axial Load
VTS8P	A.S Elnashai	60.96	2.54	121.92	31.5	20	2.087	434	8.787	0.884	310	Shear - Axial	20.59 20.59	Variable Axial Load
VTL4P	A.S Elnashai	60.96	2.54	121.92	31.5	20	2.087	434	8.787	0.884	310	Shear - Flexure	19.03 16.27	Variable Axial Load
CS1	M.J.N. Priestley	460	15.24	915	29.3	20	15.87	462	95.3	6.35	369	Shear - Flexure	1690	Constant
CS2	M.J.N. Priestley	460	15.24	915	35.8	20	15.87	462	95.3	6.35	369	Shear - Flexure	-512	Constant

CS3	M.J.N. Priestley	460	15.24	915	37	20	15.87	462	95.3	6.35	369	Shear - Flexure	1690	589+2.25V
													-512	589-3.39V
CS4	M.J.N. Priestley	460	15.24	915	32.3	30	19.05	534	95.3	6.35	369	Bond Failure	1690	589+2.25V
													-512	589-3.39V